Systematic Analysis and Design of Multimode Antennas Based on Symmetry Properties of Characteristic Modes

Von der Fakultät für Elektrotechnik und Informatik
der Gottfried Wilhelm Leibniz Universität Hannover
zur Erlangung des akademischen Grades

Doktor-Ingenieur
(Dr.-Ing.)

genehmigte Dissertation

von Herrn
M. Sc. Nikolai Peitzmeier

2021

1. Referent:
Professor Dirk Manteuffel

2. Referent:
Professor Miloslav Čapek

Vorsitzender der Prüfungskommission:
Professor Heyno Garbe

Tag der Promotion:
15.07.2021

Danksagung

Diese Dissertation entstand während meiner Tätigkeit als wissenschaftlicher Mitarbeiter am Institut für Hochfrequenztechnik und Funksysteme der Leibniz Universität Hannover. An dieser Stelle möchte ich mich herzlichst bei allen Personen bedanken, die mich während dieser Zeit unterstützt haben.

Mein besonderer Dank gilt Prof. Dr.-Ing. Dirk Manteuffel, der mir die Möglichkeit zur Promotion in diesem spannenden Themenfeld gab und mir jederzeit mit Rat und Tat zur Seite stand. Des Weiteren möchte ich mich bei apl. Prof. Dr.-Ing. Bernd Geck bedanken, der mich nach meinem Studium als wissenschaftlicher Mitarbeiter einstellte. Mein weiterer Dank gilt Prof. Dr.-Ing. Heyno Garbe für die Übernahme des Vorsitzes der Prüfungskommission sowie Prof. Miloslav Čapek für seine Tätigkeit als Zweitgutachter.

Weiterhin möchte ich mich herzlich bei meinen ehemaligen Kolleginnen und Kollegen am Institut für Hochfrequenztechnik und Funksysteme für anregende Diskussionen, das angenehme Arbeitsklima und die viele Unterstützung bedanken. Dieser Dank gilt insbesondere Herrn Dr.-Ing. Johannes Meyer, Herrn Eckhard Denicke, Herrn Christian Zietz, Herrn Dr.-Ing. Quang Huy Dao, Frau Dr.-Ing. Aline Friedrich, Herrn Steffen Probst, Herrn Henning Hartmann, Herrn Bernard Lüers, Herrn Lukas Berkelmann, Herrn Steffen Seewald, Herrn Timo Martinelli, Herrn Lukas Grundmann, Herrn Axel Hoffmann, Herrn Leonardo Mörlein, Frau Saba Harke sowie Herrn Eckehard Batzdorfer und Frau Bettina Richter.

Außerdem sei an dieser Stelle allen Studierenden gedankt, die mich im Rahmen einer Abschlussarbeit oder als studentische Hilfskraft bei meiner Arbeit unterstützten, insbesondere Herrn Ghaleb Albeesh, Herrn Tarek Alhasan, Herrn Quy Le Xuan, Frau Gülsüm Elif Gül, Herrn Lennart Trunk und Herrn Adrian Mrochen. Mein besonderer Dank gilt hierbei Herrn Tim Hahn für sein unermüdliches Engagement beim Entwurf des Prototypen.

Schließlich bedanke ich mich bei meiner Familie und meiner Frau dafür, dass sie mir über all die Jahre stets den Rücken freigehalten haben.

Kurzfassung

Diese Arbeit beschäftigt sich mit der Analyse und dem Entwurf von Multimoden-Antennen unter Nutzung von charakteristischen Moden. Eine Multimoden-Antenne besteht aus einem einzelnen physischen Antennenelement, welches mehrere unabhängige Antennentore besitzt. Die Tore sollen zueinander orthogonale Richtcharakteristiken erzeugen, um Richt- und Polarisationsdiversität zu erzielen. Die Nutzung von Multimoden-Antennen stellt daher im Vergleich zu Gruppenantennen mit räumlich verteilten Antennenelementen eine kompakte Alternative für MIMO-Systeme (multiple-input multiple-output) dar.

Die systematische Analyse und der systematische Entwurf von Multimoden-Antennen wird durch die Theorie der charakteristischen Moden ermöglicht. Dies ist auf die vorteilhaften Orthogonalitätseigenschaften der charakteristischen Moden einer beliebigen Antenne zurückzuführen. Insbesondere sind die modalen Richtcharakteristiken orthogonal zueinander. Die Tore einer Multimoden-Antenne sollten daher unterschiedliche Sätze von charakteristischen Moden anregen. Auf diese Weise ergeben sich ideal unkorrelierte Antennentore.

Um einen gewissen Satz von charakteristischen Moden selektiv anzuregen, müssen ihre charakteristischen Flächenstromdichten orthogonal zu jenen aller anderen Moden sein. Dabei stellt sich heraus, dass die Orthogonalität der charakteristischen Flächenstromdichten durch die Symmetrie der Antennen bedingt ist. Dies ist auf die grundlegende Tatsache zurückzuführen, dass die charakteristischen Flächenstromdichten Basisfunktionen der irreduziblen Darstellungen der Symmetriegruppe einer Antenne sind. Charakteristische Flächenstromdichten, die zu unterschiedlichen irreduziblen Darstellungen oder zu unterschiedlichen Zeilen einer mehrdimensionalen irreduziblen Darstellung gehören, sind orthogonal zueinander. Die zueinander orthogonalen Sätze von charakteristischen Flächenstromdichten können also ermittelt werden, indem die charakteristischen Moden einer Antenne den irreduziblen Darstellungen ihrer Symmetriegruppe zugeordnet werden. Die Anzahl der zueinander orthogonalen Sätze von charakteristischen Flächenstromdichten wird von der endlichen Anzahl der irreduziblen Darstellungen und ihren Dimensionen bestimmt und ist folglich begrenzt.

Diese unterschiedlichen Sätze von charakteristischen Moden können durch Antennentore, welche die Symmetrieanforderungen der irreduziblen Darstellun-

gen erfüllen, getrennt voneinander angeregt werden. Dies hat zur Folge, dass ein einzelnes Antennentor aus mehreren symmetrisch auf der Antenne platzierten Speisepunkten besteht. Die Eingangssignale der Antennentore werden mithilfe eines Speisenetzwerkes zu den Speisepunkten verteilt. Die optimalen Torkonfigurationen sind ausschließlich durch die Symmetrie einer Antenne bestimmt und sind damit unabhängig von der letztendlichen Ausgestaltung und Größe der Antenne. Das bedeutet, dass die optimalen Torkonfigurationen *a priori* bekannt sind und dass eine obere Grenze für die Realisierung orthogonaler Tore existiert.

Weiteres *a priori* Wissen kann gewonnen werden, indem Beziehungen zwischen unterschiedlichen Symmetriegruppen ausgenutzt werden. Symmetriegruppen können isomorph sein oder können als direktes Produkt ausgedrückt werden, was erlaubt, auf der Analyse einfacherer Symmetriegruppen aufzubauen. Zudem können verwandte Symmetriegruppen in Familien zusammengefasst werden. Die charakteristischen Moden der entsprechenden Antennengeometrien besitzen ähnliche Eigenschaften sowohl hinsichtlich der Eigenwerte als auch hinsichtlich der charakteristischen Flächenstromdichten. Außerdem können diese Eigenschaften anhand der modalen Analyse einer verallgemeinerten Antennengeometrie mit unendlicher Symmetriegruppe abgeschätzt werden. Diese Verwandtschaftsbeziehungen werden ausgenutzt, um für die Realisierung einer gewünschten Anzahl an orthogonalen Antennentoren potentiell geeignete Antennengeometrien zu vergleichen und die minimale Antennengröße abzuschätzen.

Anhand dieser verallgemeinerten modalen Analyse und des *a priori* Wissens aus der Symmetrieanalyse wird eine kompakte Sechs-Tor-Multimoden-Antenne basierend auf einer quadratischen Geometrie entwickelt. Die Speisepunkte der optimalen Torkonfigurationen werden durch Schlitze ersetzt, um eine flexible Impedanzanpassung durchzuführen. Ein Speisenetzwerk, welches die Torsignale zu den Schlitzen mit den von den irreduziblen Darstellungen geforderten Amplituden- und Phasenbeziehungen verteilt, wird in Mehrlagentechnologie realisiert. Einem modularen Entwurfsansatz folgend werden das Antennenelement und das Speisenetzwerk zunächst getrennt optimiert und dann zusammengesetzt. Die Simulations- und Messergebnisse zeigen, dass die sechs Antennentore praktisch unkorreliert sind und damit die gewünschte Richt- und Polarisationsdiversität aufweisen. Der gefertigte Prototyp bestätigt damit die praktische Nutzbarkeit und Relevanz der vorgestellten Entwurfskonzepte.

Schlagwörter: Antennenentwicklung, Antennendiversität, Antennentheorie, Charakteristische Moden, Eigenwerte und Eigenfunktionen, Gruppentheorie, Multiple-Input Multiple-Output (MIMO), Multimoden-Antennen, Symmetrie.

Abstract

This thesis deals with the systematic analysis and design of multimode antennas based on characteristic modes. A multimode antenna is a single physical antenna element with several independent antenna ports. The ports are intended to excite mutually orthogonal radiation patterns in order to provide pattern and polarization diversity. Therefore, the use of multimode antennas is a space-efficient alternative for multiple-input multiple-output (MIMO) systems compared to conventional antenna arrays with spatially distributed antenna elements.

A systematic analysis and design of multimode antennas is enabled by means of the theory of characteristic modes. This is due to the fact that the characteristic modes of an arbitrary antenna object possess advantageous orthogonality properties. In particular, the modal radiation patterns are orthogonal to each other. Therefore, the ports of a multimode antenna should excite mutually exclusive sets of characteristic modes. This way, perfectly uncorrelated antenna ports are realized by exploiting the diversity potential of the characteristic modes.

In order to selectively excite a certain set of characteristic modes, their characteristic surface current densities must be orthogonal to those of all other modes. This orthogonality property, however, is not guaranteed by the theory of characteristic modes. It is found, though, that the orthogonality of the characteristic surface current densities is governed by the symmetry of the antenna. This is due to the fundamental fact that the characteristic surface current densities are basis functions of the irreducible representations of the symmetry group of an antenna. Characteristic surface current densities belonging to different irreducible representations or belonging to different rows of a multi-dimensional irreducible representation are orthogonal to each other. The mutually orthogonal sets of characteristic surface current densities are thus found by assigning the characteristic modes to the irreducible representations of the symmetry group of a given antenna, which can be done automatically by means of the projection operator method. Consequently, the number of mutually orthogonal sets of characteristic surface current densities is governed by the finite number and dimensions of the irreducible representations and thus limited.

These mutually exclusive sets of characteristic modes can be excited separately by antenna ports that fulfill the symmetry requirements of the irreducible

representations. This means that a single antenna port consists of several feed points placed symmetrically on the antenna element. The input signals of the antenna ports are distributed to the feed points by means of a feed network. The optimal port configurations are governed solely by the symmetry of an antenna and are thus independent of the actual antenna shape and size. In other words, the optimal port configurations are known *a priori* and there is an upper bound for realizing orthogonal antenna ports. These optimal port configurations can be constructed automatically by means of the projection operator method.

Further *a priori* knowledge is gained by exploiting relationships between different symmetry groups. Symmetry groups may be isomorphic or may be decomposed as direct-product groups, allowing to reuse or build upon the analysis of simpler symmetry groups. Additionally, related symmetry groups can be collected into families. The characteristic modes of the corresponding antenna geometries have similar properties in terms of both eigenvalues and characteristic surface current densities. Moreover, these properties can be estimated by means of a modal analysis of a generalized antenna geometry with an infinite symmetry group. These relationships are exploited in order to compare potentially suitable antenna geometries and estimate the minimum antenna size for realizing a desired number of orthogonal antenna ports.

Based on this generalized modal analysis and the *a priori* knowledge gained from the symmetry analysis, a compact six-port multimode antenna based on a square geometry is designed. The feed points of the optimal port configurations are replaced by excitation slots in order to flexibly perform impedance matching. A feed network which distributes the port signals to the excitation slots with the correct amplitude and phase relations as required by the irreducible representations is realized in multilayer technology. Following a modular design approach, the antenna element and the feed network are first optimized separately and then assembled. The simulation and measurement results show that the six antenna ports are practically uncorrelated, offering the desired pattern and polarization diversity. With these results, the fabricated prototype demonstrates the practical feasibility and relevance of the presented design concepts.

Contents

List of Author's Publications

The following list contains the publications of the author which are related to the the content of this thesis. The relevant publications together with the corresponding copyright information are referenced in the respective chapters as well as the respective table and figure captions.

[PM18a]   N. Peitzmeier and D. Manteuffel, "Selective excitation of characteristic modes on an electrically large antenna for MIMO applications," in *2018 12th European Conference on Antennas and Propagation (EuCAP)*, 2018, pp. 1–5.

> Abstract: The selective excitation of individual characteristic modes for MIMO applications on an electrically large antenna structure is investigated. The characteristic mode analysis yields that a large number of modes is significant and thus basically suited for use in a multi-mode antenna. In order to find appropriate excitation arrangements for the individual characteristic modes, they are grouped according to their symmetry properties. It is found that characteristic currents belonging to the same group are correlated and thus cannot be excited separately, resulting in a reduced set of uncorrelated antenna ports.

> The author developed the content. Prof. Manteuffel supervised the work.

[PM18b]   N. Peitzmeier and D. Manteuffel, "Beamforming concept for multi-beam antennas based on characteristic modes," in *2018 IEEE International Symposium on Antennas and Propagation & USNC/URSI National Radio Science Meeting*, 2018, pp. 1113–1114.

> Abstract: A novel beamforming concept for small cells in 5G cellular systems at millimeter wave frequencies is proposed. Base station antenna arrays may be mounted on street lights or similar elevated structures to form small, densely deployed cells. In such a scenario, the power received by a mobile user within a cell depends on the scan angle due to varying directivity and propagation losses which has considerable impact on the base station efficiency. In order to overcome these issues, multi-beam antennas are employed as array elements. Depending on the scan angle, a suitable beam is selected and then steered towards the user. The multi-beam antennas are designed by means of the theory of characteristic modes. The basic feasibility of the proposed concept is demonstrated.

> The author developed the content. Prof. Manteuffel supervised the work.

[PM19a]   N. Peitzmeier and D. Manteuffel, "Multi-mode antenna concept based on symmetry analysis of characteristic modes," in *2019 13th European Conference on Antennas and Propagation (EuCAP)*, 2019, pp. 1–5.

Abstract: A multi-mode antenna concept based on a symmetry analysis of characteristic modes is presented for use in massive MIMO antenna arrays. A hexagonal plate is chosen as the basis of the antenna concept due to its interesting geometric properties. In particular, a symmetry analysis using group theory and representation theory is conducted in conjunction with a characteristic mode analysis, yielding that a hexagonal plate offers eight mutually orthogonal sets of characteristic surface current densities. On this basis, eight uncorrelated antenna ports are defined by means of the irreducible representations of the symmetry group.

The author developed the content. Prof. Manteuffel supervised the work.

[PM19b]   N. Peitzmeier and D. Manteuffel, "Upper bounds and design guidelines for realizing uncorrelated ports on multimode antennas based on symmetry analysis of characteristic modes," *IEEE Transactions on Antennas and Propagation*, vol. 67, no. 6, pp. 3902–3914, 2019.

Abstract: The design of multi-port antennas for MIMO applications utilizing characteristic modes is investigated. For good MIMO performance, uncorrelated antenna ports are generally required. In order to analyze the port correlation, symmetry analysis based on group theory and matrix representations is applied to the theory of characteristic modes. The characteristic surface current densities act as basis functions of the irreducible representations of the symmetry group of the antenna. Current densities belonging to different representations or belonging to different rows of the same representation are orthogonal to each other and can thus be excited separately. Therefore, an upper bound for the number of uncorrelated antenna ports can be derived for a given antenna structure based on the symmetry analysis of the characteristic modes. Furthermore, design guidelines on which antenna geometry to choose in order to realize a given number of uncorrelated antenna ports and on how to implement these ports can be deduced. The concept is illustrated by means of examples.

The author developed the content. Prof. Manteuffel supervised the work.

[MP19]   D. Manteuffel and N. Peitzmeier, "Mobilfunk-Basisstation zur Ausbildung einer Mobilfunk-Zelle," German Patent DE 10 2018 114 879, July 11, 2019.

Abstract: A novel cellular base station architecture for mobile communications is proposed. The base station uses an array of multimode antennas. A single multimode antenna is designed in such a way that each antenna port drives a beam which points in a distinct cell area (multibeam antenna). Depending on the position of the mobile user within the cell, the relevant beam is selected and beamforming is performed by means of the array of multimode antennas in order to track the user.

If the user enters another cell area, the base station switches to the relevant beam of that area and performs beamforming. As different beams are used for beamforming within the complete cell, the individual cell areas are subject to reduced power variations. The corresponding antenna ports are connected to power amplifiers which are adjusted to the respective cell areas. This way, the power amplifiers suffer less power variations compared to the complete cell, so that the base station operates more efficiently.

[PM19c] N. Peitzmeier and D. Manteuffel, "Systematic design of an ultra-wideband six-port multi-mode antenna element using symmetry properties of characteristic modes," in *2019 International Conference on Electromagnetics in Advanced Applications (ICEAA)*, 2019, pp. 466–471.

Abstract: A design of an ultra-wideband six-port multi-mode antenna element intended for use in a massive MIMO array is presented. By leveraging symmetry properties of characteristic modes, six uncorrelated antenna ports can be defined on a square plate while offering wideband potential with minimum dimensions. Excitation slots are introduced and systematically optimized based on symmetry considerations in such a way that an inherent impedance match is realized for all six ports. In order to cover the desired ultra-wide bandwidth from 6 GHz to 8.5 GHz, the excitation slots are stepped in width and the feed network is adjusted accordingly, achieving the design goals.

The author developed the content. Prof. Manteuffel supervised the work.

[JPHM20a] N. L. Johannsen, N. Peitzmeier, P. A. Hoeher, and D. Manteuffel, "On the feasibility of multi-mode antennas in UWB and IoT applications below 10 GHz," *IEEE Communications Magazine*, vol. 58, no. 3, pp. 69–75, 2020.

Abstract: While on the one hand 5G and beyond 5G networks are challenged by ultra-high data rates in wideband applications like 100+ Gb/s wireless Internet access, on the other hand they are expected to support reliable low-latency Internet of Things applications with ultra-high connectivity. These conflicting challenges are addressed in a system proposal dealing with both extremes. In contrast to most recent publications, focus is on the frequency domain below 10 GHz. Toward this goal, multi-mode antenna technology is used, and different realizations, offering up to eight uncorrelated ports per radiator element, are studied. Possible baseband architectures tailored to multimode antennas are discussed, enabling different options regarding precoding and beamforming.

The author developed the content regarding the design of multimode antennas. Mr. Johannsen developed the content regarding the system architecture and evaluation. Prof. Hoeher and Prof. Manteuffel supervised the work.

[PM20] N. Peitzmeier and D. Manteuffel, "Systematic design method for asymmetric multiport antennas based on characteristic modes," in

2020 14th European Conference on Antennas and Propagation (EuCAP), 2020, pp. 1–5.

Abstract: A systematic design procedure for placing ports with low correlation on an asymmetric antenna geometry is presented. By applying the mathematical description of symmetry based on group theory and group representations to the theory of characteristic modes, it is shown that it is in general not possible to realize uncorrelated antenna ports on an asymmetric antenna. Therefore, a port placement procedure based on characteristic modes is proposed for such geometries in order to realize ports with low correlation. The design procedure is based on modal parameters alone. Thus, only one full simulation run is needed in order to perform the modal analysis. The proposed procedure is illustrated by means of numerical examples.

The author developed the content. Prof. Manteuffel supervised the work.

[JPHM20b] N. L. Johannsen, N. Peitzmeier, P. A. Hoeher, and D. Manteuffel, "M4 — Multi-Mode Massive MIMO," in *Wireless 100 Gbps And Beyond. Architectures, Approaches and Findings of German Research Foundation (DFG) Priority Programme SPP1655*, 1st ed., R. Kraemer and S. Scholz, Eds.   Frankfurt (Oder), Germany: IHP – Innovations for High Performance Microelectronics, 2020, ch. 6.

Abstract: In this book, the research results of the priority program SPP1655 of the German Research Foundation (DFG) aiming at wireless ultra-high data rate communications of $100 \, \text{Gbit} \, \text{s}^{-1}$ and beyond are compiled. The chapter 6 summarizes the findings of the project M4 (Multi-Mode Massive MIMO), which achieves the targeted data rate by combining a massive MIMO approach with an ultra-wide bandwidth (UWB) from 6 GHz to 8.5 GHz, i.e., at frequencies below 10 GHz. In order to obtain compact massive MIMO antenna arrays at these frequencies, multimode antennas are employed as antenna elements. Within this interdisciplinary project, system architectures and MIMO techniques using multimode antennas are investigated in conjunction with systematic antenna design strategies.

The author developed the content regarding the systematic design of multimode antennas based on symmetry properties of characteristic modes. Mr. Johannsen developed the content regarding the system architecture, signal processing, and overall performance evaluation. Prof. Hoeher and Prof. Manteuffel supervised the work.

[PHM21]   N. Peitzmeier, T. Hahn, and D. Manteuffel, "Systematic Design of Multimode Antennas for MIMO Applications by Leveraging Symmetry," *IEEE Transactions on Antennas and Propagation*, in press, 2021.

Abstract: A systematic procedure for constructing orthogonal antenna ports on arbitrary symmetric multimode antennas is proposed. The procedure is based on the

projection operator method from group theory. With this method, optimal orthogonal port configurations are generated analytically. Electromagnetic simulations, modal analyses, or optimization techniques are not required. The optimal port configurations are solely governed by the symmetry of an antenna and can thus be considered as *a priori* knowledge. Accordingly, this knowledge is available right from the beginning of the design process and can be purposefully used to compare different suitable antenna geometries with respect to the practical implementation effort. The procedure is illustrated by means of an application example resulting in a complete prototype of a six-port multimode antenna.

The author developed the content. Mr. Hahn designed the feed network and optimized the prototype antenna. Prof. Manteuffel supervised the work.

List of Abbreviations and Symbols

Abbreviations

3D	Three-Dimensional
CMC	Characteristic Mode Computation
ECC	Envelope Correlation Coefficient
EFIE	Electric Field Integral Equation
MIMO	Multiple-Input Multiple-Output
MoM	Method of Moments
MS	Modal Significance
PEC	Perfectly Electrically Conducting
RF	Radio Frequency
RWG	Rao-Wilton-Glisson (MoM basis functions)
SINR	Signal-to-Interference-plus-Noise Ratio
SMD	Surface-Mount Device
TE	Transverse Electric
TEM	Transverse Electromagnetic
TM	Transverse Magnetic
UWB	Ultra-Wide Band

Physical Quantities

$\mathbf{A}$	Magnetic vector potential	$\mathrm{V\,s\,m^{-1}}$
$A_i^{\pm}$	Area of plus- or minus-triangle of i-th RWG basis function	$\mathrm{m^2}$
a	Edge length	m
a_n	Modal weighting coefficient of n-th characteristic mode	$\mathrm{W^{1/2}}$
$a_{n,u}$	Modal weighting coefficient of n-th characteristic mode due to u-th antenna port	$\mathrm{W^{1/2}}$
$\mathbf{B}$	Magnetic flux density	$\mathrm{V\,s\,m^{-2}}$
b_n	Normalized modal weighting coefficient of n-th characteristic mode	1
$b_{n,u}$	Normalized modal weighting coefficient of n-th characteristic mode due to u-th antenna port	1
c	Spheroidal electrical size	1

$\mathbf{D}$	Electric flux density	$\mathrm{A\,s\,m^{-2}}$
$\bar{d}$	Focal distance of spheroidal coordinate system	m
$\mathbf{E}$	Electric field strength	$\mathrm{V\,m^{-1}}$
$\mathbf{E}_i$	Impressed electric field strength	$\mathrm{V\,m^{-1}}$
$\mathbf{E}_n$	Electric field strength of n-th characteristic mode	$\mathrm{Vm^{-1}W^{-1/2}}$
$\mathbf{E}_s$	Radiated or scattered electric field strength	$\mathrm{V\,m^{-1}}$
$\mathbf{E}_u$	Radiated electric far field of u-th antenna port	$\mathrm{V\,m^{-1}}$
ECC_{uv}	Envelope correlation coefficient between u-th and v-th antenna port	1
G	Integral kernel of EFIE (Green's function)	$\mathrm{m^{-1}}$
$\mathbf{H}$	Magnetic field strength	$\mathrm{A\,m^{-1}}$
$\mathbf{H}_n$	Magnetic field strength of n-th characteristic mode	$\mathrm{Am^{-1}W^{-1/2}}$
h	Height	m
h_{GND}	Height above ground plane	m
$\mathbf{I}$	MoM current vector	$\mathrm{A\,m^{-1}}$
I_i	i-th MoM current coefficient	$\mathrm{A\,m^{-1}}$
$\mathbf{I}_n$	Eigenvector of n-th characteristic mode	$\mathrm{Am^{-1}W^{-1/2}}$
$\mathbf{J}$	Electric surface current density	$\mathrm{A\,m^{-1}}$
$\mathbf{J}_n$	n-th characteristic surface current density	$\mathrm{Am^{-1}W^{-1/2}}$
k	Angular wave number	$\mathrm{m^{-1}}$
l_i	Common-edge length of i-th RWG basis function	m
MS_n	Modal significance of n-th characteristic mode	1
P_n	Normalized complex power of n-th characteristic mode	1
P_{rad}	Radiated power	W
$P_{\mathrm{rad},n}$	Normalized radiated power of n-th characteristic mode	1
$P_{\mathrm{rad},u}$	Radiated power of u-th antenna port	W
q	Electric charge density	$\mathrm{A\,s\,m^{-3}}$
R	Real part of impedance operator	Ω
$\mathbf{R}$	Real part of MoM impedance matrix	$\Omega\,\mathrm{m^2}$
$\mathbf{r}$	Point in space	m
$\tilde{\mathbf{r}}$	Transformed point in space	m
$\mathbf{r}'$	Point on antenna surface	m
r	Radial coordinate	m
R_i	Inradius	m
R_u	Circumradius	m
S	Surface of volume enclosing the antenna	$\mathrm{m^2}$
S'	Antenna surface	$\mathrm{m^2}$
S_∞	Surface of sphere at infinity	$\mathrm{m^2}$

S_{uu}	Input reflection coefficient of u-th antenna port	dB,°
S_{uv}	Transmission coefficient from v-th to u-th antenna port	dB,°
t	Time	s
U	Source voltage	V
V	Volume enclosing the antenna	m^3
V'	Source volume	m^3
$\mathbf{V}$	MoM excitation vector	V m
V_i	i-th MoM excitation coefficient	V m
$V_{\mathrm{i},n}$	Modal excitation coefficient of n-th characteristic mode	W$^{1/2}$
X	Imaginary part of impedance operator	Ω
$\mathbf{X}$	Imaginary part of MoM impedance matrix	Ω m^2
x,y,z	Cartesian coordinates	m
Z	Impedance operator	Ω
$\mathbf{Z}$	MoM impedance matrix	Ω m^2
Z_{ij}	ij-th MoM impedance coefficient	Ω m^2
$Z_{\mathrm{in},u}$	Input impedance of u-th antenna port	Ω
Z_0	Wave impedance	Ω
α_n	Characteristic angle of n-th characteristic mode	rad
$\boldsymbol{\beta}_i$	i-th RWG basis function	1
ε	Permittivity	A s V^{-1} m^{-1}
ε_{r}	Relative permittivity	1
θ	Polar angle	rad
κ	Conductivity	Ω^{-1} m^{-1}
λ_{g}	Stripline wavelength	m
λ_n	Eigenvalue of n-th characteristic mode	1
μ	Permeability	V s A^{-1} m^{-1}
$\boldsymbol{\rho}_i^{\pm}$	Direction vector of i-th RWG basis function	m
ρ	Radial coordinate	m
ϱ_{mn}	Characteristic current correlation coefficient between m-th and n-th characteristic mode	1
Φ	Rotation angle	rad
ϕ	Electric scalar potential	V
φ	Azimuthal angle	rad
ω	Angular frequency	s^{-1}

Symbols, Functions, and Operators

$\cdot$	Scalar product of two vectors
$\langle\,\cdot\,,\cdot\,\rangle$	Inner product

$\lvert \cdot \rvert$	Absolute value of complex quantity
$\lVert \cdot \rVert$	Norm of a vector
arg	Argument of complex quantity
$\otimes$	Direct product of two matrices
$\times$	Cross product of two vectors
*	Complex conjugate
$^{-1}$	Inverse
$\mathbf{a}$	Vector for constructing the vector wave functions
$\mathbb{C}$	Complex numbers
C	Class of a group
C_n^p	p-fold rotation by angle $\frac{2\pi}{n}$ about an axis
d	Dimension of square matrix
d_p	Dimension of p-th irreducible representation
div	Divergence operator
$\mathrm{d}\mathbf{S}$	Vector infinitesimal surface element
$\mathrm{d}S, \mathrm{d}S', \mathrm{d}S''$	Infinitesimal surface element
$\mathrm{d}V, \mathrm{d}V'$	Infinitesimal volume element
E	Identity
$\mathbf{E}$	Identity matrix
$\mathbf{e}$	Unit vector
$\mathbf{F}$	Vector field
$\mathcal{F}$	Group mapping
f	Scalar function
$\tilde{f}$	Transformed scalar function
$\mathbf{f}$	Vector-valued function
$\tilde{\mathbf{f}}$	Transformed vector-valued function
$\mathcal{G}$	Symmetry group
g	Group order
$\mathcal{g}$	Density of group elements
grad	Gradient operator
$^{\mathrm{H}}$	Conjugate transpose of a matrix
$h_t^{(1)}$	Spherical Hankel function of the first kind of order t
$h_t^{(2)}$	Spherical Hankel function of the second kind of order t
I	Spatial inversion
Im	Imaginary part of complex quantity
j	Imaginary unit
j_t	Spherical Bessel function of the first kind of order t
K	Constant

L	Irrotational vector wave function
L	Number of parameters of continuous group
$\mathcal{L}_t^s$	Associated Legendre function of degree t and order s
M	Solenoidal vector wave function
M	Number of discrete regions of continuous group
$\mathbb{N}$	Natural numbers
$\mathbb{N}_{>0}$	Natural numbers without 0
N	Solenoidal vector wave function
N	Number of RWG basis functions
N_C	Number of group elements in a class
n	Unit normal vector
P	Transformation operator
$\mathcal{P}_{\mu\nu}^{(p)}$	Projection operator
$\mathcal{P}^{(p)}$	Character projection operator
$\mathbb{R}$	Real numbers
R	Rotation matrix
$\mathcal{R}_{st}^{(1)}$	Spheroidal radial function of the first kind
$\mathcal{R}_{st}^{(2)}$	Spheroidal radial function of the second kind
$\mathcal{R}_{st}^{(3)}$	Spheroidal radial function of the third kind
$\mathcal{R}_{st}^{(4)}$	Spheroidal radial function of the fourth kind
Re	Real part of complex quantity
rot	Curl operator
S	Similarity transformation matrix
S_n	Rotoreflection by angle $\frac{2\pi}{n}$ about an axis
$\mathcal{S}_{st}$	Spheroidal angular function
T	Transpose of a matrix
T	Coordinate transformation (element of symmetry group)
tan	Tangential component of a vector
$T_i^{\pm}$	Plus- or minus-triangle of i-th RWG basis function
tr	Trace of a matrix
v	Vector
y_t	Spherical Bessel function of the second kind of order t
Γ	Representation of a group
$\bar{\Gamma}$	Equivalent representation of a group
$\Gamma^{(p)}$	p-th irreducible representation of a group
$\mathbf{\Gamma}$	Representation matrix
Δ	Laplace operator
δ	Dirac delta function

δ_{mn}	Kronecker delta
ζ	Solution to the homogeneous scalar Helmholtz equation
η	Spheroidal hyperboloidal coordinate
ξ	Spheroidal ellipsoidal coordinate
σ	Reflection through a plane
σ_h	Reflection through a plane perpendicular to principal rotation axis
Φ	Parameter of continuous group
χ	Character
Ψ	Discrete region of continuous group
$\boldsymbol{\psi}_\nu^{(p)}$	Basis function belonging to the ν-th row of the p-th irreducible representation (vector-valued)
$\psi_\nu^{(p)}$	Basis function belonging to the ν-th row of the p-th irreducible representation (scalar)

1 Introduction

The use of multiantenna systems has become ubiquitous in modern wireless communications. Multiple antennas at the transmitter and/or the receiver of a wireless communication system enable numerous techniques which are indispensable for current and future wireless applications [1–3]. Systems employing multiple antennas are oftentimes simply referred to as multiple-input multiple-output (MIMO) systems [3]. Common examples for multiantenna techniques in a MIMO system are beamforming, spatial diversity, and spatial multiplexing [2–4]. These are certainly the most prominent MIMO techniques and thus serve best for giving an overview about the various benefits of using multiple antennas.

Beamforming typically aims at exploiting the gain provided by an array of antennas (array gain) in order to increase the signal-to-interference-plus-noise ratio (SINR) [3]. This is achieved by steering the main beam of an antenna array [5] at the transmitter and/or receiver towards a desired direction, focusing the signal power in this direction and simultaneously suppressing interfering signals from unwanted directions [6].[1] Spatial diversity works in a similar way as beamforming, but is used to combat fading due to multipath signal propagation, ultimately reducing the error probability at the receiver [3]. The diversity offered by spatially distributed antennas allows to purposefully exploit independent multipath components of a single signal (diversity gain) [7, 8]. This can be achieved by recombining the multipath components at a multiantenna receiver (diversity combining) [9], or by transmitting the same signal via different antennas at a multiantenna transmitter (space-time coding) [10]. Spatial multiplexing, finally, relies on multiple antennas at both the transmitter and the receiver (true MIMO). In contrast to spatial diversity, different signals are transmitted simultaneously via spatially independent propagation paths, yielding an increased data rate (multiplexing gain) [3, 11, 12].

The multiple antennas at the transmitter and/or the receiver are commonly realized as antenna arrays. In order to enable the above-mentioned multiantenna techniques, an antenna array has to provide antenna diversity [7, 13, 14]. This denotes the capability of an antenna to potentially enable spatially independent

---

[1] Beamforming is related to direction-of-arrival estimation, which is yet another technique enabled by multiple antennas at the receiver [6].

propagation paths (e.g., in a rich-scattering scenario).[2] Typically, an antenna array consists of several identical antennas with a certain spacing [5] in order to provide so-called spatial diversity [14, 15].[3] However, identical antennas that are placed in close proximity to each other in general have correlated radiation patterns [16]. Due to this correlation, the spatial channels of a MIMO system are not independent, resulting in performance degradations [17]. The correlation should thus be as low as possible [14]. This is achieved by spacing the antennas of an array appropriately apart (e.g., a half-wavelength spacing) [16]. However, increasing the number of spatial MIMO channels requires more antennas. As a consequence, there is a tradeoff between MIMO performance and array size [18].

There are, however, two further types of antenna diversity, which are called pattern diversity and polarization diversity [14, 15]. Polarization diversity is achieved by using different orthogonal polarizations, comprising the well-known dual-polarized antennas [19], whereas pattern diversity relies on independent radiation patterns, e.g., directional antennas whose beams point in different directions. These two types of diversity have in common that they do not necessarily require an antenna array. Instead, a single physical antenna element with several antenna ports can be employed. Each port drives a specific antenna mode with independent pattern and/or polarization. This concept is called multimode antenna [18, 20], which may be interpreted as a virtual antenna array whose elements are all located at the same point in space. For example, a dual-polarized patch antenna [5] can be considered a two-port multimode antenna. The two ports drive orthogonal polarizations, providing polarization diversity. Ideally, a single multimode antenna enables the decorrelation of the MIMO channels due to pattern and polarization diversity and thus constitutes a space-efficient alternative to an antenna array with spatially distributed antennas.

Early multimode antenna designs reported in the literature are based on well-known antenna types, e.g., patch antennas [21], biconical antennas [20, 22], and spiral antennas [18]. In more recent publications, the theory of characteristic modes [23–25] is employed in order to enable a systematic design of multimode antennas with arbitrary shape, as detailed in subsection 1.1. The characteristic modes of an antenna possess orthogonal radiation patterns [24], offering a mixture of pattern and polarization diversity. That is why they are ideally suited for the design of multimode antennas. The antenna ports are realized in such a way that they excite different sets of characteristic modes in order to exploit

---

[2]In contrast, diversity as a system concept comprises the wireless propagation channel, the antennas, and the signal processing.

[3]Not to be confused with spatial diversity as a system concept [3].

the diversity. This way, a compact diversity antenna is created. Combined with suitable signal processing capabilities, a multimode antenna enables the MIMO techniques introduced above with a single physical antenna element.

1.1 State of the Art and Background

The theory of characteristic modes was originally introduced in order to treat the scattering of electromagnetic waves at arbitrarily shaped perfectly electrically conducting (PEC) objects [23, 24, 26]. The applicability of this theory to radiation problems, i.e., antenna designs, is extensively treated in [27–29]. In these publications, it is demonstrated how the characteristic modes can be applied in order to understand the radiation mechanisms of a given antenna geometry and how this knowledge can be used in order to systematically synthesize a desired antenna performance. In contrast to optimization procedures, the characteristic modes enable a deterministic design approach based on physical insight [27, 30]. Thanks to this, they have found widespread use in the solution of antenna analysis and design problems [25, 31]. Applications comprise polarization synthesis [27], bandwidth manipulation and tuning [32], wideband and multiband operation [33], antenna equivalent circuits [34], systematic geometry manipulation [35, 36], and reactive loading [37], among many more.

Another field of antenna research that has gained considerable attention thanks to the beneficial properties of characteristic modes is the design of multimode antennas. As stated above, the principal design goal is to realize antenna ports which generate orthogonal radiation patterns by exciting different sets of characteristic modes. The basic design work flow is well described by some of the early pioneering works [38–41]. It starts with a modal analysis of a given antenna object in order to identify those characteristic modes which are suitable for excitation. By inspecting the corresponding modal near fields or surface current densities, appropriate antenna ports are designed. For example, in [38, 40] a rectangular PEC plate offering four suitable characteristic modes is considered. Electrically small capacitive excitation elements [42] are placed at the corners of the plate where the maxima of the modal electric near fields occur in order to realize an effective coupling via the electric field. The excitation elements are interconnected by a feed network in such a way that the resulting four antenna ports excite different characteristic modes and thus mutually orthogonal radiation patterns. In a similar way, a three-port multimode antenna also based on a rectangular plate is designed in [41, 43] using electrically small inductive

excitation elements [42]. These are placed at the maxima of the modal surface current densities in order to realize an effective coupling via the magnetic field.

Early multimode antenna designs based on characteristic modes are predominantly focused on mobile terminals with an electrically small rectangular geometry [40, 43–45]. Based on the multimode antenna concept in conjunction with characteristic modes, MIMO operation with up to four antenna ports is enabled in such a spatially restricted environment, thereby efficiently utilizing the given design space. More recent publications explore different geometries, e.g., for base station applications. Multimode antennas based on a square plate [46], a square cuboid [47], and a hexagonal plate [48] are reported, all offering four antenna ports providing pattern and polarization diversity. Another notable example is a three-port multimode antenna based on a biomimetic geometry [49]. Besides the actual antenna design, signal processing with multimode antennas has also attracted significant research interest. Recent publications are dedicated to beamforming [50], direction-of-arrival estimation [51], and massive MIMO [52, 53], demonstrating that multimode antennas readily enable the above-mentioned multiantenna techniques.

In particular, this thesis was elaborated in the context of the project M4 (Multi-Mode Massive MIMO) within the priority program SPP1655 of the German Research Foundation (DFG) aiming at wireless ultra-high data rate communications of $100\,\mathrm{Gbit\,s^{-1}}$ and beyond [54]. In this project, the targeted data rate is achieved by combining a massive MIMO approach with an ultra-wide bandwidth (UWB) from $6\,\mathrm{GHz}$ to $8.5\,\mathrm{GHz}$, i.e., at frequencies below $10\,\mathrm{GHz}$ [52, 55]. In order to obtain compact massive MIMO antenna arrays at these frequencies, multimode antennas are employed as antenna elements. In the first phase of the project, a compact 11×11 antenna array consisting of 121 four-port multimode antennas (yielding a total of 484 antenna ports) was presented [46], demonstrating the feasibility and the potential of the concept. These promising results are the motivation for aiming at even more antenna ports per multimode antenna.

Contemplating the multimode antennas reported in the literature (see above), it is found that the maximum number of antenna ports achieved so far does not exceed four. Furthermore, all reported multimode antennas rely on the intuitive design approach enabled by the characteristic modes, i.e., inspecting the modal near fields or surface current densities in order to place excitations, introduced more than ten years ago as described above. However, towards more antenna ports, the intuitive design approach becomes increasingly cumbersome as the number of the characteristic modes to be taken into account grows. So far, no general guidelines are available to systematically tackle this problem. This is

illustrated in [56] by means of a rectangular plate, where the intuitive design approach fails despite the simple geometry. Instead, it is found that the maximum number of orthogonal antenna ports seems to be limited. Furthermore, there seems to be a connection between the characteristic modes of the rectangular plate and its symmetry. In this regard, it is noted that some of the multimode antenna designs referenced above explicitly recognize the benefits of exploiting symmetries. In these cases, the antenna ports consist of several symmetrically placed excitation elements, respectively, which are driven by means of a feed network in order to excite different sets of characteristic modes [40, 43, 46–48].

As a matter of fact, a connection between the theory of characteristic modes and the theory of symmetry [57] was established in [58]. It was used to reduce computational time and memory requirements in the numerical computation of characteristic modes [59] by block diagonalizing the underlying impedance matrix. This block diagonalization is possible as the characteristic modes can be classified according to the symmetry properties of their respective modal surface current densities. However, further applications to this connection have surfaced only recently. In [60, 61], the classification of the characteristic modes is employed in order to understand and predict so-called crossing avoidances occurring during the tracking [62] of characteristic modes over a given frequency range. Based on this approach, a complete tracking algorithm is presented in [63].

1.2 Objectives and Outline

In this thesis, the connection between the theory of characteristic modes and the theory of symmetry is utilized in order to systematically analyze and design multimode antennas with the goal to realize more orthogonal antenna ports than reported so far in the literature. To this end, the consequences of the symmetry of an antenna on its characteristic modes are examined in full detail in order to gain an enhanced understanding of the fundamental properties of characteristic modes. Based on this, mathematical techniques from the theory of symmetry are applied in order to enable a systematic and automatic analysis of symmetric multimode antennas in terms of characteristic modes. This way, *a priori* knowledge is gained which allows to predict the diversity potential of arbitrary symmetric antenna geometries. Moreover, general design guidelines and automatic techniques for realizing orthogonal antenna ports are derived. With this knowledge, a prototype multimode antenna is fabricated demonstrating the feasibility of the presented concepts.

First of all, the theory of characteristic modes is recapped in chapter 2 in order to provide the analytical basis for this thesis. In particular, those properties of characteristic modes which make them most suitable for the design of multimode antennas are highlighted. Based on this, the state-of-the-art design work flow for multimode antennas is illustrated by means of an example. This example also serves to motivate the connection of the theory of characteristic modes to the theory of symmetry and the potential consequences of this connection.

In order to gain a fundamental understanding about this connection, chapter 3 is dedicated to the theory of symmetry. Group theory and matrix representations are introduced as the basic mathematical concepts of this theory. With these concepts, the connection to the theory of characteristic modes is established. In order to exploit this connection, advanced techniques from group theory are presented which enable a systematic and automatic symmetry analysis.

The techniques from chapter 3 are applied in chapter 4 in order to analyze the symmetry properties of characteristic modes. It is shown that the symmetry group of a multimode antenna governs the number of mutually exclusive sets of characteristic modes. These sets can be excited separately by appropriately designed antenna ports. Consequently, there is an upper bound for realizing orthogonal antenna ports. Advanced techniques from group theory are applied in order to realize the optimal orthogonal antenna ports, enabling a systematic and automatic port generation based on symmetry considerations alone.

In chapter 5, the relations between a family of geometries and their respective symmetry groups are exploited in order to find a representative geometry. By performing a modal analysis of this representative geometry, *a priori* knowledge about the modal behavior of all geometries within the family is gained, which is used to compare suitable antenna geometries and estimate the minimum antenna size for realizing a desired number of orthogonal antenna ports.

Based on the findings in chapters 4 and 5, a six-port multimode antenna is designed systematically in chapter 6. Excitation elements are introduced in order to perform impedance matching and a feed network is realized which distributes the signals from the antenna ports to the excitation elements. Finally, a prototype is fabricated and simulation and measurement results are presented which demonstrate the performance of the multimode antenna.

For the sake of completeness, the consequences of asymmetry on the design of multimode antennas are discussed briefly in chapter 7. It is found that perfectly uncorrelated antenna ports cannot be realized in this case. Therefore, a procedure for realizing weakly correlated antenna ports is presented. In chapter 8, finally, the principal results and conclusions of this thesis are summarized.

2 Theory of Characteristic Modes and Multimode Antenna Design

Characteristic modes were introduced in [23] as a generalized expansion for electromagnetic fields scattered or radiated by a PEC object. The theory of characteristic modes states that an arbitrary surface current density on a PEC object and its corresponding electromagnetic field can be decomposed into a set of characteristic surface current densities and corresponding characteristic fields with certain orthogonality properties.

The principal aim of this chapter is to introduce the fundamental properties of characteristic modes which make them most suitable for multimode antenna design. In order to achieve this goal, first, the electric field integral equation (EFIE) is derived from Maxwell's equations in order to formulate an impedance operator. Based on this operator formulation, the definition of characteristic modes is given and fundamental properties are presented. Next, the basic steps of the numerical computation of characteristic modes for arbitrary PEC objects are introduced. Finally, it will be demonstrated how the characteristic modes can be used purposefully for the design of multimode antennas.

2.1 Electric Field Integral Equation and Impedance Operator

With the EFIE, the electric field strength produced by an arbitrary current density is computed. If PEC objects are considered, it can be combined with the boundary condition of the tangential electric field strength on a PEC surface, yielding an impedance operator that links the surface current density with an impressed electric field. This impedance operator is the basis for the computation of characteristic modes. In this section, the fundamental steps for deriving the EFIE and the impedance operator are presented.[4]

The derivation of the EFIE is based on Maxwell's equations. Throughout this thesis, harmonic time dependence is assumed and all field quantities

---

[4]A detailed compilation of the employed field quantities and equations is provided in appendix A.

are expressed as complex amplitudes. In the time-harmonic case, Maxwell's equations are written as follows [64]:

$$\text{rot}\big(\mathbf{H}(\mathbf{r})\big) = \mathbf{J}(\mathbf{r}) + j\omega\mathbf{D}(\mathbf{r}), \tag{2.1a}$$

$$\text{rot}\big(\mathbf{E}(\mathbf{r})\big) = -j\omega\mathbf{B}(\mathbf{r}), \tag{2.1b}$$

$$\text{div}\big(\mathbf{B}(\mathbf{r})\big) = 0, \tag{2.1c}$$

$$\text{div}\big(\mathbf{D}(\mathbf{r})\big) = q(\mathbf{r}), \tag{2.1d}$$

where $\mathbf{E}$ denotes the electric field strength, $\mathbf{H}$ the magnetic field strength, $\mathbf{D}$ the electric flux density, and $\mathbf{B}$ the magnetic flux density; $\mathbf{J}$ is the electric current density and q is the electric charge density; ω denotes the angular frequency, j is the imaginary unit, and $\mathbf{r} = (x, y, z)^{\text{T}}$ a point in space; rot and div are the curl and divergence operators, respectively.

The field strengths and the flux densities are connected via the constitutive relationships [64]. In this thesis, only simple matter will be of interest.[5] Therefore, the constitutive relationships are written as proportional relations using the permittivity ε and the permeability μ [64]:

$$\mathbf{D}(\mathbf{r}) = \varepsilon\mathbf{E}(\mathbf{r}), \tag{2.2a}$$

$$\mathbf{B}(\mathbf{r}) = \mu\mathbf{H}(\mathbf{r}). \tag{2.2b}$$

The magnetic flux density $\mathbf{B}$ and the electric field strength $\mathbf{E}$ can also be written in terms of the magnetic vector potential $\mathbf{A}$ and the electric scalar potential ϕ [64, 65]:

$$\mathbf{B}(\mathbf{r}) = \text{rot}\big(\mathbf{A}(\mathbf{r})\big), \tag{2.3}$$

$$\mathbf{E}(\mathbf{r}) = -j\omega\mathbf{A}(\mathbf{r}) - \text{grad}\big(\phi(\mathbf{r})\big), \tag{2.4}$$

where grad denotes the gradient operator. The magnetic vector potential is computed by solving the inhomogeneous vector Helmholtz equation and the electric scalar potential is computed by solving the inhomogeneous scalar Helmholtz equation [64, 65]:

$$\Delta\mathbf{A}(\mathbf{r}) + k^2\mathbf{A}(\mathbf{r}) = -\mu\mathbf{J}(\mathbf{r}), \tag{2.5}$$

$$\Delta\phi(\mathbf{r}) + k^2\phi(\mathbf{r}) = -\frac{q(\mathbf{r})}{\varepsilon}, \tag{2.6}$$

---

[5]Lossless, linear, homogeneous, and isotropic.

where Δ denotes the Laplace operator[6] and k is the angular wave number ($k^2 = \omega^2 \varepsilon \mu$). For harmonic time dependence, the electric charge density is proportionally related to the divergence of the electric current density through the continuity equation [64]:

$$\mathrm{div}\big(\mathbf{J}(\mathbf{r})\big) = -j\omega q(\mathbf{r}). \tag{2.7}$$

The solutions to the differential equations (2.5) and (2.6) are integrals which, using (2.7), can both be formulated in terms of the current density [24, 65]:

$$\mathbf{A}(\mathbf{r}) = \mu \iiint\limits_{V'} \mathbf{J}(\mathbf{r}')G(\mathbf{r},\mathbf{r}')\mathrm{d}V', \tag{2.8}$$

$$\phi(\mathbf{r}) = -\frac{1}{j\omega\varepsilon} \iiint\limits_{V'} \mathrm{div}\big(\mathbf{J}(\mathbf{r}')\big)G(\mathbf{r},\mathbf{r}')\mathrm{d}V'. \tag{2.9}$$

The integration is taken over the source volume V', i.e., the region where current densities exist. The integral kernel $G(\mathbf{r},\mathbf{r}')$ for free space (Green's function) is given by [5, 66]:

$$G(\mathbf{r},\mathbf{r}') = \frac{e^{-jk\|\mathbf{r}-\mathbf{r}'\|}}{4\pi\|\mathbf{r}-\mathbf{r}'\|}, \tag{2.10}$$

where $\|\cdot\|$ denotes the norm of a vector.

If PEC objects are considered, current densities can only exist on the object surface. The volume integrals thus reduce to integrals over the object surface S' and the electric field strength $\mathbf{E}_\mathrm{s}$ due to the surface current density can be expressed by inserting (2.8) and (2.9) into (2.4), yielding the electric field integral equation (EFIE):

$$\mathbf{E}_\mathrm{s}(\mathbf{r}) = -j\omega\mu \iint\limits_{S'} \mathbf{J}(\mathbf{r}')G(\mathbf{r},\mathbf{r}')\mathrm{d}S' + \frac{1}{j\omega\varepsilon}\mathrm{grad}\Big(\iint\limits_{S'} \mathrm{div}\big(\mathbf{J}(\mathbf{r}')\big)G(\mathbf{r},\mathbf{r}')\mathrm{d}S'\Big). \tag{2.11}$$

From this point onward throughout this thesis, $\mathbf{J}$ denotes a surface current density on a PEC object and $\mathbf{r}'$ denotes a point on the object surface, whereas $\mathbf{r}$ denotes a point in space outside of the PEC object.

---

[6]In general, the Laplace operator applied to a vector field takes the form given in (5.3). In Cartesian coordinates x, y, z, however, this reduces to applying the Laplace operator to each scalar component of the vector field, decomposing the vector Helmholtz equation into three independent scalar Helmholtz equations [65].

As stated above, the impedance operator to be derived links an impressed electric field with the current density on a PEC surface. In order to connect (2.11) with the electric field strength $\mathbf{E}_i$ of an incident field, the boundary condition of the electric field strength on a perfectly conducting surface is employed. This states that the tangential component of the total electric field strength, which is the superposition of the incident and the radiated or scattered electric field strength, is zero on the PEC surface [24, 65]:

$$\big(\mathbf{E}_i(\mathbf{r}') + \mathbf{E}_s(\mathbf{r}')\big)_{\tan} = 0, \tag{2.12}$$

where $_{\tan}$ denotes the component of a vector tangential to a surface. Combining this equation with (2.11) finally yields the impedance operator Z [24]:

$$\begin{aligned}
\big(\mathbf{E}_i(\mathbf{r}')\big)_{\tan} &= Z\mathbf{J}(\mathbf{r}') \\
&= \bigg(j\omega\mu \iint\limits_{S'} \mathbf{J}(\mathbf{r}'')G(\mathbf{r}',\mathbf{r}'')\mathrm{d}S'' \\
&\quad - \frac{1}{j\omega\varepsilon}\operatorname{grad}\bigg(\iint\limits_{S'} \operatorname{div}\big(\mathbf{J}(\mathbf{r}'')\big)G(\mathbf{r}',\mathbf{r}'')\mathrm{d}S''\bigg)\bigg)_{\tan}.
\end{aligned} \tag{2.13}$$

In contrast to the EFIE (2.11), the field quantities are evaluated on the object surface S' (primed coordinates). The integration is taken over the object surface S' as well, which is distinguished by the double primed coordinates.

If the impressed electric field strength is known, the surface current density induced on a PEC object can be computed by inverting the impedance operator. This is usually done numerically by means of the method of moments, as will be shown in section 2.3. The radiated or scattered fields can then be calculated in the common way using the EFIE (2.11).

2.2 Theory of Characteristic Modes

Based on the impedance operator Z given in (2.13), the characteristic modes can now be defined in a general way by means of the following generalized eigenvalue problem [24]:

$$X\mathbf{J}_n(\mathbf{r}') = \lambda_n R\mathbf{J}_n(\mathbf{r}'), \tag{2.14}$$

where $\mathbf{J}_n$ is the n-th characteristic surface current density and λ_n the corresponding eigenvalue. The linear operators R and X are the Hermitian parts of the

complex impedance operator $Z = R + jX$ [24], i.e., R is the real part

$$
\begin{aligned}
R\mathbf{J}(\mathbf{r}') &= \frac{1}{2}\big(Z\mathbf{J}(\mathbf{r}') + Z^*\mathbf{J}(\mathbf{r}')\big) \\
&= \bigg(\omega\mu \iint\limits_{S'} \mathbf{J}(\mathbf{r}'')\frac{\sin\big(k\|\mathbf{r}' - \mathbf{r}''\|\big)}{4\pi\|\mathbf{r}' - \mathbf{r}''\|}\mathrm{d}S'' \\
&\quad + \frac{1}{\omega\varepsilon}\mathrm{grad}\bigg(\iint\limits_{S'} \mathrm{div}\big(\mathbf{J}(\mathbf{r}'')\big)\frac{\sin\big(k\|\mathbf{r}' - \mathbf{r}''\|\big)}{4\pi\|\mathbf{r}' - \mathbf{r}''\|}\mathrm{d}S''\bigg)\bigg)_{\mathrm{tan}},
\end{aligned} \tag{2.15}
$$

and X is the imaginary part

$$
\begin{aligned}
X\mathbf{J}(\mathbf{r}') &= \frac{1}{2j}\big(Z\mathbf{J}(\mathbf{r}') - Z^*\mathbf{J}(\mathbf{r}')\big) \\
&= \bigg(\omega\mu \iint\limits_{S'} \mathbf{J}(\mathbf{r}'')\frac{\cos\big(k\|\mathbf{r}' - \mathbf{r}''\|\big)}{4\pi\|\mathbf{r}' - \mathbf{r}''\|}\mathrm{d}S'' \\
&\quad + \frac{1}{\omega\varepsilon}\mathrm{grad}\bigg(\iint\limits_{S'} \mathrm{div}\big(\mathbf{J}(\mathbf{r}'')\big)\frac{\cos\big(k\|\mathbf{r}' - \mathbf{r}''\|\big)}{4\pi\|\mathbf{r}' - \mathbf{r}''\|}\mathrm{d}S''\bigg)\bigg)_{\mathrm{tan}},
\end{aligned} \tag{2.16}
$$

where * denotes complex conjugate. It is obvious that these operators yield a real result if they are applied to a real surface current density. Therefore, both R and X are denoted as real operators.

Furthermore, the impedance operator Z is a symmetric operator due to the reciprocity theorem [64]. For this reason, its real part R and its imaginary part X both are real symmetric operators. In addition, R is positive definite, i.e., the power radiated by a surface current density (cf. (2.20)) is always greater than 0, regardless of how small it is [24].[7] This has the consequence that both the eigenvalues λ_n and the characteristic surface current densities $\mathbf{J}_n$ are real quantities [24], as derived in appendix C.1.

2.2.1 Orthogonality and Power

As a consequence of their definition according to (2.14), characteristic modes possess several interesting orthogonality properties. With respect to the characteristic surface current densities, the following orthogonality relationships hold

---

[7]For the definitions of real, symmetric, and positive definite operators, refer to appendix C.

due to the symmetry of the operators [24]:[8]

$$\left\langle \mathbf{J}_m(\mathbf{r}'), R\mathbf{J}_n(\mathbf{r}') \right\rangle = 0, \tag{2.17a}$$

$$\left\langle \mathbf{J}_m(\mathbf{r}'), X\mathbf{J}_n(\mathbf{r}') \right\rangle = 0, \tag{2.17b}$$

$$\left\langle \mathbf{J}_m(\mathbf{r}'), Z\mathbf{J}_n(\mathbf{r}') \right\rangle = 0, \tag{2.17c}$$

where $m \neq n$ and $\langle \cdot, \cdot \rangle$ denotes the inner product as defined in appendix B. The characteristic surface current densities are orthogonal with respect to the impedance operator and its Hermitian parts.[9]

In order to uniquely define the characteristic surface current densities, they are commonly normalized to radiate unit power, having dimension $A/(m\sqrt{W})$. This normalization is used throughout this thesis as well, if not stated otherwise. The orthogonality relationships in (2.17) can then be rewritten as [24]

$$\frac{1}{2}\left\langle \mathbf{J}_m(\mathbf{r}'), R\mathbf{J}_n(\mathbf{r}') \right\rangle = \delta_{mn}, \tag{2.18a}$$

$$\frac{1}{2}\left\langle \mathbf{J}_m(\mathbf{r}'), X\mathbf{J}_n(\mathbf{r}') \right\rangle = \lambda_n\delta_{mn}, \tag{2.18b}$$

$$\frac{1}{2}\left\langle \mathbf{J}_m(\mathbf{r}'), Z\mathbf{J}_n(\mathbf{r}') \right\rangle = \left(1 + j\lambda_n\right)\delta_{mn}, \tag{2.18c}$$

where δ_{mn} is the Kronecker delta (which yields 1 if $m = n$ and 0 otherwise). In the case $m = n$, and due to the absence of any losses, (2.18a) denotes the radiated power of the n-th characteristic mode (normalized to unity) and (2.18b) denotes the reactive power of the n-th characteristic mode. The normalized complex power P_n of the n-th characteristic mode can thus be written as [67]

$$\begin{aligned}
P_n &= \frac{1}{2}\left\langle \mathbf{J}_n(\mathbf{r}'), Z\mathbf{J}_n(\mathbf{r}') \right\rangle = 1 + j\lambda_n \\
&= \frac{1}{2}\left\langle \mathbf{J}_n(\mathbf{r}'), R\mathbf{J}_n(\mathbf{r}') \right\rangle + j\frac{1}{2}\left\langle \mathbf{J}_n(\mathbf{r}'), X\mathbf{J}_n(\mathbf{r}') \right\rangle \\
&= \frac{1}{2}\oiint_{S=\partial V} \left(\mathbf{E}_n(\mathbf{r}) \times \mathbf{H}_n^*(\mathbf{r})\right)\mathrm{d}\mathbf{S} + j\frac{\omega}{2} \iiint_V \left(\mu\|\mathbf{H}_n(\mathbf{r})\|^2 - \varepsilon\|\mathbf{E}_n(\mathbf{r})\|^2\right)\mathrm{d}V.
\end{aligned} \tag{2.19}$$

---

[8]A general derivation is given in appendix C.2.

[9]In contrast, the characteristic surface current densities are in general not directly orthogonal to each other, see section 2.4.3.

The last line is derived from the complex Poynting theorem as introduced in appendix A.5. $\mathbf{E}_n$ and $\mathbf{H}_n$ are the electric field strength and the magnetic field strength, respectively, of the n-th characteristic mode (characteristic fields). The first integral in the last line is taken over the closed surface $S = \partial V$ of an arbitrary volume V completely enclosing the PEC object. It describes the complex power leaving or entering the volume through its surface.[10] The second integral is taken over the volume V. Due to the assumption of simple matter in section 2.1, the integrand is purely real. The second integral thus denotes the reactive power within the volume, i.e., it is a measure for the energy storage of the electromagnetic field.

If the surface S is now chosen to be the sphere at infinity S_∞ (far field), the first integral in the last line of (2.19) is purely real, too, as the electric and magnetic far fields are in phase [5]. In this special case, the decomposition of the complex power into real and imaginary part is obvious and the first integral reduces to the radiated power $P_{\mathrm{rad},n}$ of the n-th characteristic mode [25], which can then be rewritten in terms of the characteristic electric far field (see appendix A.5):

$$P_{\mathrm{rad},n} = \frac{1}{2}\big\langle \mathbf{J}_n(\mathbf{r}'), R\mathbf{J}_n(\mathbf{r}') \big\rangle = \frac{1}{2} \oiint_{S_\infty} \big(\mathbf{E}_n(\mathbf{r}) \times \mathbf{H}_n^*(\mathbf{r}) \big) \mathrm{d}\mathbf{S}$$

$$= \frac{1}{2Z_0} \oiint_{S_\infty} \big\| \mathbf{E}_n(\mathbf{r}) \big\|^2 \mathrm{d}S = 1, \qquad (2.20)$$

where Z_0 is the wave impedance. The last line can be generalized to any two combinations of characteristic modes, denoting the mutually radiated power of two modes (far field correlation). However, due to the orthogonality of the characteristic modes (2.18a), there is no far field correlation, yielding the orthogonality relationship of the characteristic far fields [67]:

$$\frac{1}{2Z_0} \oiint_{S_\infty} \big(\mathbf{E}_m^*(\mathbf{r}) \cdot \mathbf{E}_n(\mathbf{r}) \big) \mathrm{d}S = \frac{1}{2}\big\langle \mathbf{J}_m(\mathbf{r}'), R\mathbf{J}_n(\mathbf{r}') \big\rangle = \delta_{mn}, \qquad (2.21)$$

i.e., the characteristic far fields are always orthogonal to each other. This is one of the most important properties of characteristic modes and in particular most suitable for the design of multimode antennas, as will be shown in section 2.4 at the end of this chapter.

---

[10]This power flow is typically associated with an electromagnetic wave.

2.2.2 Modal Expansion

An arbitrary surface current density $\mathbf{J}$ on a given PEC object can now be expressed as a weighted sum of the characteristic surface current densities $\mathbf{J}_n$ [24]:

$$\mathbf{J}(\mathbf{r}') = \sum_{n=1}^{\infty} a_n \mathbf{J}_n(\mathbf{r}') = \sum_{n=1}^{\infty} \frac{V_{\mathrm{i},n}}{1 + j\lambda_n} \mathbf{J}_n(\mathbf{r}'). \tag{2.22}$$

As the characteristic fields $\mathbf{E}_n$ are linearly related to the surface current densities, the total electric field $\mathbf{E}_\mathrm{s}$ can be expressed in the same way:

$$\mathbf{E}_\mathrm{s}(\mathbf{r}) = \sum_{n=1}^{\infty} a_n \mathbf{E}_n(\mathbf{r}) = \sum_{n=1}^{\infty} \frac{V_{\mathrm{i},n}}{1 + j\lambda_n} \mathbf{E}_n(\mathbf{r}). \tag{2.23}$$

In both equations, a_n is called the modal weighting coefficient of the n-th characteristic mode.[11] The numerator of the modal weighting coefficient is called the modal excitation coefficient $V_{\mathrm{i},n}$ and it is defined as the inner product of the n-th characteristic surface current density $\mathbf{J}_n$ and the impressed electric field strength $\mathbf{E}_\mathrm{i}$ (e.g., a plane wave) evaluated on the object surface, which is a measure for the similarity of a characteristic mode and a given excitation:

$$V_{\mathrm{i},n} = \frac{1}{2}\left\langle \mathbf{J}_n(\mathbf{r}'), \mathbf{E}_\mathrm{i}(\mathbf{r}') \right\rangle = \frac{1}{2} \iint_{S'} \left(\mathbf{J}_n^*(\mathbf{r}') \cdot \mathbf{E}_\mathrm{i}(\mathbf{r}') \right) \mathrm{d}S'. \tag{2.24}$$

The modal weighting coefficient a_n expresses to what degree a characteristic mode contributes to the total radiation. This property is also made clear by the fact that the sum of the squared weighting coefficients is equal to the total radiated power P_rad, as derived in [67]:

$$P_\mathrm{rad} = \sum_{n=1}^{\infty} |a_n|^2. \tag{2.25}$$

Based on this, the normalized modal weighting coefficients b_n are introduced in [67] in order to express the relative contribution of each mode to the total radiation and thus allow a better comparison between modes:

$$b_n = \frac{a_n}{\sqrt{P_\mathrm{rad}}}, \qquad \sum_{n=1}^{\infty} |b_n|^2 = 1. \tag{2.26}$$

---

[11]For a detailed derivation, refer to appendix C.4.

The normalized modal weighting coefficients can also be interpreted as the correlation coefficients between the total electric far field and the modal electric far fields [67].

2.2.3 Modal Parameters

The modal weighting coefficients a_n as defined in (2.22) and (2.23) depend on the modal excitation coefficients $V_{i,n}$ and the eigenvalues λ_n. Whereas the modal excitation coefficient is controlled by the impressed electric field, e.g., an incident plane wave, the eigenvalue is a modal property independent of any excitation. It only depends on the geometry of a given PEC object as well as the frequency and thus expresses the potential of a characteristic mode to contribute to the total radiation. This potential contribution is maximum if the eigenvalue is zero ($\lambda_n = 0$). As the eigenvalue is a measure for the reactive power of a characteristic mode, this case is called modal resonance (cf. (2.18) and (2.19)). Consequently, a characteristic mode is said to be inductive if $\lambda_n > 0$, and capacitive if $\lambda_n < 0$ [27].[12]

The range of possible eigenvalues stretches from $-\infty$ to ∞. In order to get a more compact representation, the modal significance MS_n is introduced [27]:

$$MS_n = \left| \frac{1}{1 + j\lambda_n} \right|, \tag{2.27}$$

which maps the eigenvalues to the range from 0 ($\lambda_n \to \pm\infty$) to 1 ($\lambda_n = 0$). This offers the advantage that a significance criterion can be defined rather intuitively. Throughout this thesis, a characteristic mode is said to be significant if $MS_n \geq \frac{1}{\sqrt{2}}$ ($-1 \leq \lambda_n \leq 1$) [25]. This way, the modal significance even enables the definition of a modal bandwidth as will be made use of in later chapters. However, the information on the energy storage of a mode (inductive, capacitive) is lost. This may be recovered by introducing the characteristic angle α_n [27]:

$$\alpha_n = \pi - \arctan \lambda_n, \tag{2.28}$$

which corresponds to the phase difference between a characteristic surface current density and its corresponding characteristic electric field. The characteristic angle ranges from $90°$ ($\lambda_n \to +\infty$) over $180°$ ($\lambda_n = 0$) to $270°$ ($\lambda_n \to -\infty$).

---

[12]In general, the eigenvalue is the ratio of reactive power to radiated power of a characteristic mode, as shown in appendix C.3. Due to the normalization of the radiated power, this reduces to (2.18).

2.3 Numerical Computation of Characteristic Modes

The computation of characteristic modes requires the solution of a generalized eigenvalue problem (2.14). This is commonly done numerically by applying the method of moments (MoM) [68] as presented in [59]. By means of the MoM, the impedance operator (2.13) is converted into an impedance matrix so that the eigenvalue problem can be solved using well known matrix algebra. In the context of characteristic modes, the MoM is thus needed to derive the impedance matrix of an arbitrary PEC object.

2.3.1 Impedance Matrix

In order to transfer the impedance operator into a matrix, the continuous surface current density $\mathbf{J}$ is approximated by a weighted sum of N basis functions $\boldsymbol{\beta}_1, \boldsymbol{\beta}_2, \ldots, \boldsymbol{\beta}_N$ [68]:

$$\mathbf{J}(\mathbf{r}') \approx \sum_{j=1}^{N} I_j \boldsymbol{\beta}_j(\mathbf{r}'). \tag{2.29}$$

The basis functions are chosen *a priori* (see section 2.3.2) and are thus known so that the current coefficients I_j are the unknowns in the usual application of the MoM. Equation (2.29) is now inserted into (2.13), yielding

$$\left(\mathbf{E}_i(\mathbf{r}')\right)_{\text{tan}} \approx Z\left(\sum_{j=1}^{N} I_j \boldsymbol{\beta}_j(\mathbf{r}')\right) = \sum_{j=1}^{N} I_j Z \boldsymbol{\beta}_j(\mathbf{r}') \tag{2.30}$$

due to the linearity of the impedance operator. The integrations of the impedance operator are only taken over the known basis functions $\boldsymbol{\beta}_j$, which are chosen in such a way that the integrations can be performed numerically.

However, the electric field and the basis functions are still vector-valued and continuous. In order to discretize these functions, the so-called testing is performed. Both sides of (2.30) are multiplied by the basis functions forming an inner product [68]. Using the basis functions for testing is called Galerkin method and ensures that the impedance matrix is symmetric, which is mandatory for characteristic mode computation [59]. Testing the left-hand side of (2.30) with the i-th basis function $\boldsymbol{\beta}_i$ yields the i-th excitation coefficient V_i:

$$V_i = \left\langle \boldsymbol{\beta}_i(\mathbf{r}'), \mathbf{E}_i(\mathbf{r}') \right\rangle. \tag{2.31}$$

This is equivalent to sampling the continuous field and projecting it onto the basis function, i.e., evaluating the tangential component. Likewise, testing the right-hand side of (2.30) yields

$$\left\langle \beta_i(\mathbf{r}'), \sum_{j=1}^{N} I_j Z \beta_j(\mathbf{r}') \right\rangle = \sum_{j=1}^{N} I_j \left\langle \beta_i(\mathbf{r}'), Z \beta_j(\mathbf{r}') \right\rangle = \sum_{j=1}^{N} I_j Z_{ij}. \qquad (2.32)$$

Exploiting the linearity of the inner product shows that the impedance coefficient Z_{ij} is the inner product of the i-th basis function and the j-th basis function transformed by the impedance operator, expressing the mutual coupling between these functions. Combining (2.31) and (2.32) and performing the testing with all N basis functions yields the following linear system of equations [68]:

$$V_i = \sum_{j=1}^{N} Z_{ij} I_j, \qquad i = 1, 2, \ldots, N, \qquad (2.33)$$

which can be written conveniently in matrix form:

$$\mathbf{V} = \mathbf{ZI}, \qquad (2.34)$$

where

$$\mathbf{V} = \begin{pmatrix} \left\langle \beta_1(\mathbf{r}'), \mathbf{E}_i(\mathbf{r}') \right\rangle \\ \left\langle \beta_2(\mathbf{r}'), \mathbf{E}_i(\mathbf{r}') \right\rangle \\ \vdots \\ \left\langle \beta_N(\mathbf{r}'), \mathbf{E}_i(\mathbf{r}') \right\rangle \end{pmatrix}, \qquad \mathbf{I} = \begin{pmatrix} I_1 \\ I_2 \\ \vdots \\ I_N \end{pmatrix}, \qquad (2.35)$$

and

$$\mathbf{Z} = \begin{pmatrix} \left\langle \beta_1(\mathbf{r}'), Z\beta_1(\mathbf{r}') \right\rangle & \left\langle \beta_1(\mathbf{r}'), Z\beta_2(\mathbf{r}') \right\rangle & \cdots & \left\langle \beta_1(\mathbf{r}'), Z\beta_N(\mathbf{r}') \right\rangle \\ \left\langle \beta_2(\mathbf{r}'), Z\beta_1(\mathbf{r}') \right\rangle & \left\langle \beta_2(\mathbf{r}'), Z\beta_2(\mathbf{r}') \right\rangle & \cdots & \left\langle \beta_2(\mathbf{r}'), Z\beta_N(\mathbf{r}') \right\rangle \\ \vdots & \vdots & \ddots & \vdots \\ \left\langle \beta_N(\mathbf{r}'), Z\beta_1(\mathbf{r}') \right\rangle & \left\langle \beta_N(\mathbf{r}'), Z\beta_2(\mathbf{r}') \right\rangle & \cdots & \left\langle \beta_N(\mathbf{r}'), Z\beta_N(\mathbf{r}') \right\rangle \end{pmatrix}.$$

$$(2.36)$$

$\mathbf{Z}$ is the $N \times N$ impedance matrix containing the geometry information of the underlying PEC object.

For the numerical computation of characteristic modes, the generalized eigenvalue equation can now be written in matrix form with $\mathbf{Z} = \mathbf{R} + j\mathbf{X}$ [59]:

$$\mathbf{X}\mathbf{I}_n = \lambda_n\mathbf{R}\mathbf{I}_n, \tag{2.37}$$

where $\mathbf{I}_n$ is the n-th real eigenvector containing the characteristic current coefficients which may be used to approximately construct the characteristic surface current densities according to (2.29).

Accordingly, all equations introduced in section 2.2 containing current densities and impedance operators can now be written in matrix form. In particular, the orthogonality relationships (2.18) reduce to [59]

$$\frac{1}{2}\mathbf{I}_m^{\mathrm{T}}\mathbf{R}\mathbf{I}_n = \delta_{mn}, \tag{2.38a}$$

$$\frac{1}{2}\mathbf{I}_m^{\mathrm{T}}\mathbf{X}\mathbf{I}_n = \lambda_n\delta_{mn}, \tag{2.38b}$$

$$\frac{1}{2}\mathbf{I}_m^{\mathrm{T}}\mathbf{Z}\mathbf{I}_n = \left(1 + j\lambda_n\right)\delta_{mn}. \tag{2.38c}$$

Furthermore, the modal excitation coefficients (2.24) are expressed as a matrix product using the MoM-excitation vector:

$$V_{\mathrm{i},n} = \frac{1}{2}\mathbf{I}_n^{\mathrm{T}}\mathbf{V}. \tag{2.39}$$

These relationships enable the convenient numerical computation of characteristic modes and their derived quantities and parameters in a MoM environment.

2.3.2 Triangular Mesh and RWG Basis Functions

Before applying the method of moments as described above, the PEC object under consideration needs to be discretized (meshing). A popular discretization choice is the triangular mesh as it is capable of reproducing any arbitrarily shaped surface with sufficient accuracy and low complexity [69]. An example of a meshed rectangular plate is shown in Fig. 2.1(a).

On this mesh, a set of subsectional basis functions has to be defined. A common and suitable choice are the so-called Rao-Wilton-Glisson (RWG) basis functions, which are defined on two adjacent triangles (triangle pair) as exemplarily marked in red in Fig. 2.1(a) and shown in detail in Fig. 2.1(b). The
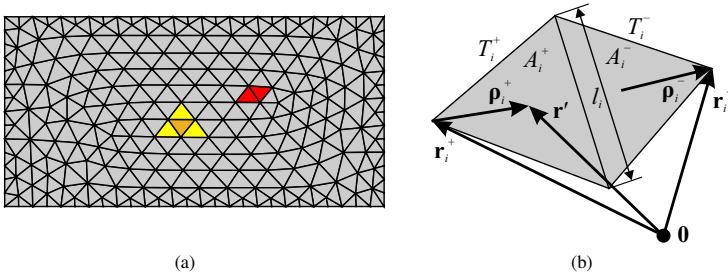
Figure 2.1   Triangular mesh and RWG basis function. (a) Triangular mesh of a rectangular plate with one triangle pair highlighted in red and a group of three overlapping triangle pairs highlighted in yellow/orange. (b) Definition of one RWG basis function on a triangle pair.

definition of the i-th RWG basis function is given as follows [69]:

$$\boldsymbol{\beta}_i(\mathbf{r}') = \begin{cases} \frac{l_i}{2A_i^+}\boldsymbol{\rho}_i^+(\mathbf{r}'), & \mathbf{r}' \in T_i^+ \\ \frac{l_i}{2A_i^-}\boldsymbol{\rho}_i^-(\mathbf{r}'), & \mathbf{r}' \in T_i^- \\ 0, & \text{otherwise} \end{cases} . \qquad (2.40)$$

The i-th RWG basis function only exists on the i-th triangle pair consisting of the triangle T_i^+ (plus-triangle) and the triangle T_i^- (minus-triangle). On the plus-triangle with area A_i^+, the basis function points from the remote edge, denoted by $\mathbf{r}_i^+$ in Fig. 2.1(b), towards the shared edge with edge length l_i. The direction is expressed by the vector $\boldsymbol{\rho}_i^+$, whose length and direction within the triangle depend on the position vector $\mathbf{r}'$. On the minus-triangle with area A_i^-, in contrast, the basis function points towards the remote edge, denoted by $\mathbf{r}_i^-$ in Fig. 2.1(b). The direction is expressed by the vector $\boldsymbol{\rho}_i^-$.

From the definition, it is obvious that a basis function has no component normal to the boundary of the triangle pair it is defined on. This has the consequence that only one basis function models the current flow over the corresponding shared mesh edge. In contrast, the current flow within a triangle is a superposition of up to three basis functions as exemplarily marked in yellow and orange in Fig. 2.1(a). Furthermore, it is noteworthy that each basis function is continuous over its shared edge. This has the consequence that all mesh edges are free of line charges [69].

In addition to the basis functions themselves for modeling the current density according to (2.29), their divergence is needed as well for discretizing the second

integral of the impedance operator (2.13). The divergence of the i-th RWG basis function is computed as follows [69]:

$$\text{div}\big(\boldsymbol{\beta}_i(\mathbf{r}')\big) = \begin{cases} \frac{l_i}{A_i^+}, & \mathbf{r}' \in T_i^+ \\ -\frac{l_i}{A_i^-}, & \mathbf{r}' \in T_i^- \\ 0, & \text{otherwise} \end{cases} \quad . \tag{2.41}$$

The divergence of a basis function is proportional to the surface charge density and it is constant in each triangle. The total charge of the plus- and the minus triangle, respectively, is therefore the same with opposite sign so that the total charge of a triangle pair is zero. One triangle pair with RWG basis function can thus be interpreted as a small electric dipole.

2.3.3 Delta-Gap Source

During the work flow of multimode antenna design, at some point after the modal analysis it will be necessary to define excitations. In a first step, it would be desirable to have exciters which do not alter the PEC object under consideration in order to evaluate the coupling to the characteristic modes, e.g., by means of the modal weighting coefficients (2.22). For this purpose, delta-gap sources are ideally suited as they are compatible with the RWG basis functions and do not require any modifications of the given PEC object.

The delta-gap source is defined by introducing a gap with a small width Δ within the PEC object. This way, two terminals are created across which an ideal voltage source with voltage U is connected [70], as shown in Fig. 2.2(a). This is most easily understood if an electric dipole antenna is envisioned.

Due to the small gap size, the electric field strength $\mathbf{E}_i$ within the gap is assumed to be uniform and can thus be written as [70]

$$\mathbf{E}_i = \frac{U}{\Delta}\mathbf{e}_y \tag{2.42}$$

with respect to the coordinate system chosen in Fig. 2.2, where $\mathbf{e}_y$ denotes the unit vector in y-direction. If the gap width tends to zero, the electric field strength can be expressed using the Dirac delta function δ:

$$\mathbf{E}_i = U\delta(y')\mathbf{e}_y. \tag{2.43}$$

Integrating the electric field strength over the gap width yields the voltage U applied across the terminals, as required.
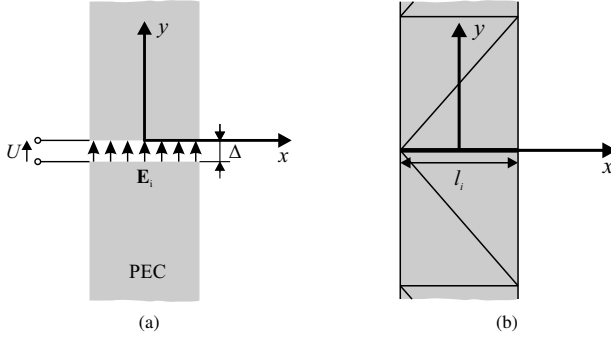
Figure 2.2   Delta-gap source. (a) Feeding edge model. (b) Feeding edge as part of triangular mesh and RWG basis function.

The mesh for the method of moments is now created in such a way that the delta-gap source coincides with the i-th mesh edge of length l_i, as depicted in Fig. 2.2(b). Using (2.31), the i-th MoM excitation coefficient V_i can be computed explicitly [70]. With respect to the coordinate system in Fig. 2.2, this yields

$$V_i = \iint_{S'} \Big(\boldsymbol{\beta}_i(\mathbf{r}') \cdot \mathbf{E}_i(\mathbf{r}')\Big)\mathrm{d}S' = \int_{-l_i/2}^{l_i/2} \int_{-\infty}^{\infty} \Big(\boldsymbol{\beta}_i(x',y') \cdot U\delta(y')\mathbf{e}_y\Big)\mathrm{d}y'\mathrm{d}x'$$

$$= \int_{-l_i/2}^{l_i/2} \beta_{i,y}(y' = 0)U\mathrm{d}x' = Ul_i. \qquad (2.44)$$

In this derivation, it is exploited that the RWG basis function is zero outside of the i-th triangle pair and its component normal to the edge (here: $\beta_{i,y}$) is constant and unity [69]. The MoM excitation vector $\mathbf{V}$ can thus be simplified to

$$\mathbf{V} = Ul_i\big(0, \cdots ,0,1,0, \cdots ,0\big)^{\mathrm{T}}, \qquad (2.45)$$

where only the i-th component is unequal to 0. This concept can easily be generalized to more than one delta-gap source, as will be made extensive use of throughout this thesis.

2.3.4 Practical Considerations

The modal analyses in this thesis are conducted using a characteristic mode computation (CMC) software developed at the Institute of Microwave and Wireless Systems of Leibniz University Hannover. This software is implemented in MATLAB [71]. It is based on the MoM MATLAB code presented in [70]. This code is modified by advanced computational techniques introduced in [72] in order to enhance the accuracy of the calculation of the impedance matrix. The eigenvalue problem is solved by means of built-in MATLAB functions. In this subsection, some practical considerations regarding the characteristic mode computation are discussed.

The CMC software possesses a built-in meshing algorithm based on the Delaunay triangulation [73] in order to create the triangular mesh and introduce the RWG basis functions. In [25], it is recommended for characteristic mode analyses to choose the mesh density in such a way that the maximum edge length occurring in the mesh is less than $\frac{1}{15}$ of the smallest wavelength to be considered. Throughout this thesis, the mesh density is set such that the maximum edge length does not exceed $\frac{1}{20}$ of the smallest wavelength. This is primarily done in order to obtain accurate surface current densities.

For the numerical computation of characteristic modes, it is beneficial to restrict the number of modes to be taken into account [62]. This is motivated by the fact that there is usually only a limited number of modes which contribute significantly to the modal expansion (cf. section 2.2.2). Throughout this thesis, only modes with an eigenvalue $|\lambda_n| \leq 100$ are taken into account. This restriction has been found to be sufficient so that (2.26) is fulfilled approximately.

The generalized eigenvalue problem (2.14) defining characteristic modes is frequency dependent. It can only be solved at single frequency points. If a range of frequencies is of interest, the eigenvalue problem has to be solved at each frequency point within the range independently [25]. The aim of eigenvalue tracking is to relate the characteristic modes at different frequency points such that the eigenvalue curves are reasonably smooth, i.e., there are no discontinuities, and characteristic surface current densities do not change abruptly.

Several tracking algorithms are presented in the literature. An overview is provided in [62]. The correlation-based tracking introduced therein is used by the CMC software. It correlates the characteristic currents at two adjacent frequency points setting up a correlation matrix. Those mode pairs with highest correlation each are assigned the same mode index and are thus considered the same mode over frequency. This procedure is repeated for all frequency points.

The correlation-based tracking algorithm is generally very robust. However, it suffers from the presence of degenerate modes [62]. This problem will be revisited in section 4.2.

2.4 Multimode Antenna Design

In section 2.2, it was shown that the characteristic modes of an arbitrary PEC object possess particular orthogonality properties. Especially, the far fields of the characteristic modes (characteristic far fields) are orthogonal to each other (2.21). As discussed in section 1, this is an interesting property for MIMO applications. If it is possible to selectively excite different characteristic modes with different antenna ports, a diversity antenna with uncorrelated (orthogonal) antenna ports can be realized. This is the basic goal of multimode antenna design.[13]

2.4.1 Selective Excitation of Characteristic Modes

According to (2.22) and (2.23), the total surface current density and the total radiated field are weighted sums of characteristic modes. Throughout this thesis, a characteristic mode is said to be excited if it contributes to these weighted sums. In order to achieve antenna diversity, it would be desirable that an antenna port excites only a limited set of characteristic modes (ideally only one mode) whose weighting coefficients are unequal to zero. In short terms, this is called "selective excitation of characteristic modes" [41].

A basic measure of the correlation between two antenna ports is the envelope correlation coefficient (ECC). The ECC between the u-th and the v-th antenna port of a multimode antenna ECC_{uv} is computed as follows [67]:

$$\text{ECC}_{uv} = \frac{\frac{1}{2Z_0} \oiint_{S_\infty} \left(\mathbf{E}_u^*(\mathbf{r}) \cdot \mathbf{E}_v(\mathbf{r}) \right) \mathrm{d}S}{\sqrt{P_{\text{rad},u}} \sqrt{P_{\text{rad},v}}}, \tag{2.46}$$

where $\mathbf{E}_{u;v}$ denotes the total electric far field radiated by the u-th and the v-th antenna port, respectively. The integration is taken over the sphere at infinity S_∞ (far field). $P_{\text{rad},u;v}$ denotes the total radiated power of the u-th and the v-th antenna port, respectively. The ECC is a measure of how much power is radiated by the u-th antenna port if the v-th port is driven. If $u = v$, it yields 1 due to the normalization.

---

[13]The following publications are related to the content of this section: [PM18a] (© 2018 IET), [PM19b] (© 2019 IEEE), and [JPHM20a] (© 2020 IEEE).

The total radiated far fields in (2.46) can be expanded in terms of characteristic modes (2.23):

$$\text{ECC}_{uv} = \frac{\frac{1}{2Z_0} \oiint_{S_\infty} \left(\sum_{m=1}^{\infty} a_{m,u}^* \mathbf{E}_m^*(\mathbf{r}) \cdot \sum_{n=1}^{\infty} a_{n,v} \mathbf{E}_n(\mathbf{r}) \right) \mathrm{d}S}{\sqrt{P_{\text{rad},u}} \sqrt{P_{\text{rad},v}}}. \tag{2.47}$$

It is noted that the excitation information is completely represented by the modal weighting coefficients $a_{m,u}$ and $a_{n,v}$ of the u-th and the v-th antenna port, respectively, as the characteristic far fields themselves are independent of any excitation. Due to the linearity of the integration, (2.47) can be rearranged:

$$\text{ECC}_{uv} = \frac{\sum_{m=1}^{\infty} \sum_{n=1}^{\infty} a_{m,u}^* a_{n,v} \frac{1}{2Z_0} \oiint_{S_\infty} \left(\mathbf{E}_m^*(\mathbf{r}) \cdot \mathbf{E}_n(\mathbf{r}) \right) \mathrm{d}S}{\sqrt{P_{\text{rad},u}} \sqrt{P_{\text{rad},v}}}. \tag{2.48}$$

Exploiting the orthogonality of characteristic far fields (2.21), this reduces to

$$\text{ECC}_{uv} = \frac{\sum_{m=1}^{\infty} \sum_{n=1}^{\infty} a_{m,u}^* a_{n,v} \delta_{mn}}{\sqrt{P_{\text{rad},u}} \sqrt{P_{\text{rad},v}}}, \tag{2.49}$$

which is unequal to zero only if $m = n$:

$$\text{ECC}_{uv} = \frac{\sum_{n=1}^{\infty} a_{n,u}^* a_{n,v}}{\sqrt{P_{\text{rad},u}} \sqrt{P_{\text{rad},v}}} = \sum_{n=1}^{\infty} b_{n,u}^* b_{n,v}, \tag{2.50}$$

where $b_{n,u;v}$ are the normalized modal weighting coefficients of the u-th and the v-th antenna port, respectively, as defined in (2.26). Equation (2.50) demonstrates the fact that two antenna ports are orthogonal if they excite mutually exclusive sets of characteristic modes, i.e., $b_{n,u} = 0$ if $b_{n,v} \neq 0$ and vice versa, and hence confirms the statements given above.

The aim of multimode antenna design for MIMO is thus to realize antenna ports that excite mutually exclusive sets of characteristic modes. In order to achieve this aim, it is necessary to evaluate the requirements for a characteristic mode to contribute significantly to the total radiation. To this end, the modal weighting coefficients in (2.22) and (2.23) need to be inspected more closely. There are basically two criteria that have to be fulfilled so that a characteristic mode contributes significantly.

The necessary criterion is that a characteristic mode needs to be significant, i.e., its modal significance must be greater than or equal to $\frac{1}{\sqrt{2}}$, as introduced in

section 2.2.3. This ensures that the mode offers the potential to contribute significantly. The sufficient criterion is then that the excitation couples adequately to the mode, which is measured by means of the modal excitation coefficient (2.24). Obviously, if the exciting field is orthogonal to the characteristic surface current density, the excitation coefficient is zero and the mode does not contribute to the total radiation. However, finding an excitation consisting of a limited number of field sources such that the mode contributes significantly is not that obvious and is usually done by manually inspecting the characteristic surface current densities, as demonstrated in the following subsections.

2.4.2 State-of-the-Art Design Work Flow

Having laid the foundations of multimode antenna design, the state-of-the-art design work flow as reported in the literature is now reviewed by means of an example. A rectangular PEC plate with dimensions $120\,\text{mm} \times 60\,\text{mm}$ as shown in Fig. 2.3 is chosen as a simple model for a typical smart phone chassis, which shall be used as a multimode antenna for MIMO applications by selectively exciting characteristic modes [43].
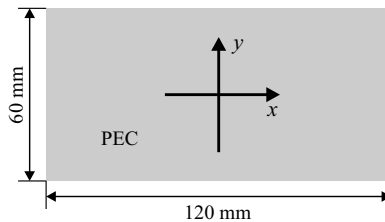

Figure 2.3   Rectangular PEC plate and coordinate system. © 2018 IET [PM18a].

The design process starts with a characteristic mode analysis. As a first step, the modal parameters should be evaluated (section 2.2.3). To this end, the eigenvalues and the modal significances of the rectangular PEC plate are shown in Fig. 2.4 from 1 GHz to 6 GHz. With these plots, it is possible to decide which modes are available for potential excitation as a function of frequency. The region where modes are considered significant is marked by the black dashed lines. For the rectangular plate, it is observed that each mode enters the significance region at a specific frequency and then stays significant. In particular, the number of significant modes increases with increasing frequency.
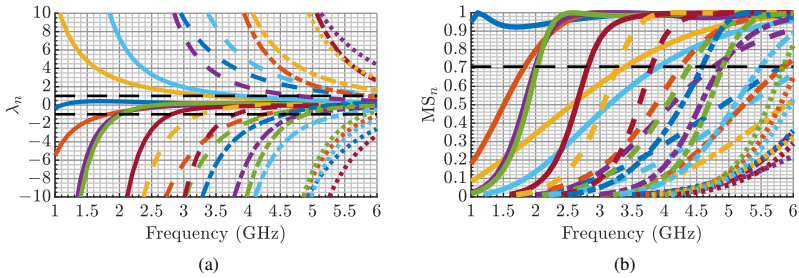
Figure 2.4   Modal parameters of rectangular PEC plate over frequency. Significance region denoted by black dashed lines. (a) Eigenvalues. (b) Modal significances.
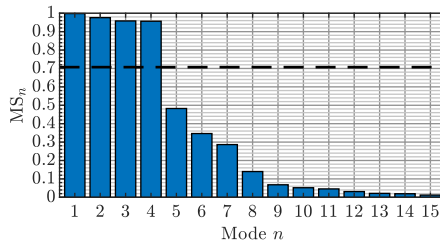

Figure 2.5   Modal significances of rectangular PEC plate at 2.5 GHz. Modes sorted according to their significance. Modes are considered significant if their modal significance is greater than $\frac{1}{\sqrt{2}} \approx 0.71$.

It is now supposed that the operating frequency is chosen to be 2.5 GHz. The modes can then be sorted according to their significance at that frequency, yielding the significance plot in Fig. 2.5. It is clearly visible that there are four significant modes which have the potential to contribute significantly to the radiation. The corresponding surface current densities are shown in Fig. 2.6. Interestingly, they are reminiscent of current modes of fundamental antenna types. Mode 1 (Fig. 2.6(a)) is similar to a full-wave dipole mode. Mode 2 (Fig. 2.6(b)), in contrast, has a differential mode behavior. Modes 3 (Fig. 2.6(c)) and 4 (Fig. 2.6(d)), finally, can be considered as half-wave dipole modes over the long and the short edge, respectively.

Based on these characteristic surface current densities, antenna ports can now be defined. Delta-gap sources (section 2.3.3) are placed on the plate and driven in such a way that the resulting ports reproduce the above-described current

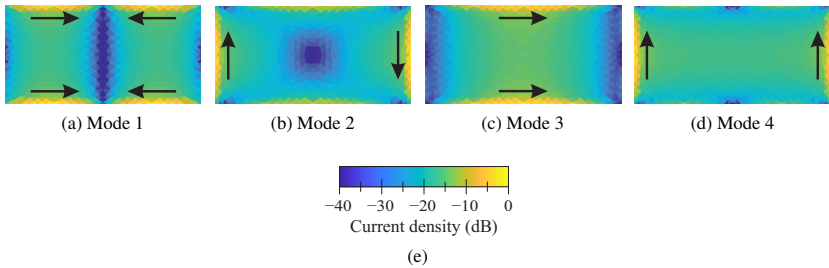|(a) Mode 1|(b) Mode 2|(c) Mode 3|(d) Mode 4|

(e)

Figure 2.6 Normalized surface current densities of significant characteristic modes of rectangular PEC plate at 2.5 GHz. Principal current directions denoted by arrows. (a)–(d) Modes 1 to 4 as sorted in Fig. 2.5. (e) Color bar. © 2020 IEEE [JPHM20a].

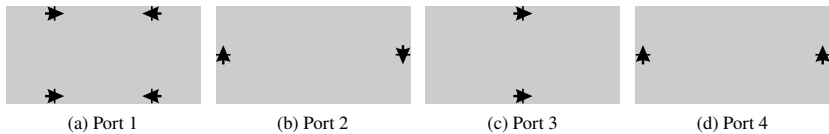|(a) Port 1|(b) Port 2|(c) Port 3|(d) Port 4|

Figure 2.7 Port configuration on rectangular PEC plate. Positions of delta-gap sources denoted by black lines and voltage directions denoted by arrows. (a)–(d) Ports 1 to 4. © 2020 IEEE [JPHM20a].

characteristics. One possible solution is shown in Fig. 2.7. Port 1 (Fig. 2.7(a)), for example, is designed to excite mode 1 (Fig. 2.6(a)). It consists of four delta-gap sources which are driven simultaneously with the same amplitude. The relative phases (voltage directions) between the delta-gap sources are denoted by the arrows. As intended, this configuration corresponds to the principal current directions of mode 1. In the same way, ports 2, 3, and 4 (Fig. 2.7(b)–(d)) are designed to excite modes 2, 3, and 4 (Fig. 2.6(b)–(d)), respectively.

The effectiveness of the chosen port configuration can now be evaluated by means of the normalized modal weighting coefficients (2.26), which are depicted in Fig. 2.8(a). As intended, the antenna ports excite the respective modes to a high degree. However, non-significant modes are also excited to some extent. Nevertheless, each port excites a different set of modes. In subsection 2.4.1, this was found to be a prerequisite for a good multimode antenna design. Indeed, the antenna ports are uncorrelated as demonstrated by the ECC in Fig. 2.8(b) calculated according to (2.46). This is due to the fact that the antenna ports excite mutually exclusive sets of characteristic modes.
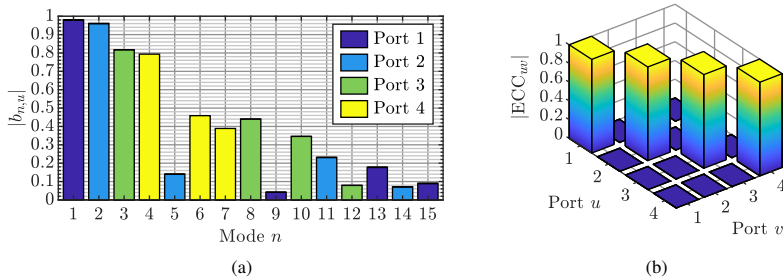
Figure 2.8   Excitation parameters of rectangular PEC plate at 2.5 GHz with port configuration according to Fig. 2.7. (a) Normalized modal weighting coefficients. (b) Envelope correlation coefficients.

The next design step would be to replace the delta-gap sources by practical excitation structures (coupling elements) [42] and perform impedance matching. Furthermore, a feed network is necessary in order to distribute the input signals of the antenna ports to the respective coupling elements on the antenna with the correct amplitude and phase relations [74]. These steps are not focused here and will be postponed to chapter 6. The basic steps of the design work flow are summarized as follows:

1. Conduct a modal analysis yielding characteristic surface current densities and eigenvalues.

2. Evaluate the modal parameters and identify significant modes.

3. Evaluate the corresponding characteristic surface current densities in order to derive suitable port configurations.

4. Check the antenna ports by means of the modal weighting coefficients.

5. Implement the coupling elements and, if required, the feed network.

It may be necessary to repeat steps 3 and 4 with different port configurations in order to determine a suitable antenna setup iteratively.

The important design step for MIMO applications is the placement of the delta-gap sources forming the antenna ports. This has been done here intuitively by inspecting the characteristic surface current densities, yielding four orthogonal antenna ports. The following example will show that this intuitive approach is limited and a systematic design procedure is necessary.

2.4.3 Towards More Antenna Ports

In the previous subsection, an idealized four-port multimode antenna has been designed. The simple question arises how more orthogonal antenna ports may be realized. An obvious answer to this question might be to increase the number of significant characteristic modes. This approach is followed now.
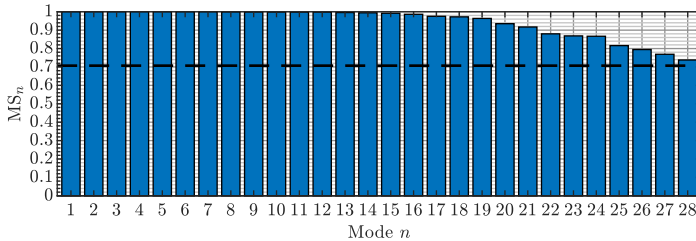

Figure 2.9   Modal significances of rectangular PEC plate at 7.25 GHz. Modes sorted according to their significance. Only the significant modes are taken into account for the sake of conciseness. © 2018 IET [PM18a].

Again, the rectangular PEC plate in Fig. 2.3 is considered. The modal analysis in Fig. 2.4 has shown that with increasing frequency the number of significant modes increases. It is now supposed that the ultra-wide frequency range from 6 GHz to 8.5 GHz is of interest (section 1.1) [52, 54]. To get a first impression of how many modes are significant in this frequency band, the modal significances are evaluated at the center frequency 7.25 GHz, as shown in Fig. 2.9. A total of 28 modes are significant. If it were possible to excite all these modes separately, a huge diversity potential could be exploited.

Following the work flow presented in the previous subsection, the characteristic surface current densities as depicted in Fig. 2.10 are inspected. Compared to those shown in Fig. 2.6, the current distributions are now rather complex and difficult to interpret. In particular, it proves intricate to place delta-gap sources in such a way that only certain desired modes are excited. Obviously, the intuitive design approach is not adequate to tackle this problem.

However, a closer inspection of Fig. 2.10 reveals that several characteristic surface current densities exhibit certain qualitative similarities, e.g., with respect to the distribution of nulls and maxima. It is thus purposeful to group the characteristic modes according to such similarities. A fundamental classification can be carried out based on the symmetry properties of the characteristic surface current densities. By examining the current densities in Fig. 2.10, it is found

(a) Mode 1 (b) Mode 2 (c) Mode 3 (d) Mode 4

(e) Mode 5 (f) Mode 6 (g) Mode 7 (h) Mode 8

(i) Mode 9 (j) Mode 10 (k) Mode 11 (l) Mode 12

(m) Mode 13 (n) Mode 14 (o) Mode 15 (p) Mode 16

(q) Mode 17 (r) Mode 18 (s) Mode 19 (t) Mode 20

(u) Mode 21 (v) Mode 22 (w) Mode 23 (x) Mode 24

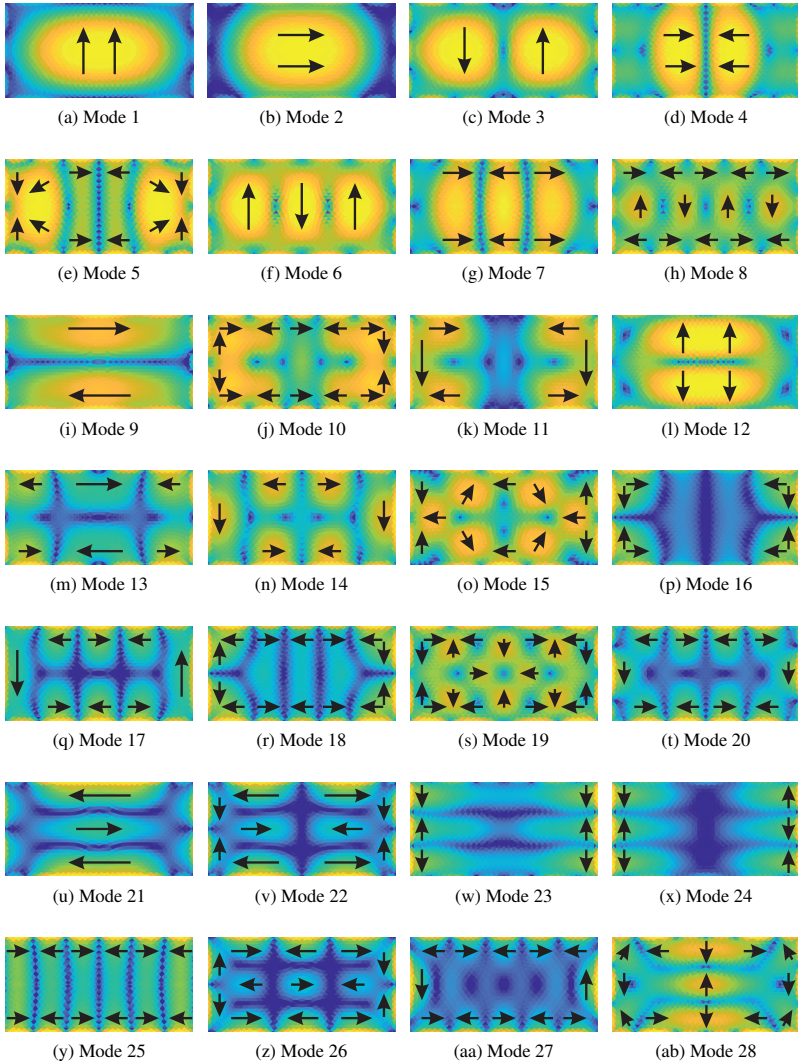(y) Mode 25 (z) Mode 26 (aa) Mode 27 (ab) Mode 28

Figure 2.10   Normalized surface current densities of significant characteristic modes of rectangular PEC plate at 7.25 GHz. Principal current directions denoted by arrows. Color bar in Fig. 2.6(e). (a)–(ab) Modes 1 to 28 as sorted in Fig. 2.9.

Set	Symmetry	Modes	Port
1	Reflection about x-axis Reflection about y-axis Rotation about z-axis	4, 5, 12, 16, 19, 22, 25	1
2	Rotation about z-axis	3, 8, 9, 13, 17, 24, 27	2
3	Reflection about x-axis	2, 7, 10, 15, 18, 21, 26	3
4	Reflection about y-axis	1, 6, 11, 14, 20, 23, 28	4

Table 2.1   Grouping of significant characteristic modes of rectangular PEC plate at 7.25 GHz according to their symmetry properties with respect to coordinate system in Fig. 2.3. © 2018 IET [PM18a].
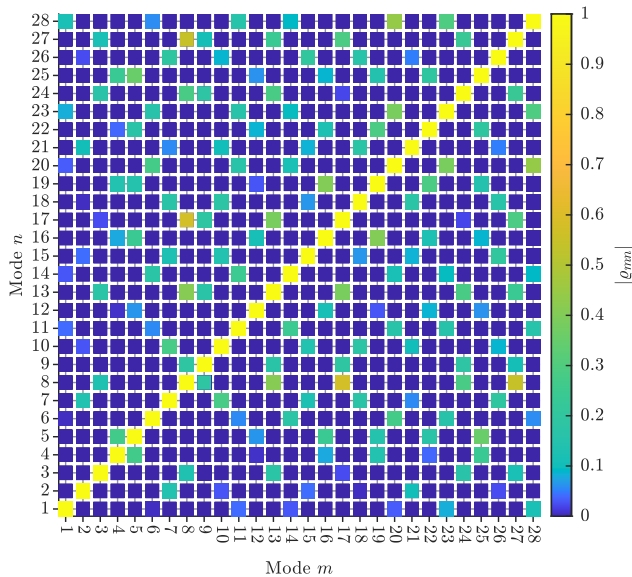

Figure 2.11   Characteristic current correlation coefficients of rectangular PEC plate at 7.25 GHz computed according to (2.51). © 2018 IET [PM18a].

that some modes possess reflection symmetry about the x-axis, some possess reflection symmetry about the y-axis, some possess rotational symmetry about the z-axis, and some possess all three symmetries with respect to the coordinate system in Fig. 2.3. It should be noted that these are exactly the symmetry operations that leave the rectangular plate invariant. The symmetry properties
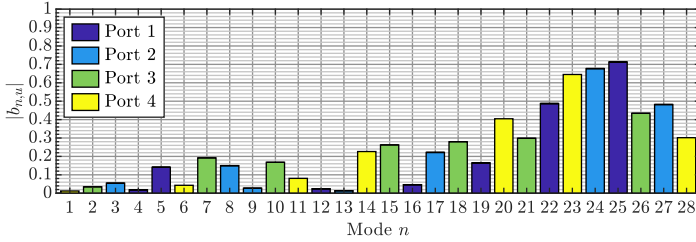
Figure 2.12   Normalized modal weighting coefficients of rectangular PEC plate at 7.25 GHz with port configuration according to Fig. 2.7. © 2018 IET [PM18a].

of the 28 significant characteristic modes are summarized in Table 2.1 and the modes are grouped accordingly into four sets.

In order to investigate whether the characteristic surface current densities of these sets are somehow related, the current correlation coefficient ϱ_{mn} between the m-th and the n-th characteristic surface current density is defined:

$$\varrho_{mn} = \frac{\left\langle \mathbf{J}_m(\mathbf{r}'), \mathbf{J}_n(\mathbf{r}') \right\rangle}{\left\langle \mathbf{J}_m(\mathbf{r}'), \mathbf{J}_m(\mathbf{r}') \right\rangle \left\langle \mathbf{J}_n(\mathbf{r}'), \mathbf{J}_n(\mathbf{r}') \right\rangle}. \tag{2.51}$$

The characteristic current correlation coefficients computed this way are shown in Fig. 2.11. It is observed that the characteristic surface current densities belonging to the same set, i.e., possessing the same symmetry, are correlated, whereas those belonging to different sets are apparently orthogonal to each other.

At this point, it is noted that the antenna ports defined in Fig. 2.7 can also be distinguished by their symmetry properties. Accordingly, they are also listed in Table 2.1. These ports are now used on the rectangular plate at 7.25 GHz. The evaluation of the normalized modal weighting coefficients in Fig. 2.12 reveals that each port only excites modes which belong to the same set as the port. On the one hand, this is a positive result for multimode antenna design as the antenna ports are again uncorrelated, as shown in Fig. 2.13. Exploiting symmetries may be a possible way towards a systematic design procedure. On the other hand, all 28 significant modes are to some extent in use, leaving no further degree of freedom for realizing a fifth uncorrelated antenna port. Bearing in mind Fig. 2.8(a), even non-significant modes are affected. Apparently, no more than four uncorrelated antenna ports may be realized on a rectangular plate. However, some modes in Fig. 2.12 are only weakly excited. This is due to
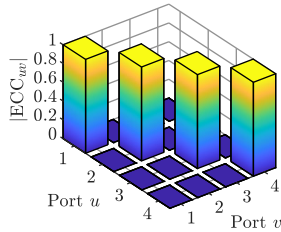
Figure 2.13 Envelope correlation coefficients of rectangular PEC plate at 7.25 GHz with port configuration according to Fig. 2.7. © 2018 IET [PM18a].

the actual port implementation. It may thus be possible to define further antenna ports that are not perfectly uncorrelated, but only weakly correlated.

This last example has shown that the characteristic modes seem to be fundamentally governed by the symmetry of the underlying PEC object. In particular, this relationship has obviously direct consequences on multimode antenna design. Therefore, the theory of symmetry and its connection to the theory of characteristic modes will be investigated more closely in the following chapters.

3 Theory of Symmetry

A symmetry operation is a transformation which maps an arbitrary geometric object onto itself. In other words, such an operation leaves the object unaltered or invariant. Mathematically, symmetry operations are described as coordinate transformations. Those transformations that leave a specific object invariant form the so-called symmetry group of that object [57].

   This chapter is intended to present the fundamental concepts of the theory of symmetry. To this end, first, the basics of coordinate transformations are recapped. After that, the mathematical concept of group theory is introduced. It is then shown how group theory is used to describe symmetry (symmetry group). Based on this, advanced topics, in particular representation theory, are discussed in order to establish a connection to the theory of characteristic modes. The final goal of this chapter is to derive general properties of characteristic modes which are governed by the symmetry group of the underlying PEC object.[14]

3.1 Coordinate Transformations

Coordinate transformations are the basic elements of a symmetry group. Therefore, it is necessary to introduce the nomenclature of coordinate transformations and explain how to work with them.

3.1.1 Symbolic Notation

Throughout this thesis, the Schoenflies notation will be employed [75]. If objects of finite extent are considered, as is typical of antenna problems, there are two basic types of coordinate transformations [57]: The rotation about an axis and the reflection through a plane.

   A rotation about an axis by an angle $\frac{2\pi}{n}$, where n is a positive integer, is denoted by C_n [57]. This operation may be repeated p times, which is written as an exponentiation C_n^p. The case $p = n$ yields the identity transformation $E = C_n^n$. As an example, the rotation by $90°$ ($\frac{2\pi}{4}$) is considered. Its symbol is C_4. Repeating

---

[14]The following publications are related to the content of this chapter: [PM19b] (© 2019 IEEE), [PHM21] (© 2021 IEEE).

this operation two times yields the rotation $C_4^2 = C_2$ by $180°$. Repeating the operation three times yields the rotation C_4^3 by $270°$, which is equal to the rotation C_4^{-1} by $-90°$. Repeating the operation four times yields the rotation C_4^4 by $360°$, which finally is equal to the identity transformation E.

A reflection through a plane is denoted by σ [57]. Performing a reflection twice through the same plane is equal to the identity transformation $\sigma^2 = E$. Performing a rotation C_n about an axis by an angle $\frac{2\pi}{n}$ followed by a reflection σ_h through a plane perpendicular to the rotation axis is called a rotary reflection or rotoreflection S_n [57]:[15]

$$S_n = C_n \sigma_h = \sigma_h C_n. \tag{3.1}$$

As a special case, the rotation by $180°$ yields the spatial inversion operator I (point reflection):

$$I = S_2 = C_2 \sigma_h = \sigma_h C_2. \tag{3.2}$$

Any reflection can thus also be expressed as a combination of the inversion and the rotation by $180°$ about the axis normal to the reflection plane [57]:

$$\sigma_h = IC_2^{-1} = IC_2 = C_2^{-1}I = C_2 I. \tag{3.3}$$

Combining (3.1) and (3.3), any rotoreflection S_n can also be written in terms of two rotations about the same axis and the inversion:

$$S_n = IC_2 C_n. \tag{3.4}$$

All coordinate transformations can be expressed as combinations of rotations and the inversion, which will be exploited in the following subsection.

3.1.2 Rotation Matrices

All coordinate transformations symbolically introduced above have in common that at least one point in a real three-dimensional Euclidian space $\mathbb{R}^3$ is left invariant. The coordinate system is usually chosen such that this point is the coordinate origin. An arbitrary coordinate transformation T can then be explicitly expressed by a corresponding orthogonal rotation matrix $\mathbf{R}(T)$ [75]:

$$\mathbf{R}(T) = \begin{pmatrix} R_{11}(T) & R_{12}(T) & R_{13}(T) \\ R_{21}(T) & R_{22}(T) & R_{23}(T) \\ R_{31}(T) & R_{32}(T) & R_{33}(T) \end{pmatrix}, \quad \text{with} \quad \mathbf{R}^{-1}(T) = \mathbf{R}^{\mathrm{T}}(T). \tag{3.5}$$

---

[15]The application of several coordinate transformations in succession is written as a product, e.g., in (3.1). By convention, the operator on the right acts first in this notation [75]. In general, coordinate transformations are not commutative so that the order of operations is of importance.

If the original coordinates are denoted by $\mathbf{r} = (x,y,z)^{\mathrm{T}}$, the transformed coordinates $\tilde{\mathbf{r}} = (\tilde{x},\tilde{y},\tilde{z})^{\mathrm{T}}$ are computed as follows [75]:

$$\tilde{\mathbf{r}} = \mathbf{R}(T)\mathbf{r}. \tag{3.6}$$

The rotations C_n are called proper rotations as the determinant of the corresponding rotation matrices is equal to 1 [75]. For a rotation by $\frac{2\pi}{n}$ about an arbitrary axis through the origin whose direction is denoted by the unit vector $\mathbf{n} = (n_x,n_y,n_z)^{\mathrm{T}}$, the elements of the rotation matrix in (3.5) are [75]:

$$R_{11}(C_n) = n_x^2\left(1 - \cos\frac{2\pi}{n}\right) + \cos\frac{2\pi}{n}, \tag{3.7a}$$

$$R_{12}(C_n) = n_x n_y\left(1 - \cos\frac{2\pi}{n}\right) + n_z\sin\frac{2\pi}{n}, \tag{3.7b}$$

$$R_{13}(C_n) = n_x n_z\left(1 - \cos\frac{2\pi}{n}\right) - n_y\sin\frac{2\pi}{n}, \tag{3.7c}$$

$$R_{21}(C_n) = n_y n_x\left(1 - \cos\frac{2\pi}{n}\right) - n_z\sin\frac{2\pi}{n}, \tag{3.7d}$$

$$R_{22}(C_n) = n_y^2\left(1 - \cos\frac{2\pi}{n}\right) + \cos\frac{2\pi}{n}, \tag{3.7e}$$

$$R_{23}(C_n) = n_y n_z\left(1 - \cos\frac{2\pi}{n}\right) + n_x\sin\frac{2\pi}{n}, \tag{3.7f}$$

$$R_{31}(C_n) = n_z n_x\left(1 - \cos\frac{2\pi}{n}\right) + n_y\sin\frac{2\pi}{n}, \tag{3.7g}$$

$$R_{32}(C_n) = n_z n_y\left(1 - \cos\frac{2\pi}{n}\right) - n_x\sin\frac{2\pi}{n}, \tag{3.7h}$$

$$R_{33}(C_n) = n_z^2\left(1 - \cos\frac{2\pi}{n}\right) + \cos\frac{2\pi}{n}. \tag{3.7i}$$

The matrix is defined in such a way that the coordinate system is rotated counterclockwise for positive angles. In Fig. 3.1, this is illustrated for a rotation about the z-axis. Adopting the example from above, the rotation C_{4z} by 90° about the z-axis ($n = 4$, $\mathbf{n} = \mathbf{e}_z = (0,0,1)^{\mathrm{T}}$) is expressed by the rotation matrix

$$\mathbf{R}(C_{4z}) = \begin{pmatrix} 0 & 1 & 0 \\ -1 & 0 & 0 \\ 0 & 0 & 1 \end{pmatrix}. \tag{3.8}$$

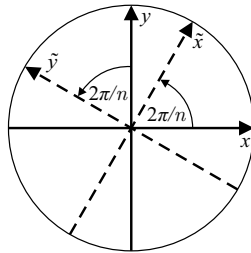Hence, the transformed coordinates expressed in terms of the original coordinates

Figure 3.1   Rotation of coordinate system by $\frac{2\pi}{n}$ about the z-axis.

(a)   (b)   (c)
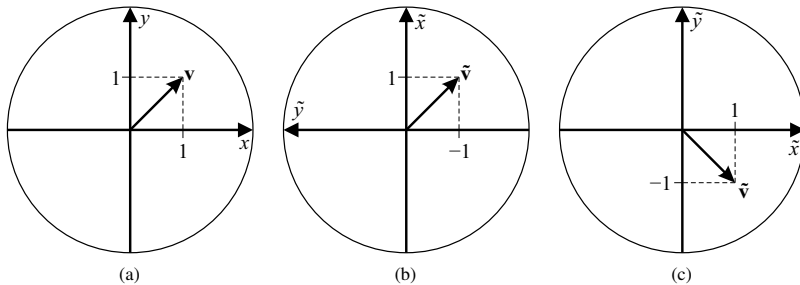
Figure 3.2   Rotation by 90° about the z-axis. (a) Original coordinate system and vector. (b) Fixed vector, coordinate system rotated counterclockwise. (c) Vector rotated clockwise, fixed coordinate system.

are computed in the following way:

$$
\begin{pmatrix} \tilde{x} \\ \tilde{y} \\ \tilde{z} \end{pmatrix} = \begin{pmatrix} 0 & 1 & 0 \\ -1 & 0 & 0 \\ 0 & 0 & 1 \end{pmatrix} \begin{pmatrix} x \\ y \\ z \end{pmatrix} = \begin{pmatrix} y \\ -x \\ z \end{pmatrix},
$$

i.e., the new $\tilde{x}$-axis corresponds to the original y-axis and the new $\tilde{y}$-axis points in negative x-direction, whereas the new $\tilde{z}$-axis is identical to the original z-axis.

Due to the counterclockwise rotation of the coordinate system, an arbitrary vector $\mathbf{v}$ appears to rotate clockwise. As an example, it is supposed that $\mathbf{v} = (1,1,0)^{\mathrm{T}}$ (Fig. 3.2(a)). Applying the rotation matrix yields

$$
\tilde{\mathbf{v}} = \begin{pmatrix} 0 & 1 & 0 \\ -1 & 0 & 0 \\ 0 & 0 & 1 \end{pmatrix} \begin{pmatrix} 1 \\ 1 \\ 0 \end{pmatrix} = \begin{pmatrix} 1 \\ -1 \\ 0 \end{pmatrix}.
$$

This result can be interpreted in two ways: The vector remains fixed and the coordinate system is rotated by $+90°$ about the z-axis, as illustrated in Fig. 3.2(b), or the vector is rotated by $-90°$ about the z-axis and the coordinate system remains fixed, as illustrated in Fig. 3.2(c). Both interpretations are equivalent [76, 77] and some care must be taken when implementing, evaluating, and interpreting coordinate transformations. The second interpretation is useful for comparing the effects of different coordinate transformations with respect to a fixed reference and will be adopted throughout this thesis.

Reflections, rotoreflections, and the inversion are summarized as improper rotations as the determinant of their respective rotation matrices is equal to -1 [75]. In order to compute the rotation matrices of the improper rotations, the rotation matrix of the inversion should be introduced first [75]:

$$\mathbf{R}(I) = \begin{pmatrix} -1 & 0 & 0 \\ 0 & -1 & 0 \\ 0 & 0 & -1 \end{pmatrix} = -\mathbf{E}, \tag{3.9}$$

where $\mathbf{E}$ is the identity matrix. This rotation matrix simply states that every point is inverted, i.e., $\tilde{\mathbf{r}} = -\mathbf{r}$. Now, it is exploited that the rotation matrix of the product of two coordinate transformations T_1 and T_2 can be written as a matrix multiplication [75]:[16]

$$\mathbf{R}(T_1 T_2) = \mathbf{R}(T_1)\mathbf{R}(T_2). \tag{3.10}$$

Taking into account (3.3), the rotation matrix of a reflection can thus be expressed as the product of the rotation matrices of the rotation by $180°$ about the axis normal to the reflection plane and the inversion:

$$\mathbf{R}(\sigma_h) = \mathbf{R}(IC_2) = \mathbf{R}(C_2 I) = \mathbf{R}(I)\mathbf{R}(C_2) = \mathbf{R}(C_2)\mathbf{R}(I). \tag{3.11}$$

As an example, the reflection σ_{xy} through the xy-plane is considered. The normal axis is the z-axis so that the rotation C_{2z} is needed, whose rotation matrix is computed using (3.7). The rotation matrix of σ_{xy} is therefore

$$\mathbf{R}(\sigma_{xy}) = \mathbf{R}(I)\mathbf{R}(C_{2z}) = \begin{pmatrix} -1 & 0 & 0 \\ 0 & -1 & 0 \\ 0 & 0 & -1 \end{pmatrix}\begin{pmatrix} -1 & 0 & 0 \\ 0 & -1 & 0 \\ 0 & 0 & 1 \end{pmatrix} = \begin{pmatrix} 1 & 0 & 0 \\ 0 & 1 & 0 \\ 0 & 0 & -1 \end{pmatrix}.$$

---

[16]In general, $T_1 T_2 \neq T_2 T_1$. Consequently, $\mathbf{R}(T_1)\mathbf{R}(T_2) \neq \mathbf{R}(T_2)\mathbf{R}(T_1)$ [75].

In the same manner, the rotation matrix of the rotoreflection S_{4z} by 90° about the z-axis can now be computed using either (3.1) or (3.4):

$$\mathbf{R}(S_{4z}) = \mathbf{R}(\sigma_{xy})\mathbf{R}(C_{4z}) = \begin{pmatrix} 1 & 0 & 0 \\ 0 & 1 & 0 \\ 0 & 0 & -1 \end{pmatrix}\begin{pmatrix} 0 & 1 & 0 \\ -1 & 0 & 0 \\ 0 & 0 & 1 \end{pmatrix} = \begin{pmatrix} 0 & 1 & 0 \\ -1 & 0 & 0 \\ 0 & 0 & -1 \end{pmatrix}.$$

Consequently, the rotation matrices of all proper and improper rotations can be readily computed in a systematic way. As will become apparent throughout this chapter, the rotation matrices are the basic building blocks of most symmetry-related operations to be introduced.

3.1.3 Transformation Operators

So far, the transformation of the coordinate system has been discussed. When working with characteristic modes, it will be of particular interest how the characteristic surface current densities are affected by a transformation of the coordinate system. It is therefore necessary to describe the transformation of a function under a coordinate transformation.

If an arbitrary scalar function $f(\mathbf{r}') \colon \mathbb{R}^3 \to \mathbb{C}$ is considered,[17] the transformed function $\tilde{f}(\mathbf{r}')$ due to a coordinate transformation T is written as [75]

$$\tilde{f}(\mathbf{r}') = P(T)f(\mathbf{r}') = f(\mathbf{R}^{-1}(T)\mathbf{r}'). \tag{3.12}$$

If instead a vector-valued function $\mathbf{f}(\mathbf{r}') = \big(f_x(\mathbf{r}'), f_y(\mathbf{r}'), f_z(\mathbf{r}')\big)^{\mathrm{T}} \colon \mathbb{R}^3 \to \mathbb{C}^3$ is considered, the transformed function $\tilde{\mathbf{f}}(\mathbf{r}')$ is expressed by

$$\tilde{\mathbf{f}}(\mathbf{r}') = P(T)\mathbf{f}(\mathbf{r}') = \mathbf{R}(T)\mathbf{f}(\mathbf{R}^{-1}(T)\mathbf{r}'). \tag{3.13}$$

In both cases, $P(T)$ is called the transformation operator of the coordinate transformation T operating on the function f or $\mathbf{f}$, respectively [75].[18] The corresponding rotation matrix and its inverse (transpose) are the basic building blocks of this operator. In particular, the inverse of the rotation matrix $\mathbf{R}^{-1}$ effects

---

[17]The primed coordinate vector $\mathbf{r}'$ is used in conjunction with transformation operators as the functions to be operated on throughout this thesis are restricted to a geometric object, e.g., a surface current density on a PEC object.

[18]In this thesis, the symbol P is used interchangeably for both (3.12) and (3.13). This is mirrored by the fact that all operations based on transformation operators to be introduced in this chapter can be applied to both scalar and vector-valued functions. The distinction becomes clear from the context, i.e., the type of function being operated on.
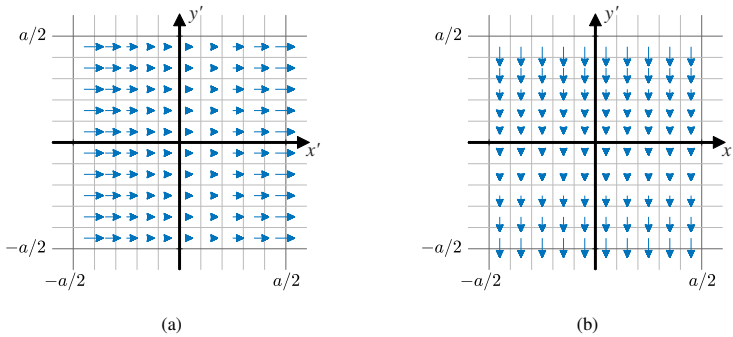
Figure 3.3 Transformation operator of rotation C_{4z} applied to vector-valued function. (a) Original function $\mathbf{f}(\mathbf{r}') = |x'|\mathbf{e}_x$. (b) Transformed function $\bar{\mathbf{f}}(\mathbf{r}') = P(C_{4z})(|x'|\mathbf{e}_x) = -|y'|\mathbf{e}_y$.

a change of the coordinate dependence such that both the original function and the transformed function are expressed in terms of the original coordinates $\mathbf{r}'$ [75]. This corresponds to the interpretation of coordinate transformations with a fixed reference coordinate system as depicted in Fig. 3.2(c).

In order to illustrate this concept, the rotation C_{4z} by $90°$ about the z-axis is considered again and applied to a vector-valued function. The corresponding rotation matrix has already been computed above (3.8) so that the transformation operator has the form

$$P(C_{4z})\mathbf{f}(\mathbf{r}') = \begin{pmatrix} 0 & 1 & 0 \\ -1 & 0 & 0 \\ 0 & 0 & 1 \end{pmatrix} \mathbf{f}\left(\begin{pmatrix} 0 & -1 & 0 \\ 1 & 0 & 0 \\ 0 & 0 & 1 \end{pmatrix} \begin{pmatrix} x' \\ y' \\ z' \end{pmatrix} \right) = \begin{pmatrix} f_y(-y',x',z') \\ -f_x(-y',x',z') \\ f_z(-y',x',z') \end{pmatrix}.$$

Now, it is supposed that the function $\mathbf{f}(\mathbf{r}') = |x'|\mathbf{e}_x$ restricted to a square domain $x',y' \in \left[-\frac{a}{2}, \frac{a}{2}\right]$ as shown in Fig. 3.3(a) is given. Applying the transformation operator yields

$$P(C_{4z})(|x'|\mathbf{e}_x) = -|y'|\mathbf{e}_y,$$

which is shown in Fig. 3.3(b). The x-dependence and the x-direction are replaced by a y-dependence and $-y$-direction, respectively. The transformed function appears to be rotated by $-90°$, which is equivalent to a rotation of the coordinate system by $+90°$ (cf. Fig. 3.2) [77]. As hinted at by this example, the

transformation operators are the basic operators to treat surface current densities under coordinate transformations.

In this context, some fundamental properties of the transformation operators need to be introduced [75, 77]. First of all, the operators are linear:

$$P(T)\big(a_1 f_1(\mathbf{r}') + a_2 f_2(\mathbf{r}')\big) = a_1 P(T) f_1(\mathbf{r}') + a_2 P(T) f_2(\mathbf{r}'), \tag{3.14a}$$

$$P(T)\big(a_1 \mathbf{f}_1(\mathbf{r}') + a_2 \mathbf{f}_2(\mathbf{r}')\big) = a_1 P(T) \mathbf{f}_1(\mathbf{r}') + a_2 P(T) \mathbf{f}_2(\mathbf{r}'), \tag{3.14b}$$

with $a_1, a_2 \in \mathbb{C}$. Another important property is that the transformation operator of a succession of coordinate transformations T_1 and T_2 is equal to applying the two respective transformation operators in succession:[19]

$$P(T_1 T_2) f(\mathbf{r}') = P(T_1)\big(P(T_2) f(\mathbf{r}')\big), \tag{3.15a}$$

$$P(T_1 T_2) \mathbf{f}(\mathbf{r}') = P(T_1)\big(P(T_2) \mathbf{f}(\mathbf{r}')\big). \tag{3.15b}$$

Finally, the transformation operators are unitary operators:

$$\Big\langle P(T) f_1(\mathbf{r}'), P(T) f_2(\mathbf{r}') \Big\rangle = \Big\langle f_1(\mathbf{r}'), f_2(\mathbf{r}') \Big\rangle, \tag{3.16a}$$

$$\Big\langle P(T) \mathbf{f}_1(\mathbf{r}'), P(T) \mathbf{f}_2(\mathbf{r}') \Big\rangle = \Big\langle \mathbf{f}_1(\mathbf{r}'), \mathbf{f}_2(\mathbf{r}') \Big\rangle. \tag{3.16b}$$

The unitarity of the transformation operators can be interpreted as the norm or length preserving property. In particular, if $\mathbf{f}_1 = \mathbf{f}_2$, it is obvious that the norm of a vector-valued function is not affected by a coordinate transformation.[20]

3.2 Group Theory

In mathematics, a group $\mathcal{G}$ is defined by the following four axioms [66, 75, 77]:

1. The product $T_3 = T_1 T_2$ of two elements T_1 and T_2 of the group is again an element of the group, i.e., a group is closed under multiplication.

2. The group multiplication is associative: $(T_1 T_2) T_3 = T_1 (T_2 T_3)$.[21]

---

[19] This corresponds to the interpretation already encountered in subsection 3.1.1 that the operator on the right (here: T_2) acts first.

[20] Based on the definition of the inner product and the corresponding norm in appendix B, the functions to be operated on need to be square-integrable. This condition is fulfilled by all functions considered in this thesis due to the restriction to a finite geometric object.

[21] The group multiplication is in general not commutative.

3. There is always an identity element E such that $TE = ET = T$.

4. To each element T there exists an inverse element T^{-1} in the group such that $TT^{-1} = T^{-1}T = E$.

The following sections will focus on finite groups as they are more common in antenna problems and easier to understand at the beginning. Finite groups have a finite number of elements, which is called the group order g. The concepts to be introduced in the following sections will be generalized to specific groups with an infinite number of elements in section 3.6 at the end of this chapter.
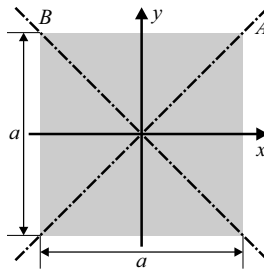

Figure 3.4   Square plate in xy-plane with coordinate system and symmetry axes. © 2019 IEEE [PM19b].

Symmetry operation	Symbol
Identity	E
Rotation by 90° about the z-axis	C_{4z}
Rotation by 180° about the z-axis	C_{2z}
Rotation by 270° about the z-axis	C_{4z}^3
Rotation by 180° about the x-axis	C_{2x}
Rotation by 180° about the y-axis	C_{2y}
Rotation by 180° about the diagonal A	C_{2A}
Rotation by 180° about the diagonal B	C_{2B}

Table 3.1   The eight elements of symmetry group D_4.

For example, the symmetry operations of a square plate as shown in Fig. 3.4 form a finite group, which is called D_4. It consists of eight coordinate transformations ($g = 8$) that leave the square plate invariant [78]. These symmetry operations are listed in Table 3.1.

D_4	E	C_{4z}	C_{2z}	C_{4z}^3	C_{2x}	C_{2y}	C_{2A}	C_{2B}
E	E	C_{4z}	C_{2z}	C_{4z}^3	C_{2x}	C_{2y}	C_{2A}	C_{2B}
C_{4z}	C_{4z}	C_{2z}	C_{4z}^3	E	C_{2B}	C_{2A}	C_{2x}	C_{2y}
C_{2z}	C_{2z}	C_{4z}^3	E	C_{4z}	C_{2y}	C_{2x}	C_{2B}	C_{2A}
C_{4z}^3	C_{4z}^3	E	C_{4z}	C_{2z}	C_{2A}	C_{2B}	C_{2y}	C_{2x}
C_{2x}	C_{2x}	C_{2A}	C_{2y}	C_{2B}	E	C_{2z}	C_{4z}	C_{4z}^3
C_{2y}	C_{2y}	C_{2B}	C_{2x}	C_{2A}	C_{2z}	E	C_{4z}^3	C_{4z}
C_{2A}	C_{2A}	C_{2y}	C_{2B}	C_{2x}	C_{4z}^3	C_{4z}	E	C_{2z}
C_{2B}	C_{2B}	C_{2x}	C_{2A}	C_{2y}	C_{4z}	C_{4z}^3	C_{2z}	E

Table 3.2   Multiplication table of symmetry group D_4. The table lists the products $T_1 T_2$, where T_1 is found in the first column from the left and T_2 is found in the first row from the top.

Symmetry groups whose coordinate transformations leave at least one point of the coordinate system invariant are called point groups [76].[22] Point groups can only contain proper and improper rotations. Single antenna elements, and in particular multimode antennas, typically fall in this category, as will become clear throughout this thesis.[23]

Performing two symmetry operations in succession, as introduced in section 3.1.1, is the group multiplication (cf. (3.10) and (3.15)). By multiplying all elements of a group with each other, the group multiplication table is set up [77]. For the symmetry group D_4, this is shown in Table 3.2. The product of any two elements is again an element of the group, as required. Obviously, the identity transformation is the identity element of the group. Furthermore, the inverse elements can be identified by the products yielding E. In particular, $C_{4z}^3 = C_{4z}^{-1}$, i.e., the rotation by $270°$ is equal to the rotation by $-90°$.

3.2.1 Classes

An element T_1 of a group $\mathcal{G}$ is said to be conjugate to another element T_2 of the same group if [75, 77]

$$T_2 = X T_1 X^{-1} \qquad \text{or} \qquad T_1 = X^{-1} T_2 X, \tag{3.17}$$

where X is some element of the group.

---

[22] The coordinate system is usually chosen such that this point is the coordinate origin.

[23] In contrast, so called space groups additionally contain translations, which are found for example in infinite crystal lattices [76].

A class C of a group $\mathcal{G}$ is defined as a set of mutually conjugate elements of $\mathcal{G}$ [75, 77]. Classes have the following properties [75]:

- Every element of a group is a member of one class of the group.

- No element of a group can be a member of more than one class.

- The identity always forms a class on its own.

Class	C_1	C_2	C_3	C_4	C_5
Elements	E	C_{4z}, C_{4z}^{-1}	C_{2z}	C_{2x}, C_{2y}	C_{2A}, C_{2B}

Table 3.3   The five classes of symmetry group D_4.

According to its definition, a class can be constructed by forming the product (3.17) for every $X \in \mathcal{G}$. As an example, the element C_{2x} of the symmetry group D_4 is considered. With the help of the multiplication table (Table 3.2), the product (3.17) can be computed and the necessary inverse elements can be found for every X of D_4, yielding

$$XC_{2x}X^{-1} = \begin{cases} C_{2x}, & X = E, C_{2z}, C_{2x}, C_{2y} \\ C_{2y}, & X = C_{4z}, C_{4z}^{-1}, C_{2A}, C_{2B} \end{cases} .$$

This means that C_{2y} is conjugate to C_{2x} and vice versa and both elements form a class of the group. This procedure can be repeated for all elements of the group, resulting in five classes [75, 78], as listed in Table 3.3.

3.2.2 Group Mappings

A mapping $\mathcal{F}$ of a group $\mathcal{G}$ onto another group $\mathcal{G}'$ describes how an element T of $\mathcal{G}$ is assigned to an element $T' = \mathcal{F}(T)$ of $\mathcal{G}'$ [75]. The mapping is said to be homomorphic if

$$\mathcal{F}(T_1)\mathcal{F}(T_2) = \mathcal{F}(T_1 T_2) \quad \forall\, T_1, T_2 \in \mathcal{G}. \tag{3.18}$$

If (3.18) is fulfilled and, additionally, the mapping is one-to-one, i.e., both groups are of the same order and each element T of $\mathcal{G}$ is assigned to exactly one element T' of $\mathcal{G}'$, the mapping is called isomorphic [75].

Such an isomorphic mapping has already been encountered in section 3.1.2. The rotation matrices corresponding to the symmetry operations of the symmetry

T	E	C_{4z}	C_{2z}	C_{4z}^{-1}
$\mathbf{R}(T)$	$\begin{pmatrix} 1 & 0 & 0 \\ 0 & 1 & 0 \\ 0 & 0 & 1 \end{pmatrix}$	$\begin{pmatrix} 0 & 1 & 0 \\ -1 & 0 & 0 \\ 0 & 0 & 1 \end{pmatrix}$	$\begin{pmatrix} -1 & 0 & 0 \\ 0 & -1 & 0 \\ 0 & 0 & 1 \end{pmatrix}$	$\begin{pmatrix} 0 & -1 & 0 \\ 1 & 0 & 0 \\ 0 & 0 & 1 \end{pmatrix}$

T	C_{2x}	C_{2y}	C_{2A}	C_{2B}
$\mathbf{R}(T)$	$\begin{pmatrix} 1 & 0 & 0 \\ 0 & -1 & 0 \\ 0 & 0 & -1 \end{pmatrix}$	$\begin{pmatrix} -1 & 0 & 0 \\ 0 & 1 & 0 \\ 0 & 0 & -1 \end{pmatrix}$	$\begin{pmatrix} 0 & 1 & 0 \\ 1 & 0 & 0 \\ 0 & 0 & -1 \end{pmatrix}$	$\begin{pmatrix} 0 & -1 & 0 \\ -1 & 0 & 0 \\ 0 & 0 & -1 \end{pmatrix}$

Table 3.4   Rotation matrices of symmetry group D_4. © 2019 IEEE [PM19b].

group D_4 form a group themselves with matrix multiplication as the group multiplication rule [75]. Taking into account (3.10), the mapping $\mathcal{F}(T) = \mathbf{R}(T)$ is homomorphic. Moreover, as each element of D_4 can be assigned to a unique rotation matrix, the mapping is one-to-one and thus isomorphic. The rotation matrices corresponding to the elements of D_4 are summarized in Table 3.4. It is noted that the multiplication table is fulfilled by both groups, as required.

3.2.3 Direct-Product Groups

A direct-product group is a group whose elements result from the multiplication of the elements of two different groups. If T is an element of a group $\mathcal{G}$ of order g and T' is an element of another group $\mathcal{G}'$ of order g', the product TT' is an element of the direct-product group $\mathcal{G} \otimes \mathcal{G}'$ [75]. The direct-product group is set up by forming all possible products TT' and its order is gg'.

The concept of direct-product groups is best illustrated by means of an example. The group D_4 has been introduced at the beginning of this section as the symmetry group of a square plate consisting of eight elements ($g = 8$). Another common symmetry group is C_s, which consists of the identity E and the reflection through the xy-plane σ_{xy} ($g' = 2$) [78].[24] The corresponding direct-product group $D_4 \otimes C_s$ is now formed by multiplying each element of D_4 with each element of C_s.

The multiplications of the elements of D_4 with the identity E of C_s simply yield the elements of D_4. The first eight elements of the direct-product group are hence the elements of D_4 (proper rotations). The multiplications of C_{4z} and C_{4z}^{-1} of D_4 with σ_{xy} of C_s respectively result in the rotoreflections S_{4z}

---

[24]For example, C_s is the symmetry group of an ideal, z-oriented dipole antenna.

	E	C_{4z}	C_{4z}^{-1}	C_{2z}	C_{2x}	C_{2y}	C_{2A}	C_{2B}
E	E	C_{4z}	C_{4z}^{-1}	C_{2z}	C_{2x}	C_{2y}	C_{2A}	C_{2B}
σ_{xy}	σ_{xy}	S_{4z}	S_{4z}^{-1}	I	σ_{xz}	σ_{yz}	σ_{Az}	σ_{Bz}

Table 3.5 Direct-product group $D_4 \otimes C_s$. The table lists the products TT', where T of D_4 is found in the first row from the top and T' of C_s is found in the first column from the left.

and S_{4z}^{-1} according to (3.1). The multiplication of C_{2z} of D_4 with σ_{xy} of C_s results in the inversion I according to (3.2). Finally, the multiplications of C_{2x}, C_{2y}, C_{2A}, and C_{2B} of D_4 with σ_{xy} of C_s are equal to the reflections σ_{xz}, σ_{yz}, σ_{Az}, and σ_{Bz}, respectively. In summary, the products of the elements of D_4 with σ_{xy} yield eight further elements (improper rotations) of the direct-product group, which consequently contains a total of $8 \cdot 2 = 16$ elements. These are listed in Table 3.5. It is noted that all products are commutative.

As a matter of fact, the direct-product group $D_4 \otimes C_s$ is the symmetry group D_{4h} [78]. This is the symmetry group of a square cuboid (Fig. 4.37). The fact that it is built up from the simpler symmetry groups D_4 and C_s simplifies its analysis [77],[25] as will be further investigated in section 3.3.6.

3.3 Matrix Representations

A group of non-singular $d \times d$ square matrices $\mathbf{\Gamma}$ with matrix multiplication as the group multiplication rule is called a representation Γ of dimension d of a group $\mathcal{G}$ if it is homomorphic to $\mathcal{G}$ according to (3.18) with $\mathcal{F}(T) = \mathbf{\Gamma}(T)$ [75, 77]. The matrix $\mathbf{\Gamma}(T)$ is called the representation matrix corresponding to the element T of $\mathcal{G}$. If the mapping is isomorphic, i.e., to every T there belongs a unique $\mathbf{\Gamma}(T)$, the representation is said to be faithful.

As an example, the rotation matrices of the symmetry group D_4 as listed in Table 3.4 fulfill all criteria of a representation. In fact, they form a faithful, three-dimensional ($d = 3$) representation of the symmetry group D_4 [75].

3.3.1 Irreducible Representations

In general, a group has an infinite number of representations [75]. However, these can be decomposed into the so-called irreducible representations having minimum dimension. In particular, finite groups have only a finite number of

---

[25] D_4 and C_s form subgroups [75] of D_{4h}.

irreducible representations which are unique up to a similarity transformation. It thus proves purposeful to work only with the irreducible representations.

Before defining irreducible representations, the concept of equivalent representations needs to be introduced. A d-dimensional representation $\bar{\Gamma}$ of a group $\mathcal{G}$ is equivalent to a d-dimensional representation Γ of the same group $\mathcal{G}$ if their representation matrices are related by a similarity transformation [75]:

$$\bar{\Gamma}(T) = \mathbf{S}^{-1}\Gamma(T)\mathbf{S} \qquad \forall\, T \in \mathcal{G}, \tag{3.19}$$

where $\mathbf{S}$ is an arbitrary non-singular $d \times d$ square matrix. Accordingly, one-dimensional representations can only be identical or not equivalent.

Now, a d-dimensional representation matrix $\Gamma(T)$ is considered which is partitioned into block form in the following way [75]:

$$\Gamma(T) = \begin{pmatrix} \Gamma_{11}(T) & \Gamma_{12}(T) \\ \mathbf{0} & \Gamma_{22}(T) \end{pmatrix} \qquad \forall\, T \in \mathcal{G}. \tag{3.20}$$

As $\Gamma(T)$ is a representation matrix by definition, the following statement is true for any $T_1, T_2 \in \mathcal{G}$:

$$\begin{aligned} \Gamma(T_1 T_2) &= \begin{pmatrix} \Gamma_{11}(T_1 T_2) & \Gamma_{12}(T_1 T_2) \\ \mathbf{0} & \Gamma_{22}(T_1 T_2) \end{pmatrix} = \Gamma(T_1)\Gamma(T_2) \\ &= \begin{pmatrix} \Gamma_{11}(T_1)\Gamma_{11}(T_2) & \Gamma_{11}(T_1)\Gamma_{12}(T_2) + \Gamma_{12}(T_1)\Gamma_{22}(T_2) \\ \mathbf{0} & \Gamma_{22}(T_1)\Gamma_{22}(T_2) \end{pmatrix}. \end{aligned} \tag{3.21}$$

Apparently, $\Gamma_{11}(T)$ and $\Gamma_{22}(T)$ are also representation matrices of smaller dimension. As they are part of $\Gamma(T)$, this representation is said to be reducible.

In general, a representation of a group $\mathcal{G}$ is called reducible if it is equivalent to a representation of $\mathcal{G}$ whose representation matrices have the form of (3.20) [75]. Otherwise, it is called irreducible. This has the consequence that any reducible representation can be built from the irreducible representations.

Obviously, the rotation matrices in Table 3.4 have the form of (3.20) and are thus reducible. The irreducible representations of a symmetry group may be found in the literature, e.g., [75], or can be constructed from the so-called basis functions, as will be shown in section 3.5.4.

As stated above, finite groups have a finite number of irreducible representations. Throughout this thesis, the p-th irreducible representation of a finite group will be denoted by $\Gamma^{(p)}$.

3.3.2 Basis Functions

For the d_p-dimensional p-th irreducible representation $\Gamma^{(p)}$ there exist sets of d_p linearly independent functions $\boldsymbol{\psi}_1^{(p)}, \boldsymbol{\psi}_2^{(p)}, \ldots, \boldsymbol{\psi}_{d_p}^{(p)}$ that can be expressed as linear combinations of each other when operated on by a transformation operator P [75]:[26]

$$P(T)\boldsymbol{\psi}_\nu^{(p)}(\mathbf{r}') = \sum_{\mu=1}^{d_p} \Gamma_{\mu\nu}^{(p)}(T)\boldsymbol{\psi}_\mu^{(p)}(\mathbf{r}'), \quad \nu = 1, 2, \ldots, d_p. \tag{3.22}$$

These functions are said to form a basis of the p-th irreducible representation $\Gamma^{(p)}$ and are thus called basis functions. The weighting coefficients $\Gamma_{\mu\nu}^{(p)}(T)$ are the elements of the representation matrix $\boldsymbol{\Gamma}^{(p)}(T)$ of the irreducible representation $\Gamma^{(p)}$, where μ denotes the row index and ν denotes the column index. The function $\boldsymbol{\psi}_\nu^{(p)}$ is said to belong to the ν-th row[27] of the d_p-dimensional p-th irreducible representation [77].

In order to illustrate the transformation of basis functions, the representation matrices of the symmetry group D_4 are introduced in Table 3.6. This symmetry group has five irreducible representations [78]. The first four irreducible representations $\Gamma^{(1;2;3;4)}$ are one-dimensional ($d_{1;2;3;4} = 1$), i.e., their representation matrices $\boldsymbol{\Gamma}^{(1;2;3;4)}(T)$ are scalars which are either 1 or -1. One function $\boldsymbol{\psi}^{(1;2;3;4)}$ forms a basis of each of these irreducible representations. Applying a symmetry operation of D_4, the basis function is either left invariant (multiplication with 1) or inverted (multiplication with -1) according to (3.22).

As an example, the function $\mathbf{f}(\mathbf{r}') = (-y', x', 0)^{\mathrm{T}}$ with $x', y' \in \left[-\frac{a}{2}, \frac{a}{2}\right]$ as shown in Fig. 3.5(a) is considered. Now, each symmetry operation of the symmetry group D_4 is applied to this function in turn by means of the transformation operators $P(T)$ as introduced in section 3.1.3. For reference, the transformation operators corresponding to the elements of D_4 applied to a generic function are listed in Table 3.7.[28] The transformed function is then

$$P(T)\mathbf{f}(\mathbf{r}') = \begin{cases} (-y', x', 0)^{\mathrm{T}} = \mathbf{f}(\mathbf{r}'), & T = E, C_{4z}, C_{2z}, C_{4z}^{-1} \\ (y', -x', 0)^{\mathrm{T}} = -\mathbf{f}(\mathbf{r}'), & T = C_{2x}, C_{2y}, C_{2A}, C_{2B} \end{cases}. \tag{3.23}$$

---

[26]In this chapter, the basis functions are written as vector-valued functions $\boldsymbol{\psi}_\nu^{(p)}$ as this will be the usual application case throughout this thesis. Nevertheless, basis functions may also be scalar functions, which will be denoted by $\psi_\nu^{(p)}$.

[27]This nomenclature is adopted from [75] and [77]. At this stage, it may be somewhat confusing as ν is the column index of the representation matrix. It will become more meaningful with the introduction of the projection operators in section 3.5.

[28]The transformation operators form a group isomorphic to the symmetry group [75].

D_4	E	C_{4z}	C_{4z}^{-1}	C_{2z}
$\Gamma^{(1)}$	1	1	1	1
$\Gamma^{(2)}$	1	1	1	1
$\Gamma^{(3)}$	1	-1	-1	1
$\Gamma^{(4)}$	1	-1	-1	1
$\Gamma^{(5)}$	$\begin{pmatrix} 1 & 0 \\ 0 & 1 \end{pmatrix}$	$\begin{pmatrix} 0 & 1 \\ -1 & 0 \end{pmatrix}$	$\begin{pmatrix} 0 & -1 \\ 1 & 0 \end{pmatrix}$	$\begin{pmatrix} -1 & 0 \\ 0 & -1 \end{pmatrix}$

D_4	C_{2x}	C_{2y}	C_{2A}	C_{2B}
$\Gamma^{(1)}$	1	1	1	1
$\Gamma^{(2)}$	-1	-1	-1	-1
$\Gamma^{(3)}$	1	1	-1	-1
$\Gamma^{(4)}$	-1	-1	1	1
$\Gamma^{(5)}$	$\begin{pmatrix} 1 & 0 \\ 0 & -1 \end{pmatrix}$	$\begin{pmatrix} -1 & 0 \\ 0 & 1 \end{pmatrix}$	$\begin{pmatrix} 0 & 1 \\ 1 & 0 \end{pmatrix}$	$\begin{pmatrix} 0 & -1 \\ -1 & 0 \end{pmatrix}$

Table 3.6   Representation matrices of symmetry group D_4. © 2019 IEEE [PM19b].

T	E	C_{2z}
$P(T)\mathbf{f}(\mathbf{r}')$	$\begin{pmatrix} f_x(x',y',z') \\ f_y(x',y',z') \\ f_z(x',y',z') \end{pmatrix}$	$\begin{pmatrix} -f_x(-x',-y',z') \\ -f_y(-x',-y',z') \\ f_z(-x',-y',z') \end{pmatrix}$
T	C_{4z}	C_{4z}^{-1}
$P(T)\mathbf{f}(\mathbf{r}')$	$\begin{pmatrix} f_y(-y',x',z') \\ -f_x(-y',x',z') \\ f_z(-y',x',z') \end{pmatrix}$	$\begin{pmatrix} -f_y(y',-x',z') \\ f_x(y',-x',z') \\ f_z(y',-x',z') \end{pmatrix}$
T	C_{2x}	C_{2y}
$P(T)\mathbf{f}(\mathbf{r}')$	$\begin{pmatrix} f_x(x',-y',-z') \\ -f_y(x',-y',-z') \\ -f_z(x',-y',-z') \end{pmatrix}$	$\begin{pmatrix} -f_x(-x',y',-z') \\ f_y(-x',y',-z') \\ -f_z(-x',y',-z') \end{pmatrix}$
T	C_{2A}	C_{2B}
$P(T)\mathbf{f}(\mathbf{r}')$	$\begin{pmatrix} f_y(y',x',-z') \\ f_x(y',x',-z') \\ -f_z(y',x',-z') \end{pmatrix}$	$\begin{pmatrix} -f_y(-y',-x',-z') \\ -f_x(-y',-x',-z') \\ -f_z(-y',-x',-z') \end{pmatrix}$

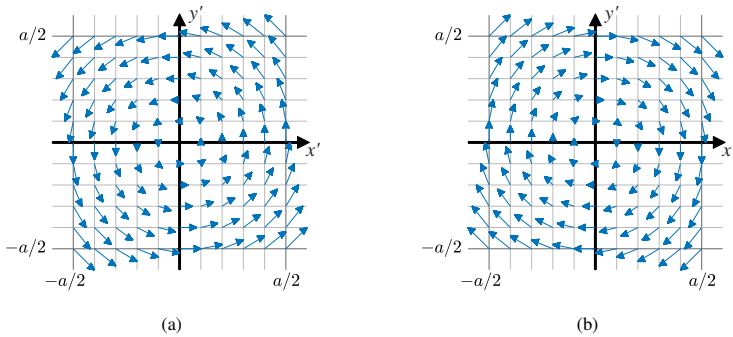Table 3.7   Transformation operators of symmetry group D_4. © 2019 IEEE [PM19b].

(a)   (b)

Figure 3.5   Basis function $\mathbf{f}(\mathbf{r}') = (-y',x',0)^{\mathrm{T}} = \boldsymbol{\psi}^{(2)}(\mathbf{r}')$ of one-dimensional second irreducible representation $\Gamma^{(2)}$ of symmetry group D_4. (a) Invariant under the identity and the rotations about the z-axis. (b) Inverted under the rotations about the other axes.

Under the identity and the rotations about the z-axis, the function is left invariant, i.e., multiplied by 1 (Fig. 3.5(a)), whereas under the other rotations it is inverted, i.e., multiplied by -1 (Fig. 3.5(b)). Comparing this result with Table 3.6, it becomes apparent that the example function is in fact a basis function of the second irreducible representation $\Gamma^{(2)}$ of the symmetry group D_4.

The fifth irreducible representation $\Gamma^{(5)}$ is two-dimensional ($d_5 = 2$). The corresponding representation matrices $\mathbf{\Gamma}^{(5)}(T)$ are two-dimensional square matrices. A pair of basis functions $\boldsymbol{\psi}_1^{(5)}, \boldsymbol{\psi}_2^{(5)}$ forms a basis of this irreducible representation. According to (3.22), the transformation of the first basis function $\boldsymbol{\psi}_1^{(5)}$ is described by the first column of the representation matrices ($\nu = 1$), whereas the transformation of the second basis function $\boldsymbol{\psi}_2^{(5)}$ is described by the second column ($\nu = 2$). The two basis functions may thus even transform into each other if a representation matrix is not diagonal.

In order to get a better understanding about this, another example is considered. The function $\mathbf{f}(\mathbf{r}') = (|x'|,0,0)^{\mathrm{T}}$, which was already examined in section 3.1.3, is chosen again. Applying the transformation operators of Table 3.7 yields

$$P(T)\mathbf{f}(\mathbf{r}') = \begin{cases} (|x'|,0,0)^{\mathrm{T}} = \mathbf{f}_1(\mathbf{r}'), & T = E, C_{2x} \\ -(|x'|,0,0)^{\mathrm{T}} = -\mathbf{f}_1(\mathbf{r}'), & T = C_{2z}, C_{2y} \\ (0,|y'|,0)^{\mathrm{T}} = \mathbf{f}_2(\mathbf{r}'), & T = C_{4z}^{-1}, C_{2A} \\ -(0,|y'|,0)^{\mathrm{T}} = -\mathbf{f}_2(\mathbf{r}'), & T = C_{4z}, C_{2B} \end{cases} . \tag{3.24}$$
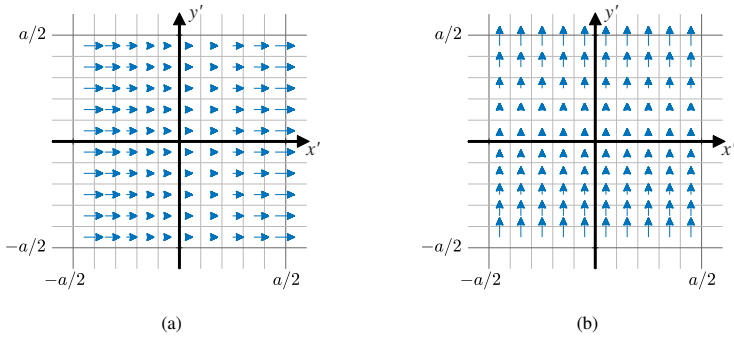
Figure 3.6   Basis functions of two-dimensional fifth irreducible representation $\Gamma^{(5)}$ of symmetry group D_4. (a) $\mathbf{f}_1(\mathbf{r}') = (|x'|,0,0)^{\mathrm{T}} = \boldsymbol{\psi}_1^{(5)}(\mathbf{r}')$ belonging to the first row. (b) $\mathbf{f}_2(\mathbf{r}') = (0,|y'|,0)^{\mathrm{T}} = \boldsymbol{\psi}_2^{(5)}(\mathbf{r}')$ belonging to the second row.

Comparing this result with Table 3.6, the function transforms according to the first column of the fifth irreducible representation $\Gamma^{(5)}$. However, it is said to belong to the first row of the irreducible representation. This somewhat confusing terminology will become more meaningful with the introduction of the projection operators in section 3.5. Its partner function is $\mathbf{f}_2(\mathbf{r}') = (0,|y'|,0)^{\mathrm{T}}$, which belongs to the second row. The two basis functions are shown in Fig. 3.6.

3.3.3 Orthogonality Theorem

As will be shown throughout this thesis, the orthogonality theorem for matrix representations is not only one of the most fundamental theorems of the theory of symmetry, but also the decisive rule for the antenna analysis and design concepts to be introduced. Not surprisingly, in [77] it is even called the "great orthogonality theorem".

Before presenting the orthogonality theorem, the concept of unitary representations should be introduced. A unitary representation of a group $\mathcal{G}$ is a representation whose representation matrices $\boldsymbol{\Gamma}(T)$ are unitary [75], i.e.,

$$\boldsymbol{\Gamma}^{\mathrm{H}}(T)\boldsymbol{\Gamma}(T) = \boldsymbol{\Gamma}(T)\boldsymbol{\Gamma}^{\mathrm{H}}(T) = \mathbf{E} \quad \Leftrightarrow \quad \boldsymbol{\Gamma}^{\mathrm{H}}(T) = \boldsymbol{\Gamma}^{-1}(T) \quad \forall\, T \in \mathcal{G}, \quad (3.25)$$

where $^{\mathrm{H}}$ denotes conjugate transpose. It can be easily checked that the representation matrices shown in Table 3.6 are unitary.

It is now supposed that there are two unitary irreducible representations $\Gamma^{(p)}$ and $\Gamma^{(q)}$ of group $\mathcal{G}$, which are not equivalent if $p \neq q$, but are identical if $p = q$. The following orthogonality theorem can then be formulated for the elements of the representation matrices [75, 77]:

$$\sum_{T \in \mathcal{G}} \Gamma_{\mu\nu}^{(p)*}(T) \Gamma_{\lambda\kappa}^{(q)}(T) = \frac{g}{d_p} \delta_{pq} \delta_{\mu\lambda} \delta_{\nu\kappa}. \tag{3.26}$$

The summation of the products of corresponding elements ($\mu = \lambda \wedge \nu = \kappa$) of the matrices of different irreducible representations ($p \neq q$) over the group elements yields zero. Likewise, the summation yields zero if different elements ($\mu \neq \lambda \vee \nu \neq \kappa$) of the same irreducible representation ($p = q$) are taken. Again, this can be checked exemplarily with the irreducible representations of the symmetry group D_4 in Table 3.6.

Even more important for the purpose of this thesis is the resulting orthogonality of basis functions [75]:

$$\left\langle \psi_\nu^{(p)}(\mathbf{r}'), \psi_\kappa^{(q)}(\mathbf{r}') \right\rangle = 0, \quad \text{for} \quad p \neq q \ \vee \ \nu \neq \kappa, \tag{3.27}$$

with the inner product as defined in appendix B. It states that

- basis functions belonging to different irreducible representations ($p \neq q$),

- basis functions belonging to different rows of the same multi-dimensional irreducible representation ($p = q$, $\nu \neq \kappa$)

are orthogonal to each other. It is noteworthy that the value of the inner product in (3.27) for $p = q$ and $\nu = \kappa$ cannot be determined in a general way. It is only specified up to the following form [75]:

$$\left\langle \psi_\nu^{(p)}(\mathbf{r}'), \psi_\kappa^{(q)}(\mathbf{r}') \right\rangle = \delta_{pq} \delta_{\nu\kappa} \frac{1}{d_p} \sum_{\mu=1}^{d_p} \left\langle \psi_\mu^{(p)}(\mathbf{r}'), \psi_\mu^{(p)}(\mathbf{r}') \right\rangle. \tag{3.28}$$

However, the basis functions may be normalized such that they form an orthonormal set ($\langle \psi_\mu^{(p)}(\mathbf{r}'), \psi_\mu^{(p)}(\mathbf{r}') \rangle = 1$). In this case, the value of the inner product is equal to 1 if $p = q$ and $\nu = \kappa$ and the orthogonality theorem can then be written in a compact form:

$$\left\langle \psi_\nu^{(p)}(\mathbf{r}'), \psi_\kappa^{(q)}(\mathbf{r}') \right\rangle = \delta_{pq} \delta_{\nu\kappa}. \tag{3.29}$$

Some examples for basis functions of the symmetry group D_4 have been introduced in subsection 3.3.2. The functions $\boldsymbol{\psi}^{(2)}(\mathbf{r}') = (-y',x',0)^{\mathrm{T}}$ and $\boldsymbol{\psi}_1^{(5)}(\mathbf{r}') = (|x'|,0,0)^{\mathrm{T}}$ are found to be basis functions of different irreducible representations. Computing the inner product

$$\left\langle \boldsymbol{\psi}^{(2)}(x',y'),\boldsymbol{\psi}_1^{(5)}(x',y') \right\rangle = \int\limits_{-a/2}^{a/2} \int\limits_{-a/2}^{a/2} \begin{pmatrix} -y' \\ x' \\ 0 \end{pmatrix} \cdot \begin{pmatrix} |x'| \\ 0 \\ 0 \end{pmatrix} \mathrm{d}y'\mathrm{d}x'$$

$$= \int\limits_{-a/2}^{a/2} \int\limits_{-a/2}^{a/2} -y'|x'|\mathrm{d}y'\mathrm{d}x'$$

$$= \int\limits_{-a/2}^{a/2} |x'| \left[-\frac{y'^2}{2} \right]_{-a/2}^{a/2} \mathrm{d}x' = 0$$

yields that the two basis functions are indeed orthogonal, as required. The functions $\boldsymbol{\psi}_1^{(5)}(\mathbf{r}') = (|x'|,0,0)^{\mathrm{T}}$ and $\boldsymbol{\psi}_2^{(5)}(\mathbf{r}') = (0,|y'|,0)^{\mathrm{T}}$ are basis functions of the two different rows of the two-dimensional irreducible representation. Computing the inner product

$$\left\langle \boldsymbol{\psi}_1^{(5)}(x',y'),\boldsymbol{\psi}_2^{(5)}(x',y') \right\rangle = \int\limits_{-a/2}^{a/2} \int\limits_{-a/2}^{a/2} \begin{pmatrix} |x'| \\ 0 \\ 0 \end{pmatrix} \cdot \begin{pmatrix} 0 \\ |y'| \\ 0 \end{pmatrix} \mathrm{d}y'\mathrm{d}x' = 0$$

yields that the two functions are orthogonal, too, as required. Both results are rather intuitive if Fig. 3.5 and 3.6 are taken into account.

3.3.4 Characters

It is stated in subsection 3.3.1 that the irreducible representations are only unique up to a similarity transformation. This has the consequence that there is some kind of arbitrariness when working with representation matrices. In order to uniquely characterize irreducible representations, the so-called characters are introduced [77].

As the trace of a matrix is invariant under similarity transformations, the character $\chi^{(p)}(T)$ of the p-th irreducible representation corresponding to the element T of a group $\mathcal{G}$ is defined as the trace (the sum of the diagonal elements)

of the representation matrix $\mathbf{\Gamma}^{(p)}(T)$ [77]:

$$\chi^{(p)}(T) = \mathrm{tr}\big(\mathbf{\Gamma}^{(p)}(T)\big) = \sum_{\mu=1}^{d_p} \Gamma_{\mu\mu}^{(p)}(T). \qquad (3.30)$$

From this definition it follows that two irreducible representations of a finite group are equivalent if they have the same character system [75] (cf. (3.19)). In particular, the representation matrices of one-dimensional irreducible representations are identical to the characters.

At this stage, it should be noted that the classes of a group as introduced in section 3.2.1 are defined by similarity transformations (cf. (3.17)). This has the consequence that all elements T of a class C have the same character [77].

D_4	C_1	C_2	C_3	C_4	C_5
$\Gamma^{(1)}$	1	1	1	1	1
$\Gamma^{(2)}$	1	1	1	−1	−1
$\Gamma^{(3)}$	1	−1	1	1	−1
$\Gamma^{(4)}$	1	−1	1	−1	1
$\Gamma^{(5)}$	2	0	−2	0	0

Table 3.8   Character table of symmetry group D_4.

Based on this, a character table can be set up [77]. For the symmetry group D_4, this can now be done by computing the traces of the representation matrices in Table 3.6. The individual symmetry operations are conveniently summarized in the classes of the group (Table 3.3). The resulting character table is given in Table 3.8. Character tables are usually provided in the literature, e.g., in [57, 75–78].

The orthogonality of representations as introduced in subsection 3.3.3 is also reflected in the characters [77]:

$$\sum_{T \in \mathcal{G}} \chi^{(p)*}(T)\chi^{(q)}(T) = g\delta_{pq}, \qquad (3.31)$$

i.e., the sum of the products of characters of different irreducible representations ($p \neq q$) over all elements of the group yields zero. It follows that

$$\sum_{T \in \mathcal{G}} \left|\chi^{(p)}(T)\right|^2 = g, \qquad (3.32)$$

which is useful for checking whether a given representation is irreducible [75]. The orthogonality theorem for characters can also be written in terms of the classes C of the group [77]:

$$\sum_{C \in \mathcal{G}} \chi^{(p)*}(C)\chi^{(q)}(C)N_C = g\delta_{pq}, \qquad (3.33)$$

where N_C is the number of group elements in the class. From this form of the orthogonality theorem it also follows that the number of irreducible representations of a finite group is equal to the number of its classes [77].

The characters are a convenient tool for checking computations and results. For the symmetry group D_4, all relationships introduced in this subsection can be easily checked by means of the character table.

3.3.5 Isomorphism

Isomorphic groups as introduced in section 3.2.2 have identical representations and thus the same character system [75, 78]. As an example, the symmetry group C_{4v} [78] is considered.[29] The rotations about the axes perpendicular to the z-axis of D_4 are replaced by reflections through planes containing the z-axis. The resulting group elements are listed in Table 3.9.

Symmetry operation	Symbol
Identity	E
Rotation by 90° about the z-axis	C_{4z}
Rotation by 180° about the z-axis	C_{2z}
Rotation by 270° about the z-axis	C_{4z}^3
Reflection through the xz-plane	σ_{xz}
Reflection through the yz-plane	σ_{yz}
Reflection through the Az-plane	σ_{Az}
Reflection through the Bz-plane	σ_{Bz}

Table 3.9   The eight elements of symmetry group C_{4v}.

Although the groups D_4 and C_{4v} consist of different symmetry operations, they have the same classes and character systems, which are those listed in Table 3.8 [78]. The two groups are consequently isomorphic and obviously have

[29]This is the symmetry group of a right square pyramid (Fig. 4.32). For details, see section 4.5.3.

similar properties. In particular, basis functions of the two groups must have the same symmetry properties as they transform according to the same representation matrices. Group isomorphisms enable the reuse of group properties and can thus be exploited conveniently in order to simplify the symmetry analysis.

3.3.6 Direct-Product Representations

The irreducible representations of a direct-product group $G \otimes G'$ can be derived from the irreducible representations of the component groups G and G'. If $\mathbf{\Gamma}^{(p)}(T)$ is the representation matrix of the p-th irreducible representation of G belonging to the element T and $\mathbf{\Gamma}^{(q)}(T')$ is the representation matrix of the q-th irreducible representation of G' belonging to T', the corresponding representation matrix $\mathbf{\Gamma}^{(pq)}(TT')$ of the direct-product group is [77]

$$\mathbf{\Gamma}^{(pq)}(TT') = \mathbf{\Gamma}^{(p)}(T) \otimes \mathbf{\Gamma}^{(q)}(T') \quad \forall \, T \in G, T' \in G', \tag{3.34}$$

where $\otimes$ denotes the direct product (Kronecker product) of two matrices [79].[30] The characters $\chi^{(pq)}(TT')$ of a direct-product representation are computed as the products of the characters $\chi^{(p)}(T)$ and $\chi^{(q)}(T')$ of the component representations [77]:

$$\chi^{(pq)}(TT') = \chi^{(p)}(T)\chi^{(q)}(T') \quad \forall \, T \in G, T' \in G'. \tag{3.35}$$

This has the consequence that all representation matrices and characters of a direct-product group can be computed from the representation matrices and the characters, respectively, of the component groups.

C_s	E	σ_{xy}
$\Gamma^{(1)}$	1	1
$\Gamma^{(2)}$	1	−1

Table 3.10   Character table of symmetry group C_s.

    The symmetry group $D_{4\mathrm{h}}$ has been found in section 3.2.3 to be the direct product of the groups D_4 and C_s. The character table of D_4 is given in Table 3.8. There are five irreducible representations. The character Table of C_s is presented in Table 3.10 [78]. It has two one-dimensional irreducible representations. By employing (3.35), the character Table 3.11 of $D_{4\mathrm{h}}$ can be set up.

---

[30]The direct product of two matrices is a matrix whose elements are all possible products of the elements of the two matrices [79].

D_{4h}	E	C_{4z}	C_{4z}^{-1}	C_{2z}	C_{2x}	C_{2y}	C_{2A}	C_{2B}
$\Gamma^{(1)}$	1	1	1	1	1	1	1	1
$\Gamma^{(2)}$	1	1	1	1	−1	−1	−1	−1
$\Gamma^{(3)}$	1	−1	−1	1	1	1	−1	−1
$\Gamma^{(4)}$	1	−1	−1	1	−1	−1	1	1
$\Gamma^{(5)}$	2	0	0	−2	0	0	0	0
$\Gamma^{(6)}$	1	1	1	1	1	1	1	1
$\Gamma^{(7)}$	1	1	1	1	−1	−1	−1	−1
$\Gamma^{(8)}$	1	−1	−1	1	1	1	−1	−1
$\Gamma^{(9)}$	1	−1	−1	1	−1	−1	1	1
$\Gamma^{(10)}$	2	0	0	−2	0	0	0	0

D_{4h}	σ_{xy}	S_{4z}	S_{4z}^{-1}	I	σ_{xz}	σ_{yz}	σ_{Az}	σ_{Bz}
$\Gamma^{(1)}$	1	1	1	1	1	1	1	1
$\Gamma^{(2)}$	1	1	1	1	−1	−1	−1	−1
$\Gamma^{(3)}$	1	−1	−1	1	1	1	−1	−1
$\Gamma^{(4)}$	1	−1	−1	1	−1	−1	1	1
$\Gamma^{(5)}$	2	0	0	−2	0	0	0	0
$\Gamma^{(6)}$	−1	−1	−1	−1	−1	−1	−1	−1
$\Gamma^{(7)}$	−1	−1	−1	−1	1	1	1	1
$\Gamma^{(8)}$	−1	1	1	−1	−1	−1	1	1
$\Gamma^{(9)}$	−1	1	1	−1	1	1	−1	−1
$\Gamma^{(10)}$	−2	0	0	2	0	0	0	0

Table 3.11   Character table of symmetry group D_{4h}. © 2019 IEEE [PM19b].

Multiplying the characters of the irreducible representations $\Gamma^{(1;2;3;4;5)}$ of D_4 with the characters of the first irreducible representation $\Gamma^{(1)}$ ($q = 1$) of C_s yields the characters of the irreducible representations $\Gamma^{(1;2;3;4;5)}$ of D_{4h}. For the proper rotations, the corresponding characters are exactly those of D_4 as the character $\chi^{(1)}(E)$ of C_s is equal to 1. The same is true for the improper rotations as the character $\chi^{(1)}(\sigma_{xy})$ of C_s is also equal to 1. Multiplying the characters of the irreducible representations $\Gamma^{(1;2;3;4;5)}$ of D_4 with the characters of the second irreducible representation $\Gamma^{(2)}$ ($q = 2$) of C_s yields the characters of the irreducible representations $\Gamma^{(6;7;8;9;10)}$ of D_{4h}. For the proper rotations, the corresponding characters are again those of D_4 as the character $\chi^{(2)}(E)$ of C_s is equal to 1. For the improper rotations, however, the corresponding characters are those of D_4 multiplied by −1 as the character $\chi^{(2)}(\sigma_{xy})$ of C_s is equal to −1.

D_{4h}	E	C_{4z}	C_{4z}^{-1}	C_{2z}
$\Gamma^{(5)}$	$\begin{pmatrix} 1 & 0 \\ 0 & 1 \end{pmatrix}$	$\begin{pmatrix} 0 & 1 \\ -1 & 0 \end{pmatrix}$	$\begin{pmatrix} 0 & -1 \\ 1 & 0 \end{pmatrix}$	$\begin{pmatrix} -1 & 0 \\ 0 & -1 \end{pmatrix}$
$\Gamma^{(10)}$	$\begin{pmatrix} 1 & 0 \\ 0 & 1 \end{pmatrix}$	$\begin{pmatrix} 0 & 1 \\ -1 & 0 \end{pmatrix}$	$\begin{pmatrix} 0 & -1 \\ 1 & 0 \end{pmatrix}$	$\begin{pmatrix} -1 & 0 \\ 0 & -1 \end{pmatrix}$

D_{4h}	C_{2x}	C_{2y}	C_{2A}	C_{2B}
$\Gamma^{(5)}$	$\begin{pmatrix} 1 & 0 \\ 0 & -1 \end{pmatrix}$	$\begin{pmatrix} -1 & 0 \\ 0 & 1 \end{pmatrix}$	$\begin{pmatrix} 0 & 1 \\ 1 & 0 \end{pmatrix}$	$\begin{pmatrix} 0 & -1 \\ -1 & 0 \end{pmatrix}$
$\Gamma^{(10)}$	$\begin{pmatrix} 1 & 0 \\ 0 & -1 \end{pmatrix}$	$\begin{pmatrix} -1 & 0 \\ 0 & 1 \end{pmatrix}$	$\begin{pmatrix} 0 & 1 \\ 1 & 0 \end{pmatrix}$	$\begin{pmatrix} 0 & -1 \\ -1 & 0 \end{pmatrix}$

D_{4h}	σ_{xy}	S_{4z}	S_{4z}^{-1}	I
$\Gamma^{(5)}$	$\begin{pmatrix} 1 & 0 \\ 0 & 1 \end{pmatrix}$	$\begin{pmatrix} 0 & 1 \\ -1 & 0 \end{pmatrix}$	$\begin{pmatrix} 0 & -1 \\ 1 & 0 \end{pmatrix}$	$\begin{pmatrix} -1 & 0 \\ 0 & -1 \end{pmatrix}$
$\Gamma^{(10)}$	$\begin{pmatrix} -1 & 0 \\ 0 & -1 \end{pmatrix}$	$\begin{pmatrix} 0 & -1 \\ 1 & 0 \end{pmatrix}$	$\begin{pmatrix} 0 & 1 \\ -1 & 0 \end{pmatrix}$	$\begin{pmatrix} 1 & 0 \\ 0 & 1 \end{pmatrix}$

D_{4h}	σ_{xz}	σ_{yz}	σ_{Az}	σ_{Bz}
$\Gamma^{(5)}$	$\begin{pmatrix} 1 & 0 \\ 0 & -1 \end{pmatrix}$	$\begin{pmatrix} -1 & 0 \\ 0 & 1 \end{pmatrix}$	$\begin{pmatrix} 0 & 1 \\ 1 & 0 \end{pmatrix}$	$\begin{pmatrix} 0 & -1 \\ -1 & 0 \end{pmatrix}$
$\Gamma^{(10)}$	$\begin{pmatrix} -1 & 0 \\ 0 & 1 \end{pmatrix}$	$\begin{pmatrix} 1 & 0 \\ 0 & -1 \end{pmatrix}$	$\begin{pmatrix} 0 & -1 \\ -1 & 0 \end{pmatrix}$	$\begin{pmatrix} 0 & 1 \\ 1 & 0 \end{pmatrix}$

Table 3.12   Representation matrices of two-dimensional irreducible representations of symmetry group D_{4h}.

The group D_{4h} has a total of ten irreducible representations. The representations $\Gamma^{(5)}$ and $\Gamma^{(10)}$ are found to be two-dimensional since the characters $\chi^{(5)}(E)$ and $\chi^{(10)}(E)$ are equal to 2 (Table 3.11).[31] In order to compute the corresponding representation matrices, (3.34) is employed. As C_s has only one-dimensional irreducible representations, the direct product reduces to a multiplication of the representation matrices of $\Gamma^{(5)}$ of D_4 (Table 3.6) with the characters of C_s (Table 3.10). The resulting representation matrices of D_{4h} are listed in Table 3.12. The matrices of $\Gamma^{(5)}$ are exactly those of $\Gamma^{(5)}$ of D_4 for both proper and improper rotations. The representation matrices of $\Gamma^{(10)}$ are equal to those of $\Gamma^{(5)}$ of D_4 for the proper rotations. For the improper rotations, however, they are equal to those of $\Gamma^{(5)}$ of D_4 multiplied by -1.

---

[31] The dimension of an irreducible representation can be directly deduced from the character $\chi^{(p)}(E)$ belonging to the identity E as its representation matrix is always the identity matrix $\mathbf{E}$.

Although the structure of the symmetry group D_{4h} is comparatively complex, its interpretation as a direct-product group and decomposition into its component groups greatly simplifies the symmetry analysis. The concepts introduced in this section can be readily applied to other direct-product groups (see, e.g., [78]).

3.4 Connection to Characteristic Modes

Having laid the foundations of mathematically describing symmetries, it is now time to turn back to the initial problem of finding a connection between the symmetry of a PEC object and its characteristic modes, as stated in section 2.4.3. For this purpose, first of all, the generalized eigenvalue problem defining the characteristic modes as introduced in section 2.2 should be recalled:

$$X\mathbf{J}_n(\mathbf{r}') = \lambda_n R\mathbf{J}_n(\mathbf{r}'). \tag{3.36}$$

3.4.1 Invariance of Impedance Operator

The impedance operator $Z = R + jX$ as defined in (2.13) describes the geometry of the underlying PEC object, i.e., it exclusively contains every information about symmetry. It is thus purposeful to start with examining the effect of a symmetry operation on the impedance operator.

Following the argument in [58], a transformation operator $P(T)$ (3.13) corresponding to a symmetry operation T leaving the underlying PEC object invariant is applied to the impedance operator Z (2.13):

$$P(T)\big(Z\mathbf{J}(\mathbf{r}')\big) = P(T)\bigg(j\omega\mu \iint\limits_{S'} \mathbf{J}(\mathbf{r}'')G(\mathbf{r}',\mathbf{r}'')\mathrm{d}S''$$

$$-\frac{1}{j\omega\varepsilon}\mathrm{grad}\bigg(\iint\limits_{S'} \mathrm{div}\big(\mathbf{J}(\mathbf{r}'')\big)G(\mathbf{r}',\mathbf{r}'')\mathrm{d}S''\bigg)\bigg)_{\mathrm{tan}}. \tag{3.37}$$

As the surface of an object is not altered by a symmetry operation, the component tangential to the surface $(\mathbf{f})_{\mathrm{tan}}$ of an arbitrary vector-valued function is still tangential to the surface after the transformation of the object:[32]

$$P(T)\big(\mathbf{f}(\mathbf{r}')\big)_{\mathrm{tan}} = \big(P(T)\mathbf{f}(\mathbf{r}')\big)_{\mathrm{tan}}. \tag{3.38}$$

---

[32] The transformation operators of the square plate in Table 3.7 illustrate this behavior: The tangential components f_x and f_y may swap their positions, but they remain tangential to the surface. The normal component f_z is unaffected by this.

Likewise, the integration is not affected by the transformation since the integration domain, i.e., the object surface, remains the same [58]:

$$P(T) \iint\limits_{S'} \mathbf{f}(\mathbf{r}'')\mathrm{d}S'' = \iint\limits_{S'} P(T)\mathbf{f}(\mathbf{r}'')\mathrm{d}S''. \tag{3.39}$$

Next, the effect of a transformation operator on an arbitrary integrand containing the integral kernel G (2.10) is examined:

$$\begin{aligned}
P(T)\big(\mathbf{f}(\mathbf{r}'')G(\mathbf{r}',\mathbf{r}'')\big) &= \mathbf{R}(T)\mathbf{f}\big(\mathbf{R}^{-1}(T)\mathbf{r}''\big)\frac{e^{-jk\left\|\mathbf{R}^{-1}(T)(\mathbf{r}'-\mathbf{r}'')\right\|}}{4\pi\left\|\mathbf{R}^{-1}(T)(\mathbf{r}'-\mathbf{r}'')\right\|} \\
&= \mathbf{R}(T)\mathbf{f}\big(\mathbf{R}^{-1}(T)\mathbf{r}''\big)\frac{e^{-jk\|\mathbf{r}'-\mathbf{r}''\|}}{4\pi\|\mathbf{r}'-\mathbf{r}''\|} \\
&= P(T)\mathbf{f}(\mathbf{r}'')G(\mathbf{r}',\mathbf{r}''), \tag{3.40}
\end{aligned}$$

where the orthogonality of the rotation matrix is exploited. As the integral kernel is a function of the distance between two points, it is not affected by a symmetry operation. This behavior is illustrated in Fig. 3.7. Although the two position vectors are rotated, the distance between them remains the same. Finally, both gradient and divergence are invariant under symmetry operations [58, 66]:

$$P(T)\big(\mathrm{grad} f(\mathbf{r}')\big) = \mathrm{grad}\big(P(T)f(\mathbf{r}')\big), \tag{3.41}$$

$$P(T)\big(\mathrm{div}\mathbf{f}(\mathbf{r}')\big) = \mathrm{div}\big(P(T)\mathbf{f}(\mathbf{r}')\big), \tag{3.42}$$

which simply means that differentiating the function first and then transforming it is equivalent to transforming first and then differentiating.

Putting all pieces together finally yields that the transformation operator can be directly applied to the surface current density:

$$\begin{aligned}
P(T)\big(Z\mathbf{J}(\mathbf{r}')\big) &= \Bigg(j\omega\mu \iint\limits_{S'} P(T)\mathbf{J}(\mathbf{r}'')G(\mathbf{r}',\mathbf{r}'')\mathrm{d}S'' \\
&\quad - \frac{1}{j\omega\varepsilon}\mathrm{grad}\bigg(\iint\limits_{S'} \mathrm{div}\big(P(T)\mathbf{J}(\mathbf{r}'')\big)G(\mathbf{r}',\mathbf{r}'')\mathrm{d}S''\bigg)\Bigg)_{\mathrm{tan}} \\
&= Z\big(P(T)\mathbf{J}(\mathbf{r}')\big), \tag{3.43}
\end{aligned}$$

i.e., the impedance operator is invariant under the symmetry operations of the underlying PEC object. Obviously, the impedance operator and the transformation operator are interchangeable. The two operators are thus said to commute [66, 77].
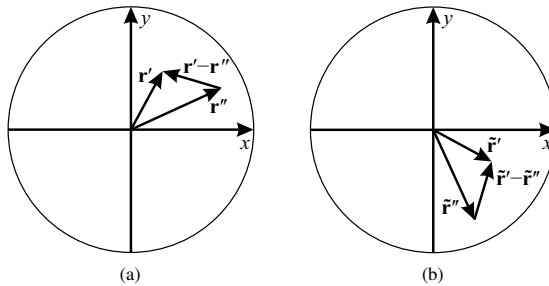
Figure 3.7   Rotation of two position vectors and their difference by $-90°$ about the z-axis. (a) Original vectors. (b) Transformed vectors. The distances are preserved by the operation.

The same argument can be applied to the real part R (2.15) and the imaginary part X (2.16) of the impedance operator. Alternatively, the linearity of the operators can be exploited:

$$P(T)\big(Z\mathbf{J}(\mathbf{r}')\big) = P(T)\big(R\mathbf{J}(\mathbf{r}')\big) + jP(T)\big(X\mathbf{J}(\mathbf{r}')\big). \tag{3.44}$$

Equivalently:

$$Z\big(P(T)\mathbf{J}(\mathbf{r}')\big) = R\big(P(T)\mathbf{J}(\mathbf{r}')\big) + jX\big(P(T)\mathbf{J}(\mathbf{r}')\big), \tag{3.45}$$

demonstrating that R and X, too, are invariant under symmetry operations.

3.4.2 Transformation of Eigenfunctions

Having established the invariance of the impedance operator under a symmetry operation of the underlying PEC object, the next step in finding a connection to the characteristic modes is to examine the behavior of the eigenvalue problem (3.36) under a symmetry operation. To this end, a transformation operator $P(T)$ is applied to both sides of the eigenvalue problem:

$$P(T)\big(X\mathbf{J}_n(\mathbf{r}')\big) = \lambda_n P(T)\big(R\mathbf{J}_n(\mathbf{r}')\big). \tag{3.46}$$

Exploiting the invariance of the impedance operator and its Hermitian parts as derived in the previous subsection yields [58]

$$X\big(P(T)\mathbf{J}_n(\mathbf{r}')\big) = \lambda_n R\big(P(T)\mathbf{J}_n(\mathbf{r}')\big). \tag{3.47}$$

Recalling that $\mathbf{J}_n$ is an eigenfunction (characteristic surface current density) corresponding to the in general d-fold degenerate eigenvalue λ_n, this result states that the transformed function $P(T)\mathbf{J}_n$, too, is an eigenfunction corresponding to this eigenvalue for any symmetry operation T.

However, an eigenfunction corresponding to a d-fold degenerate eigenvalue λ_n can most generally be expressed as a linear combination of d eigenfunctions $\mathbf{J}_{n,1}, \mathbf{J}_{n,2}, \ldots, \mathbf{J}_{n,d}$ [58, 80]. Hence, the ν-th eigenfunction $\mathbf{J}_{n,\nu}$ corresponding to the eigenvalue λ_n transformed by operator $P(T)$ solving (3.47) can also be written as follows:

$$P(T)\mathbf{J}_{n,\nu}(\mathbf{r}') = \sum_{\mu=1}^{d} \gamma_{\mu\nu}(T)\mathbf{J}_{n,\mu}(\mathbf{r}'), \qquad \nu = 1, 2, \ldots, d, \qquad (3.48)$$

with the yet unknown weighting coefficients $\gamma_{\mu\nu}(T)$.[33] In order to illustrate this concept, it is assumed that the two functions shown in Fig. 3.6 are eigenfunctions corresponding to a two-fold degenerate eigenvalue ($d = 2$). It was shown that, under symmetry operations, the two functions transform among themselves (3.24). This can also be expressed as a linear combination of the two functions, where the weighting coefficients can take the values 1, -1, or 0.

With this example in mind, it is noticed that (3.48) is reminiscent of (3.22) and the weighting coefficients can be collected into $d \times d$ square matrices $\boldsymbol{\gamma}(T)$ for every T. It may thus be deduced that (3.48) describes the transformation of basis functions according to a representation [58, 76]. In order to confirm this, it has to be proven that the matrices $\boldsymbol{\gamma}(T)$ form a homomorphic mapping according to (3.18). This proof is provided in appendix C.5, demonstrating that (3.48) indeed describes the transformation of eigenfunctions according to a representation in the same way as basis functions. A so-formed representation is even irreducible [58, 76] since the dimension of the representation is dictated by the degeneracy of the respective eigenvalue and is thus minimal.

In conclusion, it is a fundamental fact that the characteristic surface current densities act as basis functions of the irreducible representations of the symmetry group of the underlying PEC object. The characteristic surface current densities thus possess all the properties of basis functions introduced in this chapter.[34]

---

[33] If the eigenvalue is non-degenerate ($d = 1$), the corresponding eigenfunction is simply scaled by $\gamma_{11}(T)$ [66].

[34] As demonstrated in appendix C.5, the derivation of this subsection is applicable to arbitrary eigenvalue problems and is solely based on the invariance of the operators of the eigenvalue problem under symmetry operations.

3.4.3　Understanding the Rectangular Plate Example

With the connection established above, it is now possible to understand the observations made in section 2.4.3 regarding the rectangular PEC plate. To this end, the symmetry of the rectangular plate (Fig. 2.3) needs to be analyzed.

Symmetry operation	Symbol
Identity	E
Rotation by 180° about the z-axis	C_{2z}
Rotation by 180° about the x-axis	C_{2x}
Rotation by 180° about the y-axis	C_{2y}

Table 3.13　The four elements of symmetry group D_2.

The four symmetry operations of the rectangular plate are listed in Table 3.13. This symmetry group is called D_2 of order $g = 4$ [78]. It has four one-dimensional irreducible representations. The character table is given in Table 3.14 and it is recalled that, for one-dimensional representations, the characters are equal to the (one-dimensional) representation matrices.

D_2	E	C_{2z}	C_{2x}	C_{2y}
$\Gamma^{(1)}$	1	1	1	1
$\Gamma^{(2)}$	1	1	−1	−1
$\Gamma^{(3)}$	1	−1	1	−1
$\Gamma^{(4)}$	1	−1	−1	1

Table 3.14　Character table of symmetry group D_2.

As the characteristic surface current densities are basis functions of the irreducible representations, their transformation under the symmetry operations of the rectangular plate is governed by (3.22). This enables the assignment of the characteristic modes to the irreducible representations by applying all symmetry operations of the symmetry group to the characteristic surface current densities and comparing the results with Table 3.14. For the rectangular plate, this can be easily done manually. At 2.5 GHz, the transformation of the surface current densities of the significant characteristic modes under the symmetry operations of D_2 is shown in Fig. 3.8. Based on this, mode 1 is assigned to $\Gamma^{(1)}$, mode 2 to $\Gamma^{(2)}$, mode 3 to $\Gamma^{(3)}$, and mode 4 to $\Gamma^{(4)}$. At 7.25 GHz, the resulting sorting of the characteristic surface current densities has already been performed

(a) $P(E)\mathbf{J}_1 = +1 \cdot \mathbf{J}_1$ (b) $P(C_{2z})\mathbf{J}_1 = +1 \cdot \mathbf{J}_1$ (c) $P(C_{2x})\mathbf{J}_1 = +1 \cdot \mathbf{J}_1$ (d) $P(C_{2y})\mathbf{J}_1 = +1 \cdot \mathbf{J}_1$

(e) $P(E)\mathbf{J}_2 = +1 \cdot \mathbf{J}_2$ (f) $P(C_{2z})\mathbf{J}_2 = +1 \cdot \mathbf{J}_2$ (g) $P(C_{2x})\mathbf{J}_2 = -1 \cdot \mathbf{J}_2$ (h) $P(C_{2y})\mathbf{J}_2 = -1 \cdot \mathbf{J}_2$

(i) $P(E)\mathbf{J}_3 = +1 \cdot \mathbf{J}_3$ (j) $P(C_{2z})\mathbf{J}_3 = -1 \cdot \mathbf{J}_3$ (k) $P(C_{2x})\mathbf{J}_3 = +1 \cdot \mathbf{J}_3$ (l) $P(C_{2y})\mathbf{J}_3 = -1 \cdot \mathbf{J}_3$

(m) $P(E)\mathbf{J}_4 = +1 \cdot \mathbf{J}_4$ (n) $P(C_{2z})\mathbf{J}_4 = -1 \cdot \mathbf{J}_4$ (o) $P(C_{2x})\mathbf{J}_4 = -1 \cdot \mathbf{J}_4$ (p) $P(C_{2y})\mathbf{J}_4 = +1 \cdot \mathbf{J}_4$
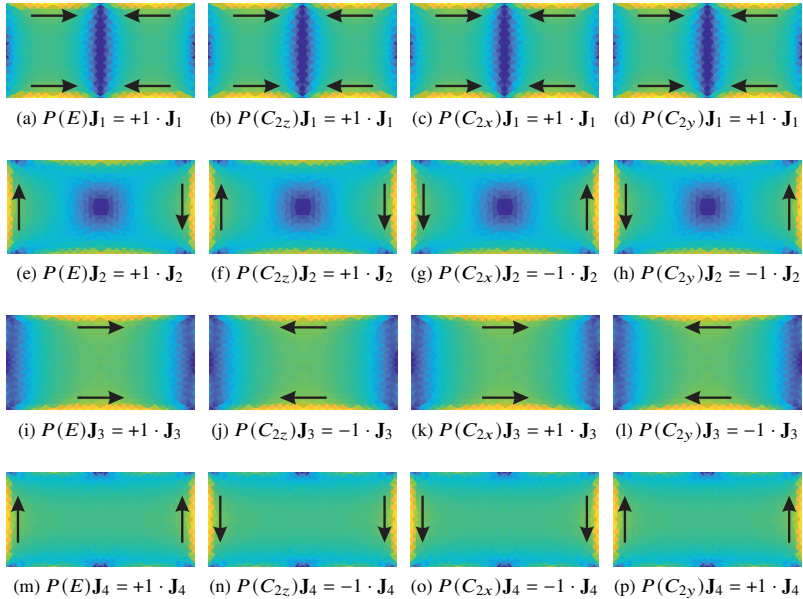
Figure 3.8 Transformation of surface current densities of significant characteristic modes of rectangular PEC plate at 2.5 GHz. As the characteristic surface current densities are basis functions of the irreducible representations, a transformation is equal to a multiplication with the corresponding character in Table 3.14. Principal current directions denoted by arrows. Mode indices according to Fig. 2.5. Color bar in Fig. 2.6(e). (a)–(d) $\mathbf{J}_1$ belonging to $\Gamma^{(1)}$. (e)–(h) $\mathbf{J}_2$ belonging to $\Gamma^{(2)}$. (i)–(l) $\mathbf{J}_3$ belonging to $\Gamma^{(3)}$. (m)–(p) $\mathbf{J}_4$ belonging to $\Gamma^{(4)}$.

intuitively in Table 2.1 and it is found that the sets defined therein correspond to the irreducible representations. With the number of representations in mind, it is now evident why there are exactly four such sets.

Moreover, it is now possible to explain the correlation of the characteristic surface current densities (2.51) as observed in Fig. 2.11. As the characteristic surface current densities are basis functions of the irreducible representations, they are governed by the orthogonality theorem (3.27). Applied to the rectangular plate, it states that characteristic surface current densities belonging to different irreducible representations are orthogonal to each other. For this reason, the four sets defined in Table 2.1 are mutually orthogonal as evidenced by Fig. 2.11.

The antenna ports as defined in Fig. 2.7 can also be assigned to the irreducible representations as shown in Table 2.1. They can thus be interpreted as basis

functions as well since they transform in the same way as the characteristic surface current densities they are intended to excite. Furthermore, the modal excitation coefficients (2.24) have the same form as the orthogonality theorem (3.27) and they are thus governed by it. This explains why the ports only excite modes belonging to the same irreducible representation as found in Fig. 2.12.

This brief example shows that with the theory of symmetry and its connection to characteristic modes it is possible to understand the observations made in section 2.4.3. Consequences and applications of this connection will be studied in full detail in chapter 4, especially with regard to multimode antenna design.

3.5 Projection Operator Method

An advanced technique from group theory is the projection operator method. Originally, projection operators are used to derive basis functions of a given irreducible representation. The projection operator method is therefore also called the "basis-function generating machine" [77].

3.5.1 Projection Operators

The projection operator $\mathcal{P}_{\mu\nu}^{(p)}$ of the d_p-dimensional p-th irreducible representation of a group $\mathcal{G}$ of order g is defined as [75]

$$\mathcal{P}_{\mu\nu}^{(p)} = \frac{d_p}{g} \sum_{T \in \mathcal{G}} \Gamma_{\mu\nu}^{(p)*}(T) P(T), \quad \mu,\nu = 1,2,\ldots,d_p. \tag{3.49}$$

It is a weighted sum of the transformation operators $P(T)$ over all group elements T, where the weighting coefficients are the complex conjugate elements $\Gamma_{\mu\nu}^{(p)*}(T)$ of the representation matrices $\mathbf{\Gamma}^{(p)}(T)$. For a d_p-dimensional irreducible representation, there exist d_p^2 such projection operators.

Due to the orthogonality of the irreducible representations (section 3.3.3), the application of a projection operator to a basis function $\psi_\kappa^{(q)}$ yields [75]

$$\mathcal{P}_{\mu\nu}^{(p)}\psi_\kappa^{(q)}(\mathbf{r}') = \delta_{pq}\delta_{\nu\kappa}\psi_\mu^{(p)}(\mathbf{r}'). \tag{3.50}$$

If the basis function does not transform according to the same irreducible representation ($p \neq q$) or the same column of the irreducible representation ($p = q$, $\nu \neq \kappa$) which the projection operator belongs to, the projection yields zero. However, if it transforms according to the same column ($\nu = \kappa$) of the same

irreducible representation ($p = q$) which the projection operator belongs to, the projection yields the basis function belonging to the μ-th row, i.e., the same row as the projection operator, of that irreducible representation.

This means that, if $\psi_\nu^{(p)}$ is a basis function belonging to the ν-th row of the d_p-dimensional p-th irreducible representation, its partner function belonging to the μ-th row of the same irreducible representation can be projected out of it by applying the projection operator $\mathcal{P}_{\mu\nu}^{(p)}$:

$$\mathcal{P}_{\mu\nu}^{(p)}\psi_\nu^{(p)}(\mathbf{r}') = \psi_\mu^{(p)}(\mathbf{r}'). \tag{3.51}$$

In particular [77]:

$$\mathcal{P}_{\nu\nu}^{(p)}\psi_\nu^{(p)}(\mathbf{r}') = \psi_\nu^{(p)}(\mathbf{r}'), \tag{3.52}$$

which finally explains why $\psi_\mu^{(p)}$ is said to belong to the μ-th row and $\psi_\nu^{(p)}$ is said to belong to the ν-th row. This property of the projection operators is especially useful for multi-dimensional irreducible representations. If one basis function is known, its partner functions can be readily computed using the appropriate projection operators.

This concept can be generalized further by applying the projection operator $\mathcal{P}_{\nu\nu}^{(p)}$ to an arbitrary function $\mathbf{f}(\mathbf{r}')$ [75]:

$$\mathcal{P}_{\nu\nu}^{(p)}\mathbf{f}(\mathbf{r}') = w_\nu^{(p)}\psi_\nu^{(p)}(\mathbf{r}'), \tag{3.53}$$

where $w_\nu^{(p)}$ is a weighting coefficient. This equation states that the application of the projection operator to an arbitrary function projects out of it that part which belongs to the ν-th row of the p-th irreducible representation [77]. This provides now an automatic procedure for deriving a basis of a given irreducible representation [75]:

1. Choose an arbitrary function $\mathbf{f}(\mathbf{r}')$ such that $\mathcal{P}_{\nu\nu}^{(p)}\mathbf{f}(\mathbf{r}')$ does not yield zero for one arbitrarily chosen ν.

2. $\mathcal{P}_{\nu\nu}^{(p)}\mathbf{f}(\mathbf{r}')$ is then a basis function belonging to the ν-th row according to (3.53).

3. Use (3.51) to find its partner functions.

4. These basis functions may be normalized to form an orthonormal set.

3.5.2 Character Projection Operators

For the construction of basis functions as described in the previous subsection, a set of representation matrices needs to be known (e.g., Table 3.6). These may not always be available as only the character tables are usually given in the literature. Furthermore, representation matrices are only unique up to a similarity transformation, as stated in section 3.3.1. In order to avoid this arbitrariness and uniquely characterize an irreducible representation, the characters were introduced in section 3.3.4. With this argument in mind, the character projection operators $\mathcal{P}^{(p)}$ are defined [75]:

$$\mathcal{P}^{(p)} = \frac{d_p}{g} \sum_{T \in \mathcal{G}} \chi^{(p)*}(T) P(T). \tag{3.54}$$

Instead of the elements of the representation matrices, the sum now contains the characters. For this reason, there is exactly one character projection operator per irreducible representation. For one-dimensional representations, in particular, the projection operators and the character projection operators are identical.

The character projection operators can also be written in terms of the projection operators for $\nu = \mu$ [75]:

$$\mathcal{P}^{(p)} = \sum_{\mu=1}^{d_p} \mathcal{P}_{\mu\mu}^{(p)}. \tag{3.55}$$

By combining this equation with (3.50), the application of a character projection operator to a basis function $\psi_\kappa^{(q)}$ yields

$$\mathcal{P}^{(p)} \psi_\kappa^{(q)}(\mathbf{r'}) = \sum_{\mu=1}^{d_p} \mathcal{P}_{\mu\mu}^{(p)} \psi_\kappa^{(q)}(\mathbf{r'}) = \sum_{\mu=1}^{d_p} \delta_{pq} \delta_{\mu\kappa} \psi_\mu^{(p)}(\mathbf{r'}) = \delta_{pq} \psi_\kappa^{(p)}(\mathbf{r'}).$$
$$\tag{3.56}$$

Again, the projection yields zero if the basis function does not belong to the same irreducible representation ($p \neq q$) as the character projection operator. However, if the basis function does belong to the same irreducible representation as the character projection operator ($p = q$), the projection yields the basis function itself regardless of which row it belongs to. This property is particularly useful for assigning a set of functions which are known to be basis functions (e.g., characteristic surface current densities) to the irreducible representations of a group.

This concept, too, can be generalized further by applying a character projection operator to an arbitrary function $\mathbf{f}$. Combining (3.55) with (3.53) yields

$$\mathcal{P}^{(p)}\mathbf{f}(\mathbf{r}') = \sum_{\mu=1}^{d_p} \mathcal{P}^{(p)}_{\mu\mu}\mathbf{f}(\mathbf{r}') = \sum_{\mu=1}^{d_p} w^{(p)}_\mu \boldsymbol{\psi}^{(p)}_\mu(\mathbf{r}'). \tag{3.57}$$

Applying a character projection operator to an arbitrary function projects out of it a linear combination of basis functions belonging to the given irreducible representation. However, a linear combination of basis functions is a basis function of an equivalent irreducible representation [75]:

$$\bar{\boldsymbol{\psi}}^{(p)}_\nu(\mathbf{r}') = \sum_{\mu=1}^{d_p} S_{\mu\nu}\boldsymbol{\psi}^{(p)}_\mu(\mathbf{r}'), \quad \nu = 1,2,\ldots,d_p, \tag{3.58}$$

where $S_{\mu\nu}$ are the elements of a non-singular $d_p \times d_p$ square matrix $\mathbf{S}$ as used in (3.19). The projected function $\mathcal{P}^{(p)}\mathbf{f}$ is thus a basis function $\bar{\boldsymbol{\psi}}^{(p)}_\nu$ of an equivalent irreducible representation whose representation matrices are given by the similarity transformation (3.19). Therefore, the character projection operator of a given irreducible representation gives a valid basis function although the corresponding representation matrices are unknown.

3.5.3 Applying Projection Operators

As the concepts introduced above will play a major role throughout this thesis, they are now illustrated by a few generic examples. The computations are performed explicitly in order to give an overview about how to work with projection operators.

First of all, the computation of projection operators is demonstrated explicitly for a simple example. The function $\boldsymbol{\psi}^{(2)}(\mathbf{r}') = (-y',x')^{\mathrm{T}}$ as shown in Fig. 3.5(a) was found in section 3.3.2 to be a basis function of the second irreducible representation $\Gamma^{(2)}$ of the symmetry group D_4.[35] Before employing the projection operators, the transformation operators are needed. For the given function, they have already been calculated in (3.23). The representation matrices (characters)

---

[35] For the sake of conciseness, the z-component is not displayed in the following examples. As the functions to be considered have no z-component (planar problem in the xy-plane), there is no loss of information.

are given in Table 3.6. Applying now the projection operator $\mathcal{P}^{(2)}$ (3.49) yields[36]

$$\mathcal{P}^{(2)}\begin{pmatrix} -y' \\ x' \end{pmatrix} = \frac{1}{8}\left(\begin{pmatrix} -y' \\ x' \end{pmatrix} + \begin{pmatrix} -y' \\ x' \end{pmatrix} + \begin{pmatrix} -y' \\ x' \end{pmatrix} + \begin{pmatrix} -y' \\ x' \end{pmatrix}\right.$$
$$\left. - \begin{pmatrix} y' \\ -x' \end{pmatrix} - \begin{pmatrix} y' \\ -x' \end{pmatrix} - \begin{pmatrix} y' \\ -x' \end{pmatrix} - \begin{pmatrix} y' \\ -x' \end{pmatrix}\right) = \begin{pmatrix} -y' \\ x' \end{pmatrix},$$

i.e., the basis function itself. In the same manner, it can be checked that applying any other of the projection operators ($p \neq 2$) yields zero, as required by (3.50).

Using projection operators becomes even more meaningful when working with multi-dimensional irreducible representations ($d_p \geq 2$). The function $\boldsymbol{\psi}_1^{(5)}(\mathbf{r}') = (|x'|, 0)^{\mathrm{T}}$ as shown in Fig. 3.6(a) was found in section 3.3.2 to be a basis function belonging to the first row ($\nu = 1$) of the two-dimensional ($d_5 = 2$) fifth irreducible representation $\Gamma^{(5)}$ of the symmetry group D_4. The transformation operators have already been computed in (3.24). The representation matrices are given in Table 3.6 and the characters in Table 3.8. First, the character projection operators (3.54) are employed. The projection with $p \neq 5$ yields zero. Applying instead $\mathcal{P}^{(5)}$ results in

$$\mathcal{P}^{(5)}\begin{pmatrix} |x'| \\ 0 \end{pmatrix} = \frac{2}{8}\left(2\begin{pmatrix} |x'| \\ 0 \end{pmatrix} - 2\begin{pmatrix} -|x'| \\ 0 \end{pmatrix}\right) = \begin{pmatrix} |x'| \\ 0 \end{pmatrix},$$

i.e., the basis function itself. If a function is known to be a basis function, the character projection operators provide a straightforward way in order to assign this function to the corresponding irreducible representation. Next, the projection operators (3.49) are applied to $\boldsymbol{\psi}_1^{(5)}$:

$$\mathcal{P}_{11}^{(5)}\begin{pmatrix} |x'| \\ 0 \end{pmatrix} = \frac{2}{8}\left(\begin{pmatrix} |x'| \\ 0 \end{pmatrix} - \begin{pmatrix} -|x'| \\ 0 \end{pmatrix} + \begin{pmatrix} |x'| \\ 0 \end{pmatrix} - \begin{pmatrix} -|x'| \\ 0 \end{pmatrix}\right) = \begin{pmatrix} |x'| \\ 0 \end{pmatrix},$$

$$\mathcal{P}_{21}^{(5)}\begin{pmatrix} |x'| \\ 0 \end{pmatrix} = \frac{2}{8}\left(-\begin{pmatrix} 0 \\ -|y'| \end{pmatrix} + \begin{pmatrix} 0 \\ |y'| \end{pmatrix} + \begin{pmatrix} 0 \\ |y'| \end{pmatrix} - \begin{pmatrix} 0 \\ -|y'| \end{pmatrix}\right) = \begin{pmatrix} 0 \\ |y'| \end{pmatrix},$$

$$\mathcal{P}_{12}^{(5)}\begin{pmatrix} |x'| \\ 0 \end{pmatrix} = \frac{2}{8}\left(\begin{pmatrix} 0 \\ -|y'| \end{pmatrix} - \begin{pmatrix} 0 \\ |y'| \end{pmatrix} + \begin{pmatrix} 0 \\ |y'| \end{pmatrix} - \begin{pmatrix} 0 \\ -|y'| \end{pmatrix}\right) = 0,$$

$$\mathcal{P}_{22}^{(5)}\begin{pmatrix} |x'| \\ 0 \end{pmatrix} = \frac{2}{8}\left(\begin{pmatrix} |x'| \\ 0 \end{pmatrix} - \begin{pmatrix} -|x'| \\ 0 \end{pmatrix} - \begin{pmatrix} |x'| \\ 0 \end{pmatrix} + \begin{pmatrix} -|x'| \\ 0 \end{pmatrix}\right) = 0.$$

---

[36]The projection operator is equivalent to the character projection operator (3.54) as the representation is one-dimensional.

The application of the projection operator $\mathcal{P}_{11}^{(5)}$ yields the function itself, which means that $\boldsymbol{\psi}_1^{(5)}$ is a basis function belonging to the first row of the irreducible representation according to (3.52). Due to this, the application of $\mathcal{P}_{21}^{(5)}$ yields its partner function $\boldsymbol{\psi}_2^{(5)}(\mathbf{r}') = (0,|y'|)^{\mathrm{T}}$ belonging to the second row according to (3.51). The two other projections yield zero according to (3.50) as $\boldsymbol{\psi}_1^{(5)}$ does not belong to the second row ($\nu \neq \kappa$). This example demonstrates how the basis functions of a multi-dimensional irreducible representation can be assigned to its rows if an explicit set of representation matrices (Table 3.6) is given.

As a last example, the new function $\mathbf{f}(\mathbf{r}') = (|x'|,|y'|)^{\mathrm{T}}$ is considered. Using the character projection operator method, it is identified to be a basis function of the fifth irreducible representation $\Gamma^{(5)}$ of the symmetry group D_4:

$$\mathcal{P}^{(5)} \begin{pmatrix} |x'| \\ |y'| \end{pmatrix} = \frac{2}{8}\left(2\begin{pmatrix} |x'| \\ |y'| \end{pmatrix} - 2\begin{pmatrix} -|x'| \\ -|y'| \end{pmatrix}\right) = \begin{pmatrix} |x'| \\ |y'| \end{pmatrix}.$$

Therefore, it must be a linear combination of $\boldsymbol{\psi}_1^{(5)}$ and $\boldsymbol{\psi}_2^{(5)}$ according to (3.57); and in fact, $\mathbf{f}(\mathbf{r}') = \boldsymbol{\psi}_1^{(5)}(\mathbf{r}') + \boldsymbol{\psi}_2^{(5)}(\mathbf{r}')$. The projection operators can now be used to project out of $\mathbf{f}$ these basis functions:

$$\mathcal{P}_{11}^{(5)} \begin{pmatrix} |x'| \\ |y'| \end{pmatrix} = \frac{2}{8}\left(\begin{pmatrix} |x'| \\ |y'| \end{pmatrix} - \begin{pmatrix} -|x'| \\ -|y'| \end{pmatrix} + \begin{pmatrix} |x'| \\ -|y'| \end{pmatrix} - \begin{pmatrix} -|x'| \\ |y'| \end{pmatrix}\right) = \begin{pmatrix} |x'| \\ 0 \end{pmatrix},$$

$$\mathcal{P}_{21}^{(5)} \begin{pmatrix} |x'| \\ |y'| \end{pmatrix} = \frac{2}{8}\left(-\begin{pmatrix} |x'| \\ -|y'| \end{pmatrix} + \begin{pmatrix} -|x'| \\ |y'| \end{pmatrix} + \begin{pmatrix} |x'| \\ |y'| \end{pmatrix} - \begin{pmatrix} -|x'| \\ -|y'| \end{pmatrix}\right) = \begin{pmatrix} 0 \\ |y'| \end{pmatrix};$$

or alternatively:

$$\mathcal{P}_{12}^{(5)} \begin{pmatrix} |x'| \\ |y'| \end{pmatrix} = \frac{2}{8}\left(\begin{pmatrix} |x'| \\ -|y'| \end{pmatrix} - \begin{pmatrix} -|x'| \\ |y'| \end{pmatrix} + \begin{pmatrix} |x'| \\ |y'| \end{pmatrix} - \begin{pmatrix} -|x'| \\ -|y'| \end{pmatrix}\right) = \begin{pmatrix} |x'| \\ 0 \end{pmatrix},$$

$$\mathcal{P}_{22}^{(5)} \begin{pmatrix} |x'| \\ |y'| \end{pmatrix} = \frac{2}{8}\left(\begin{pmatrix} |x'| \\ |y'| \end{pmatrix} - \begin{pmatrix} -|x'| \\ -|y'| \end{pmatrix} - \begin{pmatrix} |x'| \\ -|y'| \end{pmatrix} + \begin{pmatrix} -|x'| \\ |y'| \end{pmatrix}\right) = \begin{pmatrix} 0 \\ |y'| \end{pmatrix}.$$

This is a simple example for projecting out of an arbitrary function the basis functions corresponding to a given set of representation matrices.

3.5.4 Computation of Representation Matrices

The projection operators are used to construct basis functions of the irreducible representations. There may, however, be cases where an explicit knowledge of the representation matrices is needed and a set of basis functions is known

instead. In this section, it is demonstrated how representation matrices can be constructed out of a given set of basis functions.

It is supposed that an orthonormal set of basis functions $\psi_1^{(p)}, \psi_2^{(p)}, \ldots, \psi_{d_P}^{(p)}$ fulfilling (3.29) and transforming according to (3.22) is known. Now, an inner product with $\psi_\kappa^{(p)}$ is applied to (3.22):

$$
\begin{aligned}
\left\langle \psi_\kappa^{(p)}(\mathbf{r}'), P(T)\psi_\nu^{(p)}(\mathbf{r}') \right\rangle &= \left\langle \psi_\kappa^{(p)}(\mathbf{r}'), \sum_{\mu=1}^{d_p} \Gamma_{\mu\nu}^{(p)}(T)\psi_\mu^{(p)}(\mathbf{r}') \right\rangle \\
&= \sum_{\mu=1}^{d_p} \Gamma_{\mu\nu}^{(p)}(T)\left\langle \psi_\kappa^{(p)}(\mathbf{r}'), \psi_\mu^{(p)}(\mathbf{r}') \right\rangle \\
&= \sum_{\mu=1}^{d_p} \Gamma_{\mu\nu}^{(p)}(T)\delta_{\kappa\mu} = \Gamma_{\kappa\nu}^{(p)}(T), \qquad (3.59)
\end{aligned}
$$

for $\kappa, \nu = 1, 2, \ldots, d_p$. Due to the orthogonality theorem (3.29) and the normalization of the basis functions, the inner product of the basis functions on the right-hand side yields 1 only if $\mu = \kappa$ and 0 otherwise so that every element $\Gamma_{\kappa\nu}^{(p)}(T)$ of the representation matrix $\mathbf{\Gamma}^{(p)}(T)$ can be computed as follows:

$$
\Gamma_{\kappa\nu}^{(p)}(T) = \left\langle \psi_\kappa^{(p)}(\mathbf{r}'), P(T)\psi_\nu^{(p)}(\mathbf{r}') \right\rangle. \qquad (3.60)
$$

This way, the representation matrices for all $T \in \mathcal{G}$ can be computed from an orthonormal set of basis functions. The so-formed irreducible representation is unitary [75]. As an example, the two basis functions $\psi_1^{(5)}$ and $\psi_2^{(5)}$ from above can be used to compute the representation matrices of the fifth irreducible representation $\Gamma^{(5)}$ of D_4 as given in Table 3.6.

However, the function $\mathbf{f}(\mathbf{r}') = (|x'|, |y'|)^\mathrm{T}$ has also been identified as a basis function of this irreducible representation, though with a yet unknown set of representation matrices. In order to derive these matrices with (3.60), its partner function is needed first. A linearly independent function can be found by applying the transformation operators. For example, $P(C_{4z})\mathbf{f}(\mathbf{r}') = (|x'|, -|y'|)^\mathrm{T}$ is linearly independent. It is even orthogonal to $\mathbf{f}$ so that it is already a suitable partner function (appendix D.2). In more complicated cases, the Gram-Schmidt orthogonalization process (appendix B.1) has to be applied in order to obtain an orthogonal partner function [75]. The two basis functions are shown in Fig. 3.9.

After proper normalization of the basis functions, the representation matrices are computed using (3.60). The detailed computation is presented in
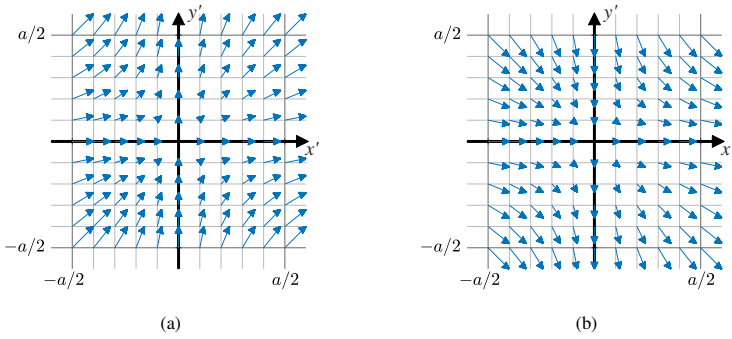
Figure 3.9 Alternative set of basis functions of two-dimensional fifth irreducible representation $\Gamma^{(5)}$ of symmetry group D_4. (a) $\check{\psi}_1^{(5)}(\mathbf{r}') = (|x'|,|y'|)^{\mathrm{T}}$ belonging to the first row. (b) $\check{\psi}_2^{(5)}(\mathbf{r}') = (|x'|,-|y'|)^{\mathrm{T}}$ belonging to the second row. This set of basis functions is equivalent to that in Fig. 3.6.

D_4	E	C_{4z}	C_{2z}	C_{4z}^{-1}
$\Gamma^{(5)}$	$\begin{pmatrix} 1 & 0 \\ 0 & 1 \end{pmatrix}$	$\begin{pmatrix} 0 & -1 \\ 1 & 0 \end{pmatrix}$	$\begin{pmatrix} -1 & 0 \\ 0 & -1 \end{pmatrix}$	$\begin{pmatrix} 0 & 1 \\ -1 & 0 \end{pmatrix}$

D_4	C_{2x}	C_{2y}	C_{2A}	C_{2B}
$\Gamma^{(5)}$	$\begin{pmatrix} 0 & 1 \\ 1 & 0 \end{pmatrix}$	$\begin{pmatrix} 0 & -1 \\ -1 & 0 \end{pmatrix}$	$\begin{pmatrix} 1 & 0 \\ 0 & -1 \end{pmatrix}$	$\begin{pmatrix} -1 & 0 \\ 0 & 1 \end{pmatrix}$

Table 3.15 Computed representation matrices of fifth irreducible representation of symmetry group D_4 corresponding to the basis functions $\check{\psi}_1^{(5)}(\mathbf{r}') = (|x'|,|y'|)^{\mathrm{T}}$ and $\check{\psi}_2^{(5)}(\mathbf{r}') = (|x'|,-|y'|)^{\mathrm{T}}$.

appendix D.2. The results are given in Table 3.15. The representation matrices differ from those in Table 3.6, as expected. It is now even possible to express the transformation matrix between the respective representation matrices. As already observed above, $\mathbf{f}(\mathbf{r}') = \psi_1^{(5)}(\mathbf{r}') + \psi_2^{(5)}(\mathbf{r}') = \check{\psi}_1^{(5)}$. Its orthogonal partner function can be expressed as $P(C_{4z})\mathbf{f}(\mathbf{r}') = \psi_1^{(5)}(\mathbf{r}') - \psi_2^{(5)}(\mathbf{r}') = \check{\psi}_2^{(5)}$. With (3.58), the transformation matrix $\mathbf{S}$ and its inverse are found to be

$$\mathbf{S} = \begin{pmatrix} 1 & 1 \\ 1 & -1 \end{pmatrix}, \qquad \mathbf{S}^{-1} = \begin{pmatrix} 0.5 & 0.5 \\ 0.5 & -0.5 \end{pmatrix}.$$

Applying the similarity transformation (3.19) to the matrices in Table 3.6 indeed yields those of Table 3.15. The two representations are thus equivalent, which can also be checked by means of their characters.

The described procedure is generally applicable if only the characters and one basis function are known. The basic steps are summarized as follows [75]:

1. Use the character projection operator method to assign the given basis function to the corresponding irreducible representation.

2. Apply the transformation operators to the basis function in order to find linearly independent partner functions.

3. Use the Gram-Schmidt orthogonalization process to form an orthonormal basis, if necessary (appendix B.1).

4. Compute the representation matrices using (3.60).

With this procedure, a complete basis and the corresponding representation matrices can be derived.

In summary, the projection operators are versatile tools in conjunction with matrix representations and basis functions. Their applications to characteristic modes and multimode antenna design will be investigated in chapter 4.

3.6 Continuous Groups

So far, finite groups, i.e., groups with a finite number of elements, have been considered. An infinite group, in contrast, is a group containing an infinite number of elements [77]. Infinite groups arise if the group elements $T(\Phi_1, \Phi_2, \ldots, \Phi_L)$ vary continuously as functions of a set of L parameters $\Phi_1, \Phi_2, \ldots, \Phi_L$. Such infinite groups are called continuous groups [77].[37]

An arbitrary function of the group elements $f(T)$ (e.g., a character) becomes a function of the parameters, i.e., $f(T(\Phi_1, \Phi_2, \ldots, \Phi_L))$ [81]. A sum over the group elements is replaced by an integral [75, 77]:

$$\sum_{T \in \mathcal{G}} f(T) \rightarrow \int_{\mathcal{G}} f(T) \mathrm{d}T, \qquad (3.61)$$

where $\mathrm{d}T$ can be interpreted as an infinitesimal variation of the group elements. This integration can be carried out explicitly as a Hurwitz invariant integral in

---

[37] In this section, only those methods and properties of continuous groups which differ from finite groups will be explained. All other methods and properties of finite groups introduced in the previous sections can be adopted directly.

parameter space [77]:

$$\int_{\mathcal{G}} f(T)\mathrm{d}T = \int_{\Phi_1}\int_{\Phi_2}\cdots\int_{\Phi_L} f\big(T(\Phi_1,\Phi_2,\ldots,\Phi_L)\big)$$
$$\cdot\, \mathcal{g}\big(T(\Phi_1,\Phi_2,\ldots,\Phi_L)\big)\mathrm{d}\Phi_L\cdots\mathrm{d}\Phi_2\mathrm{d}\Phi_1, \quad (3.62)$$

where $\mathcal{g}$ is the density of group elements.

The concept of continuous groups can be generalized further to so-called mixed continuous groups [77]. Such a group consists of a finite number of M discrete regions $\Psi_1,\Psi_2,\ldots,\Psi_M$. Every group element belongs to one of these regions. Within one region, the group elements vary continuously as functions of the already introduced parameters $\Phi_1,\Phi_2,\ldots,\Phi_L$.

In this case, the sum over the group elements is replaced by a sum over the regions and integrals over the parameters [81]:

$$\sum_{T\in\mathcal{G}} f(T) \rightarrow \sum_{T\in\Psi_1}^{T\in\Psi_M}\int_{\Phi_1}\int_{\Phi_2}\cdots\int_{\Phi_L} f\big(T(\Phi_1,\Phi_2,\ldots,\Phi_L)\big)$$
$$\cdot\, \mathcal{g}\big(T(\Phi_1,\Phi_2,\ldots,\Phi_L)\big)\mathrm{d}\Phi_L\cdots\mathrm{d}\Phi_2\mathrm{d}\Phi_1. \quad (3.63)$$

It should be noted that each region has its own density of group elements.

The group order g of a continuous group can now be defined in a general way as the sum of the integrals over the densities of group elements:

$$g = \sum_{T\in\Psi_1}^{T\in\Psi_M}\int_{\Phi_1}\int_{\Phi_2}\cdots\int_{\Phi_L} \mathcal{g}\big(T(\Phi_1,\Phi_2,\ldots,\Phi_L)\big)\mathrm{d}\Phi_L\cdots\mathrm{d}\Phi_2\mathrm{d}\Phi_1. \quad (3.64)$$

With these definitions, the methods introduced in the previous sections can be adopted to continuous groups. This will now be illustrated exemplarily by means of the symmetry group D_∞.[38] This is the symmetry group of a circular disk in the xy-plane as depicted in Fig. 3.10.[39]

Apart from the identity E, it consists of an infinite number of rotations about the z-axis by the continuous angle Φ denoted by $C_z(\Phi)$, with $0 \leq \Phi < 2\pi$. Furthermore, there is an infinite number of rotations by $180°$ about axes

---

[38] D_∞ is isomorphic to the orthogonal group in two dimensions $O(2)$.

[39] As the name suggests, this symmetry group is related to D_4. This relationship will be analyzed in full detail in chapter 5.
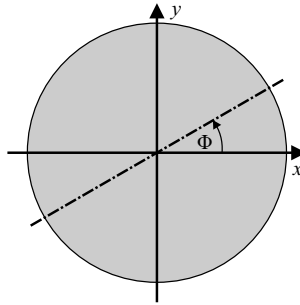
Figure 3.10 Circular disk in xy-plane and coordinate system. One exemplary axis of symmetry with rotation angle Φ with respect to the x-axis is shown.

$T(\Phi)$	E	$C_z(\Phi)$	$C_2(\Phi)$
$\mathbf{R}(T(\Phi))$	$\begin{pmatrix} 1 & 0 & 0 \\ 0 & 1 & 0 \\ 0 & 0 & 1 \end{pmatrix}$	$\begin{pmatrix} \cos(\Phi) & \sin(\Phi) & 0 \\ -\sin(\Phi) & \cos(\Phi) & 0 \\ 0 & 0 & 1 \end{pmatrix}$	$\begin{pmatrix} \cos(2\Phi) & \sin(2\Phi) & 0 \\ \sin(2\Phi) & -\cos(2\Phi) & 0 \\ 0 & 0 & -1 \end{pmatrix}$

Table 3.16 Elements and rotation matrices of symmetry group D_∞.

perpendicular to the z-axis.[40] These rotation axes are characterized by the angle Φ (one of them shown in Fig. 3.10) and the corresponding rotations are thus denoted by $C_2(\Phi)$. Such a rotation is equivalent to the rotation $C_z(2\Phi)$ by 2Φ about the z-axis followed by the rotation C_{2x} by $180°$ about the x-axis [57]:

$$C_2(\Phi) = C_{2x}C_z(2\Phi). \tag{3.65}$$

This relationship simplifies the computation of the rotation matrices. The group elements and the corresponding rotation matrices are listed in Table 3.16. The rotation matrices are computed using 3.7 by replacing the discrete angle $\frac{2\pi}{n}$ by Φ. The group elements are functions of one parameter, the rotation angle Φ.

The character table of D_∞ is given in Table 3.17 [77]. There are three classes: The identity E, the rotations $C_z(\Phi)$, and the rotations $C_2(\Phi)$ each form a class on their own. However, the identity is equal to $C_z(0)$ and it thus lies in the same

---

[40] D_∞ is isomorphic to $C_{\infty v}$, which is the symmetry group of a right circular cone. In $C_{\infty v}$, the rotations about axes perpendicular to the z-axis are replaced by reflections through planes containing the z-axis (cf. D_4 and C_{4v} in section 3.3.5). These reflections may be easier to visualize.

D_∞	E	$C_z(\Phi)$	$C_2(\Phi)$
$\Gamma^{(1)} = A_1$	1	1	1
$\Gamma^{(2)} = A_2$	1	1	-1
$\Gamma^{(3)} = E_1$	2	$2\cos(\Phi)$	0
$\Gamma^{(4)} = E_2$	2	$2\cos(2\Phi)$	0
$\vdots$	$\vdots$	$\vdots$	$\vdots$
$\Gamma^{(2+\tau)} = E_\tau$	2	$2\cos(\tau\Phi)$	0
$\vdots$	$\vdots$	$\vdots$	$\vdots$

Table 3.17   Character table of symmetry group D_∞.

region as the rotations $C_z(\Phi)$. Hence, the group D_∞ consists of two regions, one containing E as well as $C_z(\Phi)$ and one containing $C_2(\Phi)$.

The character table also reveals that there is an infinite number of irreducible representations. The first two ones are one-dimensional. They are alternatively called A_1 and A_2.[41] Furthermore, there is an infinite number of two-dimensional irreducible representations. The τ-th two-dimensional irreducible representation may alternatively be denoted by E_τ, with $\tau \in \mathbb{N}_{>0}$. In particular, the characters $\chi^{(2+\tau)}(C_z(\Phi))$ are functions of Φ. They are distinguished by τ.

Based on this knowledge, the character projection operators can now be specified by adopting (3.54) according to (3.63):

$$\mathcal{P}^{(1)} = \frac{1}{g}\left(\int_0^{2\pi} P(C_z(\Phi))\mathcal{G}(C_z(\Phi))\mathrm{d}\Phi + \int_0^{2\pi} P(C_2(\Phi))\mathcal{G}(C_2(\Phi))\mathrm{d}\Phi\right),$$

(3.66a)

$$\mathcal{P}^{(2)} = \frac{1}{g}\left(\int_0^{2\pi} P(C_z(\Phi))\mathcal{G}(C_z(\Phi))\mathrm{d}\Phi - \int_0^{2\pi} P(C_2(\Phi))\mathcal{G}(C_2(\Phi))\mathrm{d}\Phi\right),$$

(3.66b)

$$\mathcal{P}^{(2+\tau)} = \frac{2}{g}\int_0^{2\pi} 2\cos(\tau\Phi)P(C_z(\Phi))\mathcal{G}(C_z(\Phi))\mathrm{d}\Phi,$$

(3.66c)

[41]The notation using A_1, A_2, and E_τ is an alternative to the Γ-notation introduced in section 3.3 (see, e.g., [57, 77]). Although the Γ-notation is predominantly used throughout this thesis, switching temporarily to the alternative notation will prove beneficial in chapter 5.

where the group order g is computed according to (3.64) as follows:

$$g = \int_0^{2\pi} \mathcal{g}\big(C_z(\Phi)\big)\mathrm{d}\Phi + \int_0^{2\pi} \mathcal{g}\big(C_2(\Phi)\big)\mathrm{d}\Phi. \tag{3.67}$$

For explicit computations, the densities of group elements are required. These can be determined by adopting the orthogonality theorem for characters (3.31) according to (3.63):

$$g\delta_{pq} = \int_0^{2\pi} \chi^{(p)*}\big(C_z(\Phi)\big)\chi^{(q)}\big(C_z(\Phi)\big)\mathcal{g}\big(C_z(\Phi)\big)\mathrm{d}\Phi$$

$$+ \int_0^{2\pi} \chi^{(p)*}\big(C_2(\Phi)\big)\chi^{(q)}\big(C_2(\Phi)\big)\mathcal{g}\big(C_2(\Phi)\big)\mathrm{d}\Phi. \tag{3.68}$$

For $p = 1$ and $q = 2$, this yields

$$0 = \int_0^{2\pi} \mathcal{g}\big(C_z(\Phi)\big)\mathrm{d}\Phi - \int_0^{2\pi} \mathcal{g}\big(C_2(\Phi)\big)\mathrm{d}\Phi \quad \Leftrightarrow \quad \mathcal{g}\big(C_z(\Phi)\big) = \mathcal{g}\big(C_2(\Phi)\big),$$
$$\tag{3.69}$$

i.e., the densities of both regions are equal. Next, choosing $p = 1$ (or $p = 2$) and $q = 2 + \tau$ yields

$$0 = \int_0^{2\pi} 2\cos(\tau\Phi)\mathcal{g}\big(C_z(\Phi)\big)\mathrm{d}\Phi \quad \Leftrightarrow \quad \mathcal{g}\big(C_z(\Phi)\big) = \mathcal{g}\big(C_2(\Phi)\big) = K \in \mathbb{C}.$$
$$\tag{3.70}$$

This condition is always fulfilled if the densities are constant. Finally, choosing $p = 2 + \tau$ and $q = 2 + \upsilon$, with $\tau, \upsilon \in \mathbb{N}_{>0}$, yields

$$g\delta_{(2+\tau)(2+\upsilon)} = \int_0^{2\pi} 4\cos(\tau\Phi)\cos(\upsilon\Phi)K\mathrm{d}\Phi. \tag{3.71}$$

The case $\upsilon \neq \tau$ gives a true statement ($0 = 0$). The case $\upsilon = \tau$ yields

$$g = 4K\int_0^{2\pi} \cos^2(\tau\Phi)\mathrm{d}\Phi = 4\pi K. \tag{3.72}$$

The orthogonality is thus fulfilled for all constants $K \in \mathbb{C}$. For the sake of simplicity, K is chosen to be equal to 1, such that

$$g\big(C_z(\Phi)\big) = g\big(C_2(\Phi)\big) = 1 \quad \text{and} \quad g = 4\pi. \tag{3.73}$$

This example demonstrates how the methods introduced in this chapter can be readily applied to continuous groups. As a general rule, sums are replaced by integrals. The determination of the densities of group elements arises as an additional computation step. The explicit forms derived in this section for the symmetry group D_∞ will be made use of in chapter 5.

4 Symmetry Analysis
of Characteristic Modes

Having established the theoretical framework of this thesis, it is time make use of the connection between the theory of symmetry and the theory of characteristic modes. The methods introduced in the previous chapter are applied to the characteristic modes of a PEC object, which will henceforth be called symmetry analysis of characteristic modes. This symmetry analysis is intended to provide an enhanced understanding of characteristic modes and ultimately enable a systematic multimode antenna design.

To this end, first of all, the assignment of characteristic modes to the irreducible representations of the symmetry group of the underlying PEC object is discussed, which is the basis for all subsequent analyses. Next, the phenomenon of degenerate modes is investigated in full detail. The concept of fundamental modes per irreducible representation can then be introduced. Finally, and based on the preceding symmetry analysis, design guidelines for realizing orthogonal antenna ports on multimode antennas are derived. The chapter concludes with some representative examples.[42]

4.1 Assignment to Irreducible Representations

As the characteristic surface current densities are basis functions of the irreducible representations of the symmetry group of a PEC object, the principal task of the symmetry analysis is the assignment of the characteristic modes to the irreducible representations. In chapter 3, this was done manually by inspecting the basis functions of a square plate and a rectangular plate.

In this chapter, instead, an equilateral triangular PEC plate with edge length a, circumradius R_u, and inradius R_i[43] as shown in Fig. 4.1(a) is chosen for illustrating the different aspects of the symmetry analysis. Its symmetry group is D_3 consisting of the six symmetry operations ($g = 6$) listed in Table 4.1 [78].

---

[42]The following publications are related to the content of this chapter: [PM19a] (© 2019 IEEE), [PM19b] (© 2019 IEEE), [PHM21] (© 2021 IEEE).

[43]An equilateral triangle is completely determined by its edge length a: $R_u = \frac{a}{\sqrt{3}}$, $R_i = \frac{a}{2\sqrt{3}}$.
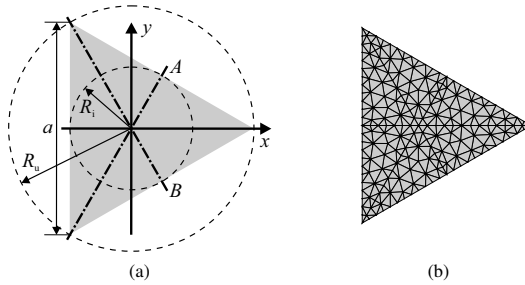
Figure 4.1 Equilateral triangular PEC plate. (a) Geometry, coordinate system, and symmetry axes. (b) An exemplary triangular mesh reproducing the symmetry of the equilateral triangular plate. © 2021 IEEE [PHM21].

Symmetry operation	Symbol
Identity	E
Rotation by 120° about the z-axis	C_{3z}
Rotation by 240° about the z-axis	C_{3z}^2
Rotation by 180° about the x-axis	C_{2x}
Rotation by 180° about the axis A	C_{2A}
Rotation by 180° about the axis B	C_{2B}

Table 4.1   The six elements of symmetry group D_3. © 2021 IEEE [PHM21].

Although, at first sight, the equilateral triangular plate may appear to be a rather simple example, it will become evident throughout this chapter that the symmetry group D_3 is both compact enough so that illustrations remain concise and complex enough so that all important effects can be demonstrated. The corresponding character table is given in Table 4.2 [78].[44] There are three irreducible representations $\Gamma^{(1)}$, $\Gamma^{(2)}$, and $\Gamma^{(3)}$. The first two are one-dimensional ($d_{1;2} = 1$), whereas the third one is two-dimensional ($d_3 = 2$).

At this point, and with (3.22) in mind, it can already be predicted that characteristic surface current densities belonging to the first irreducible representation $\Gamma^{(1)}$ (identity representation) are invariant under all symmetry operations of the equilateral triangular plate. In contrast, characteristic surface current densities belonging to the second irreducible representation $\Gamma^{(2)}$ are invariant

---

[44]The character table is usually the only information about the irreducible representations given in the literature due to the arbitrariness of the representation matrices.

D_3	E	C_{3z}	C_{3z}^2	C_{2x}	C_{2A}	C_{2B}
$\Gamma^{(1)}$	1	1	1	1	1	1
$\Gamma^{(2)}$	1	1	1	−1	−1	−1
$\Gamma^{(3)}$	2	−1	−1	0	0	0

Table 4.2   Character table of symmetry group D_3. © 2021 IEEE [PHM21].
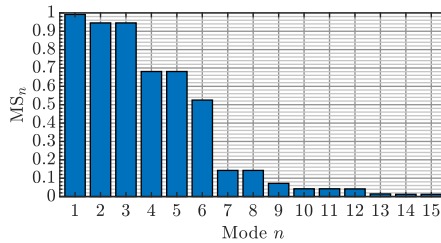
Figure 4.2   Modal significances of equilateral triangular PEC plate with circumradius $R_u = 0.6$ wavelengths. Modes sorted according to their significance.

under the rotations about the z-axis, but inverted under the rotations about the other axes. However, as the representation matrices are not known, similar statements cannot be made regarding the third irreducible representation $\Gamma^{(3)}$.

In order to compute the characteristic surface current densities, a modal analysis of the equilateral triangular PEC plate is now conducted. A circumradius $R_u = 0.6$ wavelengths is chosen arbitrarily.[45] A mesh reproducing the symmetry of the equilateral triangular plate is required. An exemplary triangular mesh fulfilling this requirement is shown in Fig. 4.1(b).[46] It can be easily checked that the mesh is invariant under the symmetry operations of D_3.

The modal analysis yields 15 characteristic modes to be taken into account, i.e., having an eigenvalue $|\lambda_n| \leq 100$ (section 2.3.4). The modal significances of these modes are shown in Fig. 4.2, where the modes are sorted according to their significance. The corresponding characteristic surface current densities are depicted in Fig. 4.3. It is apparent that the current distributions become more complex with increasing mode index n.

---

[45]For the symmetry analysis, it does not matter if the characteristic modes are significant or not.

[46]The symmetry analysis is independent of the mesh density provided that the mesh reproduces the symmetry correctly. Of course, in order to obtain reasonable modal results, the mesh density should fulfill the criteria discussed in section 2.3.4.
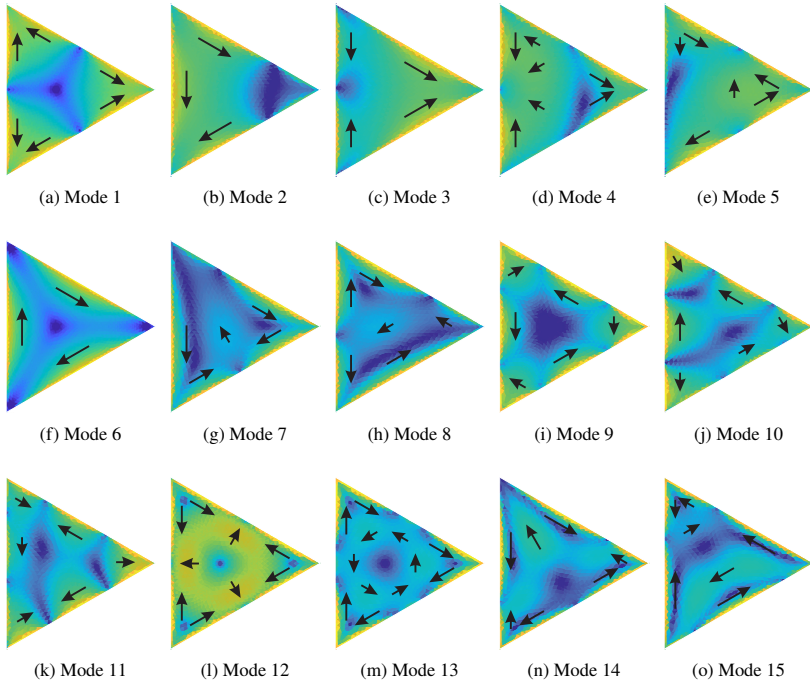
Figure 4.3   Normalized characteristic surface current densities of equilateral triangular PEC plate with circumradius R_u = 0.6 wavelengths. Principal current directions denoted by arrows. Color bar in Fig. 2.6(e). (a)–(o) Modes 1 to 15 as sorted in Fig. 4.2. © 2021 IEEE [PHM21].

Nevertheless, those characteristic surface current densities which are invariant under all symmetry operations of the symmetry group D_3 can easily be identified by a manual inspection. Modes 1 and 12 are found to belong to the first irreducible representation $\Gamma^{(1)}$. The corresponding characteristic surface current densities (Fig. 4.3(a) and (l)) each act as a basis function of this irreducible representation. This is due to the fact that applying any symmetry operation of the equilateral triangular plate is equivalent to a multiplication with 1, which is reflected by the characters of $\Gamma^{(1)}$ (Table 4.2).

In the same way, modes 6, 9, and 13 are identified to belong to the second irreducible representation $\Gamma^{(2)}$. Applying the identity or one of the rotations about the z-axis to the corresponding characteristic surface current densities (Fig. 4.3(f),

Repr.	Mode n
$\Gamma^{(1)}$	1; 12
$\Gamma^{(2)}$	6; 9; 13
$\Gamma^{(3)}$	2, 3; 4, 5; 7, 8; 10, 11; 14, 15

Table 4.3   Assignment of characteristic modes of equilateral triangular PEC plate to irreducible representations of symmetry group D_3.

(i), and (m)) is equal to a multiplication with 1, whereas applying one of the rotations about the other axes is equal to a multiplication with -1, corresponding to the characters of $\Gamma^{(2)}$ (Table 4.2).

In contrast, the assignment to the third irreducible representation $\Gamma^{(3)}$ is not that straightforward. In order to carry out the same inspection as has been done for the one-dimensional irreducible representations above, the two-dimensional representation matrices would be required, which are not available yet. However, in this special case, those modes which cannot be assigned to the first or second irreducible representation must belong to the third irreducible representation. This finally yields the assignment of all characteristic modes of the equilateral triangular PEC plate to the irreducible representations of the symmetry group D_3, which is summarized in Table 4.3.

Another argument for the assignment of the characteristic modes to the two-dimensional third irreducible representation is based on the degeneracy of the modes. Characteristic modes belonging to this irreducible representation must be two-fold degenerate. This means that a pair of characteristic surface current densities with the same eigenvalue forms a basis of the two-dimensional irreducible representation. It is found that the mode pairs 2-3, 4-5, 7-8, 10-11, and 14-15 have the same eigenvalue (modal significance, see Fig. 4.2). Hence, these pairs each form a basis of the third irreducible representation.

It has become apparent that the manual assignment of characteristic modes to the irreducible representations is illustrative, but has some severe drawbacks, in particular if only the characters are known. Only in the case of one-dimensional irreducible representations, a systematic manual assignment is possible. However, even this may become cumbersome if a symmetry group with a large number of elements and/or irreducible representations is examined. If irreducible representations of dimension higher than 1 are considered, some other criteria, e.g., the modal degeneracy, may be employed. However, if there is more than one multi-dimensional irreducible representation, the assignment becomes unfeasible without further information.

4.1.1 Automatic Assignment

The previous paragraphs have shown that there is need for a systematic way of assigning the characteristic modes to the irreducible representations. It is emphasized once again that only the characters are known and it will now be demonstrated that this information is sufficient for a complete assignment.

In section 3.5.2, the character projection operators are introduced. It is shown in (3.56) that applying a character projection operator to a basis function yields the basis function itself if it belongs to the same irreducible representation as the character projection operator and 0 otherwise.

As the characteristic surface current densities are basis functions of the irreducible representations, the character projection operator method can be readily applied to characteristic modes in order to implement a systematic and automatic assignment procedure. By applying all character projection operators of the given symmetry group to one characteristic surface current density in turn, it is identified to which irreducible representation it belongs.

According to (3.54), the three character projection operators of the symmetry group D_3 are computed as follows:

$$\mathcal{P}^{(1)} = \frac{1}{6}\Big(P(E) + P(C_{3z}) + P(C_{3z}^2) + P(C_{2x}) + P(C_{2A}) + P(C_{2B})\Big), \quad (4.1a)$$

$$\mathcal{P}^{(2)} = \frac{1}{6}\Big(P(E) + P(C_{3z}) + P(C_{3z}^2) - P(C_{2x}) - P(C_{2A}) - P(C_{2B})\Big), \quad (4.1b)$$

$$\mathcal{P}^{(3)} = \frac{1}{3}\Big(2P(E) - P(C_{3z}) - P(C_{3z}^2)\Big). \quad (4.1c)$$

The character projection operators are weighted sums of the transformation operators. Thus, all that is needed, apart from the characters, are the transformation operators (3.13). These can be readily implemented for any proper or improper rotation based on the rotation matrices as introduced in section 3.1.2. The transformation operators of the symmetry group D_3 are listed in Table 4.4.[47]

The character projection operators (4.1) are now applied to the characteristic surface current densities of the equilateral triangular PEC plate (Fig. 4.3). For example, the application to mode 2 (Fig. 4.3(b)) yields 0 for operators $\mathcal{P}^{(1)}$ and $\mathcal{P}^{(2)}$, but the characteristic surface current density itself for operator $\mathcal{P}^{(3)}$. In particular, a correct assignment to the two-dimensional third irreducible representation is possible based on the characters alone without further ado.

---

[47] The corresponding rotation matrices are given in Table D.1.

T	$P(T)\mathbf{f}(\mathbf{r}')$
E	$\begin{pmatrix} f_x(x',y',z') \\ f_y(x',y',z') \\ f_z(x',y',z') \end{pmatrix}$
C_{3z}	$\begin{pmatrix} -\frac{1}{2}f_x\left(-\frac{1}{2}x'-\frac{\sqrt{3}}{2}y',\frac{\sqrt{3}}{2}x'-\frac{1}{2}y',z'\right)+\frac{\sqrt{3}}{2}f_y\left(-\frac{1}{2}x'-\frac{\sqrt{3}}{2}y',\frac{\sqrt{3}}{2}x'-\frac{1}{2}y',z'\right) \\ -\frac{\sqrt{3}}{2}f_x\left(-\frac{1}{2}x'-\frac{\sqrt{3}}{2}y',\frac{\sqrt{3}}{2}x'-\frac{1}{2}y',z'\right)-\frac{1}{2}f_y\left(-\frac{1}{2}x'-\frac{\sqrt{3}}{2}y',\frac{\sqrt{3}}{2}x'-\frac{1}{2}y',z'\right) \\ f_z\left(-\frac{1}{2}x'-\frac{\sqrt{3}}{2}y',\frac{\sqrt{3}}{2}x'-\frac{1}{2}y',z'\right) \end{pmatrix}$
C_{3z}^2	$\begin{pmatrix} -\frac{1}{2}f_x\left(-\frac{1}{2}x'+\frac{\sqrt{3}}{2}y',-\frac{\sqrt{3}}{2}x'-\frac{1}{2}y',z'\right)-\frac{\sqrt{3}}{2}f_y\left(-\frac{1}{2}x'+\frac{\sqrt{3}}{2}y',-\frac{\sqrt{3}}{2}x'-\frac{1}{2}y',z'\right) \\ \frac{\sqrt{3}}{2}f_x\left(-\frac{1}{2}x'+\frac{\sqrt{3}}{2}y',-\frac{\sqrt{3}}{2}x'-\frac{1}{2}y',z'\right)-\frac{1}{2}f_y\left(-\frac{1}{2}x'+\frac{\sqrt{3}}{2}y',-\frac{\sqrt{3}}{2}x'-\frac{1}{2}y',z'\right) \\ f_z\left(-\frac{1}{2}x'+\frac{\sqrt{3}}{2}y',-\frac{\sqrt{3}}{2}x'-\frac{1}{2}y',z'\right) \end{pmatrix}$
C_{2x}	$\begin{pmatrix} f_x(x',-y',-z') \\ -f_y(x',-y',-z') \\ -f_z(x',-y',-z') \end{pmatrix}$
C_{2A}	$\begin{pmatrix} -\frac{1}{2}f_x\left(-\frac{1}{2}x'+\frac{\sqrt{3}}{2}y',\frac{\sqrt{3}}{2}x'+\frac{1}{2}y',-z'\right)+\frac{\sqrt{3}}{2}f_y\left(-\frac{1}{2}x'+\frac{\sqrt{3}}{2}y',\frac{\sqrt{3}}{2}x'+\frac{1}{2}y',-z'\right) \\ \frac{\sqrt{3}}{2}f_x\left(-\frac{1}{2}x'+\frac{\sqrt{3}}{2}y',\frac{\sqrt{3}}{2}x'+\frac{1}{2}y',-z'\right)+\frac{1}{2}f_y\left(-\frac{1}{2}x'+\frac{\sqrt{3}}{2}y',\frac{\sqrt{3}}{2}x'+\frac{1}{2}y',-z'\right) \\ -f_z\left(-\frac{1}{2}x'+\frac{\sqrt{3}}{2}y',\frac{\sqrt{3}}{2}x'+\frac{1}{2}y',-z'\right) \end{pmatrix}$
C_{2B}	$\begin{pmatrix} -\frac{1}{2}f_x\left(-\frac{1}{2}x'-\frac{\sqrt{3}}{2}y',-\frac{\sqrt{3}}{2}x'+\frac{1}{2}y',-z'\right)-\frac{\sqrt{3}}{2}f_y\left(-\frac{1}{2}x'-\frac{\sqrt{3}}{2}y',-\frac{\sqrt{3}}{2}x'+\frac{1}{2}y',-z'\right) \\ -\frac{\sqrt{3}}{2}f_x\left(-\frac{1}{2}x'-\frac{\sqrt{3}}{2}y',-\frac{\sqrt{3}}{2}x'+\frac{1}{2}y',-z'\right)+\frac{1}{2}f_y\left(-\frac{1}{2}x'-\frac{\sqrt{3}}{2}y',-\frac{\sqrt{3}}{2}x'+\frac{1}{2}y',-z'\right) \\ -f_z\left(-\frac{1}{2}x'-\frac{\sqrt{3}}{2}y',-\frac{\sqrt{3}}{2}x'+\frac{1}{2}y',-z'\right) \end{pmatrix}$

Table 4.4   Transformation operators of symmetry group D_3.

The character projection operator method is a systematic way of assigning the characteristic modes to the irreducible representations. In contrast to the manual assignment, the characteristic surface current densities do not even need to be visualized. It can thus be implemented as a fully automatic postprocessing without user interference directly following the modal analysis.

4.2 Degenerate Modes

In the previous section, it was shown that the assignment of the characteristic modes to the irreducible representations of a symmetry group can be conducted based on the characters alone. It was found, however, that multi-dimensional representations bring some peculiarities with them. It is thus time to shed some more light on degenerate modes.
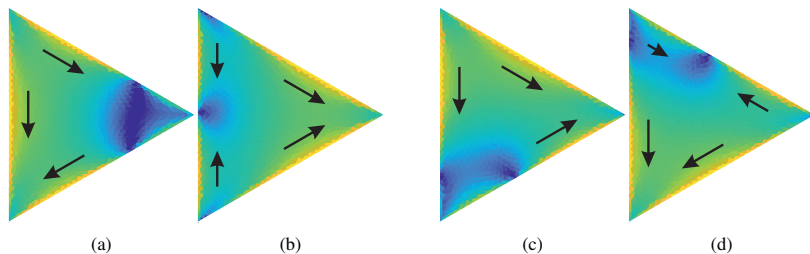
Figure 4.4   Normalized characteristic surface current densities of equilateral triangular PEC plate with circum-radius $R_u = 0.6$ wavelengths as basis functions of the two-dimensional third irreducible representation to the same eigenvalue. Principal current directions denoted by arrows. Color bar in Fig. 2.6(e). (a) $\mathbf{J}_2$ resulting from the modal analysis. (b) $\mathbf{J}_3$ resulting from the modal analysis. (c) Linear combination $\mathbf{J}_2 + \mathbf{J}_3$. (d) Orthogonal partner function of $\mathbf{J}_2 + \mathbf{J}_3$.

To a d-fold degenerate eigenvalue there belongs a set of d linearly independent eigenfunctions (characteristic surface current densities) [80].[48] Naturally, this degeneracy is due to the symmetry of the underlying PEC object[49] and the set of characteristic surface current densities can be assigned to a d-dimensional irreducible representation [58].

However, the set of characteristic surface current densities is not unique as any linear combination of d eigenfunctions is again an eigenfunction to the same eigenvalue [80]. As an example, the sum $\mathbf{J}_2 + \mathbf{J}_3$ of the characteristic surface current densities $\mathbf{J}_2$ (Fig. 4.4(a)) and $\mathbf{J}_3$ (Fig. 4.4(b)) is considered.[50] The resulting surface current density is shown in Fig. 4.4(c). It can be easily checked by means of the character projection operator method (4.1) that this constructed characteristic surface current density, too, is a basis function of the third irreducible representation. It is neither orthogonal to $\mathbf{J}_2$ nor to $\mathbf{J}_3$, though an orthogonal partner function can be constructed by means of the procedure described at the end of section 3.5.4: A linearly independent function is found, for instance, by applying the rotation C_{3z}. Then, the Gram-Schmidt orthogonalization process (appendix B.1) is used to construct the orthogonal partner function, which is shown in Fig. 4.4(d).

---

[48]The eigenfunctions are not necessarily orthogonal, though an orthogonal set can always be found, as explained in appendix C.2.

[49]According to [76], an "accidental" degeneracy, i.e., a degeneracy which is not due to symmetry, is "expected to occur only rarely".

[50]Of course, $\mathbf{J}_2 + \mathbf{J}_3$ does not radiate unit power. For this brief example, a normalization is not necessary.

The arbitrariness of the eigenfunctions is mirrored by the fact that the representation matrices are only unique up to a similarity transformation. It has already been shown in section 3.5.4 that different sets of orthogonal basis functions transform according to different sets of representation matrices. However, to one fixed set of representation matrices there belongs one fixed set of orthogonal basis functions (characteristic surface current densities). This means that, if a set of representation matrices is known, a fixed orthogonal basis belonging to this set of representation matrices can be constructed using the projection operator method (section 3.5.1).

4.2.1 Construction of Representation Matrices

It is now purposeful to construct a set of representation matrices. For the method introduced in section 3.5.4, a set of orthogonal basis functions is required.

As the characteristic surface current densities computed in section 4.1 are basis functions of the irreducible representations, the mode pairs 2-3, 4-5, 7-8, 10-11, and 14-15 could be used to compute a set of representation matrices of the two-dimensional third irreducible representation numerically. However, this approach has several drawbacks based on the following observations:

- Different mode pairs (i.e., belonging to different eigenvalues and thus having different mode indices n) in general yield different sets of representation matrices as they do not necessarily transform according to the same set of representation matrices. As a matter of fact, this is the case in Fig. 4.3, which will become clear in subsection 4.2.2.

- The same mode pair computed with different mesh densities does not necessarily transform according to the same set of representation matrices. An example is shown in Fig. 4.5, where the two mode pairs obviously cannot transform according to the same set of representation matrices.[51]

- The computation is based on numerical results and is thus not exact.

As already hinted at, there is a lot of arbitrariness when working with degenerate modes. However, a fixed set of representation matrices is able to eliminate this arbitrariness as all mode pairs can then be constructed to transform according to this set of matrices. The question arises how such a set of matrices can be found if the computed characteristic surface current densities are not adequate.

---

[51]This is quickly checked by applying the rotation C_{2x}.

(a)   (b)   (c)   (d)
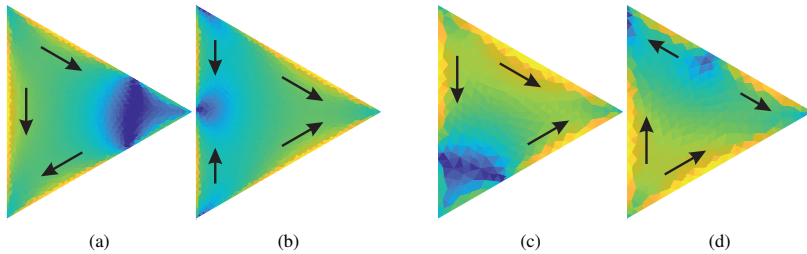
Figure 4.5   Impact of different mesh densities on degenerate characteristic surface current densities of equilateral triangular PEC plate with circumradius $R_u = 0.6$ wavelengths. Principal current directions denoted by arrows. Color bar in Fig. 2.6(e). (a) $\mathbf{J}_2$ computed using a mesh consisting of 2202 triangles. (b) $\mathbf{J}_3$ computed using a mesh consisting of 2202 triangles. (c) $\mathbf{J}_2$ computed using a mesh consisting of 618 triangles. (d) $\mathbf{J}_3$ computed using a mesh consisting of 618 triangles. Both mesh densities are chosen such that the symmetry is reproduced properly and the mesh criterion given in section 2.3.4 is fulfilled.

As a matter of fact, any set of basis functions belonging to the third irreducible representation is suitable for this task. It is thus purposeful to choose a set of functions as simple as possible. Having a closer look at modes 2 and 3, the characteristic surface current density of mode 3 (Fig. 4.5(b)) seems to be invariant under the rotation C_{2x} by 180° about the x-axis, whereas the characteristic surface current density of mode 2 (Fig. 4.5(a)) seems to be inverted by this operation.[52] It is thus a good idea to start with a pair of simple functions possessing these symmetry properties.

The scalar function $\psi_1^{(3)}(x',y') = x'$ defined on an equilateral triangular domain with $y' \in \left[\frac{1}{\sqrt{3}}x' - \frac{a}{3}, -\frac{1}{\sqrt{3}}x' + \frac{a}{3}\right]$[53] and $x' \in \left[-R_i, R_u\right]$[54] as shown in Fig. 4.6(a) is invariant under the rotation C_{2x}. Correspondingly, and rather intuitively, the scalar function $\psi_2^{(3)}(x',y') = y'$ defined on the same domain as shown in Fig. 4.6(b) is inverted by this operation. These two functions are thus proposed as suitable candidates to be basis functions of the two-dimensional irreducible representation $\Gamma^{(3)}$. As demonstrated in appendix D.1, the two proposed functions are orthogonal, which is a necessary condition to

---

[52] A close inspection reveals that this is not exactly true (cf. Fig. 4.8(a)), but approximately in order to serve as motivation. Similar statements may be found for the other degenerate mode pairs with respect to other axes, e.g., mode pair 14-15 (Fig. 4.3(n) and (o)) with respect to the axis B.

[53] $-\frac{1}{\sqrt{3}}x' + \frac{a}{3}$ and $\frac{1}{\sqrt{3}}x' - \frac{a}{3}$ describe the upper and the lower edge, respectively, of the equilateral triangular plate as linear functions of x', see Fig. 4.1(a).

[54] The function has to be square-integrable as the inner product needs to be computed (see appendix B). The function must thus be confined to the triangular domain.
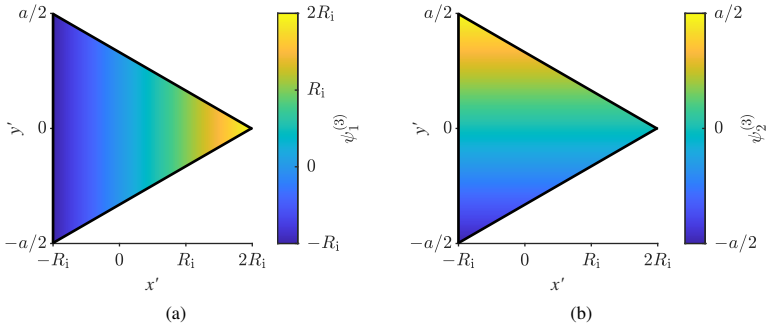
Figure 4.6 Pair of scalar basis functions of two-dimensional third irreducible representation $\Gamma^{(3)}$ of symmetry group D_3. (a) $\psi_1^{(3)}(x',y') = x'$. (b) $\psi_2^{(3)}(x',y') = y'$.

form a basis. That the two functions indeed belong to the third irreducible representation is now checked analytically by means of the character projection operator method.[55] The application of the character projection operators (4.1) to $\psi_1^{(3)}$ yields

$$
\begin{aligned}
\mathcal{P}^{(1)}x' &= \frac{1}{6}\left(x' - \frac{1}{2}x' - \frac{\sqrt{3}}{2}y' - \frac{1}{2}x' + \frac{\sqrt{3}}{2}y' \right.\\
&\left. + x' - \frac{1}{2}x' + \frac{\sqrt{3}}{2}y' - \frac{1}{2}x' - \frac{\sqrt{3}}{2}y'\right) = 0,\\
\mathcal{P}^{(2)}x' &= \frac{1}{6}\left(x' - \frac{1}{2}x' - \frac{\sqrt{3}}{2}y' - \frac{1}{2}x' + \frac{\sqrt{3}}{2}y' \right.\\
&\left. - x' + \frac{1}{2}x' - \frac{\sqrt{3}}{2}y' + \frac{1}{2}x' + \frac{\sqrt{3}}{2}y'\right) = 0,\\
\mathcal{P}^{(3)}x' &= \frac{1}{3}\left(2x' + \frac{1}{2}x' + \frac{\sqrt{3}}{2}y' + \frac{1}{2}x' - \frac{\sqrt{3}}{2}y'\right) = x'.
\end{aligned}
$$

The application to $\psi_2^{(3)}$ yields

$$
\begin{aligned}
\mathcal{P}^{(1)}y' &= \frac{1}{6}\left(y' + \frac{\sqrt{3}}{2}x' - \frac{1}{2}y' - \frac{\sqrt{3}}{2}x' - \frac{1}{2}y' \right.\\
&\left. - y' + \frac{\sqrt{3}}{2}x' + \frac{1}{2}y' - \frac{\sqrt{3}}{2}x' + \frac{1}{2}y'\right) = 0,
\end{aligned}
$$

[55]The required scalar transformation operators are given in Table D.1.

D_3	E	C_{3z}	C_{3z}^2
$\Gamma^{(3)}$	$\begin{pmatrix} 1 & 0 \\ 0 & 1 \end{pmatrix}$	$\begin{pmatrix} -1/2 & \sqrt{3}/2 \\ -\sqrt{3}/2 & -1/2 \end{pmatrix}$	$\begin{pmatrix} -1/2 & -\sqrt{3}/2 \\ \sqrt{3}/2 & -1/2 \end{pmatrix}$

D_3	C_{2x}	C_{2A}	C_{2B}
$\Gamma^{(3)}$	$\begin{pmatrix} 1 & 0 \\ 0 & -1 \end{pmatrix}$	$\begin{pmatrix} -1/2 & \sqrt{3}/2 \\ \sqrt{3}/2 & 1/2 \end{pmatrix}$	$\begin{pmatrix} -1/2 & -\sqrt{3}/2 \\ -\sqrt{3}/2 & 1/2 \end{pmatrix}$

Table 4.5   Representation matrices of the two-dimensional third irreducible representation $\Gamma^{(3)}$ of symmetry group D_3 computed with scalar basis functions $\psi_1^{(3)}(x',y') = x'$ and $\psi_2^{(3)}(x',y') = y'$. © 2021 IEEE [PHM21].

$$
\mathcal{P}^{(2)}y' = \frac{1}{6}\Big(y' + \frac{\sqrt{3}}{2}x' - \frac{1}{2}y' - \frac{\sqrt{3}}{2}x' - \frac{1}{2}y'
$$
$$
+ y' - \frac{\sqrt{3}}{2}x' - \frac{1}{2}y' + \frac{\sqrt{3}}{2}x' - \frac{1}{2}y'\Big) = 0,
$$
$$
\mathcal{P}^{(3)}y' = \frac{1}{3}\Big(2y' - \frac{\sqrt{3}}{2}x' + \frac{1}{2}y' + \frac{\sqrt{3}}{2}x' + \frac{1}{2}y'\Big) = y'.
$$

Consequently, a pair of basis functions of the two-dimensional third irreducible representation of the symmetry group D_3 is now available. In order to compute the corresponding representation matrices, the method presented in section 3.5.4 is employed. The detailed computation is given in appendix D.1. The resulting representation matrices are listed in Table 4.5. It is highlighted that all computations are performed analytically so that the results are exact.

It is observed that the representation matrices of D_3 are more complicated than those of D_4 (Table 3.6). The transformation of the characteristic surface current densities belonging to the third irreducible representation of the equilateral triangular plate is thus not as illustrative as in the case of the square plate. This explains why the manual assignment of the characteristic modes to the irreducible representations as discussed in section 4.1 is in general not purposeful when dealing with degenerate modes and the automatic assignment using character projection operators is the better choice.

Nevertheless, the representation matrix corresponding to the rotation C_{2x} of D_3 is straightforward to interpret. In fact, it exactly represents the observations discussed when introducing the scalar basis functions and thus validates the above-made choice. The same argument can basically be employed if there are more multi-dimensional irreducible representations. Alternatively, or additionally, suitable scalar basis functions can be found in the literature, e.g., [77, 78], which is recommended in more complicated cases (see section 4.5.2).

4.2.2 Construction of Unique Basis

Now that a set of representation matrices is known, a unique basis of the third irreducible representation $\Gamma^{(3)}$ of D_3 can be constructed out of an arbitrary function by means of the projection operators introduced in section 3.5.1. In the context of characteristic modes, this means that out of an arbitrary degenerate characteristic surface current density belonging to a certain eigenvalue a pair of unique characteristic surface current densities belonging to the same eigenvalue can be generated. This pair forms a fixed basis, i.e., its symmetry properties are always the same. This corresponds to the fact that the pair transforms according to a fixed set of representation matrices.

In order to illustrate this, the sum $\mathbf{J}_2 + \mathbf{J}_3$ of the characteristic surface current densities $\mathbf{J}_2$ (Fig. 4.4(a)) and $\mathbf{J}_3$ (Fig. 4.4(b)) as shown in Fig. 4.7(a) is considered again. As this is a degenerate characteristic surface current density transforming according to an unknown set of representation matrices, the projection operator method is now applied to construct a unique pair of characteristic surface current densities transforming according to the representation matrices in Table 4.5.

In order to generate the characteristic surface current density belonging to the first row of $\Gamma^{(3)}$, the projection operator $\mathcal{P}_{11}^{(3)}$ according to (3.49) is used:

$$\mathcal{P}_{11}^{(3)} = \frac{1}{3}\left(P(E) - \frac{1}{2}P(C_{3z}) - \frac{1}{2}P(C_{3z}^2) + P(C_{2x}) - \frac{1}{2}P(C_{2A}) - \frac{1}{2}P(C_{2B})\right). \quad (4.2)$$

Alternatively, the projection operator $\mathcal{P}_{12}^{(3)}$ may be used:

$$\mathcal{P}_{12}^{(3)} = \frac{1}{3}\left(\frac{\sqrt{3}}{2}P(C_{3z}) - \frac{\sqrt{3}}{2}P(C_{3z}^2) + \frac{\sqrt{3}}{2}P(C_{2A}) - \frac{\sqrt{3}}{2}P(C_{2B})\right). \quad (4.3)$$

Both operators have the same row index $\mu = 1$ and thus produce a basis function belonging to the first row, as explained in section 3.5.1. As any degenerate characteristic surface current density is always a linear combination of the basis functions to be generated, both operators yield the same result and can be used in an equivalent manner.

By applying either $\mathcal{P}_{11}^{(3)}$ or $\mathcal{P}_{12}^{(3)}$ to the characteristic surface current density shown in Fig. 4.7(a), the projected characteristic surface current density shown in Fig. 4.7(b) is generated. In particular, this characteristic surface current density is invariant under the rotation C_{2x} about the x-axis, which is reminiscent of the basis functions employed in subsection 4.2.1 to construct the representation matrices. This is a distinctive property of the basis functions transforming according to this set of representation matrices.
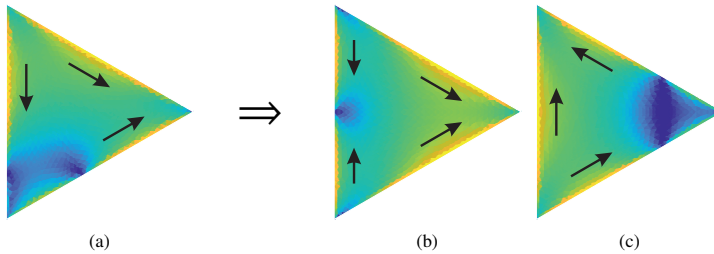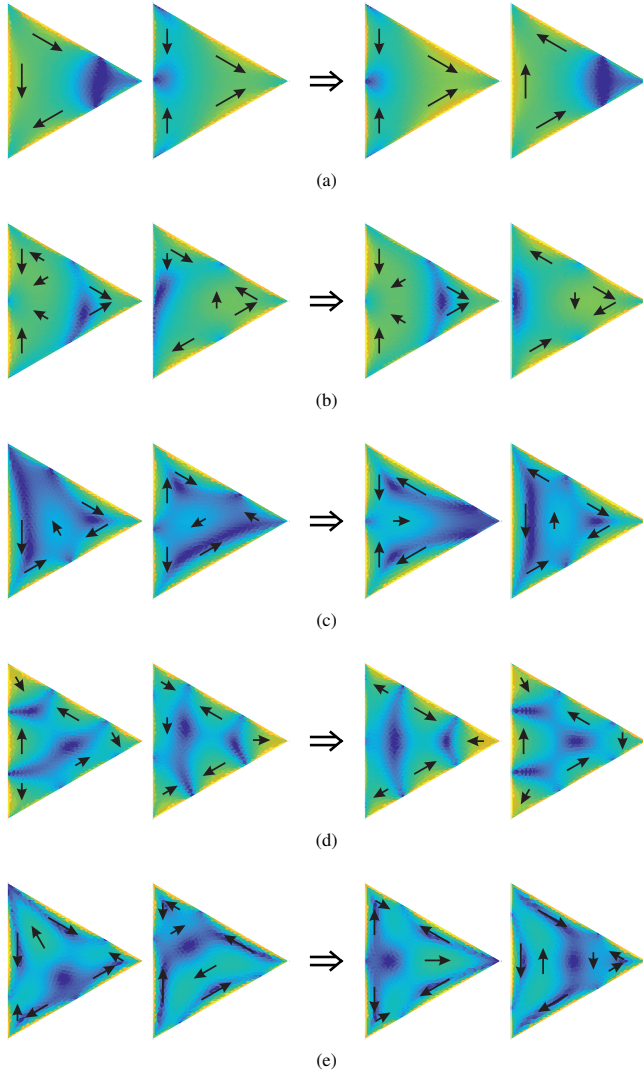
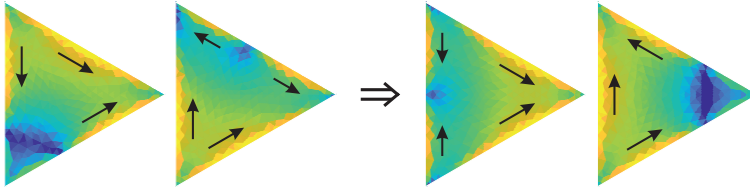Figure 4.7 Application of projection operators to degenerate characteristic surface current density of equilateral triangular PEC plate with circumradius $R_u = 0.6$ wavelengths. Principal current directions denoted by arrows. Color bar in Fig. 2.6(e). (a) Given degenerate characteristic surface current density $(\mathbf{J}_2 + \mathbf{J}_3)$ belonging to $\Gamma^{(3)}$. (b) Projected characteristic surface current density belonging to the first row of $\Gamma^{(3)}$ by applying either $\mathcal{P}_{11}^{(3)}$ or $\mathcal{P}_{12}^{(3)}$. (c) Projected characteristic surface current density belonging to the second row of $\Gamma^{(3)}$ by applying either $\mathcal{P}_{21}^{(3)}$ or $\mathcal{P}_{22}^{(3)}$.

In order to generate the characteristic surface current density belonging to the second row of $\Gamma^{(3)}$, the projection operator $\mathcal{P}_{21}^{(3)}$ according to (3.49) is used:

$$\mathcal{P}_{21}^{(3)} = \frac{1}{3}\left(-\frac{\sqrt{3}}{2}P(C_{3z}) + \frac{\sqrt{3}}{2}P(C_{3z}^2) + \frac{\sqrt{3}}{2}P(C_{2A}) - \frac{\sqrt{3}}{2}P(C_{2B})\right). \quad (4.4)$$

Alternatively, the projection operator $\mathcal{P}_{22}^{(3)}$ may be used:

$$\mathcal{P}_{22}^{(3)} = \frac{1}{3}\left(P(E) - \frac{1}{2}P(C_{3z}) - \frac{1}{2}P(C_{3z}^2) - P(C_{2x}) + \frac{1}{2}P(C_{2A}) + \frac{1}{2}P(C_{2B})\right). \quad (4.5)$$

Again, both operators can be used equivalently.

By applying either $\mathcal{P}_{21}^{(3)}$ or $\mathcal{P}_{22}^{(3)}$ to the characteristic surface current density shown in Fig. 4.7(a), the projected characteristic surface current density shown in Fig. 4.7(c) is generated. As a distinctive property, this characteristic surface current density is inverted by the rotation C_{2x}.

The projection operator method constructs out of an arbitrary degenerate characteristic surface current density a unique basis of characteristic surface current densities. It is now possible to resolve all modal degeneracies resulting from the modal analysis performed in section 4.1 by constructing unique pairs of degenerate characteristic surface current densities. To do so, the projection operators $\mathcal{P}_{11}^{(3)}$ and $\mathcal{P}_{21}^{(3)}$[56] are applied to the first characteristic surface current

---

[56] Again, $\mathcal{P}_{12}^{(3)}$ and $\mathcal{P}_{22}^{(3)}$ may be used alternatively.

Figure 4.8 Projection of degenerate characteristic surface current densities of equilateral triangular PEC plate with circumradius $R_u = 0.6$ wavelengths using the representation matrices from Table 4.5. Principal current directions denoted by arrows. Color bar in Fig. 2.6(e). (a) Mode pair 2-3. (b) Mode pair 4-5. (c) Mode pair 7-8. (d) Mode pair 10-11. (e) Mode pair 14-15.

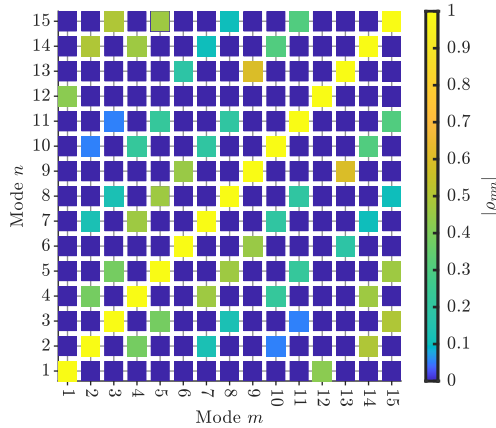Figure 4.9   Projection of a pair of degenerate characteristic surface current densities of equilateral triangular PEC plate with circumradius $R_u = 0.6$ wavelengths computed using a mesh consisting of 618 triangles. Principal current directions denoted by arrows. Color bar in Fig. 2.6(e).

density of each mode pair, i.e., mode 2, mode 4, mode 7, mode 10, and mode 14.[57] The resulting projected characteristic surface current densities together with the original characteristic surface current densities are shown in Fig. 4.8.

Obviously, there are more or less pronounced changes from the original characteristic surface current densities to the projected ones. In particular, the distinctive feature of all projected characteristic surface current densities is again that the one belonging to the first row is invariant under the rotation C_{2x}, whereas its partner function is inverted by this operation. This allows a more intuitive interpretation of the characteristic surface current densities[58] and underlines the fact that they all belong to the same irreducible representation, even re-enabling the manual assignment.

As a last example, and in order to emphasize that the symmetry analysis is independent of the mesh density, the characteristic surface current density shown in Fig. 4.5(c) computed using a mesh consisting of 618 triangles is considered again. Applying the projection operators yields the projected characteristic surface current densities shown in Fig. 4.9, which have the same shape as those in Fig. 4.7(b) and (c) computed with a higher mesh density.

By means of the projection operator method, modal degeneracies can be resolved in a systematic way. As demonstrated in subsection 4.2.1, the required representation matrices can be constructed purposefully.[59] This way, any arbitrariness due to degenerate modes is eliminated. In particular, the projection

---

[57] The second characteristic surface current density of each pair could be used as well. The important fact is that a set of degenerate modes is characterized by exactly one mode as all its partners can be generated by means of the projection operators (see section 3.5.1).

[58] For example, the modes 2 and 3 may be interpreted as orthogonally polarized "dipole modes".

[59] Representation matrices are usually not given in the literature, apart from some examples. As a rare case, representation matrices of the crystallographic point groups are listed in [75]. However, some care must be taken with respect to the employed coordinate system when using them.

operator method can be combined with the automatic assignment of modes introduced in section 4.1.1. In the same processing run, the characteristic modes are assigned to the irreducible representations by means of the character projection operators and, in the case of multi-dimensional representations, unique degenerate characteristic surface current densities are constructed by means of the projection operators. This procedure can be implemented as a fully automatic postprocessing without user interference.

4.3 Orthogonality and Fundamental Modes

Having completed the assignment of the characteristic modes to the irreducible representations, it is legitimate to ask how this can be made use of in the process of multimode antenna design. The answer lies in the orthogonality of basis functions (section 3.3.3). Applied to characteristic modes, the orthogonality theorem states that characteristic surface current densities belonging to

- different irreducible representations,

- different rows of the same multi-dimensional irreducible representation

are orthogonal to each other. Thus, with the assignment of characteristic modes to the irreducible representations, mutually orthogonal sets of characteristic surface current densities are found. Based on the observations made in section 2.4, the idea is to excite these mutually orthogonal sets separately.

The modal analysis of the equilateral triangular PEC plate carried out in section 4.1 has yielded 15 characteristic modes to be taken into account. However, there are only two one-dimensional and one two-dimensional irreducible representations. Therefore, four mutually orthogonal sets of characteristic surface current densities are expected. This is confirmed by computing the characteristic current correlation coefficients (2.51), which are depicted in Fig. 4.10. The mutually orthogonal sets are also listed in Table 4.6 together with the assignment to the irreducible representations.[60] Obviously, it does not matter how many characteristic modes are taken into account. The number of mutually orthogonal sets of characteristic surface current densities is always governed by the symmetry group of the underlying PEC object.

---

[60]In contrast to Table 4.3, the rows of the two-dimensional third irreducible representation are listed separately. This distinction is enabled by resolving the modal degeneracies as done in section 4.2.

Figure 4.10   Characteristic current correlation coefficients of equilateral triangular PEC plate with circumradius $R_\mathrm{u} = 0.6$ wavelengths computed using (2.51). © 2021 IEEE [PHM21].

Set	Repr.	Mode n
1	$\Gamma^{(1)}$	1; 12
2	$\Gamma^{(2)}$	6; 9; 13
3	$\Gamma_1^{(3)}$	2; 4; 7; 10; 14
4	$\Gamma_2^{(3)}$	3; 5; 8; 11; 15

Table 4.6   Mutually orthogonal sets of characteristic surface current densities of equilateral triangular PEC plate and assignment to irreducible representations of symmetry group D_3.

Characteristic surface current densities belonging to the same set are correlated and can in general not be excited separately. It is thus sufficient to consider only one mode per set. According to section 2.4, this one mode should be significant so that it can potentially be excited effectively. In Fig. 2.4, it is shown that the modal significance is a function of frequency. In more general terms, it depends on the electrical size of the PEC object. The electrical size of the equilateral triangular plate is characterized by the electrical circumradius $k R_\mathrm{u}$, where k is the angular wavenumber, which is equivalent to the radius of the minimum circumscribed circle (Fig. 4.1(a)).[61]

---

[61] The electrical size of the equilateral triangular plate with the arbitrarily chosen circumradius $R_\mathrm{u} = 0.6$ wavelengths is thus $k R_\mathrm{u} = 2\pi \cdot 0.6 \approx 3.77$.
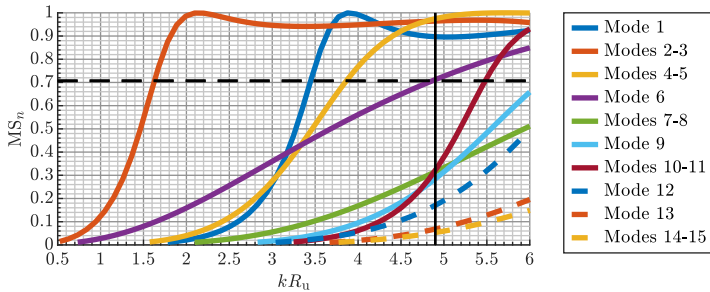
Figure 4.11   Modal significances of equilateral triangular PEC plate as functions of electrical size kR_u. At $kR_u = 4.9$, all four fundamental characteristic modes (1, 6, 2, and 3) are significant. The modes are sorted according to their significance at $kR_u = 3.77$ ($R_u \approx 0.6$ wavelengths).

The modal significances of the 15 characteristic modes identified in section 4.1 are shown in Fig. 4.11 as functions of the electrical size of the equilateral triangular PEC plate. With increasing electrical size more modes become significant. Mode 1 is the first mode belonging to the first irreducible representation $\Gamma^{(1)}$ to become significant. Likewise, mode 6 is the first mode belonging to the second irreducible representation $\Gamma^{(2)}$ to become significant. The mode pair 2-3 is the first degenerate set of modes belonging to the third irreducible representation $\Gamma^{(3)}$ to become significant.[62]

Henceforth, those characteristic modes belonging to a certain irreducible representation that first become significant as functions of the electrical size (frequency) are called the fundamental modes of this irreducible representation. Accordingly, mode 1 is the fundamental mode of $\Gamma^{(1)}$, mode 6 is the fundamental mode of $\Gamma^{(2)}$, and modes 2 and 3 are the fundamental modes of $\Gamma^{(3)}$. The remaining modes are called higher-order modes. As these modes are correlated to the fundamental modes, they do not yield additional information for multimode antenna design. It is thus sufficient to work only with the fundamental modes.

This finding provides a means to determine the minimum electrical size so that all fundamental modes are significant, i.e., for each irreducible representation (orthogonal set) there is at least one significant mode available. This would allow to maximally exploit the orthogonality provided by the symmetry of the underlying PEC object. In the case of the equilateral triangular plate, Fig. 4.11 reveals

---

[62]Degenerate mode pairs have the same eigenvalue (modal significance) independent of the electrical size as the degeneracy is due to symmetry.

that mode 6 is the last fundamental mode to become significant at $kR_\mathrm{u} \approx 4.9$. This is hence the minimum electrical size so that all four fundamental modes are significant. However, the other fundamental modes become significant at considerably smaller electrical sizes. There may thus be some tradeoff between the electrical size, the modal significance of the fundamental modes, and the number of mutually orthogonal sets of characteristic surface current densities. This tradeoff will be discussed in more detail in chapter 5.

4.4 Symmetric Excitation of Characteristic Modes

In the previous section, it has been shown that a symmetric antenna geometry offers a limited number of mutually orthogonal sets of characteristic surface current densities. In section 2.4, it was demonstrated that such sets may be excited separately in order to realize orthogonal antenna ports. The aim of this section is to systematically design orthogonal antenna ports by exploiting the symmetry properties of characteristic modes.

The excitation due to an antenna port is represented by the impressed electric field strength $\mathbf{E}_\mathrm{i}$. Its coupling to a characteristic surface current density is described by the modal excitation coefficient $V_{\mathrm{i},n}$ (2.24). As a matter of fact, the modal excitation coefficient is an inner product between the n-th characteristic surface current density and the impressed electric field strength.

The orthogonality of the characteristic surface current densities is due to the orthogonality theorem (3.27), which is an inner product between basis functions of the irreducible representations. The goal is that the impressed electric field strength of one antenna port only couples to characteristic surface current densities belonging to one orthogonal set. It thus suggests itself to design the impressed electric field strength to act as a basis function of an irreducible representation. In this case, the modal excitation coefficient is governed by the orthogonality theorem and the impressed electric field strength only excites those modes which belong to the same irreducible representation or the same row of a multi-dimensional irreducible representation.

An antenna port which is supposed to act as a basis function of an irreducible representation must fulfill certain symmetry requirements. Therefore, it generally consists of several feed points which have to be driven simultaneously.[63] These

---

[63] A feed network is required in order to distribute the input signal at the antenna port to the feed points on the antenna surface with the correct amplitude and phase relations. The feed network design will be discussed in chapter 6.

(a) Port 1   (b) Port 2   (c) Port 3   (d) Port 4
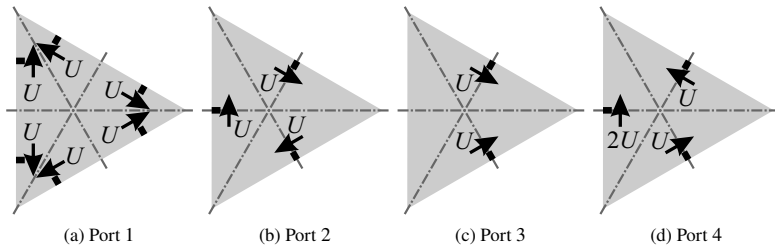
Figure 4.12 Port configuration on equilateral triangular PEC plate consisting of delta-gap sources at feed points. Positions of feed points denoted by black lines. Source voltages denoted by U. Relative voltage directions denoted by arrows. (a)–(d) Ports 1 to 4. © 2021 IEEE [PHM21].

feed points will be implemented as delta-gap sources (section 2.3.3) throughout the remaining sections of this chapter.[64]

In order to illustrate this concept, the triangular PEC plate is considered once again. Its symmetry group D_3 offers four mutually orthogonal sets of characteristic surface current densities. It is thus deduced that four orthogonal antenna ports can be realized.

An antenna port acting as a basis function of the first irreducible representation $\Gamma^{(1)}$ must be invariant under all symmetry operations of D_3. Inspired by the characteristic surface current density of the fundamental mode 1 (Fig. 4.3(a)), the port configuration shown in Fig. 4.12(a) is found. It consists of six feed points placed at the half-edge centers and driven with the same source voltage U. It is easily checked that this port configuration is invariant under all symmetry operations of the equilateral triangular plate.

In the same way, a port configuration for the second irreducible representation $\Gamma^{(2)}$ is found by inspecting the characteristic surface current density of the fundamental mode 6 (Fig. 4.3(f)). The antenna port shown in Fig. 4.12(b) consists of three feed points placed at the edge centers in a circular arrangement. This port configuration is invariant under the rotations about the z-axis, but inverted under the other rotations, as required.

However, such a straightforward argument cannot be given for the two-dimensional third irreducible representation $\Gamma^{(3)}$. The port configurations shown in Fig. 4.12(c) and (d) are in fact derived by means of the method presented in subsection 4.4.1. They transform according to the representation matrices in

---

[64]Practical excitation elements replacing the ideal delta-gap sources will be discussed in section 6.1.
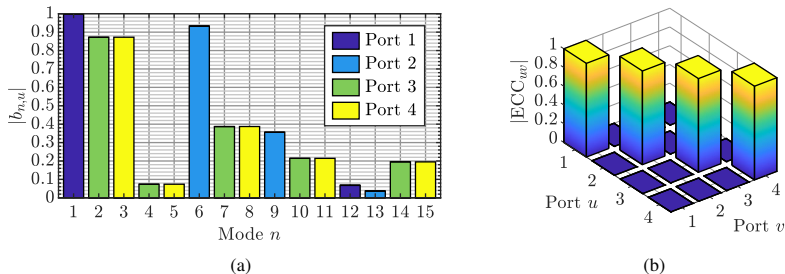
Figure 4.13   Excitation parameters of equilateral triangular PEC plate with circumradius R_u = 0.6 wavelengths and port configuration according to Fig. 4.12. (a) Normalized modal weighting coefficients. (b) Envelope correlation coefficients. © 2021 IEEE [PHM21].

Table 4.5. As a distinctive property, port 3 (Fig. 4.12(c)) is invariant under the rotation C_{2x} about the x-axis, whereas port 4 (Fig. 4.12(d)) is inverted by this operation. However, the other transformations are difficult to check manually. In particular, port 4 even has a feed point with double the source voltage of the other feed points, which is hard to find intuitively. All in all, the ports 3 and 4 cannot be derived in a straightforward way like the ports 1 and 2, which is the motivation for the port generation method presented in subsection 4.4.1.

Nevertheless, the antenna ports shown in Fig. 4.12 excite mutually orthogonal sets of characteristic modes, as evidenced by the normalized modal weighting coefficients in Fig. 4.13(a). In particular, the excited sets are exactly the sets given in Table 4.6, as intended. Consequently, the antenna ports are orthogonal, which is confirmed by the envelope correlation coefficients in Fig. 4.13(b). Obviously, implementing symmetric excitations which act as basis functions of the irreducible representations is a purposeful way to realize orthogonal antenna ports. Based on this approach, a systematic method for generating orthogonal antenna ports is introduced in the following subsection.

4.4.1 Systematic Port Generation

It has become apparent in the previous paragraphs that a general and systematic port generation procedure is required. This is where the projection operators come into play again. According to section 3.5.1, basis functions can be constructed out of an arbitrary function by employing the appropriate projection operators.

Applied to the port generation problem, it is possible to project out of an arbitrarily chosen initial port configuration the desired orthogonal ports.

This method is best demonstrated by means of an example. The configurations of the ports 3 and 4 in Fig. 4.12(c) and (d), respectively, are found to be difficult to derive intuitively. Now, a single delta-gap source is considered. It is placed arbitrarily at $x' = -R_i, y' = 0$ pointing in positive y-direction, as shown in Fig. 4.14(a). The corresponding impressed electric field strength $\mathbf{E}_{i,1}$ can be expressed analytically (section 2.3.3):[65]

$$\mathbf{E}_{i,1}(x',y') = U\delta(x' + R_i,y') \begin{pmatrix} 0 \\ 1 \end{pmatrix}. \tag{4.6}$$

In order to obtain a basis function belonging to the first row of the third irreducible representation, the projection operator $\mathcal{P}_{12}^{(3)}$ (4.3) with $p = 3$, $\mu = 1$ is applied to this initial impressed electric field strength:

$$\mathcal{P}_{12}^{(3)}\mathbf{E}_{i,1}(x',y') = \frac{U}{\sqrt{3}}\left(\delta\left(x' - \frac{1}{2}R_i,y' - \frac{\sqrt{3}}{2}R_i\right)\begin{pmatrix} \sqrt{3}/2 \\ -1/2 \end{pmatrix}\right.$$
$$\left. + \delta\left(x' - \frac{1}{2}R_i,y' + \frac{\sqrt{3}}{2}R_i\right)\begin{pmatrix} \sqrt{3}/2 \\ 1/2 \end{pmatrix}\right), \tag{4.7}$$

resulting in the port configuration of port 3 as shown in Fig. 4.14(b). In order to obtain a basis function belonging to the second row of the third irreducible representation, the projection operator $\mathcal{P}_{22}^{(3)}$ (4.5) with $p = 3$, $\mu = 2$ is applied to the initial impressed electric field strength:

$$\mathcal{P}_{22}^{(3)}\mathbf{E}_{i,1}(x',y') = \frac{U}{3}\left(2\delta(x' + R_i,y')\begin{pmatrix} 0 \\ 1 \end{pmatrix}\right.$$
$$+ \delta\left(x' - \frac{1}{2}R_i,y' - \frac{\sqrt{3}}{2}R_i\right)\begin{pmatrix} -\sqrt{3}/2 \\ 1/2 \end{pmatrix}$$
$$\left. + \delta\left(x' - \frac{1}{2}R_i,y' + \frac{\sqrt{3}}{2}R_i\right)\begin{pmatrix} \sqrt{3}/2 \\ 1/2 \end{pmatrix}\right), \tag{4.8}$$

resulting in the port configuration of port 4 as shown in Fig. 4.14(c). The common factors $\frac{U}{\sqrt{3}}$ in (4.7) and $\frac{U}{3}$ in (4.8) can be discarded in the implementation as they do not affect the orthogonality of the ports.

---

[65] For the sake of conciseness, neither the z-dependence of the Dirac delta function nor the z-component of the vector are displayed. As the problem is planar in the xy-plane, there is no loss of information.
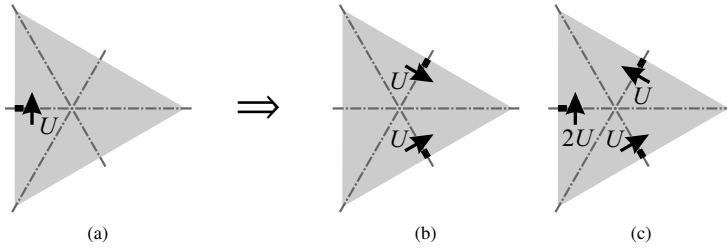
Figure 4.14 Construction of orthogonal ports on equilateral triangular PEC plate belonging to the two-dimensional third irreducible representation $\Gamma^{(3)}$ of symmetry group D_3. (a) Initial port configuration consisting of one delta-gap source at $x' = -R_i, y' = 0$. (b) Port 3 belonging to the first row constructed with projection operator $\mathcal{P}_{12}^{(3)}$. (c) Port 4 belonging to the second row constructed with projection operator $\mathcal{P}_{22}^{(3)}$.
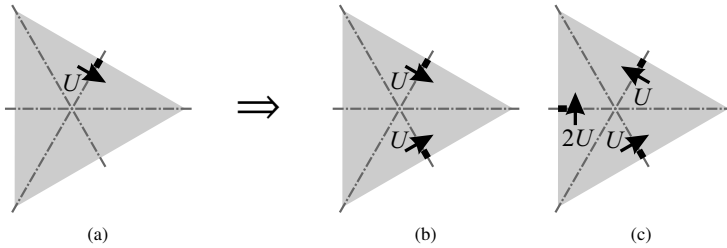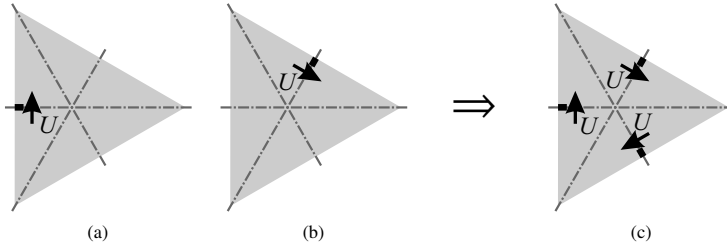

Figure 4.15 Construction of orthogonal ports on equilateral triangular PEC plate belonging to the two-dimensional third irreducible representation $\Gamma^{(3)}$ of symmetry group D_3. (a) Alternative initial port configuration consisting of one delta-gap source at $x' = R_i/2, y' = \sqrt{3}R_i/2$. (b) Port 3 belonging to the first row constructed with projection operator $\mathcal{P}_{11}^{(3)}$ or $\mathcal{P}_{12}^{(3)}$. (c) Port 4 belonging to the second row constructed with projection operator $\mathcal{P}_{21}^{(3)}$ or $\mathcal{P}_{22}^{(3)}$. © 2021 IEEE [PHM21].

The projection operator method is obviously suitable for constructing orthogonal antenna ports. However, some care must be taken when choosing the initial port configuration. In this special case, the application of $\mathcal{P}_{11}^{(3)}$ and $\mathcal{P}_{21}^{(3)}$ yields

$$\mathcal{P}_{11}^{(3)}\mathbf{E}_{i,1}(x',y') = \mathbf{0}, \qquad \mathcal{P}_{21}^{(3)}\mathbf{E}_{i,1}(x',y') = \mathbf{0}. \tag{4.9}$$

This is due to the fact that the chosen initial impressed electric field strength does not contain any part belonging to the first row ($\nu = 1$) of the third irreducible representation ($p = 3$). In fact, it can be expressed as a linear combination of the ports 2 (Fig. 4.12(b)) and 4 (Fig. 4.12(d)) alone.[66] According to (3.50), the

---

[66]This can be quickly checked by adding (4.11) and (4.8), yielding (4.6).

projection with $\nu = 1$ yields zero as port 2 belongs to the second irreducible representation ($q = 2 \neq p$) and port 4 belongs to the second row of the third irreducible representation ($q = 3 = p$, but $\kappa = 2 \neq \nu$). Although at first glance this may be confusing, the important fact is that, if at least one set of projection operators yields a result unequal to zero, this result is a suitable port configuration.

This fact is underlined by considering an alternative initial port configuration. The initial impressed electric field strength $\mathbf{E}_{i,2}$ is now chosen to be

$$\mathbf{E}_{i,2}(x',y') = U\delta\big(x' - \tfrac{1}{2}R_i, y' - \tfrac{\sqrt{3}}{2}R_i\big)\begin{pmatrix}\sqrt{3}/2\\-1/2\end{pmatrix}, \qquad (4.10)$$

as shown in Fig. 4.15(a). Applying either $\mathcal{P}_{11}^{(3)}$ or $\mathcal{P}_{12}^{(3)}$ yields the port configuration of port 3 as shown in Fig. 4.15(b). Applying either $\mathcal{P}_{21}^{(3)}$ or $\mathcal{P}_{22}^{(3)}$ yields the port configuration of port 4 as shown in Fig. 4.15(c). In this case, both pairs of projection operators can be used equivalently.

The projection operator method is not only suitable for the multi-dimensional irreducible representations. In fact, it can be used to generate all orthogonal ports offered by a symmetric antenna. For the second irreducible representation, the projection operator $\mathcal{P}^{(2)}$ can be applied to either $\mathbf{E}_{i,1}$ or $\mathbf{E}_{i,2}$:

$$\begin{aligned}
\mathcal{P}^{(2)}\mathbf{E}_{i,1}(x',y') &= \mathcal{P}^{(2)}\mathbf{E}_{i,2}(x',y')\\
&= \frac{U}{3}\Big(\delta\big(x' + R_i, y'\big)\begin{pmatrix}0\\1\end{pmatrix}\\
&\quad + \delta\big(x' - \tfrac{1}{2}R_i, y' - \tfrac{\sqrt{3}}{2}R_i\big)\begin{pmatrix}\sqrt{3}/2\\-1/2\end{pmatrix}\\
&\quad + \delta\big(x' - \tfrac{1}{2}R_i, y' + \tfrac{\sqrt{3}}{2}R_i\big)\begin{pmatrix}-\sqrt{3}/2\\-1/2\end{pmatrix}\Big), \qquad (4.11)
\end{aligned}$$

yielding the port configuration of port 2 as shown in Fig. 4.16.

In the case of the first irreducible representation, the application of $\mathcal{P}^{(1)}$ to either $\mathbf{E}_{i,1}$ or $\mathbf{E}_{i,2}$ yields

$$\mathcal{P}^{(1)}\mathbf{E}_{i,1}(x',y') = \mathbf{0}, \qquad \mathcal{P}^{(1)}\mathbf{E}_{i,2}(x',y') = \mathbf{0}. \qquad (4.12)$$

Obviously, both initial port configurations are not suitable to construct a port belonging to the first irreducible representation. This result is, however, not surprising as a basis function belonging to this irreducible representation must be invariant under all symmetry operations and can thus not contain the given
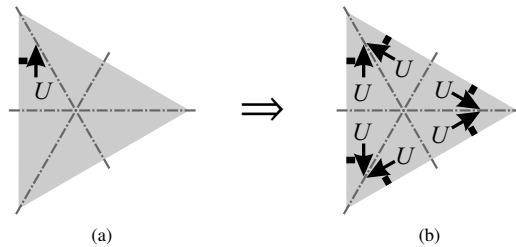
Figure 4.16   Construction of orthogonal port on equilateral triangular PEC plate belonging to the second irreducible representation $\Gamma^{(2)}$ of symmetry group D_3. (a) Initial port configuration consisting of one delta-gap source at $x' = -R_i, y' = 0$. (b) Alternative initial port configuration consisting of one delta-gap source at $x' = R_i/2, y' = \sqrt{3}R_i/2$. (c) Port 2 belonging to $\Gamma^{(2)}$ constructed with projection operator $\mathcal{P}^{(2)}$. © 2021 IEEE [PHM21].

delta-gap sources on an edge center, i.e., a symmetry axis. Instead, the initial delta-gap source is now shifted to $x' = -R_i, y' = \frac{a}{4} = \frac{\sqrt{3}}{2}R_i$:

$$\mathbf{E}_{i,3}(x',y') = U\delta\left(x' + R_i, y' - \frac{\sqrt{3}}{2}R_i\right)\begin{pmatrix}0\\1\end{pmatrix}, \qquad (4.13)$$

as shown in Fig. 4.17(a). Applying $\mathcal{P}^{(1)}$ to this electric field strength yields

$$\begin{aligned}
\mathcal{P}^{(1)}\mathbf{E}_{i,3}(x',y') = \frac{U}{6}\Bigg(&\delta\left(x' + R_i, y' - \frac{\sqrt{3}}{2}R_i\right)\begin{pmatrix}0\\1\end{pmatrix} \\
&+ \delta\left(x' + \frac{1}{4}R_i, y' - \frac{3\sqrt{3}}{4}R_i\right)\begin{pmatrix}-\sqrt{3}/2\\1/2\end{pmatrix} \\
&+ \delta\left(x' - \frac{5}{4}R_i, y' - \frac{\sqrt{3}}{4}R_i\right)\begin{pmatrix}\sqrt{3}/2\\-1/2\end{pmatrix} \\
&+ \delta\left(x' - \frac{5}{4}R_i, y' + \frac{\sqrt{3}}{4}R_i\right)\begin{pmatrix}\sqrt{3}/2\\1/2\end{pmatrix} \\
&+ \delta\left(x' + \frac{1}{4}R_i, y' + \frac{3\sqrt{3}}{4}R_i\right)\begin{pmatrix}-\sqrt{3}/2\\-1/2\end{pmatrix} \\
&+ \delta\left(x' + R_i, y' + \frac{\sqrt{3}}{2}R_i\right)\begin{pmatrix}0\\-1\end{pmatrix}\Bigg), \qquad (4.14)
\end{aligned}$$

i.e., the port configuration of port 1 as shown in Fig. 4.17(b). It should be noted that the other ports could be generated with this initial delta-gap source as well.

Figure 4.17 Construction of orthogonal port on equilateral triangular PEC plate belonging to the first irreducible representation $\Gamma^{(1)}$ of symmetry group D_3. (a) Initial port configuration consisting of one delta-gap source at $x' = -R_i, y' = a/4$. (b) Port 1 belonging to $\Gamma^{(1)}$ constructed with projection operator $\mathcal{P}^{(1)}$. © 2021 IEEE [PHM21].

In this case, however, they would also consist of six feed points, i.e., more than necessary. Throughout this thesis, orthogonal antenna ports are considered optimal if they consist of as few feed points as possible.[67] For this reason, only port 1 is generated this way.

All four orthogonal antenna ports offered by the equilateral triangular plate can be generated systematically by means of the projection operator method. The examples above have shown that its success depends to some degree on the choice of the initial impressed electric field strength. However, the two choices made above, i.e., placement of a delta-gap source at an edge center (Fig. 4.14(a)) and placement of a delta-gap source at a half-edge center (Fig. 4.17(a)), are certainly the most intuitive ones and already yield the optimal port configurations. That these choices are not only suitable for the equilateral triangular plate, but applicable to a wide range of geometries, will become clear in section 4.5. Therefore, the following general guideline is proposed: A single delta-gap source placed on a symmetry axis should be used as the initial port configuration. Those ports which cannot be generated with this setup are subsequently constructed from the alternative initial port configuration consisting of a single delta-gap source placed half-way between two symmetry axes.

Finally, it should be emphasized that the results obtained above have all been computed analytically (and checked numerically). The systematic port generation based on projection operators is independent of any modal analysis. It solely depends on the symmetry of the underlying PEC object. *A priori*

---

[67]This criterion is motivated by the fact that the complexity of the corresponding feed networks generally grows with an increasing number of feed points (cf. section 6.2).

knowledge about the number of orthogonal antenna ports and how to implement them is thus gained from the symmetry analysis of a potential antenna geometry without even conducting a modal analysis.

4.4.2 Upper Bound for Realizing Orthogonal Antenna Ports

The number of orthogonal antenna ports that can be realized on a symmetric antenna geometry is limited. It is governed by the number and the dimensions of the irreducible representations of the symmetry group of an antenna. In other words, there is an upper bound for realizing orthogonal antenna ports.

The maximum number of orthogonal antenna ports is achieved if they are designed as basis functions of the irreducible representations, as illustrated above. In this case, each port couples to exactly one orthogonal set of characteristic surface current densities (Fig. 4.13(a)).

An arbitrary port configuration can be expressed as a linear combination of the optimal orthogonal port configurations.[68] Such a port configuration thus couples to more than one orthogonal set of characteristic surface current densities so that the upper bound cannot be reached anymore.
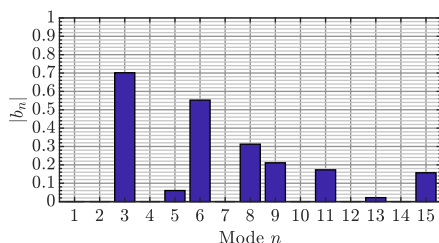
Figure 4.18   Normalized modal weighting coefficients of equilateral triangular PEC plate with circumradius $R_u = 0.6$ wavelengths and port configuration according to Fig. 4.14(a).

As an example, the port configuration in Fig. 4.14(a) with the impressed electric field strength $\mathbf{E}_{i,1}$ (4.6) is considered. The normalized modal weighting coefficients due to this excitation are shown in Fig. 4.18. Those characteristic modes which are originally excited by either port 2 (Fig. 4.12(b)) or port 4 (Fig. 4.12(d)) are now excited together (cf. Fig. 4.13(a)). This is due to the fact that the chosen excitation is a linear combination of port 2 and

---

[68] An arbitrary function can be expressed as a linear combination of basis functions [75].

Antenna geometry	Symmetry group	No. of irreducible representations			No. of ortho. ports
		1-D	2-D	3-D	
Rectangular plate	D_2	4	0	0	4
Rectangular pyramid	C_{2v}	4	0	0	4
Equilateral triangular plate	D_3	2	1	0	4
Regular triangular pyramid	C_{3v}	2	1	0	4
Square plate	D_4	4	1	0	6
Square pyramid	C_{4v}	4	1	0	6
Regular hexagonal plate	D_6	4	2	0	8
Regular hexagonal pyramid	C_{6v}	4	2	0	8
Rectangular cuboid	D_{2h}	8	0	0	8
Regular triangular prism	D_{3h}	4	2	0	8
Regular tetrahedron	T_d	2	1	2	10
Square cuboid	D_{4h}	8	2	0	12
Regular hexagonal prism	D_{6h}	8	4	0	16
Cube	O_h	4	2	4	20

Table 4.7 Symmetry group, number of irreducible representations, and number of feasible orthogonal antenna ports for different symmetric antenna geometries. © 2019 IEEE [PM19b].

port 4 (see subsection 4.4.1). One degree of freedom is thus lost and only three orthogonal antenna ports may be realized yet.

The equilateral triangular plate with the symmetry group D_3 offers four orthogonal antenna ports as there are two one-dimensional and one two-dimensional irreducible representations. The square plate with symmetry group D_4 used as an example throughout chapter 3 has four one-dimensional and one two-dimensional irreducible representations, offering six mutually orthogonal sets of characteristic surface current densities and thus six orthogonal antenna ports. This simple calculation can be generalized to any symmetric antenna geometry. All information that is needed, i.e., the number and the dimensions of the irreducible representations, can be derived from the character tables, which are readily available in the literature. Based on this, an exemplary list of antenna geometries with their respective symmetry groups, numbers of irreducible representations, and numbers of feasible orthogonal antenna ports is given in Table 4.7. As a general guideline, geometries with high symmetry order, i.e., whose symmetry groups have a lot of irreducible representations or irreducible representations of higher dimension, offer a large number of

mutually orthogonal sets of characteristic surface current densities and thus a large number of orthogonal antenna ports.

The number of feasible orthogonal antenna ports is dictated by the symmetry group of an antenna, i.e., it is known *a priori*. A suitable antenna geometry can thus be chosen depending on the desired number of orthogonal antenna ports. Furthermore, suitable orthogonal port configurations can be computed with the projection operator method introduced in subsection 4.4.1.[69] Still, a modal analysis needs to be conducted in order to find an appropriate electrical size so that the fundamental characteristic modes are significant (section 4.3). How this can be done systematically is discussed in chapter 5.

4.5 Examples and Applications

At the end of this chapter, symmetry analyses of exemplary symmetric antenna geometries are conducted using the methods introduced in this chapter in order to illustrate the general procedure and hint at possible applications.

4.5.1 Square Plate

The square PEC plate as shown in Fig. 3.4 is chosen as the first example. Its symmetry group is D_4, which was thoroughly analyzed throughout chapter 3. The symmetry group D_4 has four one-dimensional and one two-dimensional irreducible representations, whose representation matrices are given in Table 3.6. It is thus predicted that there are six mutually orthogonal sets of characteristic surface current densities. Therefore, six orthogonal antenna ports are expected to be feasible. This will now be demonstrated by first conducting a modal analysis in order to identify the fundamental modes and a suitable antenna size, and then generating the six orthogonal antenna ports.

Repr.	$\Gamma^{(1)}$	$\Gamma^{(2)}$	$\Gamma^{(3)}$	$\Gamma^{(4)}$	$\Gamma_1^{(5)}$	$\Gamma_2^{(5)}$
Mode n	6, 12	5, 15, 17	4, 11	3, 16, 18	1, 7, 9, 13, 19	2, 8, 10, 14, 20
Port u	1	2	3	4	5	6

Table 4.8   Assignment of characteristic modes and orthogonal antenna ports of square PEC plate to irreducible representations of symmetry group D_4. © 2019 IEEE [PM19b].

---

[69]If the required representation matrices are not available, they can be computed using the method presented in section 4.2.1.
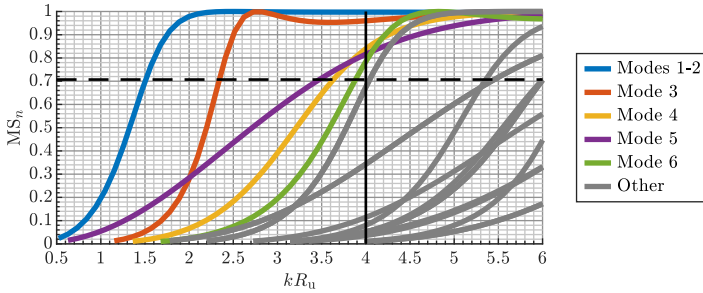
Figure 4.19 Modal significances of square PEC plate as functions of electrical size kR_u. Fundamental characteristic modes in color, higher-order modes in gray. At $kR_u = 4$, all six fundamental modes are significant. The modes are sorted according to their significance at $kR_u = 4$.
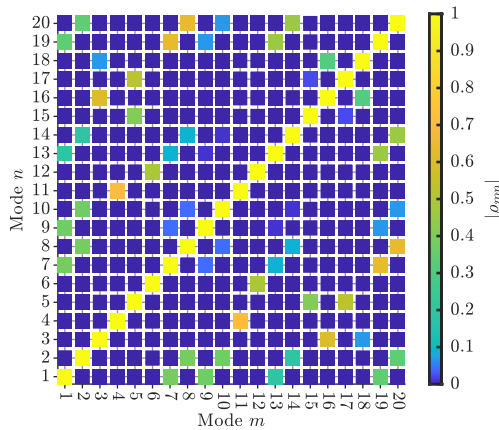
Figure 4.20 Characteristic current correlation coefficients of square PEC plate with electrical size $kR_u = 4$ computed using (2.51). © 2019 IEEE [PM19b].

The modal significances of the first 20 characteristic modes as functions of the electrical size kR_u are shown in Fig. 4.19.[70] The modes are sorted according to their significance at $kR_u = 4$, where all six fundamental modes are significant. The assignment of all 20 modes to the irreducible representations is listed in Table 4.8. The assignment is conducted using the methods introduced

---

[70] A square is completely determined by its edge length a (Fig. 3.4). The circumradius is $R_u = \frac{a}{\sqrt{2}}$.
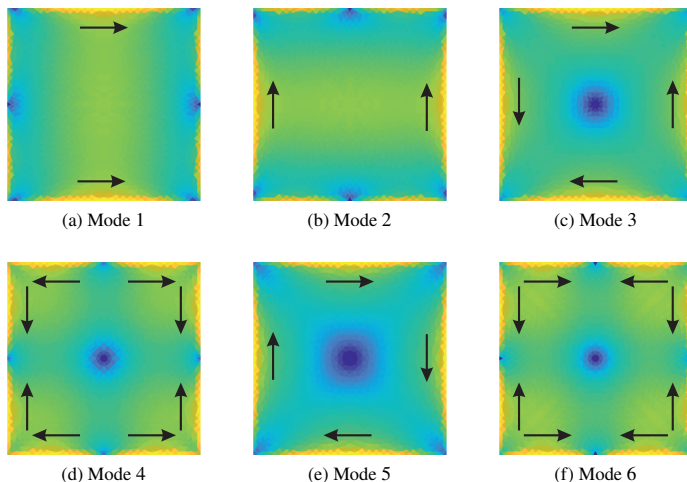
Figure 4.21   Normalized surface current densities of fundamental characteristic modes of square PEC plate with electrical size $kR_u = 4$. Principal current directions denoted by arrows. Modes sorted according to their significance. Color bar in Fig. 2.6(e). (a) Mode 1 belonging to the first row of $\Gamma^{(5)}$. (b) Mode 2 belonging to the second row of $\Gamma^{(5)}$. (c) Mode 3 belonging to $\Gamma^{(4)}$. (d) Mode 4 belonging to $\Gamma^{(3)}$. (e) Mode 5 belonging to $\Gamma^{(2)}$. (f) Mode 6 belonging to $\Gamma^{(1)}$. © 2019 IEEE [PM19b].

in section 4.1. The degenerate modes belonging to the two-dimensional fifth irreducible representation are resolved using the methods presented in section 4.2. The resulting orthogonality of the characteristic surface current densities is confirmed by the characteristic current correlation coefficients shown in Fig. 4.20.

The characteristic surface current densities of the fundamental modes are depicted in Fig. 4.21. Modes 1 and 2 (Fig. 4.21(a) and (b)) are the fundamental modes of the two-dimensional fifth irreducible representation $\Gamma^{(5)}$. Their surface current densities are reminiscent of orthogonally polarized dipole currents ("dipole modes"), where the surface current density of mode 1 is mainly oriented in *x*-direction, whereas that of mode 2 is mainly oriented in *y*-direction. Mode 3 (Fig. 4.21(c)) is the fundamental mode of $\Gamma^{(4)}$, mode 4 (Fig. 4.21(d)) is the fundamental mode of $\Gamma^{(3)}$. Both modes can be interpreted as "quadrupole modes". They are, however, not degenerate. Mode 5 (Fig. 4.21(e)) is the fundamental mode of $\Gamma^{(2)}$. It is reminiscent of a current loop ("loop mode"). Mode 6 (Fig. 4.21(f)), finally, is the fundamental mode of $\Gamma^{(1)}$. It is invariant under all symmetry operations of D_4 ("invariant mode").
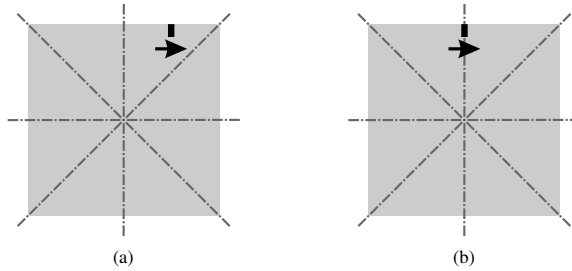
Figure 4.22 Initial port configurations for generating orthogonal antenna ports on square PEC plate. (a) Port configuration consisting of one delta-gap source at a half-edge center for generating ports 1 and 3. (b) Port configuration consisting of one delta-gap source at an edge center for generating ports 2, 4, 5, and 6. © 2021 IEEE [PHM21].

Based on the modal analysis, the fundamental modes have been identified and a suitable antenna size has been found. Now, the corresponding antenna ports are generated by means of the method presented in section 4.4.1. First of all, suitable initial port configurations need to be found. The modes 4 (Fig. 4.21(d)) and 6 (Fig. 4.21(f)) have current nulls at the edge centers and current maxima at the half-edge centers. Inspired by this, the initial port configuration shown in Fig. 4.22(a) consisting of one delta-gap source at a half-edge center is chosen for generating the ports for these two modes. The modes 1 (Fig. 4.21(a)), 2 (Fig. 4.21(b)), 3 (Fig. 4.21(c)), and 5 (Fig. 4.21(e)) have current maxima at the edge centers. Correspondingly, the initial port configuration shown in Fig. 4.22(b) consisting of one delta-gap source at an edge center is chosen for generating the ports for these four modes.

The resulting antenna ports are depicted in Fig. 4.23. They are labeled according to the irreducible representations in Table 4.8. Port 1 belonging to $\Gamma^{(1)}$ (Fig. 4.23(a)) and port 3 belonging to $\Gamma^{(3)}$ (Fig. 4.23(c)) are generated by means of the initial port configuration in Fig. 4.22(a). Both ports consist of eight feed points distributed symmetrically at the half-edge centers. Port 2 belonging to $\Gamma^{(2)}$ (Fig. 4.23(b)), port 4 belonging to $\Gamma^{(4)}$ (Fig. 4.23(d)), port 5 belonging to the first row of $\Gamma^{(5)}$ (Fig. 4.23(e)), and port 6 belonging to the second row of $\Gamma^{(5)}$ (Fig. 4.23(f)) are generated by means of the initial port configuration in Fig. 4.22(b). Ports 2 and 4 each consist of four feed points at the edge centers. Ports 5 and 6 each consist of two feed points at opposite edge centers.

The feed points of each antenna port must be driven simultaneously. The arrows in Fig. 4.23 denote the relative voltage directions which are necessary at

(a) Port 1   (b) Port 2   (c) Port 3

(d) Port 4   (e) Port 5   (f) Port 6
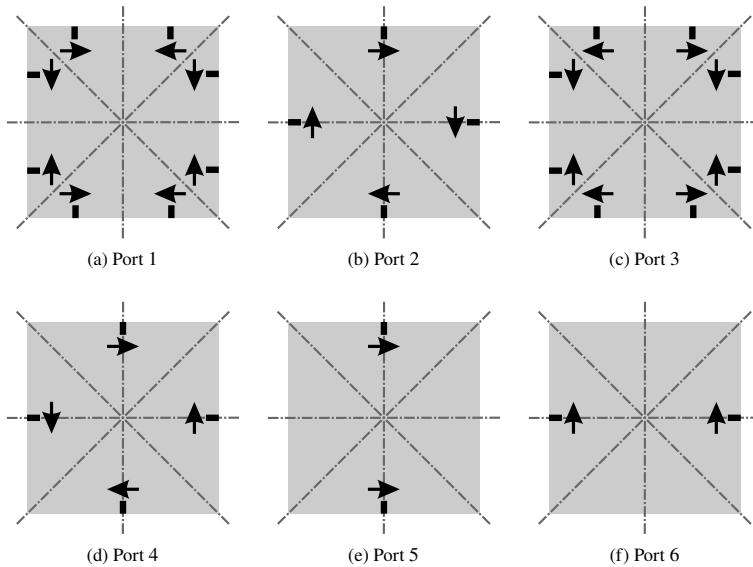
Figure 4.23   Orthogonal antenna ports on square PEC plate consisting of symmetrically distributed, simultaneously driven feed points. Positions of feed points denoted by black lines. Relative voltage directions denoted by arrows. All feed points are driven with the same source voltage. (a)–(f) Ports 1 to 6. © 2021 IEEE [PHM21].

the feed points in order to fulfill the symmetry requirements of the irreducible representations. In contrast to the equilateral triangular plate, all feed points on the square plate are driven with the same voltage.

By examining the normalized modal weighting coefficients in Fig. 4.24(a), it is confirmed that each generated antenna port excites exactly one orthogonal set of characteristic surface current densities (cf. Table 4.8). Some higher-order modes are also excited to a considerable degree. This does not affect the orthogonality of the ports as each orthogonal set is excited purely. Consequently, the antenna ports are orthogonal, as evidenced by the envelope correlation coefficients in Fig. 4.24(b). As all modes are excited to some extent, there is no further degree of freedom to realize a seventh orthogonal antenna port.

Based on the square plate, it is obviously possible to design a six-port multimode antenna. The comparatively simple square plate is thus a promising geometry in order to realize a multimode antenna with more antenna ports than reported so far in the literature.
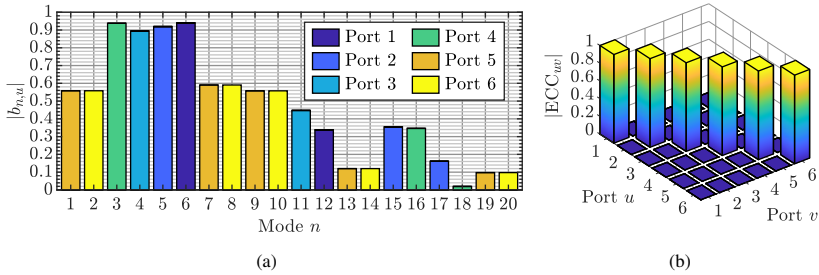
Figure 4.24 Excitation parameters of square PEC plate with electrical size $kR_u = 4$ and port configuration according to Fig. 4.23. (a) Normalized modal weighting coefficients. (b) Envelope correlation coefficients. © 2019 IEEE [PM19b].

4.5.2 Regular Hexagonal Plate

The equilateral triangular PEC plate offers four orthogonal antenna ports, the square PEC plate offers six orthogonal antenna ports. Both objects are regular polygonal plates. Towards even more orthogonal antenna ports, polygonal plates of higher order should be examined. Therefore, a more complex representative of the regular polygonal plates, the regular hexagonal plate, is now analyzed.
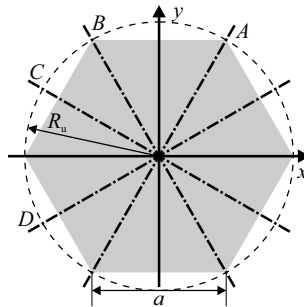
Figure 4.25 Regular hexagonal plate in xy-plane with coordinate system, symmetry axes, and circumscribed circle. © 2019 IEEE [PM19a].

The symmetry group of a regular hexagonal plate as shown in Fig. 4.25 is D_6 [78]. This symmetry group consists of twelve symmetry operations ($g = 12$), which are listed in Table 4.9. The corresponding character table is given

Symmetry operation	Symbol	Symmetry operation	Symbol
Identity	E	Rotation by 180° about the x-axis	C_{2x}
Rotation by 120° about the z-axis	C_{3z}	Rotation by 180° about the axis A	C_{2A}
Rotation by −120° about the z-axis	C_{3z}^{-1}	Rotation by 180° about the axis B	C_{2B}
Rotation by 180° about the z-axis	C_{2z}	Rotation by 180° about the y-axis	C_{2y}
Rotation by 60° about the z-axis	C_{6z}	Rotation by 180° about the axis C	C_{2C}
Rotation by −60° about the z-axis	C_{6z}^{-1}	Rotation by 180° about the axis D	C_{2D}

Table 4.9   The twelve elements of symmetry group D_6.

D_6	E	C_{3z}	C_{3z}^{-1}	C_{2z}	C_{6z}	C_{6z}^{-1}
$\Gamma^{(1)}$	1	1	1	1	1	1
$\Gamma^{(2)}$	1	1	1	1	1	1
$\Gamma^{(3)}$	1	1	1	−1	−1	−1
$\Gamma^{(4)}$	1	1	1	−1	−1	−1
$\Gamma^{(5)}$	2	−1	−1	−2	1	1
$\Gamma^{(6)}$	2	−1	−1	2	−1	−1

D_6	C_{2x}	C_{2A}	C_{2B}	C_{2y}	C_{2C}	C_{2D}
$\Gamma^{(1)}$	1	1	1	1	1	1
$\Gamma^{(2)}$	−1	−1	−1	−1	−1	−1
$\Gamma^{(3)}$	−1	−1	−1	1	1	1
$\Gamma^{(4)}$	1	1	1	−1	−1	−1
$\Gamma^{(5)}$	0	0	0	0	0	0
$\Gamma^{(6)}$	0	0	0	0	0	0

Table 4.10   Character table of symmetry group D_6. © 2019 IEEE [PM19a].

in Table 4.10 [78]. There are four one-dimensional irreducible representations $\Gamma^{(1;2;3;4)}$ and two two-dimensional irreducible representations $\Gamma^{(5;6)}$. Therefore, eight mutually orthogonal sets of characteristic surface current densities and thus eight orthogonal antenna ports are predicted.

The representation matrices of the two-dimensional irreducible representations $\Gamma^{(5)}$ and $\Gamma^{(6)}$ are computed with the method presented in section 4.2.1. The required scalar basis functions are taken from [78]. For $\Gamma^{(5)}$, the already familiar basis functions $\psi_1^{(5)}(x',y') = x'$ and $\psi_2^{(5)}(x',y') = y'$ are used. For $\Gamma^{(6)}$, the more complex functions $\psi_1^{(6)}(x',y') = x'(y'^3 - 3y'x'^2)$ and $\psi_2^{(6)}(x',y') = y'(y'^3 - 3y'x'^2)$ are employed. The resulting representation

D_6	E	C_{3z}	C_{3z}^{-1}
$\Gamma^{(5)}$	$\begin{pmatrix} 1 & 0 \\ 0 & 1 \end{pmatrix}$	$\begin{pmatrix} -1/2 & \sqrt{3}/2 \\ -\sqrt{3}/2 & -1/2 \end{pmatrix}$	$\begin{pmatrix} -1/2 & -\sqrt{3}/2 \\ \sqrt{3}/2 & -1/2 \end{pmatrix}$
$\Gamma^{(6)}$	$\begin{pmatrix} 1 & 0 \\ 0 & 1 \end{pmatrix}$	$\begin{pmatrix} -1/2 & \sqrt{3}/2 \\ -\sqrt{3}/2 & -1/2 \end{pmatrix}$	$\begin{pmatrix} -1/2 & -\sqrt{3}/2 \\ \sqrt{3}/2 & -1/2 \end{pmatrix}$

D_6	C_{2z}	C_{6z}	C_{6z}^{-1}
$\Gamma^{(5)}$	$\begin{pmatrix} -1 & 0 \\ 0 & -1 \end{pmatrix}$	$\begin{pmatrix} 1/2 & \sqrt{3}/2 \\ -\sqrt{3}/2 & 1/2 \end{pmatrix}$	$\begin{pmatrix} 1/2 & -\sqrt{3}/2 \\ \sqrt{3}/2 & 1/2 \end{pmatrix}$
$\Gamma^{(6)}$	$\begin{pmatrix} 1 & 0 \\ 0 & 1 \end{pmatrix}$	$\begin{pmatrix} -1/2 & -\sqrt{3}/2 \\ \sqrt{3}/2 & -1/2 \end{pmatrix}$	$\begin{pmatrix} -1/2 & \sqrt{3}/2 \\ -\sqrt{3}/2 & -1/2 \end{pmatrix}$

D_6	C_{2x}	C_{2A}	C_{2B}
$\Gamma^{(5)}$	$\begin{pmatrix} 1 & 0 \\ 0 & -1 \end{pmatrix}$	$\begin{pmatrix} -1/2 & \sqrt{3}/2 \\ \sqrt{3}/2 & 1/2 \end{pmatrix}$	$\begin{pmatrix} -1/2 & -\sqrt{3}/2 \\ -\sqrt{3}/2 & 1/2 \end{pmatrix}$
$\Gamma^{(6)}$	$\begin{pmatrix} -1 & 0 \\ 0 & 1 \end{pmatrix}$	$\begin{pmatrix} 1/2 & -\sqrt{3}/2 \\ -\sqrt{3}/2 & -1/2 \end{pmatrix}$	$\begin{pmatrix} 1/2 & \sqrt{3}/2 \\ \sqrt{3}/2 & -1/2 \end{pmatrix}$

D_6	C_{2y}	C_{2C}	C_{2D}
$\Gamma^{(5)}$	$\begin{pmatrix} -1 & 0 \\ 0 & 1 \end{pmatrix}$	$\begin{pmatrix} 1/2 & -\sqrt{3}/2 \\ -\sqrt{3}/2 & -1/2 \end{pmatrix}$	$\begin{pmatrix} 1/2 & \sqrt{3}/2 \\ \sqrt{3}/2 & -1/2 \end{pmatrix}$
$\Gamma^{(6)}$	$\begin{pmatrix} -1 & 0 \\ 0 & 1 \end{pmatrix}$	$\begin{pmatrix} 1/2 & -\sqrt{3}/2 \\ -\sqrt{3}/2 & -1/2 \end{pmatrix}$	$\begin{pmatrix} 1/2 & \sqrt{3}/2 \\ \sqrt{3}/2 & -1/2 \end{pmatrix}$

Table 4.11   Representation matrices of the two-dimensional irreducible representations $\Gamma^{(5)}$ and $\Gamma^{(6)}$ of symmetry group D_6 computed with the scalar basis functions $\psi_1^{(5)}(x',y') = x'$ and $\psi_2^{(5)}(x',y') = y'$ as well as $\psi_1^{(6)}(x',y') = x'(y'^3 - 3y'x'^2)$ and $\psi_2^{(6)}(x',y') = y'(y'^3 - 3y'x'^2)$. © 2019 IEEE [PM19a].

matrices are listed in Table 4.11. Similar to the symmetry group D_3 (Table 4.5), the representation matrices are difficult to interpret intuitively, highlighting once again the importance of the automatic port generation and modal assignment methods introduced in this chapter.

Having available all necessary information about the symmetry group D_6, the *a priori* knowledge gained from the symmetry analysis can now be made use of. As explained in section 4.4, orthogonal antenna ports can be constructed based on the symmetry analysis alone without conducting a modal analysis. For the port generation method introduced in section 4.4.1, initial port configurations are needed. Two regular polygonal plates (equilateral triangular plate, square plate) have already been analyzed. In both cases, a delta-gap source at a half-edge center as well as a delta-gap source at an edge center have proved to be suitable

(a)   (b)
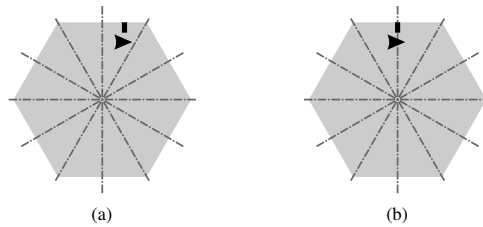
Figure 4.26   Initial port configurations for generating orthogonal antenna ports on regular hexagonal PEC plate. (a) Port configuration consisting of one delta-gap source at a half-edge center for generating ports 1 and 3. (b) Port configuration consisting of one delta-gap source at an edge center for generating ports 2, 4, 5, 6, 7, and 8. © 2021 IEEE [PHM21].

Repr.	$\Gamma^{(1)}$	$\Gamma^{(2)}$	$\Gamma^{(3)}$	$\Gamma^{(4)}$	$\Gamma_1^{(5)}$	$\Gamma_2^{(5)}$	$\Gamma_1^{(6)}$	$\Gamma_2^{(6)}$
Port u	1	2	3	4	5	6	7	8
Mode n	7, 20	6, 17	8, 18	5, 19	1, 9, 13	2, 10, 14	3, 11, 15	4, 12, 16

Table 4.12   Assignment of orthogonal antenna ports and characteristic modes of regular hexagonal PEC plate to irreducible representations of symmetry group D_6. © 2019 IEEE [PM19a].

initial port configurations. It is thus purposeful to apply these configurations to the regular hexagonal plate, yielding the initial port configurations in Fig. 4.26.

The port generation method yields the eight antenna ports as depicted in Fig. 4.27. They are sorted according to the irreducible representations as listed in Table 4.12. Port 1 belonging to $\Gamma^{(1)}$ (Fig. 4.27(a)) and port 3 belonging to $\Gamma^{(3)}$ (Fig. 4.27(c)) are generated using the initial port configuration in Fig. 4.26(a). Both ports consist of twelve feed points distributed symmetrically at the half-edge centers. Port 2 belonging to $\Gamma^{(2)}$ (Fig. 4.27(b)), Port 4 belonging to $\Gamma^{(4)}$ (Fig. 4.27(d)), Port 5 belonging to the first row of $\Gamma^{(5)}$ (Fig. 4.27(e)), Port 6 belonging to the second row of $\Gamma^{(5)}$ (Fig. 4.27(f)), Port 7 belonging to the first row of $\Gamma^{(6)}$ (Fig. 4.27(g)), and Port 8 belonging to the second row of $\Gamma^{(6)}$ (Fig. 4.27(h)) are generated using the initial port configuration in Fig. 4.26(b). Ports 2 and 4 each consist of six feed points distributed symmetrically at the edge centers. Ports 5 and 7 each consist of the same six feed points. However, four of the six feed points are driven with half the source voltage of the other feed points, which is denoted by the small arrows in Fig. 4.27(e) and (g).[71] Ports 6 and 8, finally, each consist of four feed points.

---

[71]This also occurred on the equilateral triangular plate (port 4), cf. Fig. 4.12(d).

(a) Port 1   (b) Port 2   (c) Port 3   (d) Port 4

(e) Port 5   (f) Port 6   (g) Port 7   (h) Port 8
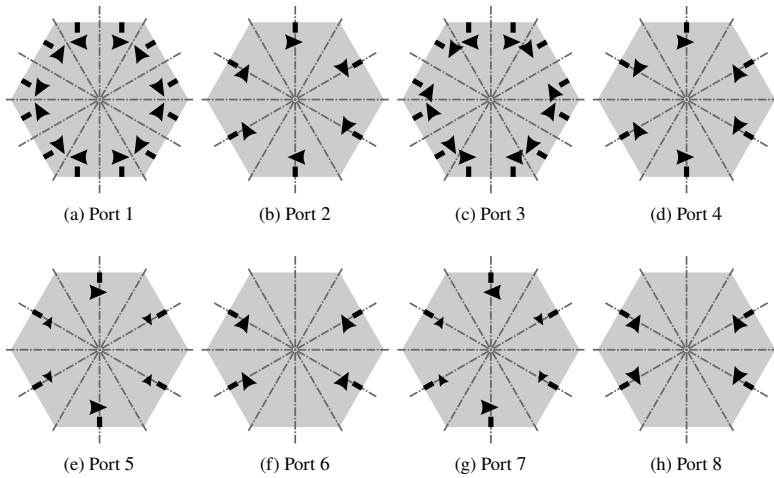
Figure 4.27   Orthogonal antenna ports on regular hexagonal PEC plate consisting of symmetrically distributed, simultaneously driven feed points. Positions of feed points denoted by black lines. Relative voltage directions denoted by arrows. The small arrows of ports 5 and 7 denote half the source voltage compared to the large arrows. (a)–(h) Ports 1 to 8. © 2019 IEEE [PM19a].

Similar to the equilateral triangular plate, and in contrast to the square plate, the transformation of the antenna ports belonging to the two-dimensional irreducible representations is not straightforward. That is why it is mandatory to use the automatic port generation method. As the antenna ports are designed as basis functions of the irreducible representations, they are guaranteed to be orthogonal. Moreover, the generated port configurations are optimal in the sense that they consist of as few feed points as possible. These results are based on the symmetry of the regular hexagonal plate alone and are thus independent of the actual antenna size. A modal analysis is now conducted in order to determine the minimum antenna size and check the excitation.

The modal significances of the first 20 characteristic modes as functions of the electrical size kR_u are shown in Fig. 4.28.[72] The modes are sorted according to their significance at $kR_u = 4.4$, where all eight fundamental modes are significant. The assignment of all 20 modes to the irreducible representations of D_6 is listed in Table 4.12. The assignment is conducted using the method

---

[72] A regular hexagon is completely determined by its edge length a (Fig. 4.25). Its circumradius R_u is equal to its edge length: $R_u = a$.
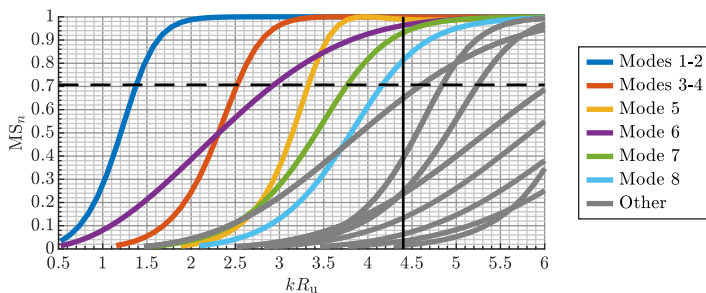
Figure 4.28   Modal significances of regular hexagonal PEC plate as functions of electrical size kR_{u}. Fundamental characteristic modes in color, higher-order modes in gray. At $kR_{\mathrm{u}} = 4.4$, all eight fundamental modes are significant. The modes are sorted according to their significance at $kR_{\mathrm{u}} = 4.4$.
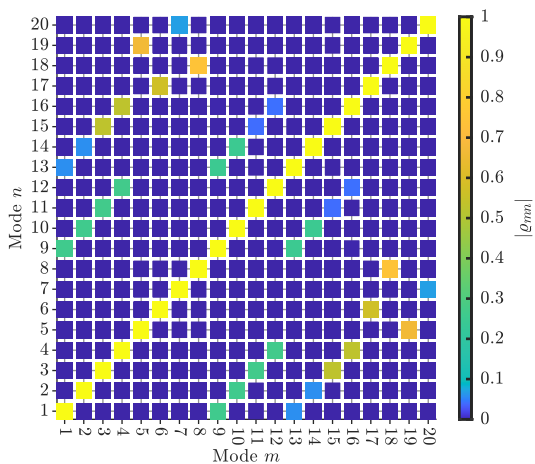
Figure 4.29   Characteristic current correlation coefficients of regular hexagonal PEC plate with electrical size $kR_{\mathrm{u}} = 4.4$ computed using (2.51). © 2019 IEEE [PM19a].

introduced in section 4.1.1. The automatic assignment procedure based on the character projection operators is recommended here as there are two two-dimensional irreducible representations. The degenerate modes belonging to the two-dimensional irreducible representations $\Gamma^{(5)}$ and $\Gamma^{(6)}$ are resolved using the method presented in section 4.2.2 with the representation matrices in Table 4.11.
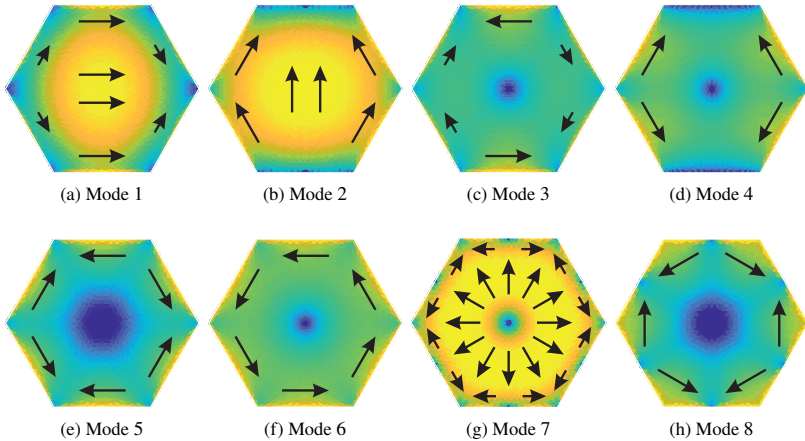
Figure 4.30 Normalized surface current densities of fundamental characteristic modes of regular hexagonal PEC plate with electrical size $kR_u = 4.4$. Principal current directions denoted by arrows. Modes sorted according to their significance. Color bar in Fig. 2.6(e). (a) Mode 1 belonging to the first row of $\Gamma^{(5)}$. (b) Mode 2 belonging to the second row of $\Gamma^{(5)}$. (c) Mode 3 belonging to first row of $\Gamma^{(6)}$. (d) Mode 4 belonging to second row of $\Gamma^{(6)}$. (e) Mode 5 belonging to $\Gamma^{(4)}$. (f) Mode 6 belonging to $\Gamma^{(2)}$. (g) Mode 7 belonging to $\Gamma^{(1)}$. (h) Mode 8 belonging to $\Gamma^{(3)}$. © 2019 IEEE [PM19a].

The resulting orthogonality of the characteristic surface current densities is confirmed by the characteristic current correlation coefficients in Fig. 4.29.

The characteristic surface current densities of the fundamental modes are depicted in Fig. 4.30. Modes 1 and 2 (Fig. 4.30(a) and (b)) are the fundamental modes of the two-dimensional fifth irreducible representation $\Gamma^{(5)}$. Similar to the square plate, their surface current densities may be interpreted as orthogonally polarized "dipole modes". Modes 3 and 4 (Fig. 4.30(c) and (d)) are the fundamental modes of the two-dimensional sixth irreducible representation $\Gamma^{(6)}$. A close inspection yields that they may be interpreted as "quadrupole modes". In contrast to the square plate, they are degenerate. Mode 5 (Fig. 4.30(e)) is the fundamental mode of $\Gamma^{(4)}$. It may be interpreted as a "hexapole mode". Such a mode is not present among the fundamental modes of the square plate. Mode 6 (Fig. 4.30(f)) is the fundamental mode of $\Gamma^{(2)}$. Similar to the square plate and the equilateral triangular plate, it is reminiscent of a current loop ("loop mode"). Correspondingly, Mode 7 (Fig. 4.30(g)) is the fundamental mode of $\Gamma^{(1)}$ and is invariant under all symmetry operations of D_6 ("invariant mode"). Finally, mode 8 (Fig. 4.30(h)) is the fundamental mode of $\Gamma^{(3)}$. Similar to mode 5, it
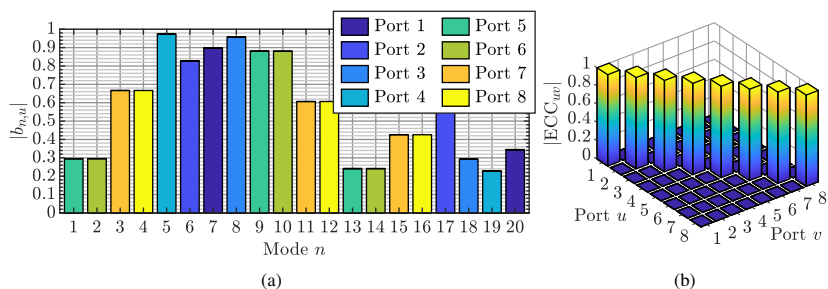
Figure 4.31   Excitation parameters of regular hexagonal PEC plate with electrical size $kR_u = 4.4$ and port configuration according to Fig. 4.27. (a) Normalized modal weighting coefficients. (b) Envelope correlation coefficients. © 2019 IEEE [PM19a].

may be interpreted as a "hexapole mode". The two "hexapole modes" are not degenerate, just like the two "quadrupole modes" of the square plate.

The evaluation of the normalized modal weighting coefficients in Fig. 4.31(a) confirms that the eight antenna ports exactly excite the mutually orthogonal sets of characteristic surface current densities offered by the regular hexagonal PEC plate. Accordingly, the antenna ports are orthogonal, which is checked by computing the envelope correlations coefficients (Fig. 4.31(b)). The regular hexagonal PEC plate offers eight orthogonal antenna ports. It is thus expected to be well suited for a multimode antenna design with a large number of ports.

Additionally, both symmetry analysis and modal analysis have revealed some relations between the regular polygonal plates considered so far. These relations will be examined more closely in chapter 5.

4.5.3 Square Pyramid

In section 3.3.5, the symmetry group C_{4v} was introduced, which is isomorphic to the symmetry group D_4 of the square plate. C_{4v} is the symmetry group of a right square pyramid as shown in Fig. 4.32. It contains four rotations about the z-axis, which are already known from the square plate (E, C_{4z}, C_{4z}^{-1}, C_{2z}), and four reflections through planes containing the z-axis (σ_{xz}, σ_{yz}, σ_{Az}, σ_{Bz}).[73]

Due to the isomorphism, C_{4v} has the same irreducible representations as D_4. Therefore, the representation matrices of D_4 as listed in Table 3.6 can be applied

---

[73]These replace the four rotations of D_4 about the axes perpendicular to the z-axis.
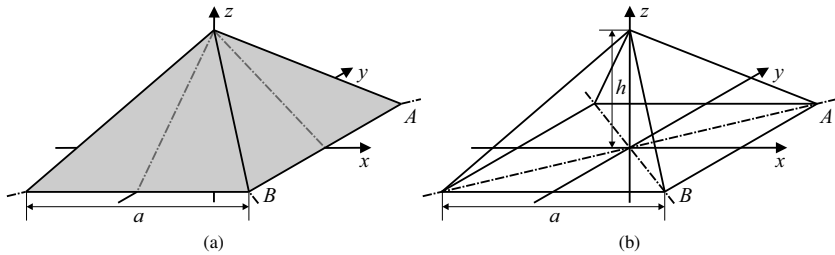
Figure 4.32   Square pyramid and coordinate system. (a) PEC object. (b) Schematic.

Repr.	$\Gamma^{(1)}$	$\Gamma^{(2)}$	$\Gamma^{(3)}$	$\Gamma^{(4)}$	$\Gamma_1^{(5)}$	$\Gamma_2^{(5)}$
Mode n	5, 16, 20	4, 14	6, 15	3, 13, 19	1, 7, 9, 11, 17	2, 8, 10, 12, 18
Port u	1	2	3	4	5	6

Table 4.13   Assignment of characteristic modes and orthogonal antenna ports of square PEC pyramid to irreducible representations of symmetry group C_{4v}.

to the square pyramid as well. This has the consequence that the characteristic surface current densities on the square pyramid transform under the symmetry operations of C_{4v} in the same way as those on the square plate under the symmetry operations of D_4. In simple terms, it is expected that the characteristic surface current densities on the square pyramid have the same symmetry properties as those on the square plate. The same argument is valid for the antenna ports.

In order to illustrate this, a modal analysis is conducted. A square pyramid as shown in Fig. 4.32 without base plate is chosen.[74] There are now two free geometry parameters: the edge length a and the height h. The height is set to $h = \frac{a}{2}$ so that the angle between the base and the sides is 45°. The circumradius R_u (radius of circumscribed sphere) is then governed by the square base of the pyramid, i.e., it is the same as that of the square plate $R_u = \frac{a}{\sqrt{2}}$.[75]

The modal significances of the characteristic modes of the square pyramid are shown in Fig. 4.33 as functions of the electrical size kR_u. The corresponding

---

[74]This allows a better comparison to the square plate as the surface of the pyramid is not closed in this case. The square pyramid without base plate may be interpreted as a deformed square plate.

[75]It is emphasized once more that the antenna size only affects the modal results, but not the symmetry. In particular, the optimal port configuration derived in this subsection is valid for all sizes of the right square pyramid.
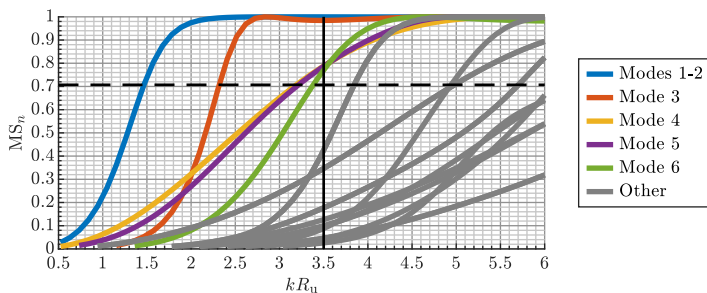
Figure 4.33   Modal significances of square PEC pyramid as functions of electrical size kR_u. Fundamental characteristic modes in color, higher-order modes in gray. At $kR_u = 3.5$, all six fundamental modes are significant. The modes are sorted according to their significance at $kR_u = 3.5$.
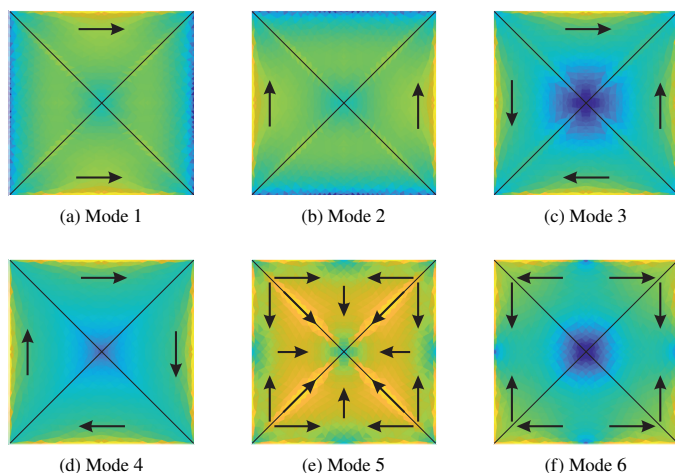
Figure 4.34   Normalized surface current densities of fundamental characteristic modes of square PEC pyramid with electrical size $kR_u = 3.5$. View from above ($z > h$). Principal current directions denoted by arrows. Modes sorted according to their significance. Color bar in Fig. 2.6(e). (a) Mode 1 belonging to the first row of $\Gamma^{(5)}$. (b) Mode 2 belonging to the second row of $\Gamma^{(5)}$. (c) Mode 3 belonging to $\Gamma^{(4)}$. (d) Mode 4 belonging to $\Gamma^{(2)}$. (e) Mode 5 belonging to $\Gamma^{(1)}$. (f) Mode 6 belonging to $\Gamma^{(3)}$.

assignment to the irreducible representations of the symmetry group C_{4v} is listed in Table 4.13. As the symmetry group C_{4v} is isomorphic to D_4, there are six fundamental characteristic modes.
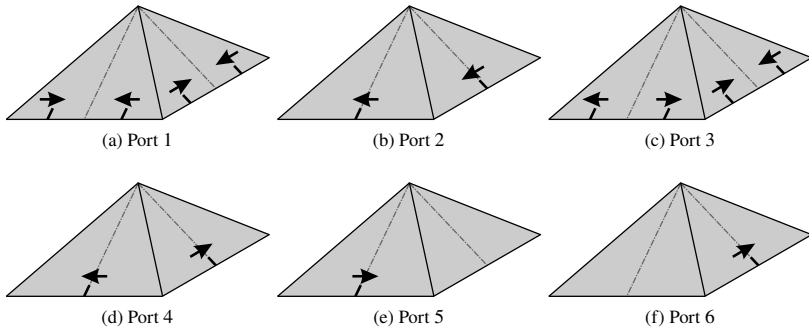
Figure 4.35   Orthogonal antenna ports on square PEC pyramid consisting of symmetrically distributed, simultaneously driven feed points. Not all feed points are visible from this point of view. For a complete view, refer to Fig. 4.23, which corresponds to the view from above ($z > h$). Positions of feed points denoted by black lines. Relative voltage directions denoted by arrows. All feed points are driven with the same source voltage. (a)–(f) Ports 1 to 6.

Compared to the square plate (Fig. 4.19), some of the significance curves appear to be shifted towards lower electrical sizes. This has the particular consequence that all six fundamental modes are significant at $kR_u = 3.5$ instead of $kR_u = 4$. Apparently, the square pyramid requires a smaller electrical size than the square plate in order to have the six fundamental modes significant. This reduced footprint is bought by introducing the third dimension.

The square pyramid may be interpreted as a folded square plate. This interpretation of the square pyramid is corroborated by inspecting the surface current densities of the fundamental characteristic modes as shown in Fig. 4.34. The view from above is chosen in order to enable a direct comparison to the characteristic surface current densities of the square plate (Fig. 4.21). Obviously, they are very similar. This is due to the fact that the characteristic surface current densities of the square pyramid and the square plate transform according to the same representation matrices (Table 3.6).

Based on this group isomorphism, the antenna ports of the square plate can be employed on the square pyramid as well. The port configurations of the square plate as presented in Fig. 4.23 are arranged on the sides of the square pyramid as illustrated in Fig. 4.35. Viewed from above, they look exactly like those in Fig. 4.23. The assignment of the ports to the irreducible representations of C_{4v} is listed in Table 4.13. The evaluation of the excitation parameters in Fig. 4.36 demonstrates that the antenna ports excite the mutually orthogonal
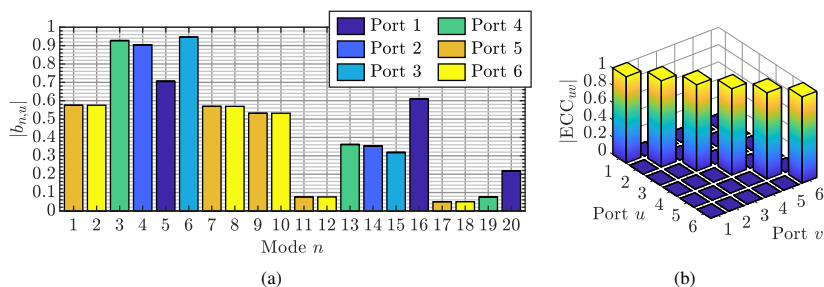
Figure 4.36   Excitation parameters of square PEC pyramid with electrical size $kR_u = 3.5$ and port configuration according to Fig. 4.35. (a) Normalized modal weighting coefficients. (b) Envelope correlation coefficients.

sets of characteristic surface current densities offered by the square pyramid and hence are orthogonal.

The square pyramid gives a first impression how group isomorphisms can be exploited in order to manipulate multimode antenna properties. The symmetry-related properties, in particular the number and the optimal configurations of the antenna ports, are basically the same as those of the square plate and can thus be adopted directly. However, additional geometry parameters, in this case the height of the pyramid, can be used in order to manipulate the modal properties. In this example, the pyramidal antenna shape, although a comparatively simple three-dimensional geometry, results in a reduced footprint compared to the square plate while the number of orthogonal antenna ports is preserved.

More sophisticated antenna shapes having the C_{4v}-symmetry may be conceived in order to improve the manipulation of the modal properties. In [82], a prototype of a three-dimensional patch antenna (one antenna port) is presented. As a matter of fact, the symmetry group of the antenna is C_{4v}. This work serves as a motivation that three-dimensional multimode antennas can in fact be realized. Exploiting group isomorphisms is thus proposed as one interesting approach for future multimode antenna designs.

4.5.4 Square Cuboid

The symmetry group D_{4h} of a square cuboid as shown in Fig. 4.37 was introduced in section 3.2.3 as a direct-product group. It will now be shown that this fact greatly simplifies the symmetry analysis and the port placement.
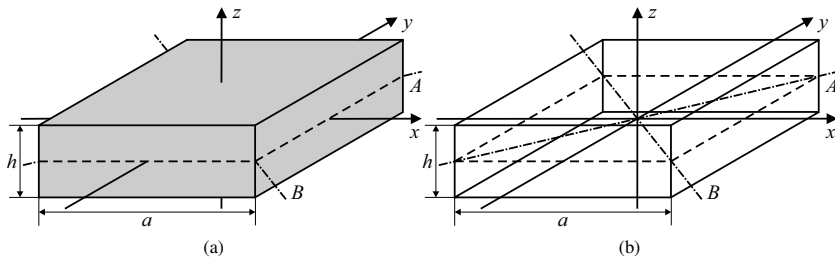
Figure 4.37 Square cuboid and coordinate system. (a) PEC object. (b) Schematic. © 2019 IEEE [PM19b].

As examined in section 3.3.6, the group D_{4h} has eight one-dimensional and two two-dimensional irreducible representations. Therefore, there is a total of twelve mutually orthogonal sets of characteristic surface current densities. Consequently, twelve orthogonal antenna ports can be realized.

A modal analysis is performed in order to check the results of the port generation.[76] For this purpose, the edge length of the cuboid is chosen to be $a = 1.5$ wavelengths and the height is chosen to be $h = \frac{a}{3}$. This size is selected for the simple reason that, out of the 40 characteristic modes taken into account, at least two belong to each irreducible representations of D_{4h}.

The characteristic current correlation coefficients are depicted in Fig. 4.38. It can be checked that there are in fact twelve mutually orthogonal sets of characteristic surface current densities. Accordingly, the characteristic modes can be sorted into these sets, though they cannot be assigned to the different irreducible representations of D_{4h} based on this information alone.[77] However, it will become clear in the following paragraphs that this step is not even necessary if the focus is put solely on realizing orthogonal antenna ports.

Based on the structure of the characters and the representation matrices of D_{4h} (Tables 3.11 and 3.12), predictions about the characteristic surface current densities to be expected can be made. Characteristic modes belonging to the first five irreducible representations $\Gamma^{(1;2;3;4;5)}$ (even representations) may be interpreted as even modes with respect to the xy-plane as their respective surface current densities transform in the same way under both proper and improper rotations. In particular, they are invariant under the reflection through the xy-

---

[76]It is recalled that a modal analysis is not necessary for the port generation as explained in section 4.4.

[77]The methods introduced in section 4.1 would have to be applied.
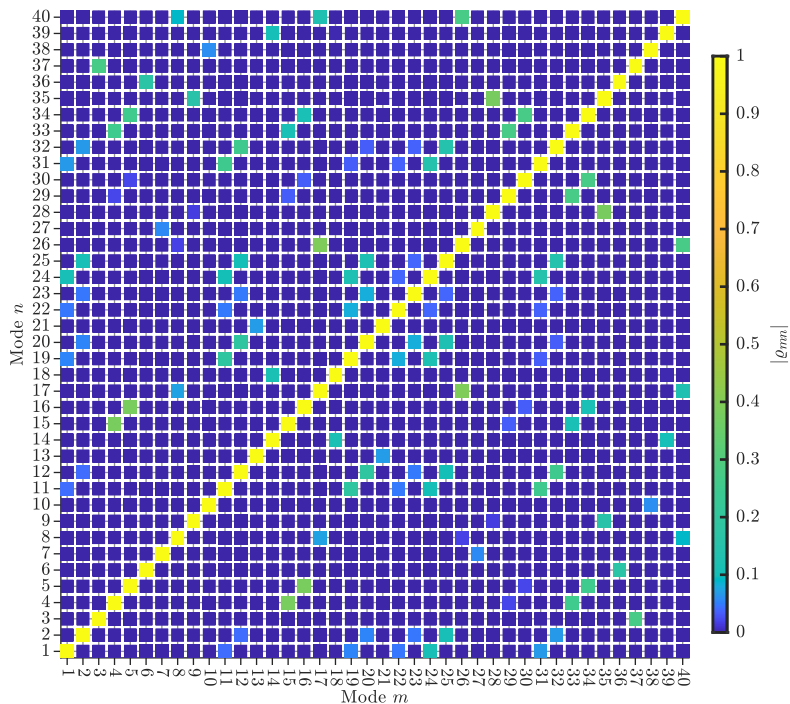
Figure 4.38   Characteristic current correlation coefficients of square PEC cuboid computed using (2.51). © 2019 IEEE [PM19b].

plane. In order to illustrate this, an exemplary even characteristic surface current density is shown in Fig. 4.39(a). It possesses the familiar circular symmetry known from the square plate (cf. Fig. 4.21(e)). In contrast, characteristic modes belonging to the irreducible representations $\Gamma^{(6;7;8;9;10)}$ (odd representations) may be interpreted as odd modes with respect to the xy-plane. Their respective surface current densities are inverted by the improper rotations compared to the proper rotations. In particular, the characteristic surface current densities are inverted by the reflection through the xy-plane. An example is shown in Fig. 4.39(b), consisting primarily of a current loop on the top plate and a current loop on the bottom plate with opposite directions.

The concept of even and odd representations is now made use of in order to implement the antenna ports. The symmetry group D_{4h} of the square cuboid is the

(a)   (b)
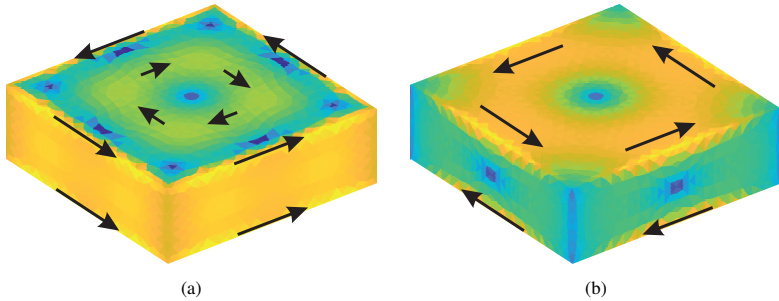
Figure 4.39   Two characteristic surface current densities of square PEC cuboid as examples for even and odd modes. Principal current directions denoted by arrows. Color bar in Fig. 2.6(e). (a) Mode 13 transforming according to $\Gamma^{(2)}$ of D_{4h} is an even mode as it is invariant under the reflection σ_{xy}. (b) Mode 9 transforming according to $\Gamma^{(6)}$ of D_{4h} is an odd mode as it is inverted by the reflection σ_{xy}.

Port u	1	2	3	4	5	6
Repr.	$\Gamma^{(1)}$	$\Gamma^{(2)}$	$\Gamma^{(3)}$	$\Gamma^{(4)}$	$\Gamma^{(5)}_1$	$\Gamma^{(5)}_2$
Mode n	10, 38	13, 21	3, 37	14, 18, 39	4, 15, 29, 33	5, 16, 30, 34
Port u	7	8	9	10	11	12
Repr.	$\Gamma^{(7)}$	$\Gamma^{(6)}$	$\Gamma^{(9)}$	$\Gamma^{(8)}$	$\Gamma^{(10)}_2$	$\Gamma^{(10)}_1$
Mode n	8, 17, 26, 40	9, 28, 35	6, 36	7, 27	2, 12, 20, 23, 25, 32	1, 11, 19, 22, 24, 31

Table 4.14   Assignment of orthogonal antenna ports and characteristic modes of square PEC cuboid to irreducible representations of symmetry group D_{4h}. © 2019 IEEE [PM19b].

direct product of the symmetry group D_4 of the square plate, which characterizes the square symmetry, and the symmetry group C_s, which introduces the reflection through the xy-plane. Inspired by the square symmetry due to D_4, it is purposeful to reuse the feed points on the square plate (Fig. 4.23). The additional reflection plane due to C_s requires to place the feed points on both the top face ($z = \frac{h}{2}$) and the bottom face ($z = -\frac{h}{2}$) of the square cuboid.

The first six antenna ports are now designed to belong to the even irreducible representations $\Gamma^{(1;2;3;4;5)}$ (Table 4.14). Therefore, the feed points on both top and bottom face of the cuboid are driven according to Fig. 4.23, i.e., in phase ("even excitation"). The ports 7 to 12 are designed to belong to the odd irreducible representations $\Gamma^{(6;7;8;9;10)}$ (Table 4.14). Hence, the feed points on the top face
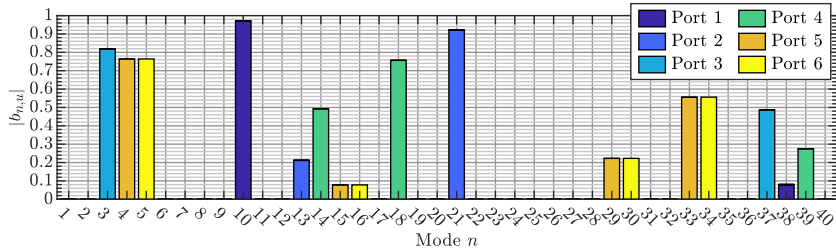
(a)
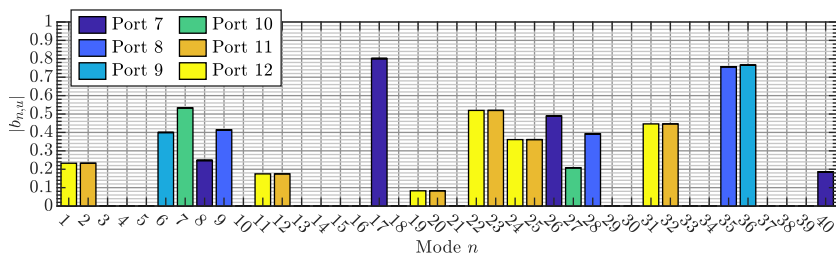
(b)
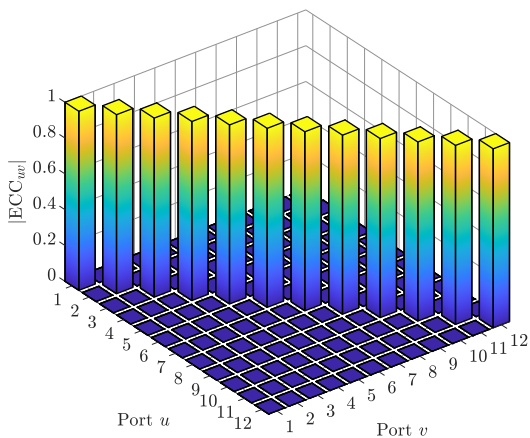
(c)

Figure 4.40   Excitation parameters of square PEC cuboid. (a)–(b) Normalized modal weighting coefficients. (c) Envelope correlation coefficients. © 2019 IEEE [PM19b].

of the cuboid are driven again according to Fig. 4.23, whereas those on the bottom face are inverted, i.e., they are driven out of phase with respect to those on the top face (all arrows in Fig. 4.23 rotated by 180°, "odd excitation").

The assignment of the antenna ports generated this way to the irreducible representations of D_{4h} is given in Table 4.14. The evaluation of the excitation parameters in Fig. 4.40 confirms once again that the antenna ports excite the mutually orthogonal sets of characteristic surface current densities offered by the square PEC cuboid and consequently are orthogonal. Besides, the characteristic modes can now be assigned to the irreducible representations retrospectively via the antenna ports by examining the normalized modal weighting coefficients in Fig. 4.40(a) and (b), resulting in the assignment listed in Table 4.14.

This last example demonstrates once more how the symmetry analysis is able to provide a lot of insight into the analysis and the excitation of characteristic modes. Although the geometric structure of the PEC object is rather complex, predictions about the properties of the characteristic surface current densities and how to excite them can be made without even conducting a modal analysis.

5 Generalized Modal Analysis
of Regular Polygonal Plates

In the previous chapter, it was demonstrated that the number of orthogonal antenna ports and how to realize them is totally governed by the symmetry of an antenna. Consequently, this information is known *a priori* and it is independent of the actual implementation of the antenna, i.e., the antenna size and shape, as long as the symmetry is preserved. It is, however, mandatory that for each antenna port the fundamental characteristic mode as defined in section 4.3 is significant. The examples considered in chapter 4 have shown that this is where the electrical size of the antenna comes into play as it governs the modal significance. The minimum antenna size is achieved if the fundamental modes of each antenna port to be realized are significant.

In this chapter, the family of the regular polygonal plates is of particular interest. The examples considered so far (triangular (Fig. 4.11), square (Fig. 4.19), hexagonal (Fig. 4.28)) have shown that the fundamental characteristic modes become significant at a certain electrical size and then stay significant. This behavior ensures that the fundamental modes can all be made significant simultaneously if the minimum electrical size is chosen or exceeded. In terms of frequencies, a potential broadband operation of all antenna ports is thus enabled above a certain minimum frequency.

The regular polygonal plates are characterized by exactly one geometry parameter, the edge length a, or alternatively, the circumradius R_u. The circumradius is the radius of the circumscribed circle of a regular polygon (see, e.g., Fig. 4.1 or Fig. 4.25). This allows the definition of the electrical size kR_u, which has already been made extensive use of in chapter 4. However, this definition also allows a comparison of all regular polygonal plates. Going even further, a circular disk of radius R_u may be considered the generalization of the regular polygonal plates of circumradius R_u. In other words, the circular disk is the limiting case of the regular polygonal plates with an infinite number of vertices.

Therefore, it is expected that a lot can be learned, in particular with respect to the antenna size, by analyzing the circular disk as the representative of all regular polygonal plates. The aim of this chapter is to derive guidelines for determining the minimum antenna size if a certain number of orthogonal antenna ports is

to be realized. The derivation will be conducted exemplarily for the family of the regular polygonal plates. To this end, the circular disk as the generalization of the regular polygonal plates is analyzed with respect to both its modal and symmetry properties. Based on this, an estimate for the minimum electrical size of the regular polygonal plates is derived.

5.1 Analysis of Circular Disk

The symmetry group of a circular disk as shown in Fig. 3.10 is D_∞, which was introduced in section 3.6. As this group has an infinite number of irreducible representations, the circular disk offers an infinite number of mutually orthogonal sets of characteristic surface current densities. In order to perform a symmetry analysis, the methods used in chapter 4 can be applied to the circular disk in conjunction with the modifications introduced in section 3.6.

However, due to the infinite number of symmetry axes (see section 3.6), a triangular mesh reproducing the symmetry of a circular disk cannot be generated. Therefore, methods relying on a symmetric mesh, in particular the projection operators, cannot be applied to numerically computed characteristic surface current densities. If, however, analytical solutions were available, the symmetry analysis could be readily carried out. This is the motivation for this section.

5.1.1 Analytical Treatment

Analytical solutions for the characteristic modes of a PEC sphere are presented in [83]. As a matter of fact, the characteristic electromagnetic fields of a PEC sphere are properly normalized spherical wave functions [29]. For this reason, the derivation of the spherical wave functions is now briefly outlined and then applied to the circular disk.

Sphere

The spherical wave functions are obtained by solving the homogeneous vector Helmholtz equation in spherical coordinates r, θ, φ (Fig. 5.1) [65]:

$$\Delta \mathbf{F}(\mathbf{r}) + k^2 \mathbf{F}(\mathbf{r}) = \mathbf{0}, \tag{5.1}$$

where $\mathbf{F}$ denotes an arbitrary vector field with spherical components F_r, F_θ, and F_φ, which may be replaced by the electric field strength $\mathbf{E}$, the magnetic

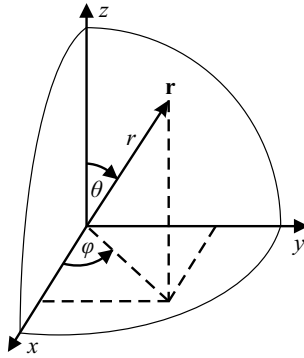Figure 5.1   Spherical coordinates.

field strength **H**, or the magnetic vector potential **A** (appendix A.2 and A.4). The coordinate vector **r** in spherical coordinates is written as

$$\mathbf{r}(r,\theta,\varphi) = \begin{pmatrix} x(r,\theta,\varphi) \\ y(r,\theta,\varphi) \\ z(r,\theta,\varphi) \end{pmatrix} = \begin{pmatrix} r\sin\theta\cos\varphi \\ r\sin\theta\sin\varphi \\ r\cos\theta \end{pmatrix}, \qquad \begin{array}{l} 0 \le r < \infty \\ 0 \le \theta \le \pi \\ 0 \le \varphi < 2\pi \end{array}. \qquad (5.2)$$

In Cartesian coordinates x,y,z, the vector Helmholtz equation can be decomposed into three independent scalar Helmholtz equations in terms of the components F_x, F_y, and F_z, respectively (cf. (2.6)) [65]. In curvilinear coordinates, however, the vector Laplace operator takes the general form

$$\Delta\mathbf{F}(\mathbf{r}) = \mathrm{grad}\Big(\mathrm{div}\big(\mathbf{F}(\mathbf{r})\big)\Big) - \mathrm{rot}\Big(\mathrm{rot}\big(\mathbf{F}(\mathbf{r})\big)\Big). \qquad (5.3)$$

This has the consequence that the vector Helmholtz equation cannot be decomposed into three independent scalar Helmholtz equations.

Instead, solutions to (5.1) can be constructed by equating **F** with the vector wave functions **L**, **M**, or **N** [65]:

$$\mathbf{L}(\mathbf{r}) = \mathrm{grad}\big(\zeta(\mathbf{r})\big), \qquad (5.4a)$$

$$\mathbf{M}(\mathbf{r}) = \mathrm{rot}\big(\mathbf{a}\zeta(\mathbf{r})\big), \qquad (5.4b)$$

$$\mathbf{N}(\mathbf{r}) = \frac{1}{k}\mathrm{rot}\big(\mathbf{M}(\mathbf{r})\big), \qquad (5.4c)$$

where **a** denotes a vector to be determined below. ζ is called the generating function and it is the solution to the homogeneous scalar Helmholtz equation:

$$\Delta\zeta(\mathbf{r}) + k^2\zeta(\mathbf{r}) = 0. \tag{5.5}$$

The solution to this equation is obtained by separation of variables in spherical coordinates, yielding [84]

$$\zeta_{st}(r,\theta,\varphi) = \begin{Bmatrix} j_t(kr) \\ y_t(kr) \\ h_t^{(1;2)}(kr) \end{Bmatrix} \mathcal{L}_t^s(\cos\theta) \begin{Bmatrix} \cos(s\varphi) \\ \sin(s\varphi) \end{Bmatrix}, \tag{5.6}$$

where j_t denotes the spherical Bessel function of the first kind, y_t denotes the spherical Bessel function of the second kind, $h_t^{(1)}$ denotes the spherical Hankel function of the first kind, and $h_t^{(2)}$ denotes the spherical Hankel function of the second kind, each of order t. $\mathcal{L}_t^s$ denotes the associated Legendre function of degree t and order s.[78] The functions in braces form sets of alternative solutions. In the context of wave propagation and, in particular, characteristic modes, the spherical Hankel function of the second kind is chosen, denoting outward traveling waves [29]. The trigonometric functions $\cos(s\varphi)$ and $\sin(s\varphi)$ distinguish even and odd solutions, respectively [84].

Based on the scalar solution, the vector wave functions $\mathbf{L}_{st}$, $\mathbf{M}_{st}$, and $\mathbf{N}_{st}$ according to (5.4) each are solutions to the vector Helmholtz equation (5.1) in spherical coordinates. $\mathbf{L}$ is always irrotational, whereas $\mathbf{M}$ and $\mathbf{N}$ are always solenoidal [87]. As the electric and magnetic field strengths of an electromagnetic wave in free space are solenoidal, the principal goal is to determine $\mathbf{M}$ and $\mathbf{N}$. Setting $\mathbf{a} = \mathbf{r}$ yields $\mathbf{M}$ transverse with respect to the radial direction (direction of wave propagation), i.e., $M_r = 0$. If a properly scaled $\mathbf{M}_{st}$ is interpreted as the electric field strength, the resulting $\mathbf{N}_{st}$ corresponds to the magnetic field strength, resulting in a transverse electric (TE) spherical wave mode [84]. If a properly scaled $\mathbf{M}_{st}$ is interpreted instead as the magnetic field strength, the resulting $\mathbf{N}_{st}$ corresponds to the electric field strength, resulting in a transverse magnetic (TM) spherical wave mode. An arbitrary electromagnetic wave can generally be expressed as a weighted sum of these spherical wave modes, where the index pair st distinguishes the different wave modes [65]. The corresponding modal surface current densities on a PEC sphere with radius R_u are computed

---

[78] A detailed reference to these special functions can be found in [85] and [86].

by means of the boundary condition of the magnetic field strength:[79]

$$\mathbf{J}_{st}(\theta',\varphi') = \mathbf{e}_r \times \mathbf{H}_{st}(R_{\mathrm{u}},\theta',\varphi'). \tag{5.7}$$

In [29], it is shown that the characteristic surface current densities given in [83] are properly normalized spherical surface current densities according to (5.7). The characteristic surface current densities on an PEC sphere can thus be subdivided into TE and TM modes, yielding [29, 83][80]

$$\mathbf{J}_{st}^{\mathrm{TE}}(\theta',\varphi') = \frac{1}{kR_{\mathrm{u}}^2\sqrt{Z_0}}\frac{1}{j_t(kR_{\mathrm{u}})}\sqrt{\frac{\epsilon_s}{4\pi}\frac{2t+1}{t(t+1)}\frac{(t-s)!}{(t+s)!}}$$
$$\cdot\left(\frac{s\mathcal{L}_t^s(\cos\theta')}{\sin\theta'}\begin{Bmatrix}-\sin(s\varphi')\\\cos(s\varphi')\end{Bmatrix}\mathbf{e}_\theta - \frac{\partial\mathcal{L}_t^s(\cos\theta')}{\partial\theta'}\begin{Bmatrix}\cos(s\varphi')\\\sin(s\varphi')\end{Bmatrix}\mathbf{e}_\varphi\right), \tag{5.8}$$

and

$$\mathbf{J}_{st}^{\mathrm{TM}}(\theta',\varphi') = \frac{1}{kR_{\mathrm{u}}^2\sqrt{Z_0}}\frac{1}{\left.\frac{\partial(krj_t(kr))}{\partial r}\right|_{r=R_{\mathrm{u}}}}\sqrt{\frac{\epsilon_s}{4\pi}\frac{2t+1}{t(t+1)}\frac{(t-s)!}{(t+s)!}}$$
$$\cdot\left(\frac{\partial\mathcal{L}_t^s(\cos\theta')}{\partial\theta'}\begin{Bmatrix}\cos(s\varphi')\\\sin(s\varphi')\end{Bmatrix}\mathbf{e}_\theta + \frac{s\mathcal{L}_t^s(\cos\theta')}{\sin\theta'}\begin{Bmatrix}-\sin(s\varphi')\\\cos(s\varphi')\end{Bmatrix}\mathbf{e}_\varphi\right), \tag{5.9}$$

with

$$\epsilon_s = \begin{cases}1 & s=0\\2 & s\neq 0\end{cases}. \tag{5.10}$$

As the characteristic electric fields are known as well from the derivation above, the eigenvalues of a PEC sphere with radius R_{u} can be computed analytically via the characteristic angle (2.28), yielding [29, 83]

$$\lambda_t^{\mathrm{TE}} = -\frac{y_t(kR_{\mathrm{u}})}{j_t(kR_{\mathrm{u}})} \quad\text{and}\quad \lambda_t^{\mathrm{TM}} = -\frac{\left.\frac{\partial}{\partial r}(kry_t(kr))\right|_{r=R_{\mathrm{u}}}}{\left.\frac{\partial}{\partial r}(krj_t(kr))\right|_{r=R_{\mathrm{u}}}}. \tag{5.11}$$

---

[79]Primed coordinates are employed in order to emphasize the evaluation on the surface of a sphere.

[80]The characteristic modes derived this way are distinguished by TE/TM, the index pair st, as well as even/odd. Alternatively, these distinctions may be mapped into one index n [88] as used in the previous chapters, e.g., in (2.14).
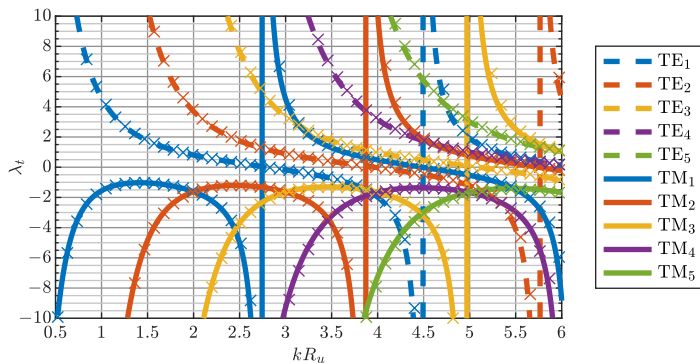
Figure 5.2   Analytically computed eigenvalues of PEC Sphere as functions of electrical size kR_{u}. The first five TE and TM eigenvalues are depicted ($t = 1,2,3,4,5$). The corresponding numerically computed eigenvalues are marked by the crosses.

The eigenvalues are distinguished by TE/TM and the index t. As $s \in [0,t]$, TE and TM modes, respectively, are $(2t + 1)$-fold degenerate, including even and odd modes [83]. Furthermore, the eigenvalues are functions of the electrical size kR_{u} alone, as expected, and can even be computed analytically. The first five TE and TM eigenvalues are shown in Fig. 5.2.[81] As proposed in [88], these results can be used in order to check the accuracy of the employed numerical characteristic mode computation. The crosses in Fig. 5.2 denote the corresponding numerically calculated eigenvalues of a PEC sphere discretized with 3168 triangles (4752 RWG basis functions), showing a good agreement between the exact analytical solutions and the numerically computed eigenvalues.

Based on the derivation outlined above, analytical forms of the characteristic surface current densities of a PEC sphere are available so that a symmetry analysis could now be performed with the methods introduced in chapters 3 and 4. Another advantageous outcome of the derivation is that analytical expressions of the eigenvalues are available as well. A direct relationship between the eigenvalues and the electrical size of the sphere is given, obviating a time-consuming numerical simulation. This result is exactly what is desired for the circular disk and the regular polygonal plates, as stated in the introduction of

---

[81]The behavior of the eigenvalues of the PEC sphere as functions of the electrical size differs considerably from that of the PEC objects analyzed so far (chapter 4). This is due to the fact that the sphere has a closed surface enabling internal resonances ($|\lambda_t| \to \infty$) [29, 88].

(a) $\xi \to \infty$ (b) $\xi = 0.5$ (c) $\xi = 0$
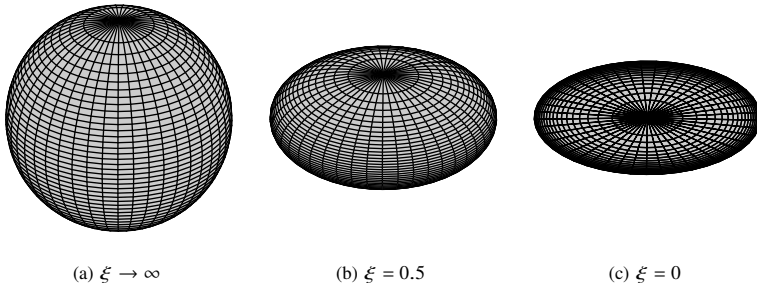
Figure 5.3 Evolution of a sphere into a circular disk using oblate spheroidal coordinates. The sphere and the circular disk are limiting cases of the oblate spheroid. (a) Sphere. (b) Oblate spheroid. (c) Circular disk.

this chapter. Motivated by this finding, it is now examined whether the same derivation can also be applied to the circular disk.

Circular Disk

Now, the idea is to flatten the sphere at its poles until it becomes a circular disk, as proposed in [29]. This approach is illustrated in Fig. 5.3. By flattening the sphere (Fig. 5.3(a)), it evolves into an oblate spheroid (Fig. 5.3(b)). By further flattening the spheroid, it finally becomes a circular disk with zero height (Fig. 5.3(c)). Obviously, the oblate spheroid is a more general geometric object which can evolve into either a sphere or a circular disk.

It is thus purposeful to introduce the oblate spheroidal coordinate system [86, 87]. In this coordinate system, it is possible to conduct the same derivation for solving the vector Helmholtz equation, i.e., based on the vector wave functions (5.4), as in spherical coordinates [29, 87]. Since the circular disk is a limiting case of the oblate spheroid (Fig. 5.3), it is expected that solutions for the circular disk are found by setting the height of the spheroid to zero.

The oblate spheroidal coordinates η, ξ, φ describe the surface of an arbitrary oblate spheroid in three-dimensional Euclidean space as illustrated in Fig. 5.4(a). The oblate spheroid (ellipsoid of revolution) is generated by rotating an ellipse about its minor axis, which is defined to lie on the z-axis [87]. Thus, the coordinate φ is the azimuthal angle already known from polar and spherical coordinates. A constant φ yields a cut plane containing the z-axis, as shown in Fig. 5.4(b) [86]. For constant ξ, the coordinate η runs along the ellipsoidal
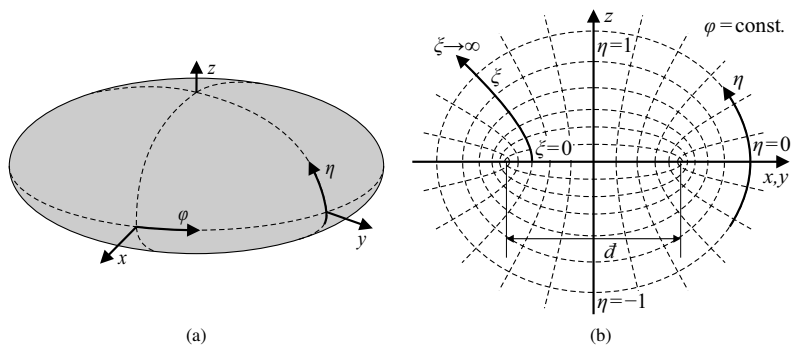
Figure 5.4   Spheroidal coordinates. (a) Oblate spheroid and coordinate system for fixed ξ. (b) Spheroidal coordinates for constant φ. The cut looks the same for all φ due to the rotational symmetry about the z-axis.

surface of a spheroid, similar to the polar angle θ in spherical coordinates. The coordinate ξ determines the shape of the spheroid, resulting in a family of confocal ellipsoids with interfocal distance d, as illustrated in Fig. 5.4(b) [86]. For constant η, ξ runs along a hyboloidal surface. Based on these relations, the coordinate vector $\mathbf{r}$ in oblate spheroidal coordinates is written as [87]

$$\mathbf{r}(\eta,\xi,\varphi) = \begin{pmatrix} x(\eta,\xi,\varphi) \\ y(\eta,\xi,\varphi) \\ z(\eta,\xi,\varphi) \end{pmatrix} = \frac{d}{2} \begin{pmatrix} \sqrt{(1-\eta^2)(\xi^2+1)}\cos\varphi \\ \sqrt{(1-\eta^2)(\xi^2+1)}\sin\varphi \\ \eta\xi \end{pmatrix}, \quad \begin{array}{l} -1 \leq \eta \leq 1 \\ 0 \leq \xi < \infty \\ 0 \leq \varphi < 2\pi \end{array}.$$

(5.12)

The unit vectors $\mathbf{e}_\eta, \mathbf{e}_\xi, \mathbf{e}_\varphi$ are computed by differentiating $\mathbf{r}$ with respect to the respective coordinate:

$$\mathbf{e}_\eta = \begin{pmatrix} -\eta\sqrt{\frac{\xi^2+1}{\xi^2+\eta^2}}\cos\varphi \\ -\eta\sqrt{\frac{\xi^2+1}{\xi^2+\eta^2}}\sin\varphi \\ \xi\sqrt{\frac{1-\eta^2}{\xi^2+\eta^2}} \end{pmatrix}, \quad \mathbf{e}_\xi = \begin{pmatrix} \xi\sqrt{\frac{1-\eta^2}{\xi^2+\eta^2}}\cos\varphi \\ \xi\sqrt{\frac{1-\eta^2}{\xi^2+\eta^2}}\sin\varphi \\ \eta\sqrt{\frac{\xi^2+1}{\xi^2+\eta^2}} \end{pmatrix}, \quad \mathbf{e}_\varphi = \begin{pmatrix} -\sin\varphi \\ \cos\varphi \\ 0 \end{pmatrix}.$$

(5.13)

The size and the shape of an oblate spheroid are determined by d and ξ, respectively. The circumradius R_u (radius in the xy-plane) is obtained from (5.12) by setting $\eta = 0$:

$$R_\mathrm{u}(d,\xi) = \sqrt{x^2(\eta=0,\xi,\varphi) + y^2(\eta=0,\xi,\varphi)} = \frac{d}{2}\sqrt{\xi^2+1}.$$
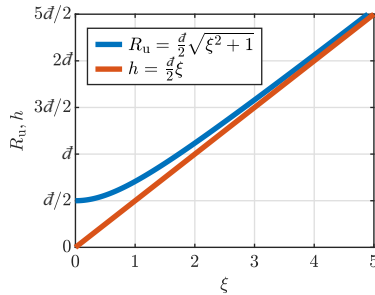
(5.14)

Figure 5.5   Circumradius R_u and height h of oblate spheroid as functions of d and ξ.

Accordingly, the height h on the z-axis is

$$h(d,\xi) = z(\eta = 1,\xi,\varphi) = \frac{d}{2}\xi. \tag{5.15}$$

The circumradius and the height as functions of d and ξ are shown in Fig. 5.5. For large ξ, the height approaches the circumradius. In the case $\xi \to \infty$, this results in a spherical surface (Fig. 5.3(a)). For $\xi = 0$, however, the height is zero, resulting in a circular disk with radius $R_u = d/2$ (Fig. 5.3(c)).

Consequently, the circular disk can be described in oblate spheroidal coordinates for $\xi = 0$. In this case, the coordinate vector $\mathbf{r}$ (5.12) reduces to[82]

$$\mathbf{r}'(\eta',\varphi') = \frac{d}{2}\sqrt{1-\eta'^2}\begin{pmatrix}\cos\varphi' \\ \sin\varphi' \\ 0\end{pmatrix} = \rho'\begin{pmatrix}\cos\varphi' \\ \sin\varphi' \\ 0\end{pmatrix} = \mathbf{r}'(\rho',\varphi'), \tag{5.16}$$

i.e., the oblate spheroidal coordinates reduce to the polar coordinates ρ',φ' as depicted in Fig. 5.6 with $\rho' = \frac{d}{2}\sqrt{1-\eta'^2}$, $\rho' \in [0,\frac{d}{2}]$. This behavior is also reflected in the unit vectors:

$$\mathbf{e}_\eta(\xi = 0) = \begin{cases}-\mathbf{e}_\rho & \eta' \in [0,1] \\ \mathbf{e}_\rho & \eta' \in [-1,0]\end{cases}, \quad \mathbf{e}_\xi(\xi = 0) = \begin{cases}\mathbf{e}_z & \eta' \in [0,1] \\ -\mathbf{e}_z & \eta' \in [-1,0]\end{cases}. \tag{5.17}$$

The unit vector $\mathbf{e}_\eta$ reduces to the unit vector in radial direction $\mathbf{e}_\rho$, spanning the circular disk together with $\mathbf{e}_\varphi$. The unit vector $\mathbf{e}_\xi$ reduces to the unit vector in

---

[82]The use of primed coordinates emphasizes that the coordinates are now confined to the surface of the circular disk.

z-direction $\mathbf{e}_z$, i.e., the unit normal vector of the circular disk. It is noted that for describing a disk, it is sufficient that η' either runs from -1 to 0 or from 0 to 1.

Now that it has been understood how a circular disk is purposefully described by means of oblate spheroidal coordinates, it is time to turn back to solving the vector Helmholtz equation (5.1). Basically, the same procedure as used above for spherical coordinates can be applied [29,87]. First of all, the generating function ζ, i.e., the solution to the homogeneous scalar Helmholtz equation (5.5) in oblate spheroidal coordinates, needs to be determined. By separation of variables, a solution is found in terms of the so-called spheroidal wave functions [87]:

$$\zeta_{st}(\eta,\xi,\varphi) = \mathcal{S}_{st}(-jc,\eta) \left\{ \mathcal{R}_{st}^{(1;2;3;4)}(-jc,j\xi) \right\} \begin{Bmatrix} \cos(s\varphi) \\ \sin(s\varphi) \end{Bmatrix}, \qquad (5.18)$$

with $c = \frac{1}{2}k\bar{d}$. $\mathcal{S}_{st}$ are the spheroidal angular functions, which are commonly expressed as infinite series expansions of the associated Legendre functions. $\mathcal{R}_{st}^{(1)}$, $\mathcal{R}_{st}^{(2)}$, $\mathcal{R}_{st}^{(3)}$, and $\mathcal{R}_{st}^{(4)}$ are the spheroidal radial functions of the first, the second, the third, and the fourth kind, respectively, which are expressed as infinite series expansions of the spherical Bessel functions of the first kind, the spherical Bessel functions of the second kind, the spherical Hankel functions of the first kind, and the spherical Hankel functions of the second kind, respectively [85–87]. Corresponding to the spherical Hankel functions of the second kind, the spheroidal radial functions of the fourth kind $\mathcal{R}_{st}^{(4)}$ denote outward traveling waves. Again, the trigonometric functions $\cos(s\varphi)$ and $\sin(s\varphi)$ distinguish even and odd solutions, respectively.

In the next step, a vector $\mathbf{a}$ has to be chosen in order to compute the vector wave functions $\mathbf{M}_{st}$ and $\mathbf{N}_{st}$ according to (5.4). Solutions for $\mathbf{a} = \mathbf{e}_x, \mathbf{e}_y, \mathbf{e}_z, r\mathbf{e}_r$ are given in [87]. In order to give an impression what the vector wave functions in oblate spheroidal coordinates look like, the choice $\mathbf{a} = \mathbf{e}_z$, which seems to be rather intuitive bearing in mind (5.17), yields $\mathbf{M}_{st}^z$ [87]:

$$M_{st,\eta}^z(\eta,\xi,\varphi) = \frac{2s\eta}{\bar{d}\sqrt{(\xi^2+\eta^2)(1-\eta^2)}} \mathcal{S}_{st}(-jc,\eta)\mathcal{R}_{st}^{(4)}(-jc,j\xi) \begin{Bmatrix} \sin(s\varphi) \\ -\cos(s\varphi) \end{Bmatrix},$$

$$M_{st,\xi}^z(\eta,\xi,\varphi) = \frac{2s\xi}{\bar{d}\sqrt{(\xi^2+\eta^2)(\xi^2+1)}} \mathcal{S}_{st}(-jc,\eta)\mathcal{R}_{st}^{(4)}(-jc,j\xi) \begin{Bmatrix} -\sin(s\varphi) \\ \cos(s\varphi) \end{Bmatrix},$$

$$M_{st,\varphi}^z(\eta,\xi,\varphi) = \frac{2\sqrt{(\xi^2+1)(1-\eta^2)}}{\bar{d}(\xi^2+\eta^2)} \left(\eta \frac{\mathrm{d}}{\mathrm{d}\eta} \mathcal{S}_{st}(-jc,\eta)\mathcal{R}_{st}^{(4)}(-jc,j\xi) \right.$$

$$\left. - \xi \mathcal{S}_{st}(-jc,\eta) \frac{\mathrm{d}}{\mathrm{d}\xi} \mathcal{R}_{st}^{(4)}(-jc,j\xi) \right) \begin{Bmatrix} \cos(s\varphi) \\ \sin(s\varphi) \end{Bmatrix}. \qquad (5.19)$$

For $\xi = 0$, this reduces to

$$M_{st,\eta}^{z}(\eta',\varphi') = \frac{2}{\bar{d}} \frac{s\mathcal{S}_{st}(-jc,\eta')}{\sqrt{1-\eta'^2}} \mathcal{R}_{st}^{(4)}(-jc,0) \left\{ \begin{array}{c} \sin(s\varphi') \\ -\cos(s\varphi') \end{array} \right\},$$

$$M_{st,\xi}^{z}(\eta',\varphi') = 0,$$

$$M_{st,\varphi}^{z}(\eta',\varphi') = \frac{2}{\bar{d}} \frac{\sqrt{1-\eta'^2}}{\eta'} \frac{\mathrm{d}}{\mathrm{d}\eta'} \mathcal{S}_{st}(-jc,\eta') \mathcal{R}_{st}^{(4)}(-jc,0) \left\{ \begin{array}{c} \cos(s\varphi') \\ \sin(s\varphi') \end{array} \right\}, \quad (5.20)$$

where $\eta' \in [0,1]$, which may be replaced by ρ' according to (5.16) and (5.17). The vector wave function $\mathbf{M}_{st}^{z}$ lies on the surface of the circular disk and can be used to compute the corresponding surface current densities, as outlined for the sphere. It is noted that the spheroidal radial functions are now functions of $c = \frac{1}{2}k\bar{d} = kR_{\mathrm{u}}$ alone, i.e., the electrical size of the circular disk.[83]

In contrast to the choice $\mathbf{a} = \mathbf{e}_z$, [29] proposes $\mathbf{a} = r\mathbf{e}_r$, which is also used in the derivation of the spherical wave modes, though it is revealed later that this choice does not yield characteristic modes. Unfortunately, none of the vector wave functions given in [87] results in characteristic modes. This is found by a thorough analysis of the solutions based on orthogonality considerations and eigenvalue computations.[84] An analytical expression for the characteristic surface current densities and the eigenvalues of a circular disk is thus not found in the same way as for the sphere.

A thorough analysis regarding the scattering of electromagnetic waves at a circular PEC disk is performed in [89]. This work, too, employs spheroidal wave functions, but includes further boundary conditions in terms of energy. The line of thought, however, is the same as in the development of characteristic modes [23], i.e., based on a scattering problem. The solutions in [89] may therefore be an alternative approach for deriving analytical expressions of the modal surface current densities and the eigenvalues. Unfortunately, the solutions in [89] are given in terms of Debye potentials so that the electromagnetic fields have to be computed by further curl operations.

---

[83]It is expected that the eigenvalues of the characteristic modes of a circular disk can be expressed in terms of the spheroidal radial functions similar to the spherical wave modes. An analytical expression for the eigenvalues could, however, not be derived within the scope of this thesis. A direct replacement of the spherical Bessel functions in (5.11) by their spheroidal counterparts does not yield the correct eigenvalues compared to numerical computations.

[84]Examining the surface current densities alone is deceiving as they may look similar to those of the characteristic modes. This is not a coincidence since the surface current densities are governed by the symmetry of the circular disk, as will be shown in subsection 5.1.2.
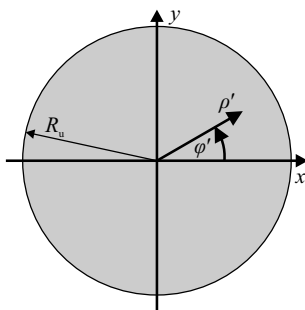
Figure 5.6 Circular disk with radius R_u in xy-plane and polar coordinates.

This directly manifests another problem when working with the spheroidal wave functions. As stated above, they are defined as infinite series expansions of the spherical wave functions. An analytical treatment of these functions is thus limited and computations are usually conducted numerically [86, 87]. For example, orthogonality relations, which are necessary for verifying characteristic modes, are not readily available [85], in contrast to the spherical wave functions [84]. For these reasons, a complete analytical expression of the characteristic modes of a circular PEC disk lies beyond the scope of this thesis.

However, this finding does not render the introduction of the spheroidal wave functions useless for the purpose of this thesis. As will be shown in the following subsection, the important coordinate for the symmetry analysis of a circular disk is the azimuthal angle φ'. The φ'-dependence of any known solution to the vector Helmholtz equation in oblate spheroidal coordinates is expressed in terms of the trigonometric functions cos and sin (cf. (5.19) and the solutions in [29, 87]), which is traced back to the generating function (5.18) and the underlying scalar Helmholtz equation in oblate spheroidal coordinates [87].

5.1.2 Symmetry Analysis

Although an analytical expression for the characteristic modes of the circular PEC disk could not be derived, the important relations in order to conduct a generic symmetry analysis are now available. To this end, the transformation operators (section 3.1.3) of the symmetry group D_∞ should be inspected first. The rotation matrices of D_∞ are given in Table 3.16 and it is recalled that the group elements are functions of one parameter, the rotation angle Φ (Fig. 3.10).

Furthermore, the symmetry group consists of two regions, one containing the rotations $C_z(\Phi)$ about the z-axis including the identity for $\Phi = 0$, and one containing the rotations $C_2(\Phi)$ about the axes perpendicular to the z-axis.

In the previous subsection, it was shown that functions on a circular disk are purposefully expressed in terms of the polar coordinates ρ',φ' (Fig. 5.6) so that the coordinate vector $\mathbf{r}'$ has the form given in (5.16). In this case, the product $\mathbf{R}^{-1}(T)\mathbf{r}'$, which is required for computing the transformation operators according to (3.12) and (3.13), can be simplified to

$$\mathbf{R}^{-1}\big(C_z(\Phi)\big)\mathbf{r}'(\rho',\varphi') = \rho' \begin{pmatrix} \cos(\varphi' + \Phi) \\ \sin(\varphi' + \Phi) \\ 0 \end{pmatrix} = \mathbf{r}'(\rho',\varphi' + \Phi), \qquad (5.21a)$$

$$\mathbf{R}^{-1}\big(C_2(\Phi)\big)\mathbf{r}'(\rho',\varphi') = \rho' \begin{pmatrix} \cos(\varphi' - 2\Phi) \\ -\sin(\varphi' - 2\Phi) \\ 0 \end{pmatrix} = \mathbf{r}'(\rho',2\Phi - \varphi'), \qquad (5.21b)$$

i.e., a coordinate transformation of D_∞ only affects the coordinate φ'. Consequently, the transformation operators of D_∞ applied to an arbitrary scalar function f only manipulate the φ'-dependence:

$$P\big(C_z(\Phi)\big)f(\rho',\varphi') = f(\rho',\varphi' + \Phi), \qquad (5.22a)$$
$$P\big(C_2(\Phi)\big)f(\rho',\varphi') = f(\rho',2\Phi - \varphi'). \qquad (5.22b)$$

Finally, applying the transformation operators to an arbitrary vector-valued function $\mathbf{f}$ yields

$$P\big(C_z(\Phi)\big)\mathbf{f}(\rho',\varphi') = \begin{pmatrix} f_x(\rho',\varphi' + \Phi)\cos\Phi + f_y(\rho',\varphi' + \Phi)\sin\Phi \\ -f_x(\rho',\varphi' + \Phi)\sin\Phi + f_y(\rho',\varphi' + \Phi)\cos\Phi \\ 0 \end{pmatrix},$$

$$(5.23a)$$

$$P\big(C_2(\Phi)\big)\mathbf{f}(\rho',\varphi') = \begin{pmatrix} f_x(\rho',2\Phi - \varphi')\cos(2\Phi) + f_y(\rho',2\Phi - \varphi')\sin(2\Phi) \\ f_x(\rho',2\Phi - \varphi')\sin(2\Phi) - f_y(\rho',2\Phi - \varphi')\cos(2\Phi) \\ 0 \end{pmatrix}.$$

$$(5.23b)$$

It is noted that the function needs to be expressed in terms of its Cartesian components f_x, f_y in order to compute the matrix product required by (3.13).

The analysis of the vector wave functions **M** and **N** given in [87] yields that a generic surface current density **J** on a circular disk may be expressed as follows:

$$\mathbf{J}_{st}(\rho',\varphi') = \mathscr{R}^{\rho}_{st}(c,\rho') \begin{Bmatrix} \cos(s\varphi') \\ \sin(s\varphi') \end{Bmatrix} \mathbf{e}_{\rho} + \mathscr{R}^{\varphi}_{st}(c,\rho') \begin{Bmatrix} -\sin(s\varphi') \\ \cos(s\varphi') \end{Bmatrix} \mathbf{e}_{\varphi}. \quad (5.24)$$

The surface current density consists of a radial and an azimuthal component. The generic functions $\mathscr{R}^{\rho}_{st}$ and $\mathscr{R}^{\varphi}_{st}$ contain the dependence on the electrical size $c = kR_{\mathrm{u}}$ and on the radial coordinate ρ' and thus, in particular, the impact of the spheroidal wave functions (cf. (5.20)). The φ'-dependence, which is required for the symmetry analysis as derived above, in contrast, is given explicitly in terms of the trigonometric functions, retaining the even/odd distinction. For $s \geq 1$, there is always an even-odd pair of surface current densities. For $s = 0$, however, the general surface current density collapses into one purely radial and one purely azimuthal surface current density:

$$\mathbf{J}^{\rho}_{0t}(\rho',\varphi') = \mathscr{R}^{\rho}_{st}(c,\rho')\mathbf{e}_{\rho}, \quad (5.25)$$

$$\mathbf{J}^{\varphi}_{0t}(\rho',\varphi') = \mathscr{R}^{\varphi}_{st}(c,\rho')\mathbf{e}_{\varphi}. \quad (5.26)$$

These special cases have no φ'-dependence.

In order to gain insight into the symmetry properties of the surface current densities which may possibly exist on a circular disk, an assignment to the irreducible representations of the symmetry group D_{∞} is now conducted by means of the character projection operators (3.66). To this end, the transformation operators (5.23) are required and the generic surface current density needs to be written in terms of its Cartesian components:

$$J_{st,x}(\rho',\varphi') = \mathscr{R}^{\rho}_{st}(c,\rho') \begin{Bmatrix} \cos(s\varphi') \\ \sin(s\varphi') \end{Bmatrix} \cos\varphi' - \mathscr{R}^{\varphi}_{st}(c,\rho') \begin{Bmatrix} -\sin(s\varphi') \\ \cos(s\varphi') \end{Bmatrix} \sin\varphi',$$
$$(5.27a)$$

$$J_{st,y}(\rho',\varphi') = \mathscr{R}^{\rho}_{st}(c,\rho') \begin{Bmatrix} \cos(s\varphi') \\ \sin(s\varphi') \end{Bmatrix} \sin\varphi' + \mathscr{R}^{\varphi}_{st}(c,\rho') \begin{Bmatrix} -\sin(s\varphi') \\ \cos(s\varphi') \end{Bmatrix} \cos\varphi'.$$
$$(5.27b)$$

Putting all pieces together, the character projection operators (3.66) are now applied to the generic surface current densities. Starting with $\mathbf{J}^{\rho}_{0t}$ (5.25), the projection yields

$$\mathcal{P}^{(1)}\mathbf{J}^{\rho}_{0t}(\rho',\varphi') = \mathscr{R}^{\rho}_{st}(c,\rho')\mathbf{e}_{\rho} = \mathbf{J}^{\rho}_{0t}(\rho',\varphi'), \quad (5.28a)$$

$$\mathcal{P}^{(2)}\mathbf{J}_{0t}^{\rho}(\rho',\varphi') = \mathbf{0}, \tag{5.28b}$$

$$\mathcal{P}^{(2+\tau)}\mathbf{J}_{0t}^{\rho}(\rho',\varphi') = \mathbf{0}. \tag{5.28c}$$

Obviously, the surface current densities $\mathbf{J}_{0t}^{\rho}$ belong to the first irreducible representation $\Gamma^{(1)} = A_1$ independent of t. This result is not surprising as they have only a radial component and no φ'-dependence. Accordingly, these surface current densities are invariant under all symmetry operations of the circular disk. The index t only affects the radial distribution and thus distinguishes the different modes belonging to A_1.

Applying the character projection operators to $\mathbf{J}_{0t}^{\varphi}$ (5.26) yields

$$\mathcal{P}^{(1)}\mathbf{J}_{0t}^{\varphi}(\rho',\varphi') = \mathbf{0}, \tag{5.29a}$$

$$\mathcal{P}^{(2)}\mathbf{J}_{0t}^{\varphi}(\rho',\varphi') = \mathscr{R}_{st}^{\varphi}(c,\rho')\mathbf{e}_{\varphi} = \mathbf{J}_{0t}^{\varphi}(\rho',\varphi'), \tag{5.29b}$$

$$\mathcal{P}^{(2+\tau)}\mathbf{J}_{0t}^{\varphi}(\rho',\varphi') = \mathbf{0}. \tag{5.29c}$$

The surface current densities $\mathbf{J}_{0t}^{\varphi}$ belong to the second irreducible representation $\Gamma^{(2)} = A_2$ independent of t. Again, this result is not surprising as they have only an azimuthal component and no φ'-dependence. Accordingly, these surface current densities are invariant under the rotations about the z-axis, but inverted by the rotations about the other axes.

Finally, the application of the character projection operators to $\mathbf{J}_{st}$ (5.24) for $s \geq 1$ yields

$$\mathcal{P}^{(1)}\mathbf{J}_{st}(\rho',\varphi') = \mathbf{0}, \tag{5.30a}$$

$$\mathcal{P}^{(2)}\mathbf{J}_{st}(\rho',\varphi') = \mathbf{0}, \tag{5.30b}$$

$$\mathcal{P}^{(2+\tau)}\mathbf{J}_{st}(\rho',\varphi') = \begin{cases} \mathbf{J}_{st}(\rho',\varphi') & s = \tau \\ \mathbf{0} & s \neq \tau \end{cases}. \tag{5.30c}$$

The surface current densities with $s \geq 1$ belong to the two-dimensional irreducible representations E_{τ}. Obviously, an even-odd pair for a given s belongs to $\Gamma^{(2+s)} = E_s$, forming a two-fold degenerate pair of modes. Thus, the index s is equivalent to the index τ of the two-dimensional irreducible representations of D_{∞} (cf. Table 3.17). Modes with $s = 1$ belong to $\Gamma^{(3)} = E_1$, modes with $s = 2$ belong to $\Gamma^{(4)} = E_2$, and so on.

This generic symmetry analysis is generally applicable to modal surface current densities on a circular disk as they take the form (5.24) based on the analysis of the homogeneous vector Helmholtz equation. If analytical expressions

of the characteristic surface current densities on a circular disk were available, the results above could be directly adopted and the modes could be assigned to the irreducible representations by means of the index s, where the index t would distinguish the fundamental mode from the higher-order modes and even-odd pairs would be degenerate. Based on this knowledge, the numerically computed characteristic modes can now be assigned manually to the irreducible representations in a quite comfortable way.

5.2 Minimum Electrical Size

It is now possible to conduct a symmetry analysis of the numerically computed characteristic modes of a circular PEC disk. The disk is supposed to serve as the representative of the regular polygonal PEC plates and it will be shown how the characteristic modes of the regular polygonal plates and the circular disk are related. Based on these relations, it is possible to use the eigenvalues of the circular disk for determining an estimate for the minimum electrical size of the regular polygonal plates.

5.2.1 Symmetry Analysis of Regular Polygonal Plates

The characteristic surface current densities of the first 16 characteristic modes of a circular PEC disk with the electrical size $kR_{\mathrm{u}} = 4$ computed numerically with a non-symmetric triangular mesh are depicted in Fig. 5.7.[85] With the knowledge gained in the previous section, the characteristic surface current densities are now assigned to the irreducible representations of the symmetry group D_∞ by means of a manual inspection.

Mode 8 (Fig. 5.7(h)) belongs to the one-dimensional first irreducible representation $\Gamma^{(1)} = A_1$ (identity representation) as it only has a radial component which is constant in azimuthal direction and thus is invariant under all symmetry operations of the circular disk (cf. (5.28)). In contrast, mode 7 (Fig. 5.7(g)), whose surface current density forms a "loop", belongs to the one-dimensional second irreducible representation $\Gamma^{(2)} = A_2$ as it only has an azimuthal component which is constant in azimuthal direction (cf. (5.29)).

The remaining characteristic modes in Fig. 5.7 form degenerate pairs of orthogonal characteristic surface current densities (even-odd pairs) belonging

---

[85]Although the mesh is not symmetric, a sufficiently fine mesh (section 2.3.4) ensures that the symmetry of the characteristic surface current densities is reproduced to a qualitatively acceptable degree.
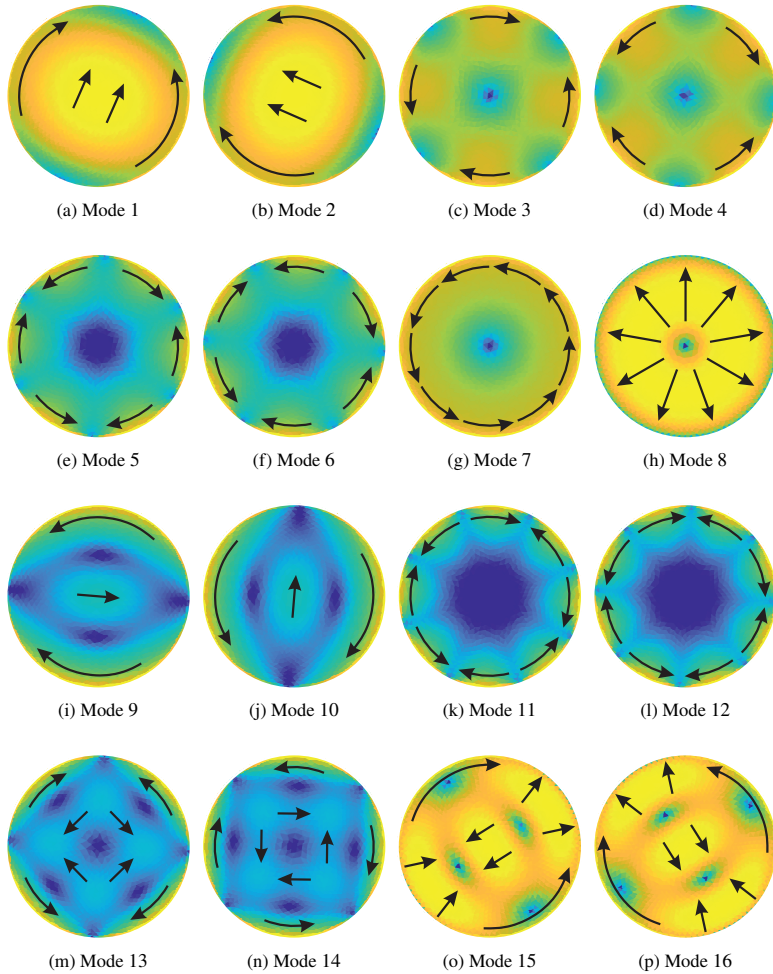
Figure 5.7 Normalized surface current densities of the first 16 characteristic modes of circular PEC disk with electrical size $kR_u = 4$. Principal current directions denoted by arrows. Modes sorted according to their significance. Color bar in Fig. 2.6(e). (a)–(b) Modes 1 and 2 belonging to E_1 ("dipole modes"). (c)–(d) Modes 3 and 4 belonging to E_2 ("quadrupole modes"). (e)–(f) Modes 5 and 6 belonging to E_3 ("hexapole modes"). (g) Mode 7 belonging to A_2 ("loop mode"). (h) Mode 8 belonging to A_1 ("invariant mode"). (i)–(j) Modes 9 and 10 belonging to E_1 (higher-order modes). (k)–(l) Modes 11 and 12 belonging to E_4 ("octopole modes"). (m)–(n) Modes 13 and 14 belonging to E_2 (higher-order modes). (o)–(p) Modes 15 and 16 belonging to E_1 (higher-order modes).

to the two-dimensional irreducible representations E_s. In order to assign them to the correct irreducible representations, the index s has to be determined. A closer inspection of the generic surface current density in (5.24) reveals that s governs the number of nulls of both the radial and the azimuthal component along the perimeter of the disk. Obviously, the number of nulls is equal to $2s$. Therefore, the mode pair 1-2 (Fig. 5.7(a) and (b)) has the index $s = 1$ and thus belongs to the third irreducible representation (the first two-dimensional irreducible representation) $\Gamma^{(3)} = E_1$. In the same way, it is found that the mode pair 3-4 (Fig. 5.7(c) and (d)) belongs to the fourth irreducible representation $\Gamma^{(4)} = E_2$, the mode pair 5-6 (Fig. 5.7(e) and (f)) belongs to the fifth irreducible representation $\Gamma^{(5)} = E_3$, and the mode pair 11-12 (Fig. 5.7(k) and (l)) belongs to the sixth irreducible representation $\Gamma^{(6)} = E_4$. All these modes are the fundamental modes of their respective irreducible representations. The mode pair 9-10 (Fig. 5.7(i) and (j)), in contrast, is a pair of higher-order modes belonging to $\Gamma^{(3)} = E_1$. Likewise, the mode pairs 13-14 (Fig. 5.7(m) and (n)) and 15-16 (Fig. 5.7(o) and (p)) are higher-order modes belonging to E_2 and E_1, respectively. The surface current densities of these higher-order modes have a more complicated radial dependence corresponding to a higher index t.

Some of the characteristic surface current densities shown in Fig. 5.7 have already been encountered qualitatively on the regular polygonal PEC plates analyzed in chapter 4, i.e., the equilateral triangular plate (section 4.1), the square plate (section 4.5.1), and the regular hexagonal plate (section 4.5.2). For example, there is always an invariant characteristic surface current density (Fig. 4.3(a), Fig. 4.21(f), Fig. 4.30(g)) and a "loop"-like characteristic surface current density (Fig. 4.3(f), Fig. 4.21(e), Fig. 4.30(f)). It thus suggests itself that the irreducible representations of the different D-groups (dihedral groups) are related.[86] In fact, each dihedral group always has an identity representation $\Gamma^{(1)} = A_1$ which the invariant characteristic surface current densities belong to. The fundamental characteristic modes of the circular PEC disk and the regular polygonal PEC plates explicitly analyzed in chapter 4 belonging to A_1 are listed in Table 5.1(a). Furthermore, there is always a second one-dimensional irreducible representation $\Gamma^{(2)} = A_2$ which the "loop"-like characteristic surface current densities belong to (Table 5.1(b)). Moreover, each dihedral group has a two-dimensional irreducible representation E_1. The fundamental modes belonging to this representation may colloquially be termed as "dipole modes" (Table 5.1(c)).

---

[86]The dihedral group D_2 is not considered here as it is the symmetry group of a rectangular plate (see section 3.4.3), which does not belong to the family of the regular polygonal plates.

Group	D_∞	D_3	D_4	D_6
Mode n	8	1	6	7
Figure	5.7(h)	4.3(a)	4.21(f)	4.30(g)
Γ-notation	$\Gamma^{(1)}$	$\Gamma^{(1)}$	$\Gamma^{(1)}$	$\Gamma^{(1)}$

(a) A_1: "Invariant modes"

Group	D_∞	D_3	D_4	D_6
Mode n	7	6	5	6
Figure	5.7(g)	4.3(f)	4.21(e)	4.30(f)
Γ-notation	$\Gamma^{(2)}$	$\Gamma^{(2)}$	$\Gamma^{(2)}$	$\Gamma^{(2)}$

(b) A_2: "Loop modes"

Group	D_∞	D_3	D_4	D_6
Mode n	1, 2	2, 3	1, 2	1, 2
Figure	5.7(a),(b)	4.3(b),(c)	4.21(a),(b)	4.30(a),(b)
Γ-notation	$\Gamma^{(3)}$	$\Gamma^{(3)}$	$\Gamma^{(5)}$	$\Gamma^{(5)}$

(c) E_1: "Dipole modes"

Table 5.1 Fundamental characteristic modes of circular PEC disk and regular polygonal PEC plates analyzed in chapter 4 belonging to the irreducible representations A_1, A_2, and E_1 of the dihedral groups. For ease of reference, the Γ-notation denotes to which $\Gamma^{(p)}$ of the respective group the given representation corresponds.

In the Γ-notation predominantly used throughout this thesis, this irreducible representation is usually the first of the two-dimensional ones following the one-dimensional irreducible representations. The corresponding fundamental modes are typically the first characteristic modes to become significant (cf. Fig. 4.11, Fig. 4.19, Fig. 4.28).

The symmetry group D_3 of the equilateral triangular plate only has these three irreducible representations. The symmetry group D_4 of the square plate has two additional one-dimensional irreducible representations $\Gamma^{(3)} = B_1$ and $\Gamma^{(4)} = B_2$. The surface current densities of the corresponding fundamental characteristic modes may be termed as non-degenerate "quadrupole modes" (Fig. 4.21(c) and (d)). Such "quadrupole modes" also appear on the regular hexagonal plate. In this case, however, they are degenerate and belong to the second two-dimensional irreducible representation $\Gamma^{(6)} = E_2$ (Fig. 4.30(c) and (d)). As a matter of fact, the symmetry group D_5 of a regular pentagonal plate already has this second two-dimensional irreducible representation E_2 instead of B_1 and B_2 [77]. Obviously, the two additional one-dimensional irreducible

Group	Irreducible representations							
D_3	A_1	A_2	E_1	N/A	N/A	N/A	N/A	N/A
D_4	A_1	A_2	E_1	B_1, B_2	N/A	N/A	N/A	N/A
D_5	A_1	A_2	E_1	E_2	N/A	N/A	N/A	N/A
D_6	A_1	A_2	E_1	E_2	B_1, B_2	N/A	N/A	N/A
D_7	A_1	A_2	E_1	E_2	E_3	N/A	N/A	N/A
D_8	A_1	A_2	E_1	E_2	E_3	B_1, B_2	N/A	N/A
D_9	A_1	A_2	E_1	E_2	E_3	E_4	N/A	N/A
D_{10}	A_1	A_2	E_1	E_2	E_3	E_4	B_1, B_2	N/A
$\vdots$				$\vdots$				
D_∞	A_1	A_2	E_1	E_2	E_3	E_4	E_5	$\cdots$

Table 5.2   Evolution of irreducible representations of symmetry groups of regular polygonal plates.

representations B_1 and B_2 evolve into an additional two-dimensional irreducible representation from one dihedral group to the next higher one. This evolution is schematically illustrated in Table 5.2. All following dihedral groups have this second two-dimensional irreducible representation E_2 until arriving at the symmetry group D_∞ of the circular disk, which consequently also offers two degenerate "quadrupole modes" (Fig. 5.7(c) and (d)). In the same way, the symmetry group D_6 of the regular hexagonal plate has two additional one-dimensional irreducible representations $\Gamma^{(3)} = B_1$ and $\Gamma^{(4)} = B_2$. In this case, the surface current densities of the corresponding fundamental characteristic modes may be termed as non-degenerate "hexapole modes" (Fig. 4.30(e) and (h)). The next higher dihedral group D_7, which is the symmetry group of a regular heptagonal plate, instead has a third two-dimensional irreducible representation E_3 (Table 5.2), which a pair of degenerate "hexapole modes" belongs to. This pair is also present on the circular disk (Fig. 5.7(e) and (f)).[87]

    Table 5.2 depicts the evolution of the irreducible representations of the dihedral groups. It illustrates how one-dimensional irreducible representations are added with increasing group order and how they evolve into a two-dimensional irreducible representation, finally arriving at D_∞ having exactly two one-dimensional

---

[87]It is noteworthy that "hexapole modes", for instance, can also be identified on the regular polygonal plates of lower order, e.g., the equilateral triangular plate (Fig. 4.3(i) and (l)). In these cases, however, they belong to the higher-order modes of one of the respective irreducible representations and are thus not of interest for the purpose of this thesis.

and an infinite number of two-dimensional irreducible representations. Furthermore, it becomes evident why it has been purposeful to temporarily switch to the alternative notation using A_1, A_2, B_1, B_2, and E_s instead of the Γ-notation as the alternative notation better reflects the evolution of the irreducible representations of the dihedral groups.

The symmetry group D_∞ (infinite dihedral group) of the circular disk is the generalization of the finite dihedral groups, i.e., the symmetry groups of the regular polygonal plates. As a consequence, the circular PEC disk qualitatively offers all possible characteristic surface current densities which may be found on an arbitrary regular polygonal PEC plate. Therefore, *a priori* knowledge about what characteristic surface current densities to expect is gained by analyzing the circular PEC disk alone. This knowledge can then be applied directly to a given regular polygonal plate taking into account the relationships between the dihedral groups in Table 5.2.

This chapter focuses on the family of the regular polygonal plates whose symmetry groups are the dihedral groups. Nevertheless, the methods introduced so far can be applied to other families of geometric objects as well. For example, the symmetry group of the family of the regular pyramids are the C_v-groups (cf. section 3.3.5). The generalization of the regular pyramids is the right circular cone whose symmetry group is $C_{\infty v}$ [77]. A generalized analysis of this family of geometric objects can thus be conducted by analyzing the circular cone. Moreover, the C_v-groups are isomorphic to the respective D-groups. In particular, the irreducible representations are the same (Table 5.2). Therefore, the isomorphism can be exploited in order to derive the symmetry properties of the characteristic modes of the regular pyramids from their polygonal counterparts, as was done in section 4.5.3 for the square pyramid.

As another example, the symmetry groups of the family of the regular prisms are the D_h-groups. The generalization of the regular prisms is the circular cylinder whose symmetry group is $D_{\infty h}$ [77]. As introduced in section 3.2.3, the D_h-groups are direct-products of the group C_s and the respective D-groups. Again, this relationship can be exploited in order to derive the symmetry properties of the characteristic modes of the regular prisms from their polygonal counterparts, as was done in section 4.5.4 for the square cuboid.

Such relations between the different families of symmetry groups allow to directly build upon the knowledge about the regular polygonal plates gained in this chapter and apply it to more complicated geometries.[88]

---

[88]For a list of examples, refer to Table 4.7.

5.2.2 Modal Significances of Regular Polygonal Plates

Having extensively analyzed the characteristic surface current densities, it is time to turn the attention towards the modal significances. The numerically computed modal significances of the circular PEC disk are shown in Fig. 5.8. Each characteristic mode becomes significant at a certain electrical size kR_u and then stays significant. This behavior is already known from the regular polygonal plates analyzed in chapter 4 (Fig. 4.11, Fig. 4.19, Fig. 4.28).
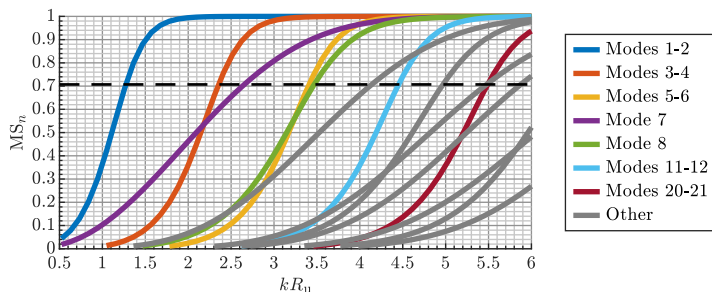

Figure 5.8   Modal significances of circular PEC disk as functions of electrical size kR_u. Fundamental characteristic modes in color, higher-order modes in gray. The modes are sorted according to their significance at $kR_u = 4$.

It is thus purposeful to directly compare the modal significances of the circular disk and the regular polygonal plates. In order to determine the minimum electrical size, only the fundamental modes of each irreducible representation are of interest, as discussed in section 4.3. In Fig. 5.9, the modal significances of the fundamental modes of the irreducible representations A_1, A_2, E_1, E_2, E_3, and E_4 are shown. The results are extracted from the modal analyses of the equilateral triangular PEC plate (D_3), the square PEC plate (D_4), the regular pentagonal PEC plate (D_5), the regular hexagonal PEC plate (D_6), the regular octagonal PEC plate (D_8), the regular decagonal PEC plate (D_{10}), and the circular PEC disk (D_∞). It has to be noted that not all of these groups have all the irreducible representations taken into account in Fig. 5.9 (cf. Table 5.2).

At first sight, it is evident that the significance curves of the circular disk and the regular polygonal plates are very similar. It is thus deduced that not only the characteristic surface current densities of the regular polygonal plates are generalized by the circular disk, but also the modal significances (eigenvalues). In other words, the fundamental behavior of the modal significances of the
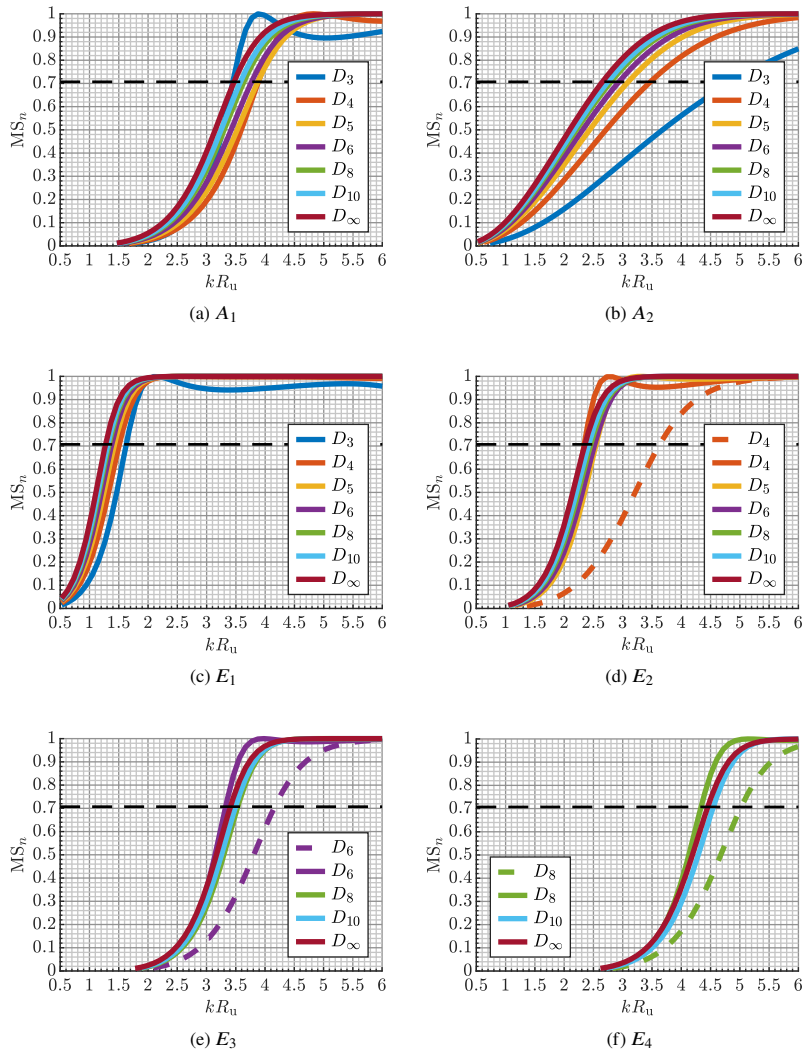
Figure 5.9 Modal significances of the fundamental characteristic modes of different irreducible representations of selected dihedral groups as functions of electrical size kR_{u}. (a) A_1. (b) A_2. (c) E_1. (d) E_2 (B_1 and B_2 in the case of D_4). (e) E_3 (B_1 and B_2 in the case of D_6) (f) E_4 (B_1 and B_2 in the case of D_8). Dashed lines denote B_1, solid lines of the same color denote B_2.

regular polygonal plates can be deduced from the circular disk, as has also been the case for the characteristic surface current densities.

Another important observation is that in most cases the characteristic mode of the circular disk is the first to become significant. With decreasing group order, the modes tend to become significant at larger electrical sizes. As the circular disk is the limiting case of the regular polygonal plates, the electrical size at which a fundamental mode of the circular disk becomes significant can thus be considered a good estimate for the minimum electrical size of the regular polygonal plates that are supposed to excite this fundamental mode. Hence, the radius of the circular disk which ensures that a certain set of fundamental modes is significant serves as a guideline to find the minimum circumradius of a regular polygonal plate supporting the same set of fundamental modes.

In Fig. 5.9(d), (e), and (f), the two fundamental modes of D_4, D_6, and D_8, respectively, belong to the irreducible representations B_1 and B_2 (Table. 5.2) and are thus non-degenerate. Notably, the fundamental modes belonging to B_2 (solid lines) become significant at slightly smaller electrical sizes than the corresponding modes of the circular disk. Nevertheless, the corresponding significance curve of the circular disk still serves as a good estimate. In contrast, the fundamental modes belonging to B_1 (dashed lines) become significant at considerably larger electrical sizes. If the number of orthogonal antenna ports to be realized is less than the number of mutually orthogonal sets of characteristic surface current densities offered by an antenna geometry, i.e., the upper bound for orthogonal antenna ports as defined in section 4.4.2 is not to be reached, it is decisive for the electrical size of the antenna which sets of modes are used in order to realize the ports. If this freedom of choice exists, it is deduced from Fig. 5.9 that the fundamental modes belonging to B_1 (dashed lines) should be avoided in order to minimize the electrical antenna size. For higher symmetry orders, however, these differences become less pronounced as the regular polygonal plates approach the circular disk.

5.2.3 Application Example

In order to illustrate how the observations made in the previous subsections can be applied purposefully to a multimode antenna design, an example is considered. The goal is to design a six-port multimode antenna, i.e., an antenna with six orthogonal antenna ports, each exciting a different set of characteristic modes. The antenna is intended to have a low profile, such that the family of the regular polygonal plates is chosen in order to find a suitable basic antenna
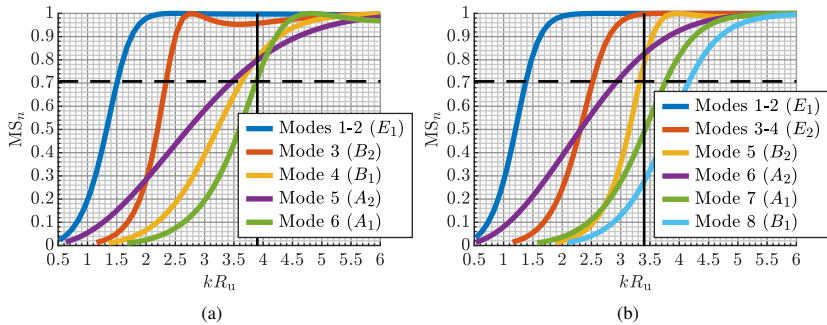
Figure 5.10   Modal significances of fundamental characteristic modes of square PEC plate and regular hexagonal PEC plate as functions of electrical size kR_u. Minimum electrical size for realizing six orthogonal antenna ports marked by vertical black line. Modes sorted according to the analyses conducted in sections 4.5.1 and 4.5.2, respectively. (a) Square PEC plate with minimum electrical circumradius $kR_u \approx 3.9$. (b) Regular hexagonal PEC plate with minimum electrical circumradius $kR_u \approx 3.4$.

geometry. A look at Table 4.7 reveals that the square plate (D_4) is the antenna geometry of lowest symmetry order within the family of the regular polygonal plates that offers six orthogonal antenna ports. In this case, the upper bound of orthogonal antenna ports offered by the square plate has to be reached. However, the regular polygonal plates of higher symmetry order (D_5, D_6, ...) also offer six orthogonal antenna ports (actually, even more). For example, the regular hexagonal plate offers eight orthogonal antenna ports, but there is nothing to be said against realizing only six. Therefore, the question arises which antenna geometry is better suited for the given task.

With respect to the electrical antenna size, this question can now be answered based on the knowledge gained in this chapter. As a first step, an estimate for the minimum electrical size of a six-port multimode antenna using regular polygonal plates is determined based on the modal analysis of the circular disk. A close inspection of Fig. 5.8 reveals that six fundamental modes are significant at a minimum electrical size of $kR_u \approx 3.5$. Coincidentally, a total of eight fundamental modes is significant at this electrical size as the degenerate mode pair 5-6 as well as mode 8 become significant at approximately the same electrical size. It is thus deduced that the fundamental modes belonging to the irreducible representations E_1 ("dipole modes"), E_2 ("quadrupole modes"), E_3 ("hexapole modes"), A_1 ("invariant mode"), and A_2 ("loop mode") have to be taken into account and a subset of these modes has to be selected.
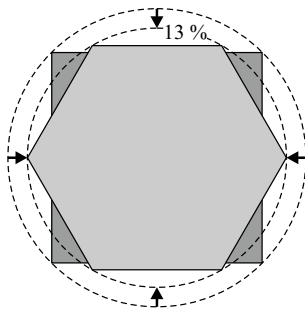
Figure 5.11   Comparison of square PEC plate and regular hexagonal PEC plate for realizing six orthogonal antenna ports with minimum size each. At a given frequency, the circumradius of the regular hexagonal plate is by approximately 13 % smaller than that of the square plate (true to scale).

In the case of the square plate, all six fundamental modes have to be used in order to realize six orthogonal antenna ports. Fig. 5.10(a) shows that its electrical size is governed by mode 6 belonging to A_1. Thus, the minimum achievable electrical circumradius is $kR_u \approx 3.9$ (vertical black line), which is equivalent to a minimum electrical edge length $ka \approx 5.5$. As expected, the minimum electrical size is greater than the estimate derived from the circular disk. The port configuration shown in Fig. 4.23, which is independent of the actual antenna size, can be used to realize the six orthogonal antenna ports.

In the case of the regular hexagonal plate, six out of the eight fundamental modes have to be selected. As is obvious from Fig. 5.10(b), mode 8 belonging to B_1 is not suitable for minimizing the electrical size as it is the last fundamental mode to become significant. This is the typical behavior of the fundamental modes belonging to B_1 already observed in subsection 5.2.2. Mode 7 belonging to A_1 should not be used, either, as it is the second last fundamental mode to become significant. Using the remaining six fundamental modes allows to reduce the electrical size to $kR_u = ka \approx 3.4$. In particular, since the fundamental mode 5 belonging to B_2 is employed as the last mode to become significant, the minimum electrical size is slightly smaller than that predicted by the circular disk, as observed in subsection 5.2.2. The corresponding port configuration consists of the antenna ports shown in Fig. 4.27(b), (d), (e), (f), (g), and (h), which, in particular, all use the same feed points.

As a result, a six-port multimode antenna based on the regular hexagonal plate can be realized with an electrical circumradius by approximately 13 % smaller than that of a six-port multimode antenna based on the square plate. A scale

drawing of the two antenna geometries and their respective circumscribed circles is shown in Fig. 5.11. This example demonstrates how the antenna size can be minimized for a given number of orthogonal antenna ports and a given set of available antenna geometries by means of the methods introduced in this chapter. The relative size reduction achieved in this example is bought by choosing an antenna geometry of higher symmetry order without exploiting its full port potential. For an actual multimode antenna design, however, other considerations have to be taken into account as well. Increasing the symmetry order generally comes at the cost of more feed points per antenna port (cf. Fig. 4.12, Fig. 4.23, and Fig. 4.27) and thus a more complex feed network. Such practical considerations to be taken into account for a complete multimode antenna design will be discussed in the following chapter.

6 Systematic Multimode Antenna Design

Towards the systematic design of multimode antennas with more antenna ports than reported so far in the literature, it has been shown up to this point, among many other things, that there is an upper bound for the number of orthogonal antenna ports. Guidelines on which antenna geometry to choose and how to realize orthogonal antenna ports for a given antenna geometry have been derived based on symmetry analyses. Now, it is time to put the theory into practice.

The aim of this chapter is the systematic design of a multimode antenna that serves as a prototype reaching the upper bound for orthogonal antenna ports. The literature review conducted in section 1.1 has found that multimode antennas with up to four antenna ports are well-established. For example, a four-port multimode antenna based on a square plate is presented in [46]. The square plate has been analyzed rather extensively throughout this thesis. Although it is a comparatively simple geometry, the symmetry analysis performed in section 4.5.1 has revealed that it offers a maximum of six orthogonal antenna ports, i.e., two more ports than reported in the literature. The square plate is thus chosen as the basic antenna geometry for designing a six-port multimode antenna reaching its upper bound for orthogonal antenna ports.

To this end, first of all, the antenna element itself is designed based on a square plate. In the next step, a feed network for driving the feed points of the antenna element is realized. Both parts are then assembled and simulations and measurements of the complete multimode antenna are conducted in order to demonstrate its performance.[89]

6.1 Antenna Element

As demonstrated in section 4.5.1, the square plate offers six mutually orthogonal sets of characteristic surface current densities and thus six orthogonal antenna ports. An ideal port configuration consisting of delta-gap sources is depicted in Fig. 4.23. Of course, delta-gap sources cannot be realized in practice. Therefore, they have to be replaced by practical excitation elements in order to enable

---

[89]The following publications are related to the content of this chapter: [PM19c] (© 2019 IEEE), [PHM21] (© 2021 IEEE).

impedance matching. Furthermore, a feed network is needed which distributes the input signals from the antenna ports to the respective feed points on the antenna element with the correct amplitude and phase relations required by the irreducible representations of the symmetry group. Such a feed network has to be placed somewhere close to the antenna element, which is why a ground plane will be introduced.

First of all, however, the size of the square plate should be determined. According to section 4.3, the minimum electrical size is achieved if the fundamental characteristic modes of each irreducible representation are significant. Based on the modal analysis in Fig. 4.19, the electrical size is chosen to be $kR_u = 4$.[90] With respect to the frequency range of interest from 6 GHz to 8.5 GHz (section 1.1), this electrical size corresponds to the lowest frequency of the frequency band, i.e., 6 GHz, yielding the edge length $a = 45$ mm. As the fundamental characteristic modes stay significant above the minimum electrical size, this choice enables a potential broadband operation over the whole desired frequency range.

6.1.1 Ground Plane

So far, all antenna geometries have been analyzed in free space, i.e., without any objects within their proximity. As stated above, however, a feed network is mandatory in order to realize the orthogonal antenna ports, which consist of several feed points in order to fulfill the symmetry requirements. A ground plane is an appropriate way of accommodating a planar feed network and, if necessary, other circuitry (see, e.g., [46, 48]).
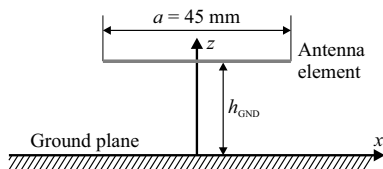
Figure 6.1 Square plate with edge length $a = 45$ mm at height h_{GND} above ground plane (xy-plane).

However, it is well known that a ground plane in close proximity to an antenna compromises its bandwidth. It is thus purposeful to examine the effect of a ground plane on the modal significances of the fundamental characteristic modes.

---

[90]This is not exactly the minimum size found in section 5.2.3, but allows for some safety margin.
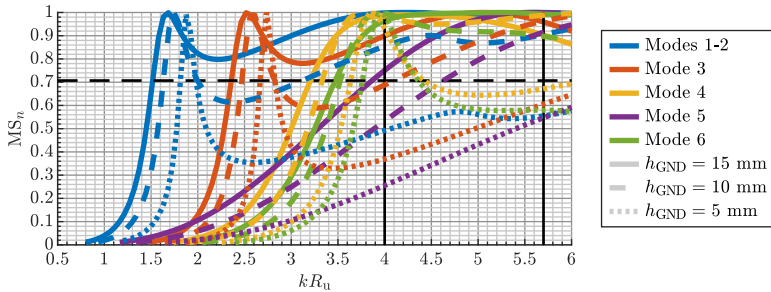
Figure 6.2 Modal significances of fundamental characteristic modes of square PEC plate with edge length $a = 45$ mm for different heights above ground h_{GND} as functions of electrical size kR_{u}. The vertical black lines denote the frequency range from 6 GHz ($kR_{\text{u}} \approx 4$) to 8.5 GHz ($kR_{\text{u}} \approx 5.7$). The modes are sorted according to their significance in free space at $kR_{\text{u}} = 4$ (Fig. 4.19).

To this end, an infinite ground plane is introduced in the xy-plane and the square plate is placed at a height h_{GND} above this ground plane, as illustrated in Fig. 6.1.

The symmetry group of this setup is not D_4 as it is not invariant under the rotations about the axes perpendicular to the z-axis (C_{2x}, C_{2y}, C_{2A}, C_{2B}). Instead, the symmetry group is $C_{4\text{v}}$, which is the already familiar symmetry group of the square pyramid (section 4.5.3), and the aforementioned rotations are replaced by reflections through planes containing the z-axis (σ_{xz}, σ_{yz}, σ_{Az}, σ_{Bz}; Table 3.9). The group $C_{4\text{v}}$ is isomorphic to D_4 so that the characteristic surface current densities are qualitatively the same as those on the square plate in free space and the port configuration according to Fig. 4.23 is still optimal.[91]

Now, a modal analysis of the square PEC plate above the infinite ground plane is conducted. The resulting modal significances of the fundamental characteristic modes for different heights above ground are shown in Fig. 6.2. If the plate is relatively close to the ground plane ($h_{\text{GND}} = 5$ mm, dotted lines), the regions where the modes are significant are narrow. Most of these regions do not overlap, i.e., the modes are significant at different electrical sizes. In particular, none of the modes is significant over the complete desired frequency range from 6 GHz to 8.5 GHz, which corresponds to the electrical size ranging from $kR_{\text{u}} \approx 4$ to $kR_{\text{u}} \approx 5.7$ (vertical black lines). Increasing the height of the square plate, the modes become significant over a larger region. For $h_{\text{GND}} = 15$ mm, all modes recover their broadband behavior, i.e., the fundamental modes become significant

---

[91] The same conclusion can be drawn for finite ground planes which fulfill the square symmetry, e.g., a square, octagonal, or circular ground plane.
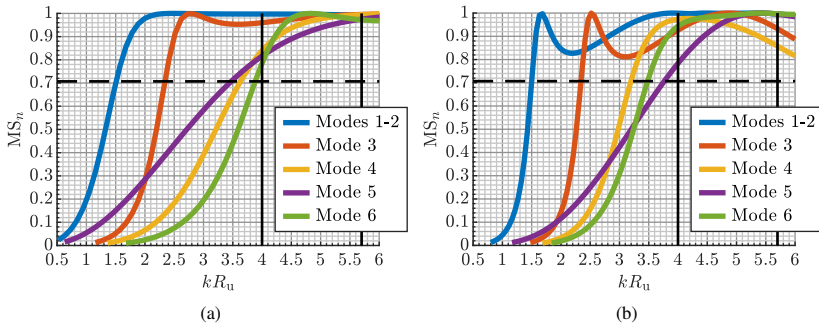
Figure 6.3   Modal significances of fundamental characteristic modes of square PEC plate with edge length $a = 45$ mm as functions of electrical size kR_u. The vertical black lines denote the frequency range from 6 GHz ($kR_u \approx 4$) to 8.5 GHz ($kR_u \approx 5.7$). (a) Square PEC plate in free space. (b) Square PEC plate at height $h_{GND} = 16$ mm above infinite ground plane. The modes are sorted according to their significance in free space at $kR_u = 4$. © 2019 IEEE [PM19c].

at a certain electrical size and then stay significant. In contrast to the free-space case, mode 5 is now the critical mode determining the minimum electrical size.

Based on this analysis, the height above ground is chosen to be $h_{GND} = 16$ mm in order to allow for some safety margin. The corresponding modal significances are shown in Fig. 6.3(b). Compared to the free-space case (Fig. 6.3(a)), the effect of the ground plane on the modal significances is still visible. In the desired frequency range marked by the vertical black lines, however, all six fundamental characteristic modes are significant and behave similar to their respective counterparts in free space.

6.1.2 Excitation Elements and Feed Network

In the next step, the ideal delta-gap sources in Fig. 4.23 have to be replaced by practical excitation elements. In antenna designs based on characteristic modes, capacitive or inductive coupling elements are typically employed [42, 90, 91]. A capacitive coupling element is a metallic structure which is placed in close proximity to the antenna element. It is usually electrically small so that the coupling takes place predominantly via the electric field. An inductive coupling element, in contrast, is some kind of slot cut into the antenna element. Such a coupling element, too, is typically electrically small so that small current loops are formed and the coupling takes place predominantly via the magnetic field.
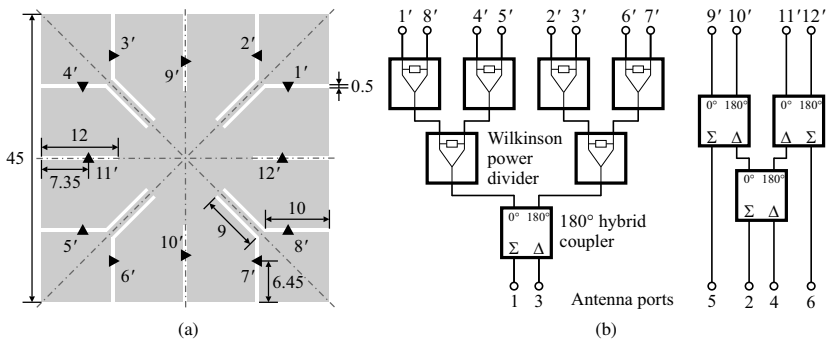
Figure 6.4 Square PEC plate with excitation slots and feed network. (a) Antenna element with symmetrically placed excitation slots. The feed points within the excitation slots are denoted by the arrows and the primed numbers. (b) Ideal feed network consisting of Wilkinson power dividers and 180° hybrid couplers. Dimensions in mm. © 2019 IEEE [PM19c].

These coupling elements have the disadvantage that additional matching circuits are needed in order to perform impedance matching.

The delta-gap sources employed so far can be visualized as electrically very small slots cut into the antenna element (section 2.3.3). It is thus legitimate to interpret them as inductive coupling elements. The input impedance of such an electrically small inductive coupling element consists of a low real part and a high positive (inductive) imaginary part. In order to increase the input resistance and decrease the input reactance, the inductive coupling element should be enlarged. As a matter of fact, there is no reason for restricting the electrical size of the coupling element, apart from the size of the antenna element, of course.

Following this argument, a natural choice for replacing the delta-gap sources is using excitation slots as illustrated in Fig. 6.4(a). The slots are placed at the edge centers and the half-edge centers according to Fig. 4.23 and reach towards the interior of the antenna element. The feed points denoted by the black arrows can be positioned somewhere along the slot length and correspond to a voltage applied across the slot width.[92] The excitation slots are not electrically small. This offers the advantage that the input impedance can be tuned flexibly by adjusting the slot length and the position of the feed point within the slot, allowing inherent impedance matching without need for a matching circuit [46].

---

[92]This kind of excitation is known from slot antennas [5].

When introducing the excitation slots, it is important to preserve the symmetry of the antenna. Although the characteristic modes will in general be modified by the slots, the orthogonality of the characteristic surface current densities and thus the orthogonality of the antenna ports is still governed by the symmetry group of the antenna. Therefore, the symmetry group C_{4v} has to be preserved and the excitation slots have to be placed symmetrically, as illustrated in Fig. 6.4(a). If this condition is fulfilled, it is known *a priori* that the antenna element with symmetrically placed excitation slots offers six orthogonal antenna ports even though the actual characteristic modes are unknown.

In order to distribute the input signals from the actual antenna ports 1, 2, 3, 4, 5, and 6 as defined in section 4.5.1 to the feed points on the antenna element, which are denoted by the primed numbers in Fig. 6.4, a feed network is required. The ports 1 and 3 use the feed points within the slots at the half-edge centers ($1'$ to $8'$), whereas the ports 2, 4, 5, and 6 use the feed points within the slots at the edge centers ($9'$ to $12'$) (cf. Fig. 4.23). Hence, there have to be two separate feed networks, one for ports 1 and 3 and one for ports 2, 4, 5, and 6.

The arrows in Fig. 6.4(a) denote the (arbitrarily chosen) reference voltage directions of the feed points. Based on this reference, the feed network for port 1 has to distribute the port signal to the respective feed points with the same phase (cf. Fig. 4.23(a)). In contrast, the feed network for port 3 has to distribute the port signal to the feed points $2'$, $3'$, $6'$, and $7'$ with a 180° phase difference compared to the feed points $1'$, $4'$, $5'$, and $8'$ (cf. 4.23(c)). These considerations result in the feed network on the left of Fig. 6.4(b) consisting of one 180° hybrid coupler[93] and six Wilkinson power dividers[94]. Since both ports share the same feed network, the 180° hybrid coupler does not only provide the phase difference of 180° for port 3, but also ensures that the two ports are decoupled [93].

In the same way, the feed network for ports 2, 4, 5, and 6 is derived, consisting of three 180° hybrid couplers as shown on the right of Fig. 6.4(b). Again, the hybrid couplers are employed for decoupling the antenna ports that use the same feed points as well as providing the correct phase relations between the feed points as required by Fig. 4.23(b), (d), (e), and (f), taking into account the reference voltage directions in Fig. 6.4(a).

---

[93]The input signal at the Σ-port of an ideal 180° hybrid coupler is split into two output signals at the 0°-port and the 180°-port which are in phase and have equal amplitude ($-3\,\mathrm{dB}$). The input signal at the Δ-port, in contrast, is split into two output signals which have equal amplitude ($-3\,\mathrm{dB}$), but a phase difference of 180°. The input ports are perfectly decoupled [92].

[94]The ideal Wilkinson power divider splits the input signal into two output signals which are in phase and have equal amplitude ($-3\,\mathrm{dB}$) [92].

In summary, the ideal feed network[95] in Fig. 6.4(b) ensures that the feed points on the antenna element are driven with the correct amplitude and phase relations as required by the irreducible representations of the symmetry group C_{4v} in order to realize the six orthogonal antenna ports. Furthermore, it guarantees that the antenna ports are decoupled although they share the same feed points.

6.1.3 Impedance Matching

As stated in the previous subsection, impedance matching can be performed by adjusting the lengths of the slots as well as the positions of the feed points within the slots. However, this task is in general intricate as several antenna ports share the same feed points. Nevertheless, a systematic optimization of the antenna ports is feasible based on symmetry considerations so that the following design guidelines can be derived.

First of all, the symmetry of the antenna must be preserved in order to ensure the orthogonality of the antenna ports, as explained in the previous subsection, resulting in symmetrically placed excitation slots (Fig. 6.4(a)). As an additional consequence, the excitation slots must not be modified independently as this would destroy the symmetry. This greatly simplifies the optimization space as there remain only two optimization parameters per port: The slot length and the feed point position.

Moreover, ports 1 and 3 should be optimized first. This is due to the fact that these ports are symmetric with respect to the x- and y-axis. Correspondingly, the surface current densities excited by these ports, too, are symmetric with respect to these axes (cf. Fig. 4.21(d) and (f)) and hence are not affected by the presence of the excitation slots 9′ to 12′ of ports 2, 4, 5, and 6. Only after optimizing ports 1 and 3, the ports 2, 4, 5, and 6 should be considered since the surface current densities excited by these ports (cf. Fig. 4.21(a), (b), (c), and (e)) and thus the input impedances are affected by the presence of the excitation slots of ports 1 and 3. A further complexity reduction due to symmetry results from the fact that ports 5 and 6 have the same input impedance as they excite degenerate surface current densities. As a consequence, only one of these two ports needs to be optimized actively.

The input impedances of the individual antenna ports are controlled by adjusting the slot lengths and the feed point positions. The slot length principally affects the frequency behavior of the input impedance. Lengthening the slots leads to a shift of the input impedance to lower frequencies. The positions of

---

[95] An ideal feed network is perfectly matched, does not allow mutual coupling, and has no losses.
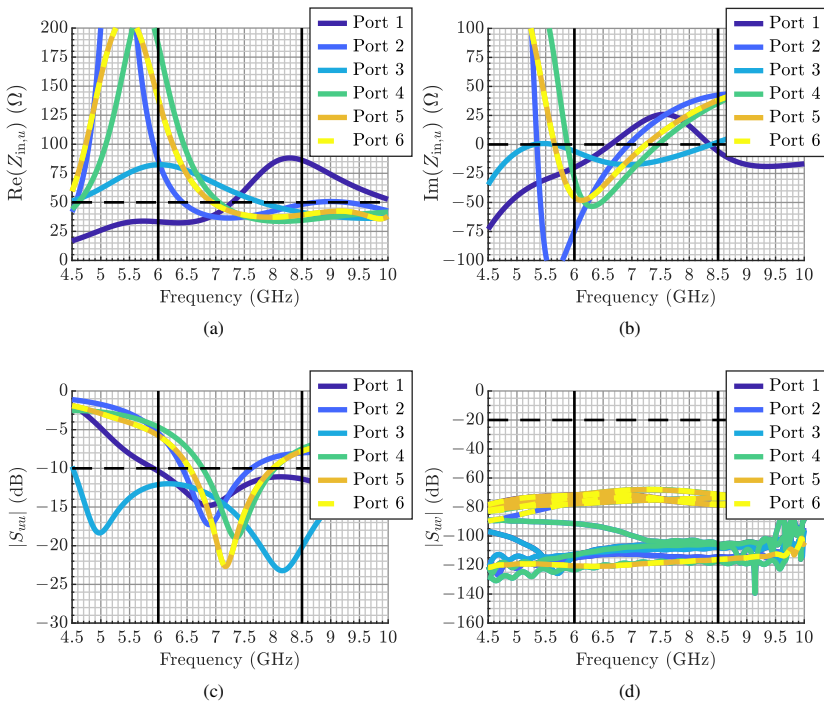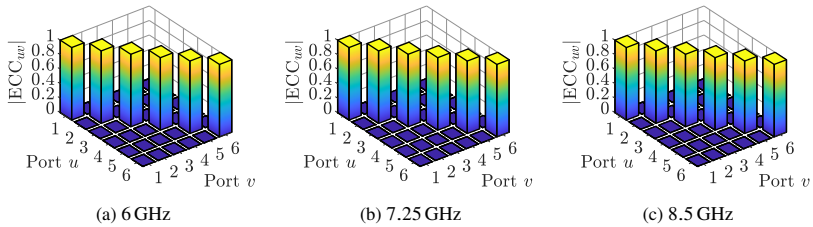
Figure 6.5 Input parameters of square PEC plate with excitation slots and feed network according to Fig. 6.4 located 16 mm above infinite ground plane. (a) Real parts of input impedances. (b) Imaginary parts of input impedances. (c) Absolute values of input reflection coefficients. (d) Absolute values of transmission coefficients from specified ports to all other ports. © 2019 IEEE [PM19c].

the feed points within the slots determine the actual values of the impedance. Shifting the feed points towards the open ends of the slots increases the input resistance and adds capacitance. Moving the feed points towards the short circuit ends of the slots decreases the resistance and adds inductance.

Based on these guidelines, the antenna ports can be optimized systematically in order to achieve an impedance match to 50 Ω within the desired frequency range from 6 GHz to 8.5 GHz. For this purpose, the antenna element according to Fig. 6.4(a) is modeled and simulated using Empire XPU [94].[96] The ideal

---

[96]Empire XPU is used for all electromagnetic simulations in this chapter except the modal analyses.

Figure 6.6 Envelope correlation coefficients of square PEC plate with excitation slots and feed network according to Fig. 6.4 located 16 mm above infinite ground plane. (a) 6 GHz. (b) 7.25 GHz. (c) 8.5 GHz. © 2019 IEEE [PM19c].

feed network according to Fig. 6.4(b) is taken into account by means of a circuit co-simulation. The optimization yields the slot dimensions depicted in Fig. 6.4(a). The slots 1′ to 8′ are bent in order to accommodate their lengths.

The corresponding simulated input parameters are shown in Fig. 6.5. The input impedances (Fig. 6.5(a) and (b)) of ports 1 and 3 show a comparatively flat behavior from 6 GHz to 8.5 GHz close to 50 Ω. This has the consequences that the input reflection coefficients (Fig. 6.5(c)) of these ports are below −10 dB within the frequency range of interest and well beyond. Obviously, the slot excitation is capable of achieving a sufficient impedance match to 50 Ω over the desired frequency range.[97] In contrast, the input impedances (Fig. 6.5(a) and (b)) of ports 2, 4, 5, and 6 show a steeper behavior. As a consequence, these ports are not matched to 50 Ω over the whole frequency range of interest. This is due to the fact that the surface current densities excited by these ports are affected by the presence of the excitation slots of ports 1 and 3. Nevertheless, each of the four ports provides input reflection coefficients (Fig. 6.5(c)) less than −10 dB around the center frequency 7.25 GHz with a reasonable bandwidth. For example, ports 5 and 6 offer a bandwidth of approximately 1.5 GHz from 6.5 GHz to 8 GHz. In summary, all six antenna ports can be sufficiently matched to 50 Ω around the center frequency, demonstrating the basic feasibility of the antenna concept.

Furthermore, the transmission coefficients shown in Fig. 6.5(d) demonstrate that all six antenna ports are highly decoupled.[98] As the feed network is ideal,

---

[97]In this thesis, a port is considered sufficiently matched if the input reflection coefficient is less than or equal to −10 dB ($|S_{uu}| \leq -10$ dB).

[98]In this thesis, two ports are considered sufficiently decoupled if their mutual transmission coefficient is less than or equal to −20 dB ($|S_{uv}| \leq -20$ dB).
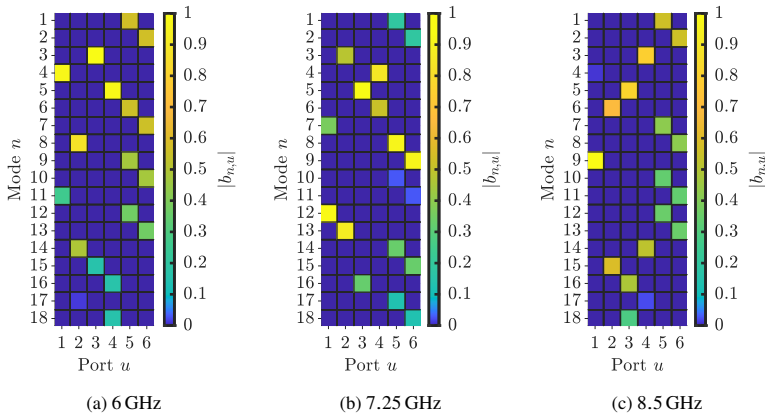
Figure 6.7   Normalized modal weighting coefficients of square PEC plate with excitation slots according to Fig. 6.4(a) located 16 mm above infinite ground plane. The modes are sorted at each frequency according to their significance. (a) 6 GHz. (b) 7.25 GHz. (c) 8.5 GHz. © 2019 IEEE [PM19c].

mutual coupling may only be introduced by the antenna element. However, since the symmetry requirements of the irreducible representations of the symmetry group C_{4v} are fulfilled by the antenna ports, the antenna element does not allow mutual coupling. This observation is confirmed by examining the envelope correlation coefficients in Fig. 6.6, proving that the antenna ports are orthogonal. In particular, the decoupling and the orthogonality of the ports is independent of frequency as both effects are governed by the symmetry of the antenna.

These conclusions can be further corroborated by conducting a modal analysis of the square PEC plate with excitation slots. In Fig. 6.7, the normalized modal weighting coefficients of the first 18 characteristic modes are shown at three different frequencies. At each frequency, the modes are sorted independently according to their significance. For this reason, the mode indices cannot be mapped from frequency to frequency. The purpose of Fig. 6.7 is to illustrate that the antenna ports excite mutually exclusive sets of characteristic modes independent of frequency, causing their orthogonality. Each mode is excited by exactly one port so that no more modes are left to be excited separately, demonstrating that the maximum number of orthogonal antenna ports is reached.

Now, the question arises whether a sufficient impedance match to $50\,\Omega$ over the complete desired frequency range can be achieved for ports 2, 4, 5, and 6 as
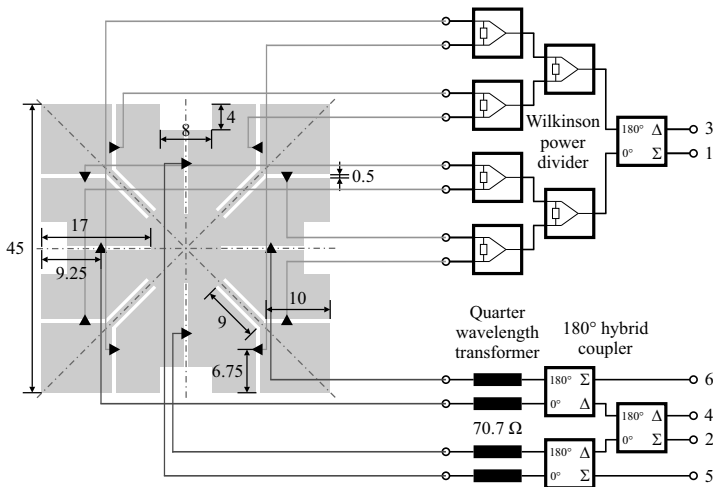
Figure 6.8 Square PEC plate with stepped excitation slots and modified feed network. Dimensions in mm. © 2019 IEEE [PM19c].

well by taking some additional measures. One suitable measure is to modify the excitation slots by introducing a step in width as proposed in [46, 48] in order to enable an enhanced control of the input impedance. Thus, such a step in width is added to the excitation slots of ports 2, 4, 5, and 6 as depicted in Fig. 6.8.[99] It is observed that the stepped excitation slots exhibit smoother impedance curves at the cost of increased input resistance and capacitance. In order to compensate for the capacitance, the slot lengths and the feed point positions are adjusted. This way, a sufficient impedance match over the desired frequency range is achieved, though to a reference impedance of $100\,\Omega$. In order to connect the antenna element to the feed network with a reference impedance of $50\,\Omega$, quarter wavelength transformers with a characteristic impedance of $70.7\,\Omega$ are added between the feed points and the respective feed network as shown in Fig. 6.8.

With these measures, a sufficient impedance match to $50\,\Omega$ is achieved for all six antenna ports over the complete frequency range of interest, as evidenced in Fig. 6.9. In particular, all input impedances now show a comparatively flat behavior close to $50\,\Omega$ (Fig. 6.9(a) and (b)) and the input reflection coefficients of

---

[99] Although the increased slot width has in general an impact on the surface current densities excited by ports 1 and 3, only a slight shift of the respective feed point positions is required compared to Fig. 6.4(a) in order to retain the impedance behavior (cf. Fig. 6.5).
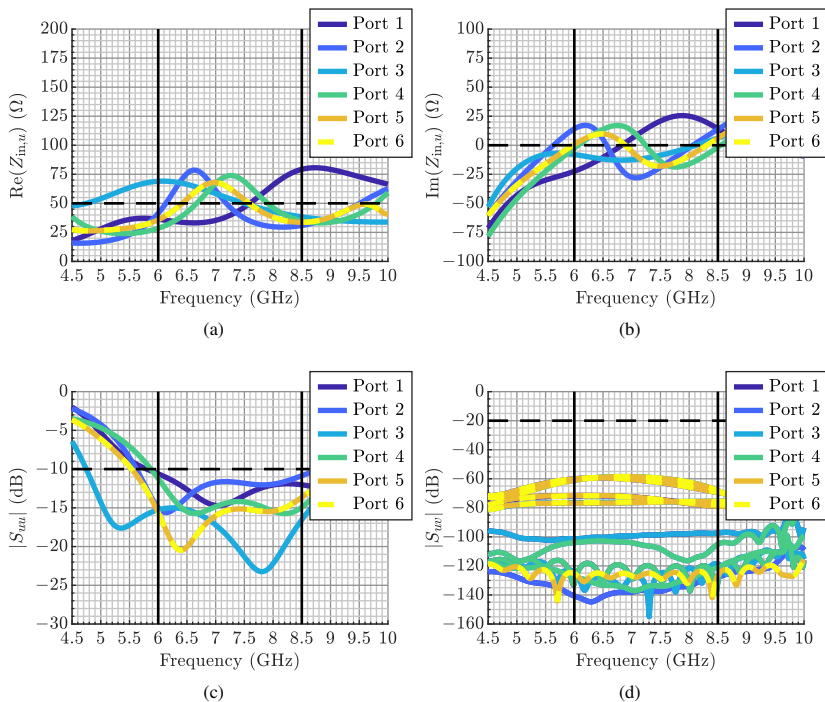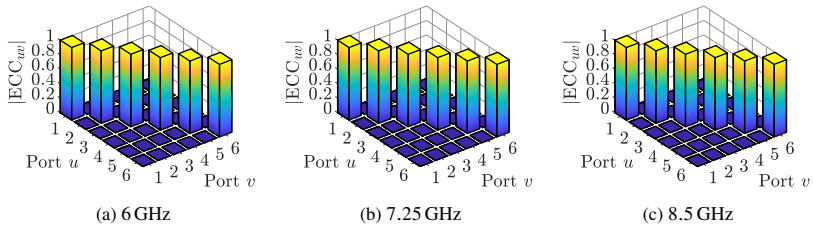
Figure 6.9   Input parameters of square PEC plate with stepped excitation slots and modified feed network according to Fig. 6.8 located 16 mm above infinite ground plane. (a) Real parts of input impedances. (b) Imaginary parts of input impedances. (c) Absolute values of input reflection coefficients. (d) Absolute values of transmission coefficients from specified ports to all other ports. © 2019 IEEE [PM19c].

all ports are below $-10\,\mathrm{dB}$ from $6\,\mathrm{GHz}$ to $8.5\,\mathrm{GHz}$ (Fig. 6.9(c)). Moreover, the antenna ports are still highly decoupled (Fig. 6.9(d)) and orthogonal (Fig. 6.10) independent of frequency. Again, this is due to the fact that the symmetry of the antenna element is not altered by introducing the stepped excitation slots.

    The stepped excitation slots are used to increase the impedance bandwidth of the respective antenna ports. This comes at the cost of additional impedance transformers in the corresponding feed network which, at first glance, may seem to be a disadvantage of the chosen concept. Quite the contrary, it will become evident with the introduction of the baluns in section 6.3.1 connecting the antenna element and the feed network that the flexibility of the antenna

Figure 6.10 Envelope correlation coefficients of square PEC plate with stepped excitation slots and modified feed network according to Fig. 6.8 located 16 mm above infinite ground plane. (a) 6 GHz. (b) 7.25 GHz. (c) 8.5 GHz. © 2019 IEEE [PM19c].

element with respect to the input impedances is in fact an advantage of the chosen concept. Hence, one of the important features of the antenna element to be highlighted is that it allows a flexible setting of the input impedances without losing the orthogonality of the antenna ports.

In conclusion, an antenna element with six sufficiently matched antenna ports from 6 GHz to 8.5 GHz is now available. In particular, the ports are decoupled and orthogonal independent of frequency due to the symmetry of the antenna element and the ideal feed network.

6.2 Feed Network Design

In the next step, the feed network schematically depicted in Fig. 6.4(b) is realized. To this end, first, a suitable technology is chosen. Then, the components of the network, i.e., the 180° hybrid couplers and the Wilkinson power dividers are designed. Finally, the components are assembled according to Fig. 6.4(b) and the performance of the resulting feed networks is checked by means of simulations.

6.2.1 Technology

As the complete feed network consists of two sub-networks, one for ports 1 and 3 and one for ports 2, 4, 5, and 6, it suggests itself to use multilayer technology and realize the two sub-networks on different layers. A suitable layer setup consisting of six metal layers, each with a thickness of 35 μm, is illustrated in Fig. 6.11. Layer 1 (top-layer) is the ground plane for the antenna element (section 6.1.1). Simultaneously, it shields the feed network from the electromagnetic fields of
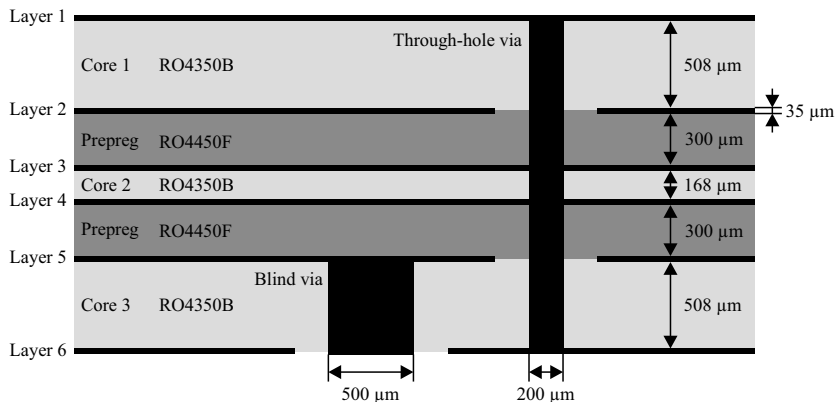
Figure 6.11   Layer setup of feed network consisting of six metal layers, three substrate cores and two prepregs. Layer 5 is the network layer for ports 1 and 3. Blind vias are used for connecting the $100\,\Omega$-SMD resistors of the Wilkinson power dividers placed on layer 6. Layer 2 is the network layer for ports 2, 4, 5, and 6. Layers 1, 3, 4, and 6 are ground layers interconnected by means of through-hole vias.

the antenna element. Layer 2 is the network layer for ports 2, 4, 5, and 6; layer 5 is the network layer for ports 1 and 3. The two network layers are separated by the ground layers 3 and 4.[100] Layer 6 (bottom-layer), finally, is the lower ground plane for shielding the network. Furthermore, it is used for placing the SMD (surface-mount device) resistors of the Wilkinson power dividers, which are connected to the network layer 5 by means of blind vias with a diameter of $500\,\mu m$. The four ground layers 1, 3, 4, and 6 are interconnected by means of through-hole vias with a diameter of $200\,\mu m$. The connections to the antenna element as well as connectors for the input ports will be added in section 6.3 as the focus of this section lies on examining the feed network alone.

The layer setup in Fig. 6.11 consists of six metal layers. Accordingly, there are three double-layered substrate cores. The substrate material is Rogers RO4350B with a relative permittivity $\varepsilon_r = 3.66$ [95]. The inner core 2 carries the two inner ground layers 3 and 4. Therefore, its height is chosen to be the minimum height available, i.e., $168\,\mu m$. The height of the other two cores is chosen to be $508\,\mu m$ in order to ensure that the stripline widths on the network layers do not become to small (see below). The three substrate cores are joined together by two prepregs

---

[100]For the feed network layout, one ground layer between the two network layers would be sufficient, resulting in five layers. However, only an even number of layers can be fabricated. For this reason, the inner ground layer is realized by the two layers 3 and 4, resulting in a total of six layers.
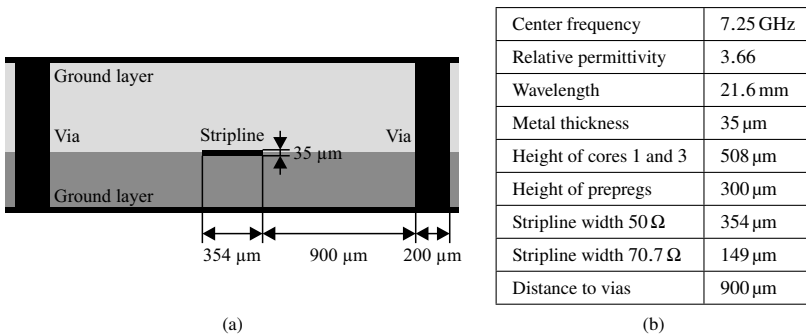
Center frequency	7.25 GHz
Relative permittivity	3.66
Wavelength	21.6 mm
Metal thickness	35 µm
Height of cores 1 and 3	508 µm
Height of prepregs	300 µm
Stripline width 50 Ω	354 µm
Stripline width 70.7 Ω	149 µm
Distance to vias	900 µm

(a)   (b)

Figure 6.12   Stripline on network layers 2 and 5. (a) Cross section of stripline with characteristic impedance of 50 Ω. (b) List of relevant design parameters.

(preimpregnated fibers). The prepreg material is Rogers RO4450F, whose relative permittivity is approximately the same as that of the core material [96]. Again, in order to make sure that the stripline widths on the network layers do not become to small, the maximum available height of 300 µm is chosen.

Based on the layer setup in Fig. 6.11, the two network layers are realized in stripline technology [92]. As the substrate core and the prepreg approximately have the same relative permittivity $\varepsilon_r = 3.66$, the stripline supports the propagation of transverse electromagnetic (TEM) waves. The corresponding wavelength λ_g is the free space wavelength divided by $\sqrt{\varepsilon_r}$ [92], i.e., $\lambda_g \approx 21.6$ mm at the center frequency 7.25 GHz. Thanks to this, the wavelength-dependent network components, like the Wilkinson power divider and the 180° hybrid coupler, realized in stripline technology are smaller if compared, for example, to microstrip technology, yielding an overall size reduction.

The only stripline parameter left is the line width, which is used for determining the characteristic impedance of the stripline. Based on simulations, the line width for a characteristic impedance of 50 Ω is found to be 354 µm. Additionally, a characteristic impedance of $50\sqrt{2}\,\Omega \approx 70.7\,\Omega$ is required for the Wilkinson power dividers and the 180° hybrid couplers. The corresponding line width is 149 µm. The distance between the stripline and the through-hole vias connecting the ground planes is set to 900 µm so that the effect of the vias on the electromagnetic fields of the stripline, and thus its characteristic impedance, is negligible. The cross section of the 50 Ω-stripline is depicted in Fig. 6.12(a). The design parameters of the stripline are summarized in Table 6.12(b).

6.2.2 Components

The feed network for ports 1 and 3 consists of one 180° hybrid coupler and six Wilkinson power dividers, the feed network for ports 2, 4, 5, and 6 consists of three 180° hybrid couplers (Fig. 6.4(b)). Hence, there are two main components: The Wilkinson power divider and the 180° hybrid coupler. It is thus purposeful to begin the network design by examining these two components separately.
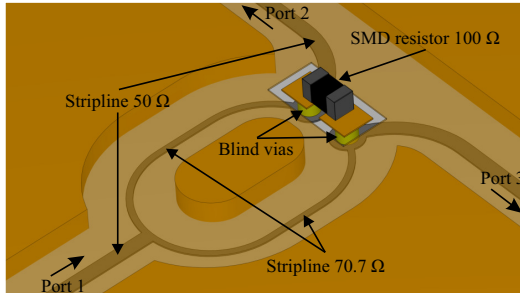

Figure 6.13   Simulation model of Wilkinson power divider in stripline technology on layer 5.

The Wilkinson power dividers are designed according to the guidelines given in [92]. The simulation model of one power divider on layer 5 is depicted in Fig. 6.13. Port 1 is considered the input port, whereas ports 2 and 3 are considered the output ports.[101] The input line is split into the two dividing arms whose length is equivalent to a quarter wavelength of the stripline and whose characteristic impedance is $50\sqrt{2}\,\Omega \approx 70.7\,\Omega$. The $100\,\Omega$ resistor between the two dividing arms is realized as an SMD resistor of size 0402 on layer 6 connected to the stripline by means of blind vias. The through-hole vias connecting the ground planes on layers 4 and 6 are idealized as solid walls.

The simulated S-parameters of one Wilkinson power divider are shown in Fig. 6.14. It is evident that all three ports are well matched to the reference impedance $50\,\Omega$ (S_{11}, S_{22}, S_{33}). The output ports 2 and 3 are highly decoupled around the center frequency (S_{32}). Towards the limits of the frequency range of interest, the coupling becomes slightly more pronounced and the transmission coefficient becomes greater than $-20\,\mathrm{dB}$. Nevertheless, the input signal is split equally by $-3\,\mathrm{dB}$ and in phase over the complete frequency range (S_{21}, S_{31}). All in all, the designed Wilkinson power divider is suitable for the feed network.

---

[101] Of course, the Wilkinson power divider can also operate as a power combiner in receive mode.
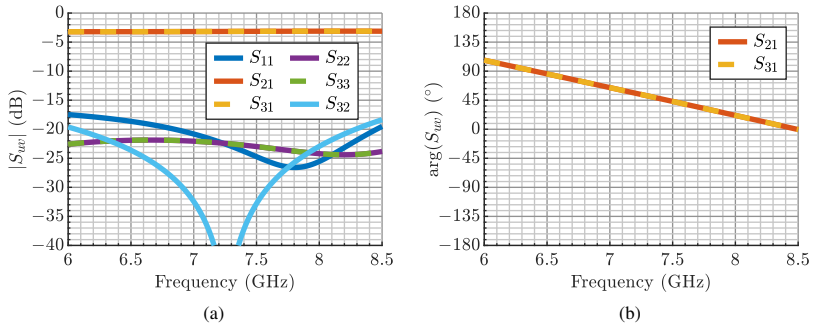
Figure 6.14 Simulated S-parameters of Wilkinson power divider depicted in Fig. 6.13. (a) Absolute value of reflection and transmission coefficients. (b) Phase of transmission coefficients from input port to output ports.
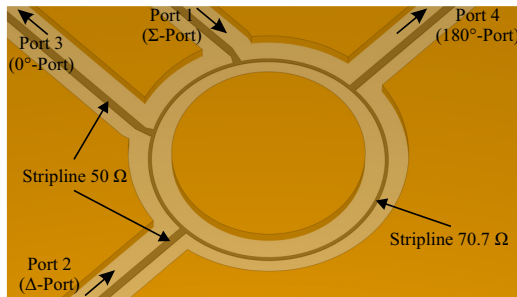

Figure 6.15 Simulation model of 180° hybrid coupler (rat-race coupler) in stripline technology on layer 2 or 5.

The 180° hybrid couplers are designed as ring hybrids (rat-race couplers) in stripline technology according to the guidelines given in [92]. The simulation model of one coupler on layer 2 or layer 5 is depicted in Fig. 6.15. Port 1 corresponds to the Σ-port, whereas port 2 corresponds to the Δ-port (input ports). Port 3 (0°-port) and port 4 (180°-port) are the output ports (cf. Fig. 6.4(b)).[102] The length of the ring section is equivalent to 1.5 wavelengths of the stripline and its characteristic impedance is $50\sqrt{2}\,\Omega \approx 70.7\,\Omega$. Again, the through-hole vias connecting the ground layers are modeled as solid walls.

---

[102]In receive mode, the sum of the signals of ports 3 and 4 is output at port 1 (sum port), whereas the difference is output at port 2 (difference port).
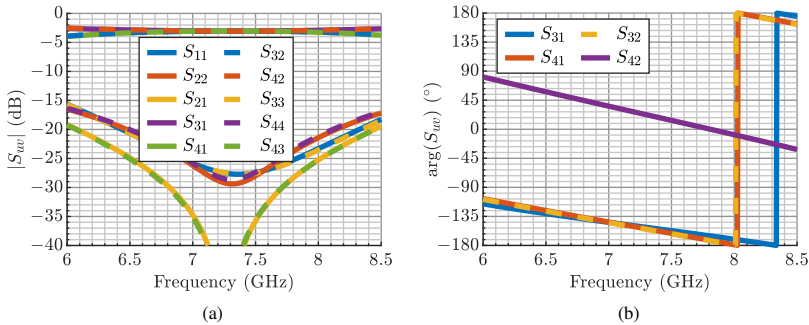
Figure 6.16   Simulated S-parameters of 180° hybrid coupler depicted in Fig. 6.15. (a) Absolute value of reflection and transmission coefficients. (b) Phase of transmission coefficients from input ports to output ports.

The simulated S-parameters of the 180° hybrid coupler are shown in Fig. 6.16. All four ports are well matched over the desired frequency range (S_{11}, S_{22}, S_{33}, S_{44}). The input ports 1 and 2 as well as the output ports 3 and 4 are highly decoupled (S_{21}, S_{43}). Similar to the Wilkison power divider, however, the transmission coefficients increase towards the limits of the frequency range and become greater than -20 dB. The input signals of both input ports are split equally by -3 dB around the center frequency (S_{31}, S_{41}, S_{32}, S_{42}). At the limits of the frequency range, the split becomes unequal, reaching a maximum deviation of about ± 1 dB from the ideal -3 dB. The output signals at ports 3 and 4 are in phase around the center frequency if port 1 is driven (S_{31}, S_{41}), whereas they have a phase difference of 180° if port 2 is driven (S_{32}, S_{42}). At the limits of the frequency range, a maximum phase error of 10° occurs. All in all, the designed 180° hybrid coupler operates as intended and is thus suitable for the feed network.

In summary, both feed network components are basically suitable for the given task. Towards the limits of the frequency range of interest, however, the decoupling behavior of both components as well as the splitting behavior of the 180° hybrid coupler with respect to both amplitude and phase become critical. This is not surprising since the Wilkinson power divider as well as the 180° hybrid coupler are in fact narrowband RF circuits [92]. It is thus expected that the complete multimode antenna will perform worse at the band limits compared to the center frequency. For the purpose of this thesis, however, this

is not detrimental at all as the feed network is just a means to put the theory into a practical antenna design. If the multimode antenna can be shown to operate as predicted around the center frequency, it will also work properly over a broader frequency range if a broadband feed network is employed since the decorrelation and the decoupling of the antenna element alone are governed by its symmetry and are thus independent of frequency (section 6.1.3). However, the feed network design should be considered a mere engineering task which, although it may be intricate, does not provide further insight for a systematic multimode antenna design and is thus covered only on a basic level within this thesis.[103] Nevertheless, it is important to note that the feed network is expected to be the principal bandwidth limiting component of the multimode antenna.

6.2.3 Networks

Now, the network components need to be connected according to Fig. 6.4(b). The principal challenge of the network design is the compact arrangement of the components. With respect to this, there is one hard boundary condition: The positions of the feed points are dictated by the antenna element (section 6.1.3). As an additional design goal, the feed network is supposed to fit completely below the antenna element in order to realize the complete multimode antenna as compact as possible.[104]

The simulation model of the feed network for ports 1 and 3 is depicted in Fig. 6.17. The two antenna ports as well as the eight feed points are modeled as stripline ports in Empire XPU (denoted by the black arrows). The 180° hybrid coupler is placed centrally. All striplines from the central coupler to the feed points including the Wilkinson power dividers must have the same lengths in order to make sure that no additional phase differences are added over the whole frequency range of interest. The lengths are dictated by the longest path, which is that from the central coupler to the feed points 6′ and 7′. The stripline paths to the other feed point pairs thus have to be lengthened, resulting in the additional bends. Simultaneously, it is ensured that the network fits entirely below the antenna element, as outlined in Fig. 6.17. It should be emphasized that the absolute phase at the feed points does not matter as long as the phase relations between the feed points are correct. This has the consequence that the stripline lengths from the individual antenna ports to the central 180° hybrid coupler

---

[103] For example, a feed network for a four-port multimode antenna using broadband components is presented in [48].

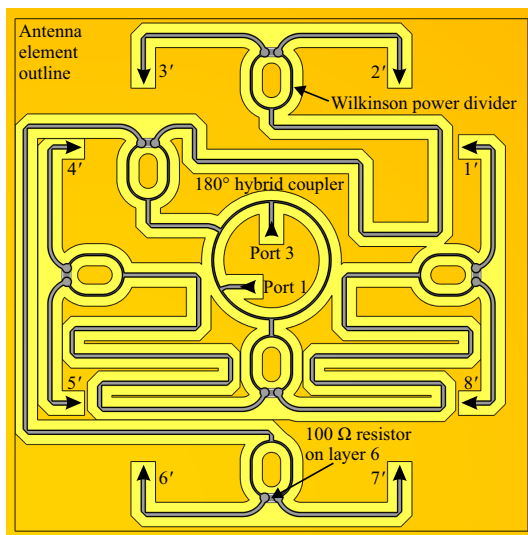[104] Such a compact design is particularly beneficial for a potential array arrangement [46].

Figure 6.17   Simulation model of feed network for ports 1 and 3 on layer 5. The antenna ports and the feed points denoted by the black arrows are modeled as stripline ports in Empire XPU.

can be adjusted at will, which will be important for the placement of the input connectors in section 6.3.2.

The absolute values of the simulated S-parameters are shown in Fig. 6.18. The antenna ports 1 and 3 are sufficiently matched to the reference impedance $50\,\Omega$ over the entire frequency range of interest (S_{11}; S_{33}). A sufficient decoupling is achieved from approximately 6.5 GHz to 8 GHz (S_{31}; S_{13}). Beyond this range, the transmission coefficients are greater than $-20\,$dB, which is due to the coupling added by the individual network components in succession. This confirms the prediction made in the previous subsection that the feed network is the principal cause for a bandwidth limitation.

The input signals of both ports are split equally by a total of $-9\,$dB around the center frequency, as expected due to the three-stage architecture ($S_{1'1}$, $S_{2'1}$, $S_{3'1}$, $S_{4'1}$, $S_{5'1}$, $S_{6'1}$, $S_{7'1}$, $S_{8'1}$; $S_{1'3}$, $S_{2'3}$, $S_{3'3}$, $S_{4'3}$, $S_{5'3}$, $S_{6'3}$, $S_{7'3}$, $S_{8'3}$). The split becomes unequal towards the limits of the frequency range with a maximum deviation of about $\pm1\,$dB, which is due to the $180°$ hybrid coupler (Fig. 6.16(a)).

The phase at the feed points is shown in Fig. 6.19. The signals excited by port 1 are well in phase at the feed points around the center frequency (Fig. 6.19(a)). A
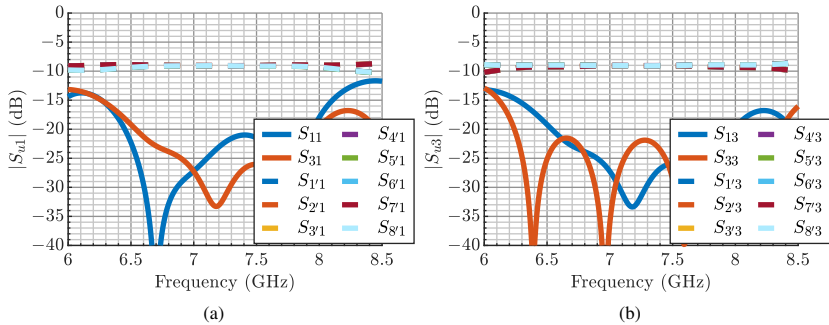
Figure 6.18   Simulated S-parameters (absolute values) of feed network for ports 1 and 3 as depicted in Fig. 6.17. (a) Port 1 active. (b) Port 3 active.
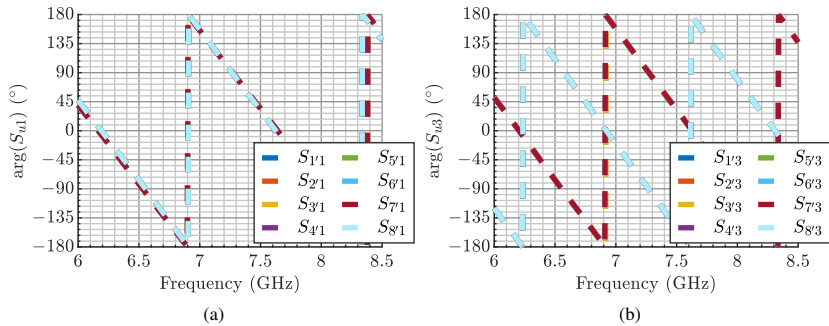

Figure 6.19   Simulated S-parameters (phase) of feed network for ports 1 and 3 as depicted in Fig. 6.17. (a) Port 1 active. (b) Port 3 active.

maximum deviation of $10°$ occurs at the limits of the frequency range. Again, this can be attributed to the coupler (Fig. 6.16(b)). The signal distribution of port 3 behaves similarly. As intended, the feed points $1'$, $4'$, $5'$, and $8'$ have a phase difference of $180°$ compared to the feed points $2'$, $3'$, $6'$, and $7'$ (Fig. 6.19(b)).[105]

---

[105]This is just the opposite of the phase relations resulting from the schematic in Fig. 6.4(b) and corresponds to the case that the feed points $1'$, $4'$, $5'$, $8'$ and $2'$, $3'$, $6'$, $7'$ have swapped places in the schematic. This is done in order to enable an easier network layout. Of course, this has no impact on the functionality of the multimode antenna as the phase relations remain the same.
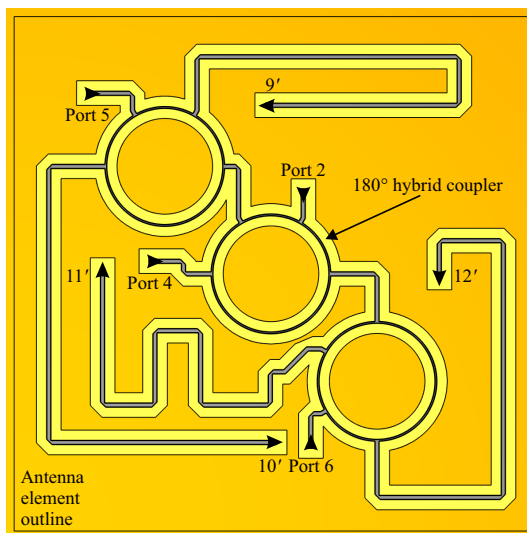
Figure 6.20   Simulation model of feed network for ports 2, 4, 5, and 6 on layer 2. The antenna ports and the feed points denoted by the black arrows are modeled as stripline ports in Empire XPU.

The simulation model of the feed network for ports 2, 4, 5, and 6 is depicted in Fig. 6.20. The 180° hybrid coupler only used by ports 2 and 4 is placed exactly below the center of the antenna element. The other two couplers are placed accordingly and, again, the stripline lengths are adjusted in such a way that no additional phase differences are added. Compared to the feed network for ports 1 and 3 (Fig. 6.17), the layout is more relaxed as there are only three network components and four feed points to be driven.

The absolute values of the simulated S-parameters are shown in Fig. 6.21. All four antenna ports are well matched to the reference impedance $50\,\Omega$ over the entire frequency range of interest (S_{22}; S_{44}; S_{55}; S_{66}). Ports 5 and 6 can be considered almost perfectly decoupled as their mutual transmission coefficients are well below $-40\,\mathrm{dB}$ (S_{65}; S_{56}; not visible within the range of Fig. 6.21). The two ports are also sufficiently decoupled from ports 2 and 4 over the entire frequency range (S_{52}, S_{62}; S_{54}, S_{64}; S_{25}, S_{45}; S_{26}, S_{46}). In contrast, ports 2 and 4 are only sufficiently decoupled up to about 8 GHz, beyond which their mutual transmission coefficients become greater than $-20\,\mathrm{dB}$ (S_{42}; S_{24}). This diverse decoupling behavior of the four ports can be attributed to the fact that ports 2
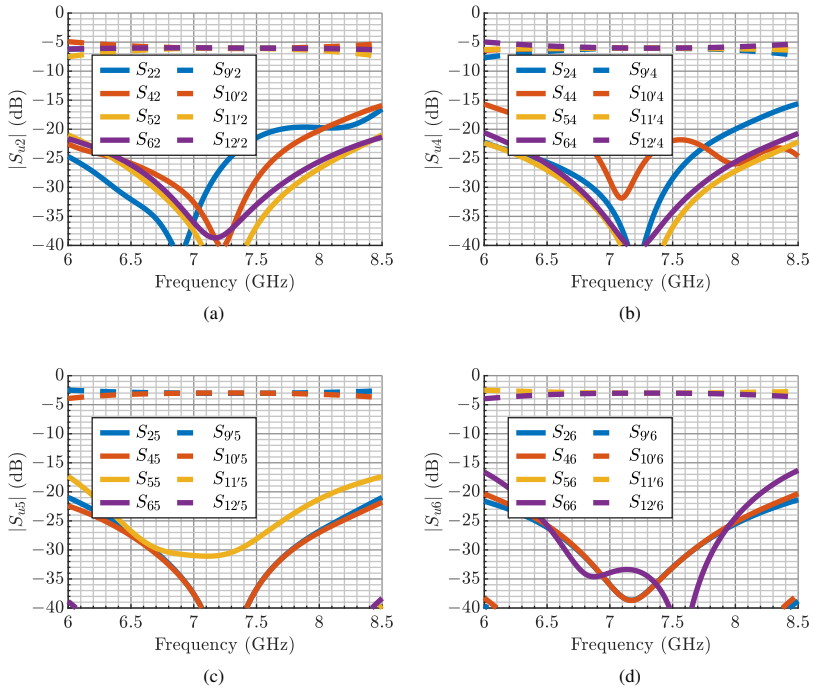
Figure 6.21   Simulated S-parameters (absolute values) of feed network for ports 2, 4, 5, and 6 as depicted in Fig. 6.20. (a) Port 2 active. (b) Port 4 active. (c) Port 5 active. (d) Port 6 active.

and 4 are decoupled only by the central 180° hybrid coupler, whereas ports 5 and 6 are separated from ports 2 and 4 by two couplers each, and separated from each other by all three couplers of the network. In conclusion, the decoupling of ports 2 and 4 is the critical bandwidth limiting parameter of this network.

As intended, the signals from ports 2 and 4 are equally split by −6 dB as they pass two couplers ($S_{9'2}$, $S_{10'2}$, $S_{11'2}$, $S_{12'2}$; $S_{9'4}$, $S_{10'4}$, $S_{11'4}$, $S_{12'4}$), whereas those of ports 5 and 6 are equally split by −3 dB as they pass only one coupler ($S_{9'5}$, $S_{10'5}$; $S_{11'6}$, $S_{12'6}$). Towards the limits of the frequency range, the split becomes unequal, with the already familiar maximum deviation of ±1 dB for ports 5 and 6 due to one coupler, but a maximum deviation of approximately ±2 dB for ports 2 and 4 since the effect of two couplers is accumulated. Furthermore,
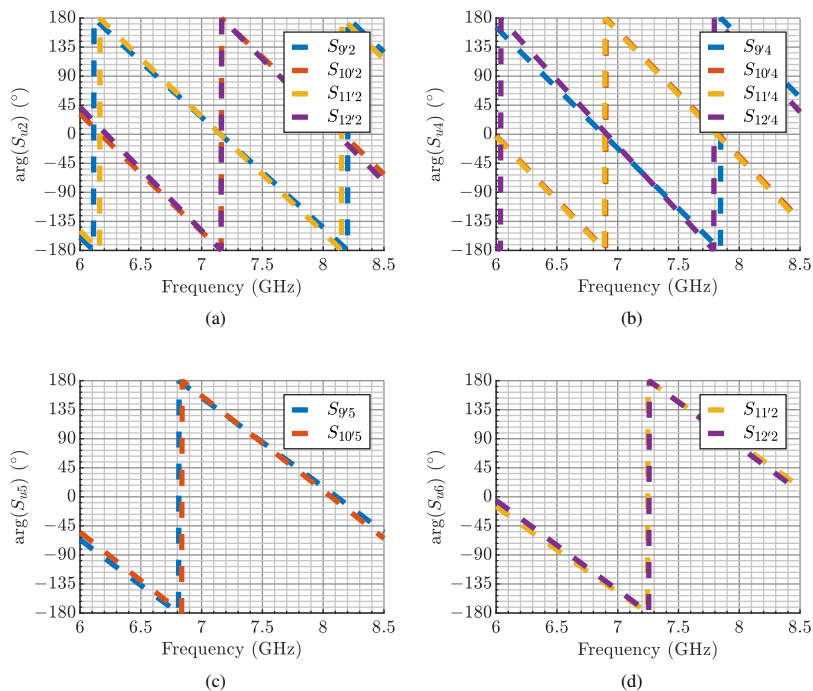
Figure 6.22   Simulated S-parameters (phase) of feed network for ports 2, 4, 5, and 6 as depicted in Fig. 6.20.
(a) Port 2 active. (b) Port 4 active. (c) Port 5 active. (d) Port 6 active.

it should be recalled that ports 5 and 6 only drive two feed points each ($S_{9'5}$, $S_{10'5}$; $S_{11'6}$, $S_{12'6}$). The transmission coefficients to the other feed points are well below −40 dB over almost the entire frequency range so that these feed points are highly decoupled from the respective antenna ports ($S_{11'5}$, $S_{12'5}$; $S_{9'6}$, $S_{10'6}$; only visible at the limits of the frequency range within the range of Fig. 6.21).

The phase at the feed points is shown in Fig. 6.22. As expected, the phase relations are reproduced exactly around the center frequency, whereas deviations due to the 180° hybrid couplers occur at the limits of the frequency range. For ports 5 (Fig. 6.22(c)) and 6 (Fig. 6.22(d)), the two respective feed points are driven in phase. For ports 2 (Fig. 6.22(a)) and 4 (Fig. 6.22(b)), there are two pairs of feed points which are driven in phase, respectively (feed points 9′ and 11′

as well as 10′ and 12′ for port 2; feed points 9′ and 12′ as well as 10′ and 11′ for port 4). The two respective pairs of feed points have a phase difference of 180° (cf. Fig. 6.4(b)).

In summary, both feed networks operate as intended. The decoupling between ports 1 and 3 as well as ports 2 and 4 is identified as the principal bandwidth limiting parameter. Furthermore, the 180° hybrid couplers are found to introduce amplitude and phase deviations at the limits of the frequency range. As already discussed in subsection 6.2.2, these limitations can be overcome by a more sophisticated design of the network components (e.g., cf. [48]). For the purpose of this thesis, however, the important result of this section is that a practical feed network is now available which sufficiently reproduces the properties of the ideal feed network as schematically depicted in Fig. 6.4(b): All six antenna ports are well matched and well decoupled and drive the feed points with the correct amplitude and phase relations as required by the irreducible representations of the symmetry group C_{4v} over a reasonable frequency range.

6.3 Assembly and Layout

Up to now, it has been shown how the antenna element and the feed network can be designed and optimized separately, enabling a modular design approach. In this section, the two parts are joined together. To this end, a connection between the antenna element and the feed network needs to be realized. This requires some further modifications of both the antenna element and the feed network, resulting in the final layouts for fabrication.

6.3.1 Baluns and Antenna Element Layout

For the connection between the antenna element and the feed network, different technologies come into question. A microstrip transition as employed in [48] can be fabricated comparatively easily. However, its electromagnetic fields are expected to interfere with the electromagnetic near fields of the antenna element. Using stripline technology instead should mitigate the interference, but comes at the cost of a complicated assembly to both the antenna element and the feed network as the inner conductor is difficult to connect (cf. Fig. 6.12). A coaxial line as used in [46] is expected to offer shielding against the near fields of the antenna as well as good connectivity since both inner and outer conductor are accessible. Based on these considerations, semi-rigid coaxial cables with an outer diameter of 3.6 mm, an inner conductor diameter of 0.91 mm, and a
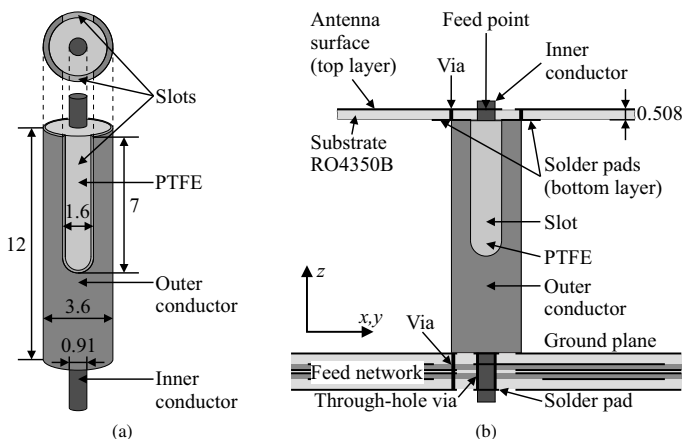
Figure 6.23 Coaxial Balun. (a) Semi-rigid coaxial cable with symmetrically slotted outer conductor and protruding inner conductor. (b) Connection to antenna element at feed point and feed network (here: layer 2, refer to Fig. 6.11 for layer setup). Dimensions in mm.

characteristic impedance of $50\,\Omega$ [97] are chosen for connecting the antenna element and the feed network.

The excitation slots of the antenna element (Fig. 6.8) act as symmetric terminations for the coaxial lines. A balun (balanced to unbalanced transformer) is thus needed in order to realize the transition from the asymmetric coaxial line to the symmetric excitation slot [5]. The balun is formed by symmetrically cutting two slots into the outer conductor and letting the inner conductor protrude, as depicted in Fig. 6.23(a). The protruding inner conductor is connected to one side of the excitation slot, whereas the slotted outer conductor is connected to both sides of the excitation slot as illustrated in Fig. 6.23(b) [5]. For this purpose, the antenna element is mounted on a Rogers RO4350B substrate with the height $508\,\mu m$ (top layer). The inner conductor of the coaxial balun is passed through the substrate and connected to one side of the excitation slot on the top layer. The outer conductor is connected to solder pads on both sides of the excitation slot on the bottom layer of the substrate. These are linked to the antenna element on the top layer by means of through-hole vias. The other end of the coaxial balun is connected to the feed network, as detailed in subsection 6.3.2.

The chosen balun performs a $4:1$ impedance transformation. Thus, it has to be taken into account as an impedance transformer between the antenna element
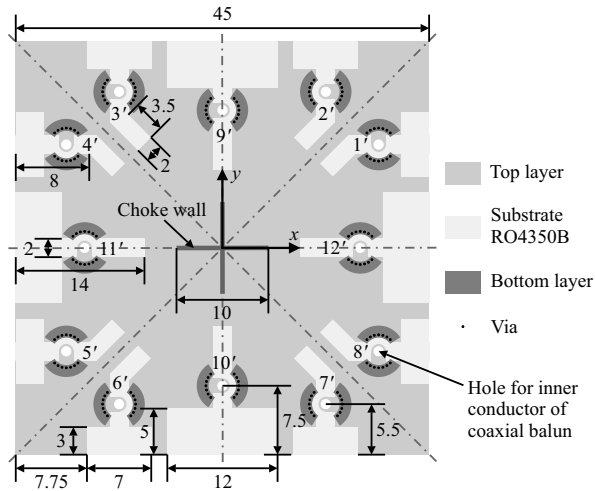
Figure 6.24 Final layout of the antenna element. The actual antenna surface derived from the square plate is placed on the top layer and is located approximately 12.5 mm above the ground plane. The feed points for connecting the coaxial baluns and the feed network are denoted by the primed numbers. The solder pads on the bottom layer connect the slotted outer conductors of the coaxial baluns to the top layer by means of through-hole vias. The cross-shaped copper sheet choke wall of 11 mm height connected to the ground plane is located below the element center. Dimensions in mm. © 2021 IEEE [PHM21].

and the feed network. As a matter of fact, this architecture has already been in use for ports 2, 4, 5, and 6 in Fig. 6.8. Using the design guidelines given in section 6.1.3, the antenna element is now adjusted such that the ports have input impedances of around 200 Ω. This is primarily achieved by widening the excitation slots and increasing the steps in width. Nevertheless, the slot lengths and feed point positions are adjusted as well in order to compensate for the additional reactance. The baluns transform the increased input impedance to the reference impedance 50 Ω. During the optimization of the excitation slots, it was found that the height of the antenna element above the ground plane can be reduced to approximately 12.5 mm without significantly compromising the impedance bandwidth of the ports, resulting in a lower profile of the antenna. The lengths of the coaxial baluns are thus 12 mm and the optimal slot lengths are found to be 7 mm (Fig. 6.23(a)). The slot widths have a negligible impact on the input impedance and a width of 1.6 mm is chosen for mechanical reasons as the slots are fabricated by milling. The resulting final layout of the antenna element and the corresponding dimensions are depicted in Fig. 6.24.
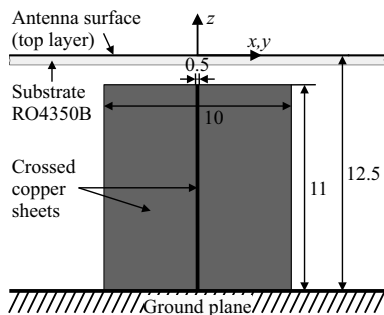
Figure 6.25   Cross-shaped copper sheet choke wall below the center of the antenna element in the xz- or yz-plane. The choke wall suppresses a resonant electromagnetic field excited by port 1 at approximately 6.83 GHz between the coaxial baluns below the antenna element. Dimensions in mm.

It is emphasized once again that the symmetry is preserved after optimizing the dimensions of the excitation slots. At the feed point positions, holes are introduced for connecting the inner conductors of the coaxial baluns to one side of the excitation slots (cf. Fig. 6.23(b)).[106]

Unfortunately, simulations show that port 1 excites a resonant electromagnetic field at approximately 6.83 GHz due to the presence of the coaxial baluns which severely compromises its impedance bandwidth. The resonant field distribution arises between the coaxial baluns below the antenna element and has its maximum at the coordinate center. In order to prevent this resonant field, a cross-shaped copper sheet choke wall with dimension 10 mm × 10 mm × 11 mm connected to the ground plane is introduced below the center of the antenna element, as shown in Fig. 6.24 and Fig. 6.25. The additional boundary condition set up by the choke wall successfully suppresses the resonant field distribution without significantly affecting the desired near fields of port 1 and the other ports. This is due to the central positioning of the choke wall as the dominant surface currents flow at the edges of the antenna element (cf. Fig. 4.21). The cross shape is chosen in order to preserve the symmetry of the antenna so that the port orthogonality is not affected.

It should be noted that for the design steps described in this subsection, the layout of the feed network as introduced in section 6.2 does not need to be known. The antenna element can still be optimized independently of the feed

---

[106]Strictly speaking, the connections at the central excitation slots destroy the symmetry. Such minor modifications, however, have a negligible impact on the port orthogonality (cf. [98]).
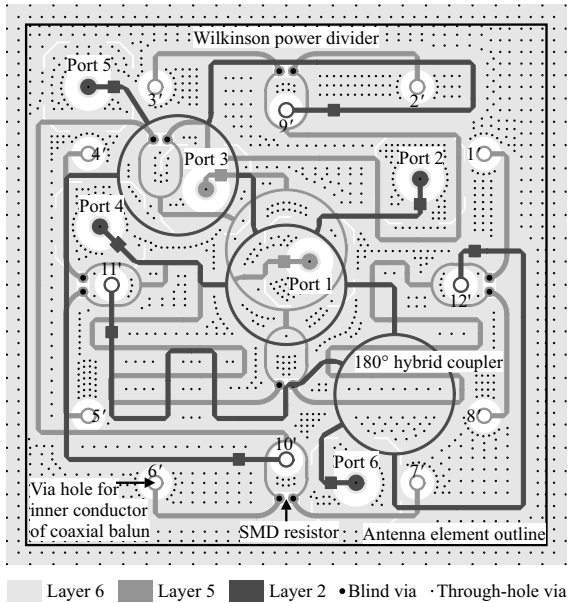
Figure 6.26   Final layout of the feed network. The network layers 2 and 5 as well as the ground layer 6 and all vias are displayed. © 2021 IEEE [PHM21].

network if the baluns (and the choke wall) are included into the process. With this amendment, the proposed modular design approach is still applicable.

6.3.2 Network Layout and Assembly

The final network layout with the feed network for ports 1 and 3 on layer 5 and the feed network for ports 2, 4, 5, and 6 on layer 2 is depicted in Fig. 6.26. As the feed point positions of the antenna element have slightly changed due to the introduction of the coaxial baluns, the stripline lengths of the feed networks from section 6.2 are adjusted accordingly. Through-hole vias interconnect the four ground layers. Due to the partial overlap of the two feed networks, it is not possible to place vias at all spots where they would be required by the individual networks in order to separate adjacent striplines (cf. Fig. 6.17 and 6.20).

The antenna ports are realized as surface-mount SMA connectors [99] placed on layer 6. The outer conductor is soldered to the ground plane on layer 6,
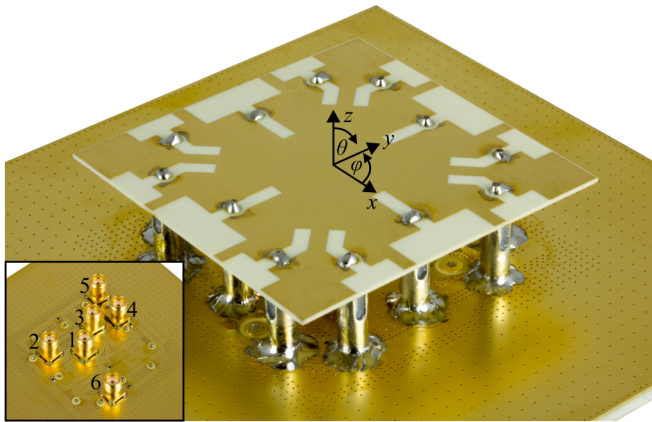
Figure 6.27   Photograph of the fabricated six-port multimode antenna showing the antenna element, the coaxial baluns, and layer 1 of the feed network. The depicted coordinate system serves as reference for the far field radiation patterns. The inset shows layer 6 of the feed network with the antenna ports realized as surface-mount SMA connectors. © 2021 IEEE [PHM21].

whereas the inner conductor is soldered to a circular pad on layer 6 which is connected to the respective network layer by means of a through-hole via. The coaxial-to-stripline transitions are designed to minimize signal reflections. This is achieved by optimizing the solder pad size on layer 6, the pad size on the respective network layer, the counter-pad size on layer 1, and adding electrically small stripline portions acting as reactances. In order to accommodate all six SMA connectors on layer 6, the stripline lengths from the antenna ports to the 180° hybrid couplers are adjusted accordingly without affecting the phase relations at the feed points as explained in section 6.2.3.

Up to this point, both the antenna element and the feed network have been optimized independently. Now, both parts are joined together. To this end, the outer conductors of the coaxial baluns are soldered to the ground plane on layer 1. The inner conductors are passed through the feed network and connected to the respective network layer by means of through-hole vias, as exemplarily illustrated for a connection to layer 2 in Fig. 6.23(b). The resulting coaxial-to-stripline transitions are optimized in the same way as those of the SMA connectors.

A photograph of the fabricated six-port multimode antenna is shown in Fig. 6.27. The antenna element, the coaxial baluns, and the ground plane on layer 1 are visible. The inset shows the SMA connectors serving as the antenna

ports mounted on layer 6. For the measurements and the final simulations, a finite square ground plane of dimensions 90 mm × 90 mm is realized.

6.4 Simulation and Measurement Results

In order to check the performance of the fabricated six-port multimode antenna, S-parameters and radiation patterns are evaluated from simulations and measurements. The simulations are carried out in Empire XPU yielding S-parameters, radiation patterns, and surface current densities. For the measurement of the S-parameters, a vector network analyzer is employed. The 3D radiation patterns (realized gains) are obtained from measurements in an anechoic chamber. The envelope correlation coefficients and the total efficiencies are computed from the simulation and measurement results.

The simulated and measured S-parameters are shown in Fig. 6.28. As a general observation, it is found that all six antenna ports are sufficiently matched to 50 Ω ($|S_{uu}| \leq -10$ dB) and sufficiently decoupled ($|S_{uv}| \leq -20$ dB) over almost the entire frequency range of interest. Deviations arise towards the limits of the frequency range. These can be attributed chiefly to the narrowband nature of the feed network, as has been discussed extensively in section 6.2. The most pronounced coupling occurs between ports 1 and 3 (Fig. 6.28(a) and (c)). The transmission coefficients $|S_{31}|$ and $|S_{13}|$ are less than −20 dB from approximately 6.7 GHz to 7.8 GHz, yielding a bandwidth of 1.1 GHz. A comparison with Fig. 6.18 confirms that this coupling originates from the feed network and is due to the fact that the two antenna ports are decoupled by only one 180° hybrid coupler (see Fig. 6.4(b) and Fig. 6.26). For the same reason, the coupling between ports 2 and 4 (Fig. 6.28(b) and (d)), too, is a critical parameter limiting the bandwidth (cf. Fig. 6.21). In contrast, the coupling between the other ports is more relaxed. In particular, ports 5 and 6 are well decoupled as they are separated by three 180° hybrid couplers (see Fig. 6.4(b) and Fig. 6.26). In conclusion, the network models from section 6.2 turn out to yield good estimates for the coupling to be expected. Additional coupling may be introduced by the network layout (Fig. 6.26), especially by missing vias between adjacent striplines due to the overlapping networks. Coupling between the two different network layers is mainly generated by the coaxial-to-stripline transitions. However, this coupling is negligible as the corresponding transmission coefficients are well below −20 dB. Furthermore, it is found that the simulated and the measured S-parameters agree quite well. Consequently, the simulation model yields a

(a) Port 1 active ($v = 1$)

(b) Port 2 active ($v = 2$)

(c) Port 3 active ($v = 3$)

(d) Port 4 active ($v = 4$)

(e) Port 5 active ($v = 5$)

(f) Port 6 active ($v = 6$)

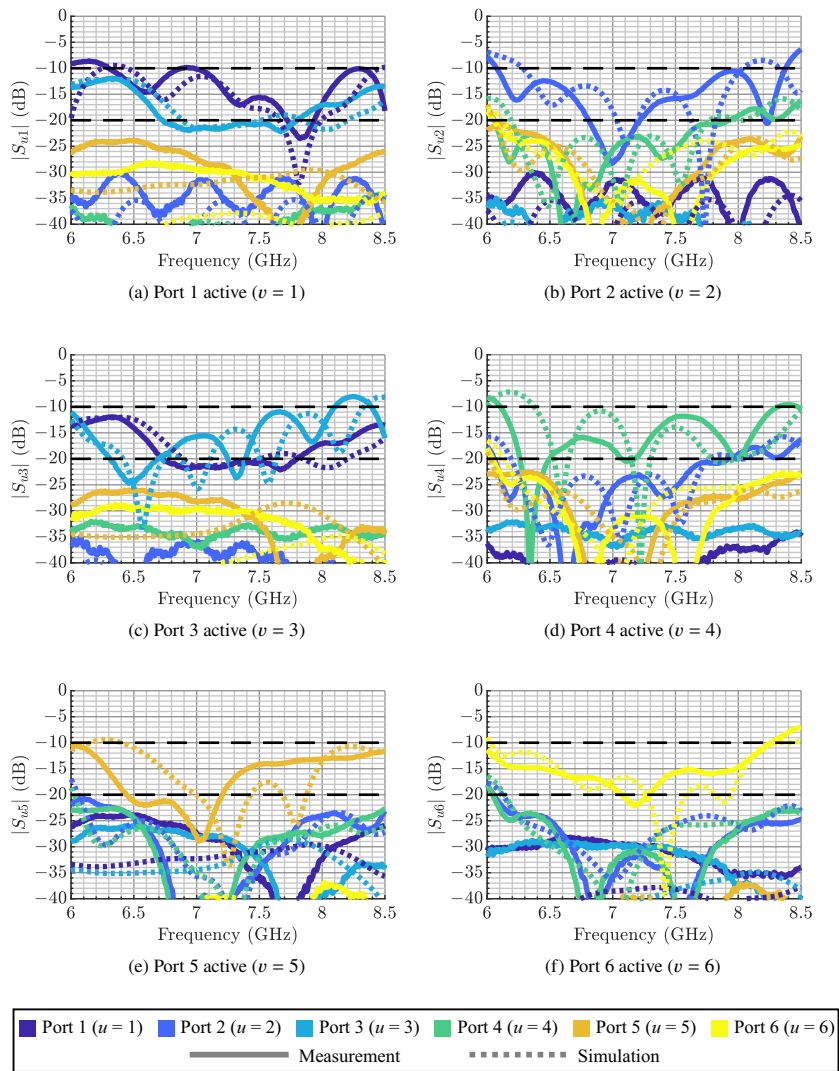| Port 1 ($u = 1$) | Port 2 ($u = 2$) | Port 3 ($u = 3$) | Port 4 ($u = 4$) | Port 5 ($u = 5$) | Port 6 ($u = 6$) |

Measurement   Simulation

(g)

Figure 6.28   Measured and simulated S-parameters S_{uv} (absolute values) from v-th port to u-th port of the fabricated six-port multimode antenna. (a)–(f) Port 1 to 6 (active port). (g) Legend. © 2021 IEEE [PHM21].
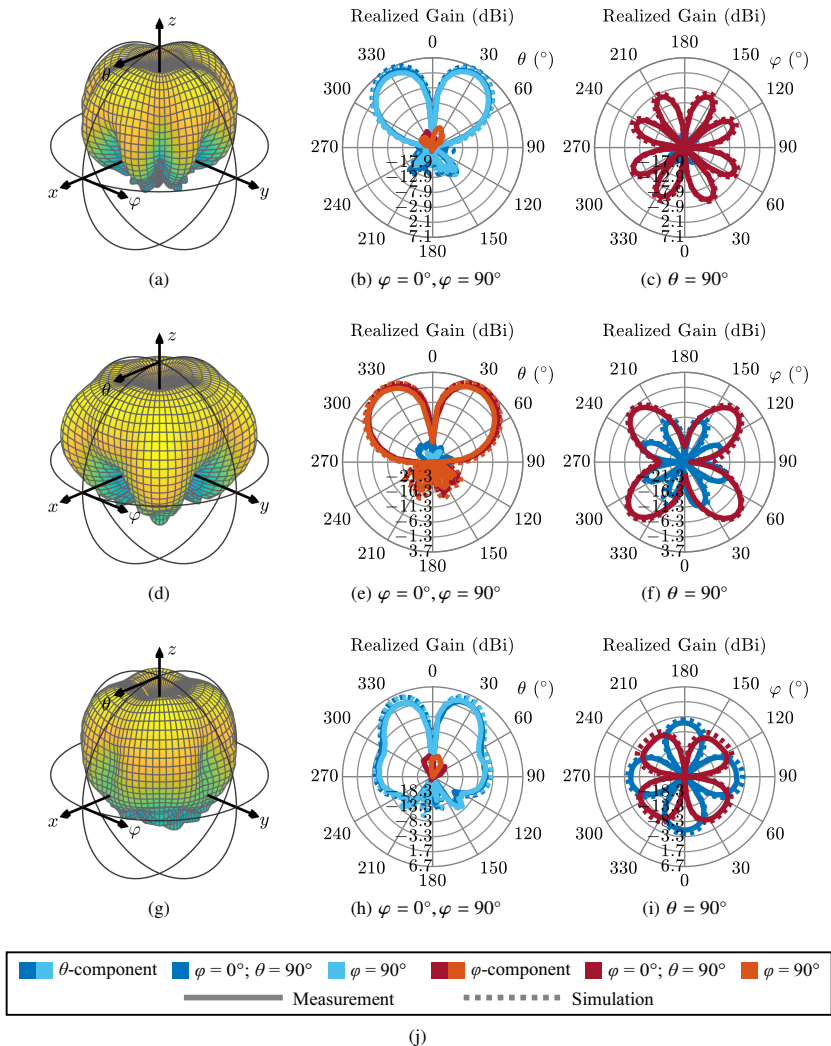
Figure 6.29   Realized gains of ports 1, 2, and 3 of the fabricated six-port multimode antenna at 7.25 GHz. The figure shows the 3D patterns (from measurement) as well as the 2D cuts (from measurement and simulation) in the xz-plane ($\varphi = 0°$), the yz-plane ($\varphi = 90°$), and the xy-plane ($\theta = 90°$). The reference coordinate system is given in Fig. 6.27. All plots are limited to the maximum realized gain of the respective port and display a dynamic range of 30 dB. (a)–(c) Port 1. (d)–(f) Port 2. (g)–(i) Port 3. (j) Legend for 2D cuts. © 2021 IEEE [PHM21].

Figure 6.30   Realized gains of ports 4, 5, and 6 of the fabricated six-port multimode antenna at 7.25 GHz. The figure shows the 3D patterns (from measurement) as well as the 2D cuts (from measurement and simulation) in the xz-plane ($\varphi = 0°$), the yz-plane ($\varphi = 90°$), and the xy-plane ($\theta = 90°$). The reference coordinate system is given in Fig. 6.27. All plots are limited to the maximum realized gain of the respective port and display a dynamic range of 30 dB. (a)–(c) Port 4. (d)–(f) Port 5. (g)–(i) Port 6. (j) Legend for 2D cuts. © 2021 IEEE [PHM21].
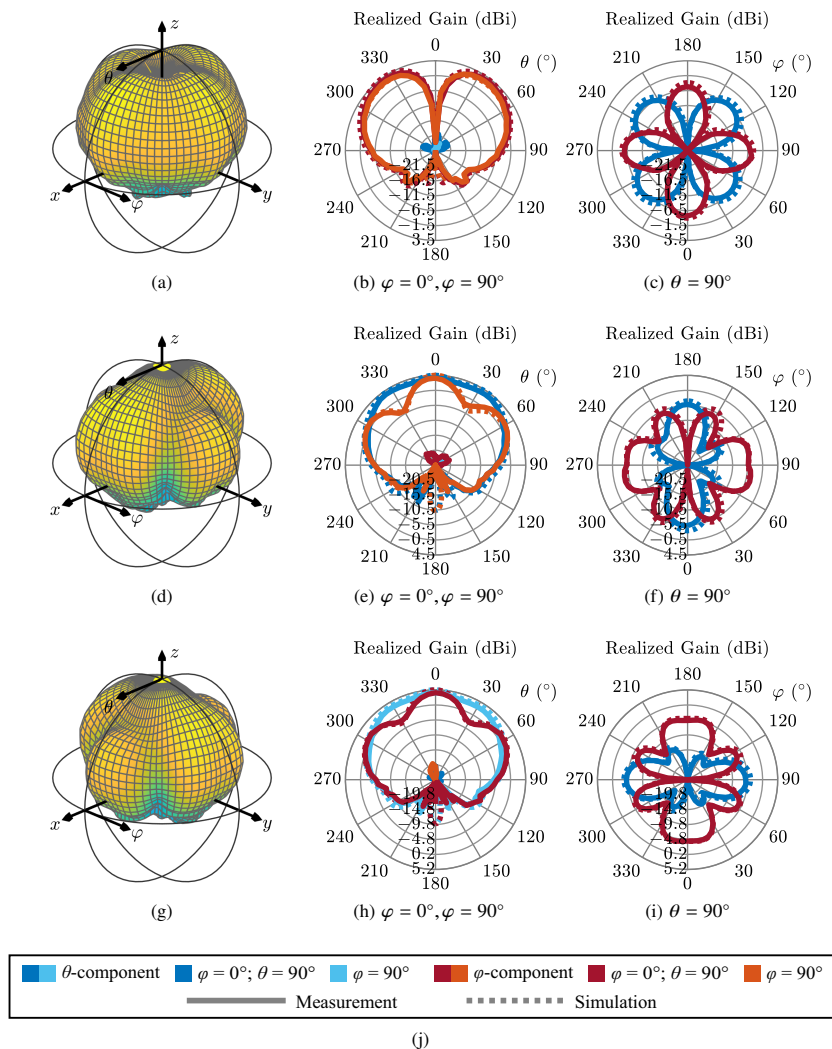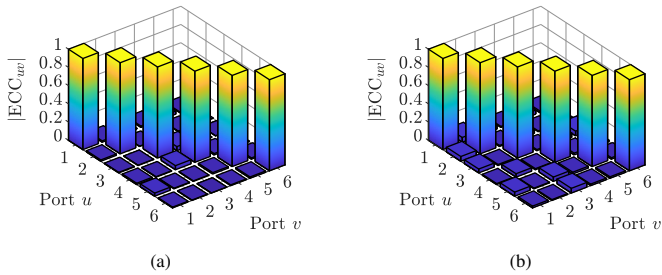
Figure 6.31 Envelope correlation coefficients of the fabricated six-port multimode antenna at 7.25 GHz. (a) Computed from simulated radiation patterns. (b) Computed from measured radiation patterns. © 2021 IEEE [PHM21].
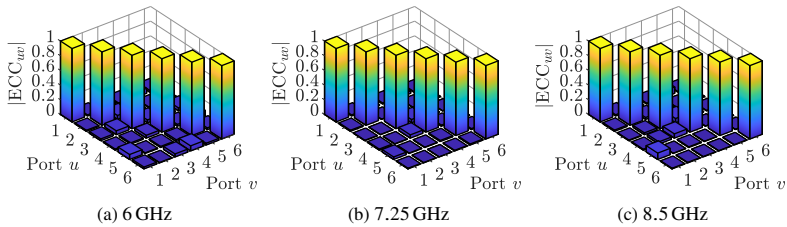

Figure 6.32 Envelope correlation coefficients of the fabricated six-port multimode antenna computed from simulated radiation patterns. (a) 6 GHz. (b) 7.25 GHz. (c) 8.5 GHz.

good estimate for the antenna performance. Deviations can be attributed to imperfections due to the fabrication process (e.g., solder contacts). All in all, it is concluded that the six antenna ports are well matched and decoupled around the center frequency with a reasonable bandwidth.

The simulated and measured realized gains of the far field radiation patterns excited by the six antenna ports at 7.25 GHz are shown in Fig. 6.29 and Fig. 6.30. The most important observation is that the simulated and measured patterns agree very well. In other words, the simulation model is well suited for predicting the far field patterns with regard to both shape and polarization as well as magnitude. Moreover, the symmetry of the radiation patterns is clearly visible. In particular, pattern nulls are well resolved.

For the purpose of this thesis, the most important parameter is the port correlation. Therefore, a more detailed analysis of the radiation patterns is

(a) Port 1   (b) Port 2   (c) Port 3

(d) Port 4   (e) Port 5   (f) Port 6

−60 −50 −40 −30 −20 −10   0
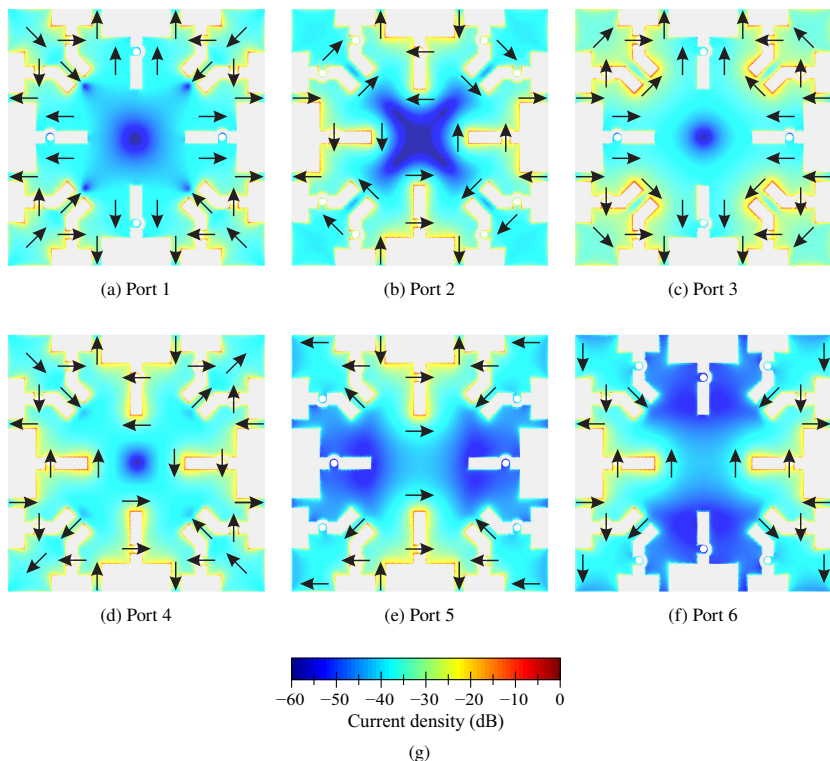Current density (dB)

(g)

Figure 6.33   Normalized simulated surface current densities on the antenna element of the fabricated six-port multimode antenna. Principal current directions and current directions at feed points denoted by arrows. (a) Port 1. (b) Port 2. (c) Port 3. (d) Port 4. (e) Port 5. (f) Port 6. (g) Color bar.

not conducted. Instead, the envelope correlation coefficients computed from the simulated and measured far field radiation patterns at 7.25 GHz according to (2.46) as shown in Fig. 6.31 are inspected. Evidently, the antenna ports are only weakly correlated. The maximum measured correlation occurs between ports 1 and 2 as well as ports 3 and 6 with an envelope correlation coefficient of approximately 0.05. From a practical point of view, the ports can thus be termed uncorrelated at the center frequency. Turning back to the radiation patterns in Fig. 6.29 and Fig. 6.30, it is deduced that the antenna ports offer pattern

and polarization diversity. In order to evaluate the port correlation at different frequencies, the simulated envelope correlation coefficients are inspected as the simulation model has been found to be well suited for predicting the antenna performance. In Fig. 6.32, the simulated envelope correlation coefficients at the center frequency and at the limits of the frequency range are shown, demonstrating that a low port correlation is achieved over the whole frequency range of interest. The maximum correlation occurs at 8.5 GHz between ports 1 and 5 with an envelope correlation coefficient of approximately 0.09. It is thus deduced that the port correlation is principally governed by the symmetry of the antenna element, which is a frequency-independent property (section 6.1.3). Again, deviations can be attributed mainly to the feed network.

As the antenna ports are practically uncorrelated (orthogonal), it is expected that the surface current densities on the antenna element fulfill the symmetry requirements of the irreducible representations of the symmetry group C_{4v} to a high degree. This is confirmed by examining the simulated surface current densities as shown in Fig. 6.33. A manual inspection of the symmetry properties of the surface current densities shows that they transform according to the irreducible representations of C_{4v} (Table 3.6). It is recalled that this is the fundamental fact enabling the port orthogonality. Although the excited surface current densities are more complex than the characteristic surface current densities of the original fundamental characteristic modes (Fig. 4.21), their symmetry is the decisive property.

Additionally, the symmetry of the surface current densities demonstrates that the feed network operates as intended, i.e., the input signals at the antenna ports are distributed to the feed points with the correct amplitude and phase relations. This is best illustrated in Fig. 6.33 by the arrows at the feed points. Furthermore, it can be seen that the surface current densities of ports 2, 4, 5, and 6 (Fig. 6.33(b), (d), (e), and (f)) couple to the feed points of ports 1 and 3 to some extent. This behavior is expected and the so excited signals would be suppressed by the ideal feed network (Fig. 6.4(b)) and could thus not reach ports 1 and 3. As discussed above, the real feed network allows some (practically negligible) coupling between the two network layers (Fig. 6.28) which can be attributed to this effect.

Finally, the total efficiencies [5] of the fabricated six-port multimode antenna computed from the measured realized gains (Fig. 6.29 and 6.30) are listed in Table 6.1. Ports 1 and 3, which share the feed network on layer 5, each have an efficiency of more than 60 %. Ports 2, 4, 5, and 6, which share the feed network on layer 2, have an average efficiency of approximately 50 %. As the

Antenna port	1	2	3	4	5	6
Total efficiency (%)	62.3	50.5	63.3	44.0	51.1	52.8

Table 6.1   Total efficiencies of the fabricated six-port multimode antenna computed from the measured realized gains at 7.25 GHz. © 2021 IEEE [PHM21].

antenna ports are sufficiently matched, the total efficiencies primarily describe the dielectric and ohmic losses of the antenna, which occur within the feed network, the coaxial baluns, and the antenna element. The feed network is identified as the main contributor to the total losses due to the stripline lengths.

In summary, the six ports of the fabricated multimode antenna are shown to be sufficiently matched, decoupled, and, in particular, uncorrelated over a reasonable frequency range. It is thus demonstrated that the upper bound for orthogonal antenna ports (section 4.4.2) can be reached based on the design guidelines derived from the symmetry analysis of characteristic modes (chapter 4) with a practical antenna design. Furthermore, the modular design approach, i.e., designing the antenna element (including baluns and choke wall) and the feed network separately, is shown to be appropriate.

The feed network has been identified as the principal source for complexity. Whereas the antenna element is designed using strict guidelines based on symmetry considerations, the feed network layout offers more degrees of freedom (choice of technology, components, layout) and is thus more challenging. These design choices have a direct impact on bandwidth, coupling, and losses. For these reasons, the feed network complexity is a limiting parameter in practical multimode antenna designs. According to Table 4.7, antenna geometries with a higher symmetry order offer more orthogonal antenna ports. However, the complexity of the feed networks will grow as well, potentially limiting the practically feasible number of orthogonal antenna ports.

7 Asymmetric Multimode Antennas

Having presented a complete and systematic design procedure for symmetric multimode antennas, the question arises what can be done if the antenna geometry does not possess any symmetry. This could, for instance, be the case if the metallic housing or chassis of a device (e.g., an IoT sensor node [55]) is supposed to be used as a multimode antenna. In such a scenario, the antenna geometry is fixed and must not be altered significantly. Naturally, the design guidelines introduced for symmetric antennas are not applicable in this case.

Even if a symmetric antenna design were potentially possible, e.g., the ground plane of a rectangular printed circuit board of a smart phone (cf. section 2.4.2), space for RF components may be strictly limited as other components have to be accommodated as well. However, the symmetry-centered design requires spatially distributed feed points and thus a space consuming feed network stretching over the complete geometry (cf. section 6.2). In scenarios as mentioned above, this is most likely to be prohibitive. In order to avoid bulky feed networks, each antenna port should consist of as few feed points as possible, ideally only one, leading again to an asymmetric antenna design.

Although this thesis is focused on leveraging symmetries for the systematic design of multimode antennas, at least some light should be shed on the above-mentioned problems. To this end, the consequences of antenna asymmetry are analyzed in this chapter. Based on this, a port placement procedure is developed which places antenna ports consisting of only one feed point each with the aim to minimize the envelope correlation coefficients. The basic feasibility of this approach is demonstrated by means of numerical examples.[107]

7.1 Consequences of Asymmetry

As there are no symmetry transformations under which an asymmetric object is invariant, the symmetry group of any asymmetric object consists of the identity E alone. This group is called C_1 of order $g = 1$ [78]. It has exactly one irreducible representation, the identity representation $\Gamma^{(1)} = A$, whose representation matrix (character) is $\mathbf{\Gamma}^{(1)} = \chi^{(1)} = 1$. Every characteristic surface current

---

[107]The following publication is related to the content of this chapter: [PM20] (© 2020 IEEE).

C_1	E
A	1

Table 7.1   Character table of symmetry group C_1. © 2020 IEEE [PM20].

density on an asymmetric PEC object is a basis function of this one irreducible representation. Applying the identity transformation to any characteristic surface current density is equal to a multiplication with 1, i.e., the current density remains unaltered. The trivial character table is given in Table 7.1.

As there is only one irreducible representation, the orthogonality theorem (3.27) states that all characteristic surface current densities are correlated ($p = q \wedge \nu = \kappa \; \forall \; n$). There are no mutually orthogonal sets. Furthermore, any impressed electric field also belongs to this one irreducible representation so that it, too, will be correlated to every characteristic surface current density, yielding nonzero modal excitation coefficients (2.24) for all n. Consequently, it is in general not possible to excite mutually exclusive sets of characteristic modes and thus realize orthogonal ports on an asymmetric antenna.

7.2 Port Placement Procedure for Asymmetric Antennas

In the previous section, it has been shown in a general way that it is not possible to realize perfectly uncorrelated ports on an asymmetric antenna. However, the actual amount of correlation between two ports cannot be predicted. Therefore, it should be possible to minimize the envelope correlation coefficients (2.46). According to (2.50), these can be expressed in terms of the normalized modal weighting coefficients alone. The objective is thus to place the antenna ports (consisting each of only one feed point) in such a way that the products of the resulting modal weighting coefficients add up destructively.

Of course, it would be rather cumbersome to do this manually, especially in a straightforward way. Instead, an automated port placement procedure is needed in order to find the port configuration which yields the minimum envelope correlation coefficients. An intuitive approach towards this goal is an exhaustive search. Although this is certainly not an efficient algorithm, it is easy to implement and able to find the global minimum. This property is important in order to investigate whether asymmetric multimode antennas with a reasonable number of only weakly correlated ports are feasible.

As the proposed method relies on modal parameters, a modal analysis of the antenna has to be conducted first. After that, delta-gap sources (section 2.3.3) can be placed on arbitrary edges of the triangular mesh (section 2.3.2). The corresponding modal weighting coefficients are computed using (2.45), (2.39), (2.22), and (2.26). It should be highlighted that the delta-gap sources do not really need to be placed physically. Instead, the MoM excitation vector according to (2.45) is simply permuted.

An advantage of the proposed port placement procedure is the fact that it works with modal parameters alone. Only one full simulation run of the antenna object is needed in order to perform the modal analysis. The computation of the modal weighting coefficients is then a mere post-processing step. As this is the principal computation step of the proposed method, it is comparatively fast.

In order to find a suitable starting point for the exhaustive search, the first delta-gap source is placed in such a way that it maximizes the normalized modal weighting coefficient of the most significant mode. This step is motivated by the fact that the most significant mode is expected to be the mode which can be excited most effectively and thus should be considered first. Simultaneously, maximizing the normalized modal weighting coefficient of one mode will minimize the normalized modal weighting coefficients of all other modes according to (2.26).

Next, a second delta-gap source is placed at every other remaining mesh edge and the position yielding the minimum correlation to the first delta-gap source computed according to (2.50) is selected. This procedure is repeated by adding further delta-gap sources as long as a predefined maximum envelope correlation coefficient ECC_{max} is not exceeded by any pair of delta-gap sources. The steps of the port placement procedure are summarized as follows:

1. Mesh the asymmetric antenna object.

2. Conduct a modal analysis of the asymmetric antenna object.

3. Choose a maximum allowed envelope correlation coefficient ECC_{max}.

4. Place the first delta-gap source at every mesh edge.

5. Compute the normalized modal weighting coefficients of the most significant mode.

6. Choose the position yielding the maximum normalized modal weighting coefficient.

7. Place another delta-gap source at every remaining mesh edge.

8. Compute the ECC to all other delta-gap sources placed before according to (2.50).

9. Choose the position yielding the minimum ECC.

10. If all ECC are below the chosen maximum ECC_{max}, repeat steps 7 to 9.

11. Else, stop the procedure and discard the last delta-gap source.

The steps 4 to 11 are post-processing steps operating only on the modal results.

7.3 Numerical Examples

In this section, two exemplary asymmetric antenna geometries are analyzed in order to demonstrate that it is basically possible to realize asymmetric multimode antennas with weakly correlated antenna ports.

7.3.1 Two-Dimensional Plate

As a first example, a two-dimensional L-shaped PEC plate as depicted in Fig. 7.1(a) is analyzed. Its outer dimensions are chosen so that it has approximately the same electrical size at 7.25 GHz as the rectangular PEC plate examined in section 2.4.2 at 2.5 GHz. The L-shaped PEC plate is discretized with a triangular mesh consisting of 3122 triangles. A modal analysis conducted at 7.25 GHz yields the modal significances shown in Fig. 7.1(b). The modes are sorted according to their significance. Three modes are found to be significant.

The resulting characteristic current correlation coefficients computed according to (2.51) are shown in Fig. 7.2. All characteristic surface current densities taken into account are correlated, confirming the general statements made in section 7.1. Although there are some modes that are only weakly correlated, there is no systematic pattern as known from symmetric objects.

Now, the port placement procedure introduced in section 7.2 is applied to the L-shaped PEC plate. The maximum allowed envelope correlation coefficient is set to $ECC_{max} = 0.2$,[108] resulting in the port configuration depicted in Fig. 7.1(a). Four antenna ports consisting each of one delta-gap source are found.

---

[108]This value is derived from [55], where the maximum tolerable correlation is given based on the evaluation of a complete MIMO system employing multimode antennas.
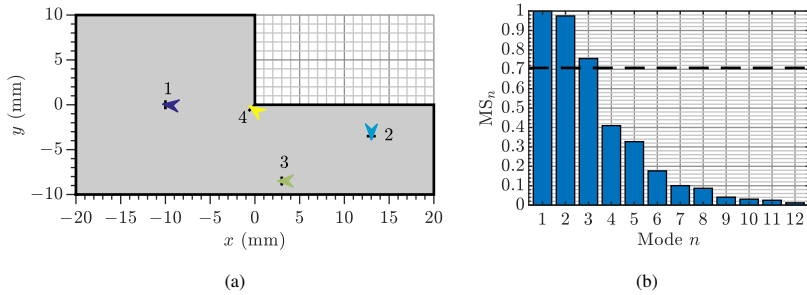
Figure 7.1 Two-dimensional asymmetric L-shaped PEC plate. (a) Plate with optimized port configuration. The four antenna ports each consist of one delta-gap source which are denoted by the black lines and the colored arrows. (b) Modal significances at 7.25 GHz. © 2020 IEEE [PM20].
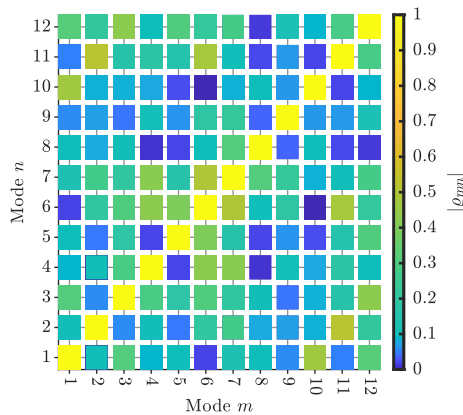
Figure 7.2 Characteristic current correlation coefficients of asymmetric L-shaped PEC plate according to Fig. 7.1(a) at 7.25 GHz computed using (2.51).

The corresponding normalized modal weighting coefficients are shown in Fig. 7.3(a). As intended, the normalized modal weighting coefficient of mode 1, the most significant mode (Fig. 7.1(b)), is close to 1, i.e., maximized by port 1. Accordingly, the other normalized modal weighting coefficients of port 1 are low, but not zero. This result corroborates that the modal weighting coefficients can in general not be made zero, as predicted in section 7.1. Port 2, in contrast,

Figure 7.3   Excitation parameters of asymmetric L-shaped PEC plate with port configuration according to Fig. 7.1(a) at 7.25 GHz. (a) Normalized modal weighting coefficients. (b) Envelope correlation coefficients. © 2020 IEEE [PM20].
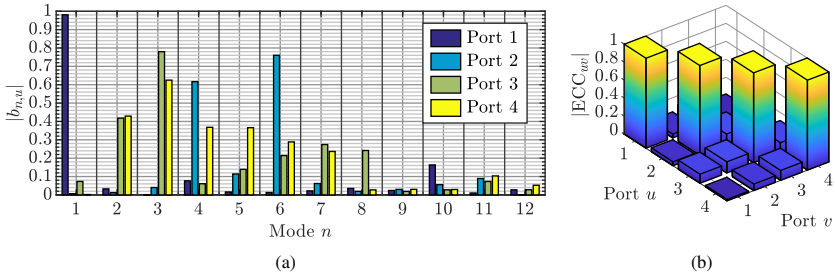
excites two dominant modes (modes 4 and 6), whereas ports 3 and 4 excite a mixture of several modes. Obviously, this is not an intuitive result which could have been found manually in a systematic way. All in all, it is observed that each mode is excited by each port at least to some extent.

The inspection of the envelope correlation coefficients in Fig. 7.3(b) confirms that the four antenna ports are only weakly correlated, as intended. The maximum correlation occurs between ports 2 and 3 with an envelope correlation coefficient of approximately 0.12, i.e., below the chosen threshold. Apparently, the successful strategy does not consist of exciting one dominant mode, but a combination of modes so that the products of the normalized modal weighting coefficients in (2.50) add up destructively.

The example demonstrates that the port placement procedure is capable of finding weakly correlated antenna ports. The question remains whether the port configuration can be realized in practice. As discussed in section 6.1.2, the delta-gap sources can be readily replaced by excitation slots. On a symmetric antenna, the placement and the form of the slots is subject to strict rules as the symmetry must be preserved. On an asymmetric antenna, in contrast, the actual form of the excitation slots is another degree of freedom. As discussed in the introduction of this chapter, the antenna object should not be altered significantly. For this reason, the excitation slots should be made electrically small.

Therefore, the delta-gap sources of ports 1 and 2 are replaced by simple short excitation slots as depicted in Fig. 7.4(a), whose orientations are inherited from the respective delta gaps (cf. Fig. 7.1(a)). Likewise, the positions of the feed
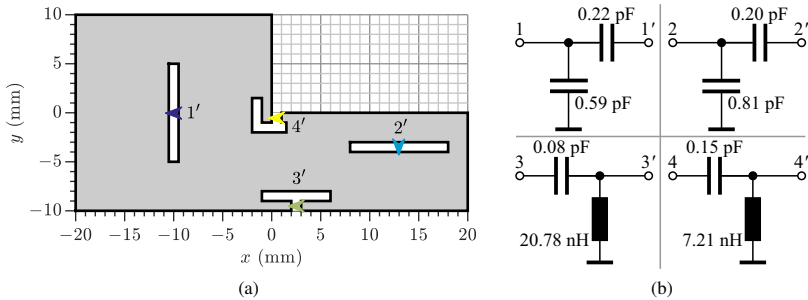
Figure 7.4 Two-dimensional asymmetric L-shaped PEC plate with excitation slots. (a) Placement of excitation slots derived from Fig. 7.1(a). The feed points within the excitation slots are denoted by the primed numbers and the colored arrows. (b) Two-component matching circuits between the antenna ports and the respective feed points derived by means of the bandwidth potential method. © 2020 IEEE [PM20].

points, which are denoted by the arrows corresponding to a voltage applied across the slot width, are inherited from the positions of the original delta-gap sources. As the delta-gap sources of ports 3 and 4 are close to the edge of the plate, they are replaced by the electrically small inductive coupling elements introduced in [42]. These offer the advantage that they do not extend towards the interior of the plate, allowing a compact implementation [43]. They consist of a short slot portion at the plate edge which is inherited from the delta gap and contains the feed point, and a long slot portion parallel to the plate edge.

As all four excitation slots are electrically small, inherent impedance matching by controlling the slot dimensions as was done in section 6.1.3 is not possible. Therefore, a matching circuit between each antenna port and its respective feed point is required [43] in order to realize a sufficient impedance match to the reference impedance 50 Ω. For the purpose of this chapter, simple two-component matching circuits consisting of ideal capacitors and/or inductors are sufficient. By means of the bandwidth potential method [100, 101], the matching circuit topologies and components offering the largest bandwidth are found.[109] The resulting matching circuits are listed in Fig. 7.4(b).

The L-shaped PEC plate with excitation slots is now simulated in Empire XPU. The matching circuits are taken into account by means of a circuit co-simulation.

---

[109]The bandwidth potential is the maximum bandwidth that can be obtained by means of a two-component matching circuit [100]. It can be computed for all possible circuit topologies. This way, different topologies can be compared and the optimum can be selected.
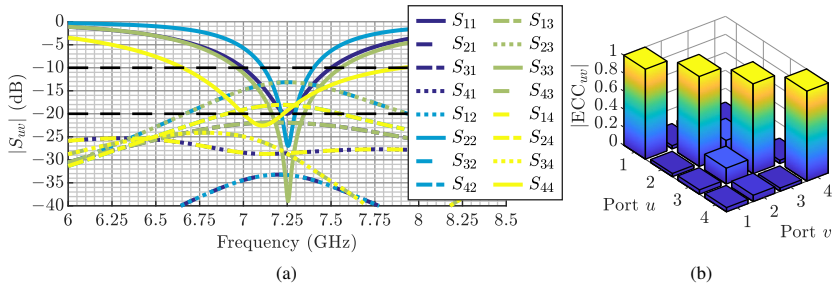
Figure 7.5   Input and excitation parameters of asymmetric L-shaped PEC plate with excitation slots and two-component matching circuits according to Fig. 7.4. (a) S-parameters (absolute values). (b) Envelope correlation coefficients at 7.25 GHz. © 2020 IEEE [PM20].

The resulting S-parameters are shown in Fig. 7.5(a). Thanks to the bandwidth potential method, all four antenna ports are sufficiently matched to $50\,\Omega$ around the center frequency 7.25 GHz with a reasonable bandwidth. Moreover, the mutual coupling between most ports is sufficiently low. However, the transmission coefficients between ports 2 and 4 (S_{42}, S_{24}) as well as ports 2 and 3 (S_{32}, S_{23}) are greater than -20 dB around the center frequency, indicating comparatively strong mutual coupling.

Nevertheless, the inspection of the envelope correlation coefficients in Fig. 7.5(b) confirms that all four antenna ports are still only weakly correlated. The maximum correlation occurs again between ports 2 and 3 with an envelope correlation coefficient of 0.18, having increased only slightly. This can be attributed to the fact that the antenna shape has not been altered significantly. It is thus concluded that the port placement procedure is basically suitable for practical asymmetric multimode antenna designs. It is found, however, that the mutual coupling between ports is more critical than the correlation and may become a limiting factor.

7.3.2 Three-Dimensional Object

In order to gain further insight and corroborate the results from the previous example, a more complex example is analyzed next. The three-dimensional asymmetric PEC object as depicted in Fig. 7.6(a) and (b) is considered. It is based on a rectangular cuboid with dimensions $40\,\text{mm} \times 20\,\text{mm} \times 10\,\text{mm}$ whose bottom face is removed. Furthermore, a rectangular portion of the cuboid
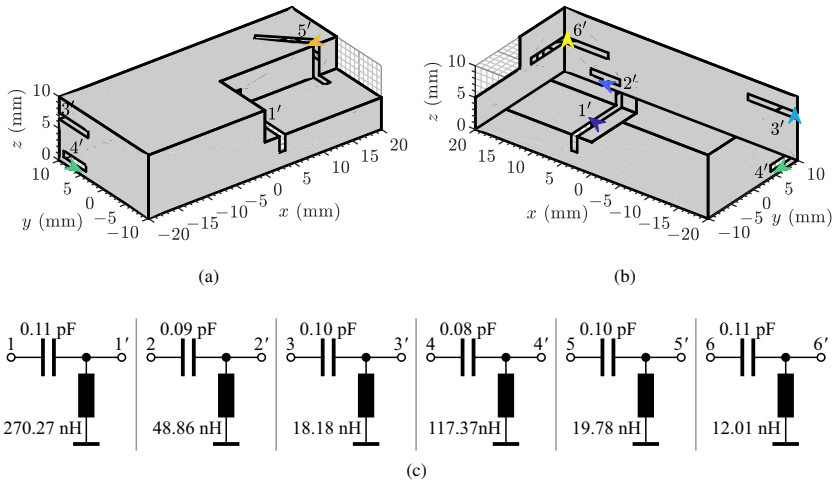
Figure 7.6 Three-dimensional asymmetric PEC object with excitation slots. The feed points within the excitation slots of the six antenna ports are denoted by the primed numbers and the colored arrows. (a) Isometric view. (b) Reversed view. (c) Two-component matching circuits between the antenna ports and the respective feed points derived by means of the bandwidth potential method. © 2020 IEEE [PM20].

with dimensions $20\,\text{mm} \times 10\,\text{mm} \times 5\,\text{mm}$ is removed in order to introduce asymmetry. A modal analysis of the object without the excitation slots conducted at 7.25 GHz with a mesh consisting of 2974 triangles yields 31 characteristic modes to be taken into account, including six significant modes.

The port placement procedure from section 7.2 is applied to this object allowing a maximum envelope correlation coefficient $\text{ECC}_{\text{max}} = 0.2$, yielding six weakly correlated antenna ports. As explained in the previous subsection, the resulting delta-gap sources are replaced by electrically small excitation slots as illustrated in Fig. 7.6(a) and (b). By means of the bandwidth potential method, the two-component matching circuits listed in Fig. 7.6(c) are determined.

The corresponding simulated S-parameters are shown in Fig. 7.7. All six antenna ports are sufficiently matched to $50\,\Omega$ around the center frequency (Fig. 7.7(a)). However, several ports exhibit strong mutual coupling (Fig. 7.7(b)). Nevertheless, the six ports are only weakly correlated as evidenced by Fig. 7.8. The maximum correlation occurs between ports 2 and 5 as well as ports 5 and 6, reaching the given threshold $\text{ECC}_{\text{max}} = 0.2$.
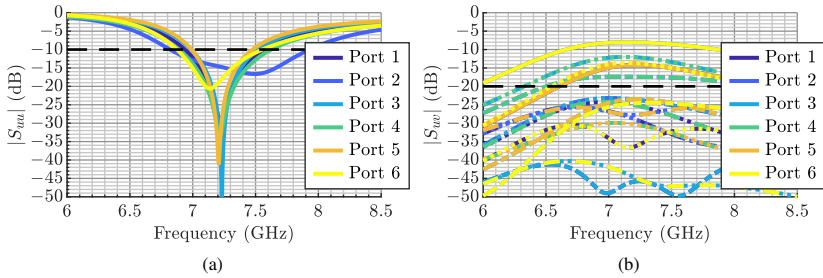
Figure 7.7   S-parameters (absolute values) of asymmetric PEC object with excitation slots and two-component matching circuits according to Fig. 7.6. (a) Input reflection coefficients. (b) Transmission coefficients from specified ports to all other ports. © 2020 IEEE [PM20].
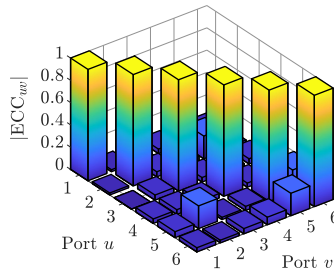
Figure 7.8   Envelope correlation coefficients of asymmetric PEC object with excitation slots and two-component matching circuits according to Fig. 7.6 at 7.25 GHz. © 2020 IEEE [PM20].

This second example demonstrates that the proposed port placement procedure can be readily applied to more complex asymmetric antenna objects. However, it also confirms that the mutual coupling is more critical than the port correlation and can become prohibitively high despite a low port correlation.

In conclusion, the two examples corroborate that it is basically possible to realize weakly correlated antenna ports on asymmetric antenna geometries. In particular, the complexity of the feed networks is greatly reduced to single matching circuits per port and feed point, which are not interconnected (cf. section 6.2). These results are facilitated by exploiting the characteristic modes and their connection to the envelope correlation coefficients. This way, the simulation effort is reduced even though an exhaustive search is employed.

The proposed port placement procedure can definitely be termed systematic as it takes into account the basic cause for the correlation of antenna ports, i.e., ports exciting the same characteristic modes, and tries to minimize it. Future work should focus on improving the procedure, e.g., by employing a more sophisticated search algorithm and taking into account mutual coupling. A disadvantage of the procedure is that it does not provide deeper insight. Gaining *a priori* knowledge and deriving systematic design guidelines as has been done in this thesis for symmetric multimode antennas, apart from the fact that perfectly uncorrelated antenna ports cannot be realized, is not possible. For example, the maximum number of weakly correlated antennas ports offered by a given antenna geometry cannot be predicted. Nevertheless, this knowledge can now quickly be gained by performing a modal analysis and conducting the port placement procedure. Therefore, such considerations should not hide the potential of the proposed method. It should rather be considered as another building block of a general design environment for multimode antennas.

8 Conclusion

The analysis and the design of multimode antennas for MIMO applications based on the theory of characteristic modes are investigated. The foremost objective of this thesis is the design of orthogonal antenna ports in order enable the diversity required for good MIMO performance. Antenna ports which excite mutually exclusive sets of characteristic modes are perfectly orthogonal to each other.

However, the characteristic surface current densities of an antenna are in general not orthogonal to each other. An antenna port will thus generally excite all modes whose respective characteristic surface current densities are correlated. It is found, though, that symmetric antenna geometries offer mutually orthogonal sets of characteristic surface current densities. This observation is rooted in the fact that the theory of characteristic modes is fundamentally connected to the theory of symmetry. The characteristic surface current densities are basis functions of the irreducible representations of the symmetry group of an antenna. Due to the fundamental orthogonality theorem, characteristic surface current densities belonging to different irreducible representations or belonging to different rows of a multi-dimensional irreducible representation are orthogonal to each other. Consequently, the number of mutually orthogonal sets of characteristic surface current densities is determined by the number and the dimensions of the irreducible representations of the symmetry group.

These mutually orthogonal sets can be excited separately by antenna ports which are designed as basis functions of the irreducible representations. Each antenna port thus consists of several feed points placed symmetrically on the antenna element which are driven by means of a feed network in such a way that the symmetry requirements of the irreducible representations are fulfilled. This way, one port only excites those modes which belong to the same row of the same irreducible representation as the port. As the number and the dimensions of the irreducible representations of a given symmetry group are limited, there is an upper bound for realizing orthogonal antenna ports which is governed by the symmetry group of the given antenna geometry.

All optimal orthogonal antenna ports offered by a given antenna geometry can be generated automatically by means of the projection operator method, yielding the minimum number of feed points per port. These optimal port configurations

are only governed by the symmetry group of the antenna and independent of the actual antenna size. However, the projection operator method does not only enable an automatic port placement for multimode antennas, but also an automatic symmetry analysis of characteristic modes. In particular, the characteristic modes can be assigned systematically to the irreducible representations. This allows the definition of the fundamental modes per irreducible representation, i.e., those modes which first become significant as functions of frequency. For the design of multimode antennas, it is sufficient that only the fundamental modes are significant and the antenna size can be minimized accordingly.

The findings of this thesis are valid for all finite antenna geometries, i.e., whose symmetry groups are point groups. The structure of group theory allows to advantageously utilize various relationships between symmetry groups for analyzing and designing potential multimode antennas. More complex geometries may be described by means of group isomorphisms or as direct-product groups, enabling the reuse of results previously derived for simpler geometries. Moreover, related symmetry groups may be collected into a family which is generalized by an infinite symmetry group. The modal results of the corresponding generalized geometry can be used to predict the modal behavior of all members of the family. The numerous examples considered within this thesis demonstrate how the introduced concepts can be readily applied.

In conclusion, the symmetry analysis of characteristic modes and its application to the design of multimode antennas yield valuable *a priori* knowledge. The maximum number of orthogonal antenna ports and their optimal configurations are determined from the symmetry of the antenna alone without even conducting a modal analysis. The generalized modal analysis allows predictions about the minimum antenna size. Based on the structure of symmetry groups, the diversity potential of completely different geometries can be compared. This knowledge enables the systematic design of multimode antennas with more orthogonal antenna ports than reported so far in the literature.

The design guidelines derived in this thesis can be readily put into practice, as demonstrated by means of the realized prototype. It is based on a square geometry which is optimized systematically starting from the symmetry analysis in conjunction with the generalized modal analysis. The feed network is identified as a major source of complexity from a practical point of view. The modular design approach results in a compact and low-profile implementation. The realized six-port multimode antenna confirms the theoretical findings of this thesis and proves that the upper bound for orthogonal antenna ports can be reached with a practical design.

Appendices

A Time-Harmonic Electromagnetic Fields

In this appendix, a detailed compilation of the field quantities and equations employed in chapter 2 is provided. They are all based on the general Maxwell's equations in time domain [64]:

$$\mathrm{rot}\big(\mathscr{H}(\mathbf{r},t)\big) = \mathscr{J}(\mathbf{r},t) + \frac{\partial}{\partial t}\mathscr{D}(\mathbf{r},t), \tag{A.1a}$$

$$\mathrm{rot}\big(\mathscr{E}(\mathbf{r},t)\big) = -\frac{\partial}{\partial t}\mathscr{B}(\mathbf{r},t), \tag{A.1b}$$

$$\mathrm{div}\big(\mathscr{B}(\mathbf{r},t)\big) = 0, \tag{A.1c}$$

$$\mathrm{div}\big(\mathscr{D}(\mathbf{r},t)\big) = \mathscr{q}(\mathbf{r},t). \tag{A.1d}$$

The script-style symbols of the field quantities introduced in (2.1) are used to emphasize a general time dependence, with t denoting time. The continuity equation expressing the conservation of charge is given by [64]

$$\mathrm{div}\,\mathscr{J}(\mathbf{r},t) = -\frac{\partial}{\partial t}\mathscr{q}(\mathbf{r},t). \tag{A.2}$$

This equation is implicitly included in Maxwell's equations and can be derived by applying the divergence to (A.1a) and then inserting (A.1d).

A.1 Harmonic Time Dependence

It is now assumed that all field quantities in (A.1) have harmonic time dependence. Any field quantity can then be expressed in the following way, e.g., the electric field strength [64]:

$$\mathscr{E}(\mathbf{r},t) = \begin{pmatrix} \mathscr{E}_x(\mathbf{r},t) \\ \mathscr{E}_y(\mathbf{r},t) \\ \mathscr{E}_z(\mathbf{r},t) \end{pmatrix} = \begin{pmatrix} \hat{E}_x(\mathbf{r})\cos\big(\omega t + \varphi_{E_x}(\mathbf{r})\big) \\ \hat{E}_y(\mathbf{r})\cos\big(\omega t + \varphi_{E_y}(\mathbf{r})\big) \\ \hat{E}_z(\mathbf{r})\cos\big(\omega t + \varphi_{E_z}(\mathbf{r})\big) \end{pmatrix} = \mathrm{Re}\big(\mathbf{E}(\mathbf{r})e^{j\omega t}\big), \tag{A.3}$$

where $\hat{E}_{x;y;z}$ is the real amplitude and $\varphi_{E_{x;y;z}}$ the phase of the respective component $\mathscr{E}_{x;y;z}$ of the time-harmonic electric field strength. The operator Re

denotes the real part of a complex function. The harmonic time dependence can be expressed by the complex exponential function, whereas the space dependent amplitude and phase are collected into the complex amplitude $\mathbf{E}$:

$$\mathbf{E}(\mathbf{r}) = \begin{pmatrix} \hat{E}_x(\mathbf{r})e^{j\varphi_{Ex}(\mathbf{r})} \\ \hat{E}_y(\mathbf{r})e^{j\varphi_{Ey}(\mathbf{r})} \\ \hat{E}_z(\mathbf{r})e^{j\varphi_{Ez}(\mathbf{r})} \end{pmatrix}. \tag{A.4}$$

This way, the time and the space dependence are separated. As the time dependence is deterministic, the important information is completely contained in the complex amplitude.

If all field quantities are expressed in this form and inserted into (A.1), Maxwell's equations can be written in terms of complex amplitudes alone. This is exemplarily shown for (A.1a):

$$\mathrm{rot}\Big(\mathrm{Re}\big(\mathbf{H}(\mathbf{r})e^{j\omega t}\big)\Big) = \mathrm{Re}\big(\mathbf{J}(\mathbf{r})e^{j\omega t}\big) + \frac{\partial}{\partial t}\Big(\mathrm{Re}\big(\mathbf{D}(\mathbf{r})e^{j\omega t}\big)\Big). \tag{A.5}$$

Due to the linearity of the operator Re [64], this can be rewritten as follows:

$$\mathrm{Re}\Big(\mathrm{rot}\big(\mathbf{H}(\mathbf{r})e^{j\omega t}\big)\Big) = \mathrm{Re}\Big(\mathbf{J}(\mathbf{r})e^{j\omega t} + \frac{\partial}{\partial t}\big(\mathbf{D}(\mathbf{r})e^{j\omega t}\big)\Big). \tag{A.6}$$

In this form, it is obvious that the equation also holds for the argument of Re. Furthermore, the derivative with respect to time can be carried out explicitly and the time dependence can be dropped, finally yielding

$$\mathrm{rot}\big(\mathbf{H}(\mathbf{r})\big) = \mathbf{J}(\mathbf{r}) + j\omega\mathbf{D}(\mathbf{r}). \tag{A.7}$$

Applying this derivation to the other equations in (A.1) yields the time-harmonic Maxwell's equations in (2.1)

If in addition the constitutive relationships (2.2) are taken into account, the time-harmonic Maxwell's equations can be expressed in terms of the field strengths alone:

$$\mathrm{rot}\big(\mathbf{H}(\mathbf{r})\big) = \mathbf{J}(\mathbf{r}) + j\omega\varepsilon\mathbf{E}(\mathbf{r}), \tag{A.8a}$$

$$\mathrm{rot}\big(\mathbf{E}(\mathbf{r})\big) = -j\omega\mu\mathbf{H}(\mathbf{r}), \tag{A.8b}$$

$$\mathrm{div}\big(\mathbf{H}(\mathbf{r})\big) = 0, \tag{A.8c}$$

$$\mathrm{div}\big(\mathbf{E}(\mathbf{r})\big) = \frac{q(\mathbf{r})}{\varepsilon}, \tag{A.8d}$$

which forms the basis for the subsequent derivations.

A.2 Homogeneous Helmholtz Equation

The homogeneous Helmholtz equation describes the propagation of time-harmonic electromagnetic waves in a homogeneous, source-free region ($\mathbf{J}(\mathbf{r}) = \mathbf{0}$, $q(\mathbf{r}) = 0$). It is derived by applying the curl to (A.8a) and (A.8b) [64]:

$$\text{rot}\big(\text{rot}(\mathbf{H}(\mathbf{r}))\big) = j\omega\varepsilon\,\text{rot}(\mathbf{E}(\mathbf{r})), \tag{A.9a}$$

$$\text{rot}\big(\text{rot}(\mathbf{E}(\mathbf{r}))\big) = -j\omega\mu\,\text{rot}(\mathbf{H}(\mathbf{r})). \tag{A.9b}$$

Inserting (A.8b) into (A.9a) and (A.8a) into (A.9b) yields

$$\text{rot}\big(\text{rot}(\mathbf{H}(\mathbf{r}))\big) = k^2\mathbf{H}(\mathbf{r}), \tag{A.10a}$$

$$\text{rot}\big(\text{rot}(\mathbf{E}(\mathbf{r}))\big) = k^2\mathbf{E}(\mathbf{r}), \tag{A.10b}$$

with $k^2 = \omega^2\varepsilon\mu$. Using $\text{rot}(\text{rot}\mathbf{F}) = \text{grad}(\text{div}\mathbf{F}) - \Delta\mathbf{F}$, where $\mathbf{F}$ is an arbitrary vector field, and exploiting the divergencelessness of the magnetic and the electric field strength yields the homogeneous vector Helmholtz equation:

$$\Delta\mathbf{H}(\mathbf{r}) + k^2\mathbf{H}(\mathbf{r}) = \mathbf{0}, \tag{A.11a}$$

$$\Delta\mathbf{E}(\mathbf{r}) + k^2\mathbf{E}(\mathbf{r}) = \mathbf{0}, \tag{A.11b}$$

which is the same for both the magnetic and the electric field strength.

A.3 Potentials

As the magnetic flux density is divergenceless (2.1c), it can be expressed as the curl of some other vector field [64]:

$$\mathbf{B}(\mathbf{r}) = \mu\mathbf{H}(\mathbf{r}) = \text{rot}(\mathbf{A}(\mathbf{r})). \tag{A.12}$$

The vector field $\mathbf{A}$ is called the magnetic vector potential. This definition is now inserted into (A.8b), yielding

$$\text{rot}(\mathbf{E}(\mathbf{r}) + j\omega\mathbf{A}(\mathbf{r})) = \mathbf{0}. \tag{A.13}$$

Any curl-free vector field can be expressed as the gradient of some scalar function [64]:

$$\mathbf{E}(\mathbf{r}) + j\omega\mathbf{A}(\mathbf{r}) = -\text{grad}(\phi(\mathbf{r})). \tag{A.14}$$

The scalar function ϕ is called the electric scalar potential. The electric and magnetic field quantities can now be expressed in terms of the magnetic vector potential and the electric scalar potential, as given in (2.3) and (2.4).

A.4 Inhomogeneous Helmholtz Equation

The potentials are introduced in order to treat the radiation of electromagnetic waves by a source region ($\mathbf{J}(\mathbf{r}) \neq \mathbf{0}$, $q(\mathbf{r}) \neq 0$) [5]. To this end, (2.3) and (2.4) are inserted into (A.8a) [64], yielding

$$\mathrm{rot}\Big(\mathrm{rot}\big(\mathbf{A}(\mathbf{r})\big)\Big) = \mu\mathbf{J}(\mathbf{r}) + \omega^2\varepsilon\mu\mathbf{A}(\mathbf{r}) - j\omega\varepsilon\mu\,\mathrm{grad}\big(\phi(\mathbf{r})\big). \qquad (A.15)$$

With $\mathrm{rot}(\mathrm{rot}\mathbf{A}) = \mathrm{grad}(\mathrm{div}\mathbf{A}) - \Delta\mathbf{A}$ and $k^2 = \omega^2\varepsilon\mu$, this can be rewritten as

$$\Delta\mathbf{A}(\mathbf{r}) + k^2\mathbf{A}(\mathbf{r}) = -\mu\mathbf{J}(\mathbf{r}) + \mathrm{grad}\Big(\mathrm{div}\big(\mathbf{A}(\mathbf{r})\big) + j\omega\varepsilon\mu\phi(\mathbf{r})\Big). \qquad (A.16)$$

The divergence of the magnetic vector potential is now chosen to be [64]

$$\mathrm{div}\big(\mathbf{A}(\mathbf{r})\big) = -j\omega\varepsilon\mu\phi(\mathbf{r}), \qquad (A.17)$$

which is known as Lorenz gauge. Applying this to (A.16) yields the inhomogeneous vector Helmholtz equation for the magnetic vector potential (2.5):

$$\Delta\mathbf{A}(\mathbf{r}) + k^2\mathbf{A}(\mathbf{r}) = -\mu\mathbf{J}(\mathbf{r}). \qquad (A.18)$$

Next, (2.4) is inserted into (A.8d) [65]:

$$-\mathrm{div}\Big(\mathrm{grad}\big(\phi(\mathbf{r})\big)\Big) - j\omega\,\mathrm{div}\big(\mathbf{A}(\mathbf{r})\big) = \frac{q(\mathbf{r})}{\varepsilon}. \qquad (A.19)$$

With $\mathrm{div}(\mathrm{grad}\phi) = \Delta\phi$, the Lorenz gauge (A.17), and $k^2 = \omega^2\varepsilon\mu$, this reduces to

$$\Delta\phi(\mathbf{r}) + k^2\phi(\mathbf{r}) = -\frac{q(\mathbf{r})}{\varepsilon}, \qquad (A.20)$$

which is the inhomogeneous scalar Helmholtz equation for the electric scalar potential (2.6). The Green's function method [66] is employed in order to find a solution to the inhomogeneous Helmholtz equation, yielding the integral equations (2.8) and (2.9).

A.5 Complex Poynting Theorem

The complex Poynting theorem describes the power flow of time-harmonic electromagnetic fields. The derivation of the complex Poynting theorem is based on the first two time-harmonic Maxwell's equations ((A.8a) and (A.8b)) as they completely characterize the dynamic behavior of electromagnetic fields. As a first step, the electric current density $\mathbf{J}$ is split into an impressed current density $\mathbf{J}_i$ and a conduction current density $\mathbf{J}_\kappa = \kappa \mathbf{E}$ due to a finite conductivity κ [64]:

$$\mathrm{rot}\big(\mathbf{H}(\mathbf{r})\big) = \mathbf{J}_i(\mathbf{r}) + \kappa \mathbf{E}(\mathbf{r}) + j\omega\varepsilon\mathbf{E}(\mathbf{r}), \qquad \text{(A.21a)}$$

$$\mathrm{rot}\big(\mathbf{E}(\mathbf{r})\big) = -j\omega\mu\mathbf{H}(\mathbf{r}). \qquad \text{(A.21b)}$$

In order to convert the field quantities into power-related quantities (power densities with unit $\mathrm{W\,m^{-3}}$), the complex conjugate of (A.21a) is multiplied by $\frac{1}{2}\mathbf{E}$ and (A.21b) is multiplied by $\frac{1}{2}\mathbf{H}^*$ [64]:[110]

$$\frac{1}{2}\mathbf{E}(\mathbf{r}) \cdot \mathrm{rot}\big(\mathbf{H}^*(\mathbf{r})\big) = \frac{1}{2}\mathbf{E}(\mathbf{r}) \cdot \mathbf{J}_i^*(\mathbf{r}) + \frac{\kappa}{2}\big\|\mathbf{E}(\mathbf{r})\big\|^2 - j\frac{\omega\varepsilon}{2}\big\|\mathbf{E}(\mathbf{r})\big\|^2, \quad \text{(A.22a)}$$

$$\frac{1}{2}\mathbf{H}^*(\mathbf{r}) \cdot \mathrm{rot}\big(\mathbf{E}(\mathbf{r})\big) = -j\frac{\omega\mu}{2}\big\|\mathbf{H}(\mathbf{r})\big\|^2. \qquad \text{(A.22b)}$$

Next, (A.22b) is subtracted from (A.22a) [64]:

$$\frac{1}{2}\mathbf{E}(\mathbf{r}) \cdot \mathrm{rot}\big(\mathbf{H}^*(\mathbf{r})\big) - \frac{1}{2}\mathbf{H}^*(\mathbf{r}) \cdot \mathrm{rot}\big(\mathbf{E}(\mathbf{r})\big) =$$

$$= \frac{1}{2}\mathbf{E}(\mathbf{r}) \cdot \mathbf{J}_i^*(\mathbf{r}) + \frac{\kappa}{2}\big\|\mathbf{E}(\mathbf{r})\big\|^2 + j\frac{\omega\mu}{2}\big\|\mathbf{H}(\mathbf{r})\big\|^2 - j\frac{\omega\varepsilon}{2}\big\|\mathbf{E}(\mathbf{r})\big\|^2. \qquad \text{(A.23)}$$

By means of the divergence theorem, the left-hand side of (A.23) is simplified to $-\frac{1}{2}\mathrm{div}\big(\mathbf{E}\times\mathbf{H}^*\big)$ [64], yielding the differential form of the complex Poynting theorem in terms of power densities:

$$0 = \frac{1}{2}\mathbf{E}(\mathbf{r})\cdot\mathbf{J}_i^*(\mathbf{r}) + \frac{\kappa}{2}\big\|\mathbf{E}(\mathbf{r})\big\|^2 + j\frac{\omega}{2}\Big(\mu\big\|\mathbf{H}(\mathbf{r})\big\|^2 - \varepsilon\big\|\mathbf{E}(\mathbf{r})\big\|^2\Big) + \frac{1}{2}\mathrm{div}\Big(\mathbf{E}(\mathbf{r})\times\mathbf{H}^*(\mathbf{r})\Big). \qquad \text{(A.24)}$$

---

[110]The factor $\frac{1}{2}$ is due to the use of complex amplitudes. Power quantities are computed using root mean square (RMS) field quantities, with $\mathbf{E}_{\mathrm{RMS}} = \frac{1}{\sqrt{2}}\mathbf{E}$ in the time-harmonic case.

Integrating this equation over a volume V enclosing a source region eventually yields the integral form of the complex Poynting theorem in terms of powers:

$$0 = \frac{1}{2} \iiint\limits_{V} \left(\mathbf{E}(\mathbf{r}) \cdot \mathbf{J}_i^*(\mathbf{r}) \right) dV + \frac{\kappa}{2} \iiint\limits_{V} \|\mathbf{E}(\mathbf{r})\|^2 dV +$$

$$+ j\frac{\omega}{2} \iiint\limits_{V} \left(\mu \|\mathbf{H}(\mathbf{r})\|^2 - \varepsilon \|\mathbf{E}(\mathbf{r})\|^2 \right) dV + \frac{1}{2} \oiint\limits_{\partial V} \left(\mathbf{E}(\mathbf{r}) \times \mathbf{H}^*(\mathbf{r}) \right) d\mathbf{S}, \quad \text{(A.25)}$$

where Gauss's law is used to convert the volume integral containing $\mathrm{div}\left(\mathbf{E} \times \mathbf{H}^*\right)$ into a surface integral. The first integral on the right-hand side of A.25 can be interpreted as the total complex power, which is impressed into the volume by a power source. In the context of characteristic modes, however, there are no sources and the term should be simply referred to as the total complex power (cf. (2.19)). The second integral in (A.25) denotes the real power dissipated due to conduction losses (finite conductivity). In the context of characteristic modes for perfect electric conductors, this term is irrelevant. The third integral in (A.25), in contrast, is related to reactive power due to magnetic and electric energy storage. The last integral in A.25, finally, describes the complex power leaving or entering the volume through its surface by means of an electromagnetic wave. In the far field ($\partial V \to S_\infty$), this term is purely real and denotes the radiated power [5], which is due to the fact that $\mathbf{E}$ and $\mathbf{H}$ are in phase. Furthermore, the direction of wave propagation is perpendicular to S_∞ [5] so that

$$P_{\mathrm{rad}} = \frac{1}{2} \oiint\limits_{S_\infty} \left(\mathbf{E}(\mathbf{r}) \times \mathbf{H}^*(\mathbf{r}) \right) d\mathbf{S} = \frac{1}{2} \oiint\limits_{S_\infty} \|\mathbf{E}(\mathbf{r}) \times \mathbf{H}^*(\mathbf{r})\| dS. \quad \text{(A.26)}$$

Additionally, it can be exploited that $\mathbf{E}$ and $\mathbf{H}$ are perpendicular in the far field (transverse electromagnetic wave) [5]:

$$P_{\mathrm{rad}} = \frac{1}{2} \oiint\limits_{S_\infty} \|\mathbf{E}(\mathbf{r}) \times \mathbf{H}^*(\mathbf{r})\| dS = \frac{1}{2} \oiint\limits_{S_\infty} \|\mathbf{E}(\mathbf{r})\| \|\mathbf{H}^*(\mathbf{r})\| \sin\left(\underbrace{\angle(\mathbf{E,H})}_{\pi/2}\right) dS$$

$$= \frac{1}{2} \oiint\limits_{S_\infty} \|\mathbf{E}(\mathbf{r})\| \|\mathbf{H}(\mathbf{r})\| dS. \quad \text{(A.27)}$$

Finally, $\|\mathbf{E}\|$ and $\|\mathbf{H}\|$ are related by the wave impedance Z_0 [5], yielding

$$P_{\mathrm{rad}} = \frac{1}{2} \oiint\limits_{S_\infty} \|\mathbf{E}(\mathbf{r})\| \|\mathbf{H}(\mathbf{r})\| dS = \frac{1}{2Z_0} \oiint\limits_{S_\infty} \|\mathbf{E}(\mathbf{r})\|^2 dS. \quad \text{(A.28)}$$

B Inner Product

The functions considered in this thesis, e.g., surface current densities, belong to the space of complex vector-valued square-integrable functions. This function space is called the Hilbert space L^2 [79]. Any function $\mathbf{f}(\mathbf{r}) = (f_x(\mathbf{r}), f_y(\mathbf{r}), f_z(\mathbf{r}))^{\mathrm{T}} : \mathbb{R}^3 \to \mathbb{C}^3$ of this space satisfies [75]

$$\int\limits_{-\infty}^{\infty} \int\limits_{-\infty}^{\infty} \int\limits_{-\infty}^{\infty} \|\mathbf{f}(\mathbf{r})\|^2 \mathrm{d}x\mathrm{d}y\mathrm{d}z = \int\limits_{-\infty}^{\infty} \int\limits_{-\infty}^{\infty} \int\limits_{-\infty}^{\infty} \left(|f_x(\mathbf{r})|^2 + |f_y(\mathbf{r})|^2 + |f_z(\mathbf{r})|^2 \right) \mathrm{d}x\mathrm{d}y\mathrm{d}z < \infty.$$
(B.1)

Physically, this can be interpreted as a power limiting property, i.e., the power cannot become infinite (cf. appendix A.5).

In this Hilbert space, the inner product of two vector-valued functions $\mathbf{f}$ and $\mathbf{g}$ is defined as follows [75, 79]:

$$\left\langle \mathbf{f}(\mathbf{r}), \mathbf{g}(\mathbf{r}) \right\rangle = \int\limits_{-\infty}^{\infty} \int\limits_{-\infty}^{\infty} \int\limits_{-\infty}^{\infty} \left(\mathbf{f}^*(\mathbf{r}) \cdot \mathbf{g}(\mathbf{r}) \right) \mathrm{d}x\mathrm{d}y\mathrm{d}z$$

$$= \int\limits_{-\infty}^{\infty} \int\limits_{-\infty}^{\infty} \int\limits_{-\infty}^{\infty} \left(f_x^*(\mathbf{r}) g_x(\mathbf{r}) + f_y^*(\mathbf{r}) g_y(\mathbf{r}) + f_z^*(\mathbf{r}) g_z(\mathbf{r}) \right) \mathrm{d}x\mathrm{d}y\mathrm{d}z$$

$$= \left\langle f_x(\mathbf{r}), g_x(\mathbf{r}) \right\rangle + \left\langle f_y(\mathbf{r}), g_y(\mathbf{r}) \right\rangle + \left\langle f_z(\mathbf{r}), g_z(\mathbf{r}) \right\rangle.$$
(B.2)

The inner product of two vector-valued functions can also be written as the sum of the inner products of their scalar components.

The norm of a vector-valued function $\mathbf{f}$ results directly from the definition of the inner product [75]:[111]

$$\left\langle \mathbf{f}(\mathbf{r}), \mathbf{f}(\mathbf{r}) \right\rangle = \int\limits_{-\infty}^{\infty} \int\limits_{-\infty}^{\infty} \int\limits_{-\infty}^{\infty} \left(\mathbf{f}^*(\mathbf{r}) \cdot \mathbf{f}(\mathbf{r}) \right) \mathrm{d}x\mathrm{d}y\mathrm{d}z = \int\limits_{-\infty}^{\infty} \int\limits_{-\infty}^{\infty} \int\limits_{-\infty}^{\infty} \|\mathbf{f}(\mathbf{r})\|^2 \mathrm{d}x\mathrm{d}y\mathrm{d}z.$$
(B.3)

---

[111] In order to avoid confusion, the symbol $\| \cdot \|$ is reserved for the norm of a vector throughout this thesis, e.g., $\|\mathbf{v}\|^2 = |v_x|^2 + |v_y|^2 + |v_z|^2$.

Based on its definition, the inner product has the following properties [75]:

$$\Big\langle \mathbf{f}_1(\mathbf{r}), \mathbf{f}_2(\mathbf{r}) \Big\rangle = \Big\langle \mathbf{f}_2(\mathbf{r}), \mathbf{f}_1(\mathbf{r}) \Big\rangle^*, \tag{B.4a}$$

$$\Big\langle a_1 \mathbf{f}_1(\mathbf{r}), a_2 \mathbf{f}_2(\mathbf{r}) \Big\rangle = a_1^* a_2 \Big\langle \mathbf{f}_1(\mathbf{r}), \mathbf{f}_2(\mathbf{r}) \Big\rangle, \tag{B.4b}$$

$$\Big\langle \mathbf{f}_1(\mathbf{r}) + \mathbf{f}_2(\mathbf{r}), \mathbf{g}(\mathbf{r}) \Big\rangle = \Big\langle \mathbf{f}_1(\mathbf{r}), \mathbf{g}(\mathbf{r}) \Big\rangle + \Big\langle \mathbf{f}_2(\mathbf{r}), \mathbf{g}(\mathbf{r}) \Big\rangle, \tag{B.4c}$$

$$\Big\langle \mathbf{g}(\mathbf{r}), \mathbf{f}_1(\mathbf{r}) + \mathbf{f}_2(\mathbf{r}) \Big\rangle = \Big\langle \mathbf{g}(\mathbf{r}), \mathbf{f}_1(\mathbf{r}) \Big\rangle + \Big\langle \mathbf{g}(\mathbf{r}), \mathbf{f}_2(\mathbf{r}) \Big\rangle, \tag{B.4d}$$

$$\Big\langle \mathbf{f}(\mathbf{r}), \mathbf{f}(\mathbf{r}) \Big\rangle \geq 0, \tag{B.4e}$$

$$\Big\langle \mathbf{f}(\mathbf{r}), \mathbf{f}(\mathbf{r}) \Big\rangle = 0 \text{ if and only if } \mathbf{f}(\mathbf{r}) = \mathbf{0}, \tag{B.4f}$$

with $a_1, a_2 \in \mathbb{C}$ and $\mathbf{f}, \mathbf{f}_1, \mathbf{f}_2, \mathbf{g} \in L^2$.

B.1 Gram-Schmidt Orthogonalization Process

Now, it is assumed that a finite set of d linearly independent vector-valued functions $\mathbf{f}_1, \mathbf{f}_2, \ldots, \mathbf{f}_d$ spans a subspace of L^2. A set of d mutually orthogonal basis functions $\psi_1, \psi_2, \ldots, \psi_d$ spanning the same subspace is constructed from the given functions by means of the Gram-Schmidt orthogonalization process [75, 79]. The ν-th basis function ψ_ν is generated in the following way:

$$\psi_\nu(\mathbf{r}) = \mathbf{f}_\nu(\mathbf{r}) - \sum_{\mu=1}^{\nu-1} \frac{\Big\langle \psi_\mu(\mathbf{r}), \mathbf{f}_\nu(\mathbf{r}) \Big\rangle}{\Big\langle \psi_\mu(\mathbf{r}), \psi_\mu(\mathbf{r}) \Big\rangle} \psi_\mu(\mathbf{r}). \tag{B.5}$$

For the first three basis functions, the procedure is conducted as follows:

$$\psi_1(\mathbf{r}) = \mathbf{f}_1(\mathbf{r}), \tag{B.6a}$$

$$\psi_2(\mathbf{r}) = \mathbf{f}_2(\mathbf{r}) - \frac{\Big\langle \psi_1(\mathbf{r}), \mathbf{f}_2(\mathbf{r}) \Big\rangle}{\Big\langle \psi_1(\mathbf{r}), \psi_1(\mathbf{r}) \Big\rangle} \psi_1(\mathbf{r}), \tag{B.6b}$$

$$\psi_3(\mathbf{r}) = \mathbf{f}_3(\mathbf{r}) - \frac{\Big\langle \psi_1(\mathbf{r}), \mathbf{f}_3(\mathbf{r}) \Big\rangle}{\Big\langle \psi_1(\mathbf{r}), \psi_1(\mathbf{r}) \Big\rangle} \psi_1(\mathbf{r}) - \frac{\Big\langle \psi_2(\mathbf{r}), \mathbf{f}_3(\mathbf{r}) \Big\rangle}{\Big\langle \psi_2(\mathbf{r}), \psi_2(\mathbf{r}) \Big\rangle} \psi_2(\mathbf{r}). \tag{B.6c}$$

The generated mutually orthogonal basis functions can be normalized after the orthogonalization process if an orthonormal set of basis functions is desired.

C Generalized Eigenvalue Problem

The beneficial properties of characteristic modes are due to the choice of the operators in the generalized eigenvalue problem (2.14). In this appendix, it is shown how these properties are derived in a general way.

The following generalized eigenvalue problem with the arbitrary linear operators A and B is considered:[112]

$$A\mathbf{J}_n(\mathbf{r}) = \lambda_n B\mathbf{J}_n(\mathbf{r}). \tag{C.1}$$

The n-th eigenfunction $\mathbf{J}_n$ corresponding to the n-th eigenvalue λ_n is in general a complex vector-valued function $\mathbf{J}_n(\mathbf{r}) : \mathbb{R}^3 \to \mathbb{C}^3$.

Now, the operators A and B are given some properties.[113] First of all, the operators are assumed to be real:

$$A\mathbf{f} \in \mathbb{R}^3, \quad B\mathbf{f} \in \mathbb{R}^3, \quad \text{if} \quad \mathbf{f} \in \mathbb{R}^3, \tag{C.2}$$

i.e., the result of the operations $A\mathbf{f}$ or $B\mathbf{f}$ is real if the arbitrary function $\mathbf{f}$ is real [68]. Furthermore, the operators are assumed to be symmetric (self-adjoint). In this case, the following identity holds for the inner product with two arbitrary functions $\mathbf{f}$ and $\mathbf{g}$ [68, 75]:

$$\left\langle \mathbf{f}(\mathbf{r}), A\mathbf{g}(\mathbf{r}) \right\rangle = \left\langle A\mathbf{f}(\mathbf{r}), \mathbf{g}(\mathbf{r}) \right\rangle, \tag{C.3a}$$

$$\left\langle \mathbf{f}(\mathbf{r}), B\mathbf{g}(\mathbf{r}) \right\rangle = \left\langle B\mathbf{f}(\mathbf{r}), \mathbf{g}(\mathbf{r}) \right\rangle. \tag{C.3b}$$

Finally, B is assumed to be positive definite [68]:

$$\left\langle \mathbf{f}(\mathbf{r}), B\mathbf{f}(\mathbf{r}) \right\rangle > 0 \quad \forall\, \mathbf{f} \neq \mathbf{0}. \tag{C.4}$$

i.e., the inner product with some arbitrary function $\mathbf{f}$ is always greater than 0.

---

[112]The simple eigenvalue problem $A\mathbf{J}_n(\mathbf{r}) = \lambda_n \mathbf{J}_n(\mathbf{r})$ arises if B is equal to the identity operator E.

[113]These are the properties of the real part R and the imaginary part X of the impedance operator Z as discussed in section 2.2 so that A may be replaced by X and B by R.

C.1 Real Eigenvalues and Eigenfunctions

An inner product with the eigenfunction $\mathbf{J}_n$ is applied to (C.1) in order to obtain an expression containing the complex conjugate eigenvalue [75]:

$$\Big\langle A\mathbf{J}_n(\mathbf{r}),\mathbf{J}_n(\mathbf{r})\Big\rangle = \Big\langle \lambda_n B\mathbf{J}_n(\mathbf{r}),\mathbf{J}_n(\mathbf{r})\Big\rangle = \lambda_n^*\Big\langle B\mathbf{J}_n(\mathbf{r}),\mathbf{J}_n(\mathbf{r})\Big\rangle$$

$$= \lambda_n^*\Big\langle \mathbf{J}_n(\mathbf{r}),B\mathbf{J}_n(\mathbf{r})\Big\rangle, \qquad \text{(C.5)}$$

where the symmetry of B is exploited. Due to the symmetry of A, this can also be written as

$$\Big\langle A\mathbf{J}_n(\mathbf{r}),\mathbf{J}_n(\mathbf{r})\Big\rangle = \Big\langle \mathbf{J}_n(\mathbf{r}),A\mathbf{J}_n(\mathbf{r})\Big\rangle = \Big\langle \mathbf{J}_n(\mathbf{r}),\lambda_n B\mathbf{J}_n(\mathbf{r})\Big\rangle$$

$$= \lambda_n\Big\langle \mathbf{J}_n(\mathbf{r}),B\mathbf{J}_n(\mathbf{r})\Big\rangle. \qquad \text{(C.6)}$$

Both equations must be equal. As $\mathbf{J}_n \neq \mathbf{0}$ by definition, $\langle \mathbf{J}_n,B\mathbf{J}_n\rangle > 0$ due to the positive definiteness of B. Therefore

$$\lambda_n^* = \lambda_n, \quad \text{i.e.,} \quad \lambda_n \in \mathbb{R}. \qquad \text{(C.7)}$$

As both the eigenvalue and the operators in (C.1) are real, the eigenfunctions, too, can be chosen to be real [25].

C.2 Orthogonality of Eigenfunctions

An inner product with another eigenfunction $\mathbf{J}_m$ corresponding to the eigenvalue $\lambda_m \neq \lambda_n$ if $m \neq n$ is applied to (C.1) [75]:

$$\Big\langle \mathbf{J}_m(\mathbf{r}),A\mathbf{J}_n(\mathbf{r})\Big\rangle = \Big\langle \mathbf{J}_m(\mathbf{r}),\lambda_n B\mathbf{J}_n(\mathbf{r})\Big\rangle = \lambda_n\Big\langle \mathbf{J}_m(\mathbf{r}),B\mathbf{J}_n(\mathbf{r})\Big\rangle. \qquad \text{(C.8)}$$

Due to the symmetry of A and B, this can also be written as

$$\Big\langle \mathbf{J}_m(\mathbf{r}),A\mathbf{J}_n(\mathbf{r})\Big\rangle = \Big\langle A\mathbf{J}_m(\mathbf{r}),\mathbf{J}_n(\mathbf{r})\Big\rangle = \Big\langle \lambda_m B\mathbf{J}_m(\mathbf{r}),\mathbf{J}_n(\mathbf{r})\Big\rangle$$

$$= \lambda_m^*\Big\langle \mathbf{J}_m(\mathbf{r}),B\mathbf{J}_n(\mathbf{r})\Big\rangle. \qquad \text{(C.9)}$$

As both equations must be equal, it follows that

$$\big(\lambda_m - \lambda_n\big)\Big\langle \mathbf{J}_m(\mathbf{r}),B\mathbf{J}_n(\mathbf{r})\Big\rangle = 0. \qquad \text{(C.10)}$$

If $m \neq n$, $\lambda_m \neq \lambda_n$ and it follows immediately that

$$\left\langle \mathbf{J}_m(\mathbf{r}), B\mathbf{J}_n(\mathbf{r}) \right\rangle = 0, \quad \text{for} \quad m \neq n. \tag{C.11}$$

In the case $m = n$, $\langle \mathbf{J}_n, B\mathbf{J}_n \rangle > 0$ due to the positive definiteness of B. Without loss of generality, the eigenfunctions are normalized so that

$$\frac{1}{2}\left\langle \mathbf{J}_n(\mathbf{r}), B\mathbf{J}_n(\mathbf{r}) \right\rangle = 1. \tag{C.12}$$

In the case of a degenerate eigenvalue, $\lambda_m = \lambda_n$ although $m \neq n$ and no direct statement regarding orthogonality can be derived. However, the eigenfunctions belonging to a d-fold degenerate eigenvalue span a closed subspace and linear combinations of eigenfunctions are again eigenfunctions to the same eigenvalue. Therefore, a set of d orthogonal eigenfunctions can always be found [76], e.g., by means of the Gram-Schmidt orthogonalization process (appendix B.1).

The orthogonality of the normalized eigenfunctions with respect to B can be written in a compact form using the Kronecker delta:

$$\frac{1}{2}\left\langle \mathbf{J}_m(\mathbf{r}), B\mathbf{J}_n(\mathbf{r}) \right\rangle = \delta_{mn}. \tag{C.13}$$

The orthogonality with respect to A is now easily derived by applying the inner product to (C.1) and exploiting the orthogonality with respect to B:

$$\frac{1}{2}\left\langle \mathbf{J}_m(\mathbf{r}), A\mathbf{J}_n(\mathbf{r}) \right\rangle = \frac{1}{2}\lambda_n\left\langle \mathbf{J}_m(\mathbf{r}), B\mathbf{J}_n(\mathbf{r}) \right\rangle = \lambda_n\delta_{mn}. \tag{C.14}$$

C.3 Rayleigh Quotient

An eigenvalue λ_n of a generalized eigenvalue problem can also be written as the Rayleigh quotient containing the operators A and B and the corresponding eigenfunction $\mathbf{J}_n$ [102]:

$$\lambda_n = \frac{\left\langle \mathbf{J}_n(\mathbf{r}), A\mathbf{J}_n(\mathbf{r}) \right\rangle}{\left\langle \mathbf{J}_n(\mathbf{r}), B\mathbf{J}_n(\mathbf{r}) \right\rangle}. \tag{C.15}$$

This notation is especially suitable for the physical interpretation of the eigenvalue. The eigenvalue of a characteristic mode, for example, denotes the ratio of reactive power to radiated power.

C.4 Modal Decomposition

An arbitrary function $\mathbf{J}$ is now written as a linear combination of eigenfunctions [24]:

$$\mathbf{J}(\mathbf{r}) = \sum_{n=1}^{\infty} a_n \mathbf{J}_n(\mathbf{r}). \tag{C.16}$$

In order to determine the weighting coefficients a_n, first, the operators of the generalized eigenvalue problem are applied to the function:

$$A\mathbf{J}(\mathbf{r}) = \sum_{n=1}^{\infty} a_n A\mathbf{J}_n(\mathbf{r}), \tag{C.17a}$$

$$B\mathbf{J}(\mathbf{r}) = \sum_{n=1}^{\infty} a_n B\mathbf{J}_n(\mathbf{r}). \tag{C.17b}$$

Next, the inner product is formed with an arbitrary eigenfunction:

$$\Big\langle \mathbf{J}_m(\mathbf{r}), A\mathbf{J}(\mathbf{r}) \Big\rangle = \sum_{n=1}^{\infty} a_n \Big\langle \mathbf{J}_m(\mathbf{r}), A\mathbf{J}_n(\mathbf{r}) \Big\rangle, \tag{C.18a}$$

$$\Big\langle \mathbf{J}_m(\mathbf{r}), B\mathbf{J}(\mathbf{r}) \Big\rangle = \sum_{n=1}^{\infty} a_n \Big\langle \mathbf{J}_m(\mathbf{r}), B\mathbf{J}_n(\mathbf{r}) \Big\rangle. \tag{C.18b}$$

Exploiting the orthogonality of the eigenfunctions with respect to the operators yields

$$\Big\langle \mathbf{J}_m(\mathbf{r}), A\mathbf{J}(\mathbf{r}) \Big\rangle = 2\lambda_m a_m, \tag{C.19a}$$

$$\Big\langle \mathbf{J}_m(\mathbf{r}), B\mathbf{J}(\mathbf{r}) \Big\rangle = 2a_m. \tag{C.19b}$$

Therefore, the weighting coefficients can in general be written as

$$a_n = \frac{1}{2} \Big\langle \mathbf{J}_n(\mathbf{r}), B\mathbf{J}(\mathbf{r}) \Big\rangle = \frac{\Big\langle \mathbf{J}_n(\mathbf{r}), A\mathbf{J}(\mathbf{r}) \Big\rangle}{2\lambda_n}. \tag{C.20}$$

In the special case of characteristic modes, the weighting coefficients can also be expressed in terms of the impedance operator Z and thus directly related to

the impressed electric field strength $\mathbf{E}_i$:

$$
\begin{aligned}
a_n &= \frac{1}{2}\Big\langle \mathbf{J}_n(\mathbf{r}), R\mathbf{J}(\mathbf{r}) \Big\rangle = \frac{1}{2}\Big\langle \mathbf{J}_n(\mathbf{r}), (Z - jX)\mathbf{J}(\mathbf{r}) \Big\rangle \\
&= \frac{1}{2}\Big\langle \mathbf{J}_n(\mathbf{r}), Z\mathbf{J}(\mathbf{r}) \Big\rangle - j\frac{1}{2}\Big\langle \mathbf{J}_n(\mathbf{r}), X\mathbf{J}(\mathbf{r}) \Big\rangle \\
&= \frac{1}{2}\Big\langle \mathbf{J}_n(\mathbf{r}), Z\mathbf{J}(\mathbf{r}) \Big\rangle - j\lambda_n a_n.
\end{aligned}
\tag{C.21}
$$

Therefore:

$$
a_n = \frac{\frac{1}{2}\Big\langle \mathbf{J}_n(\mathbf{r}), Z\mathbf{J}(\mathbf{r}) \Big\rangle}{1 + j\lambda_n} = \frac{\frac{1}{2}\Big\langle \mathbf{J}_n(\mathbf{r}), \mathbf{E}_i(\mathbf{r}) \Big\rangle}{1 + j\lambda_n}.
\tag{C.22}
$$

C.5 Consequences of Operator Invariance

It is now assumed that the operators A and B are invariant under the symmetry operations T of a given symmetry group. In this case, the operators commute with the corresponding transformation operators $P(T)$ [66, 77]:

$$
P(T)\big(A\mathbf{J}_n(\mathbf{r})\big) = A\big(P(T)\mathbf{J}_n(\mathbf{r})\big), \quad P(T)\big(B\mathbf{J}_n(\mathbf{r})\big) = B\big(P(T)\mathbf{J}_n(\mathbf{r})\big). \tag{C.23}
$$

Applying a transformation operator to both sides of the eigenvalue problem (C.1) thus yields

$$
A\big(P(T)\mathbf{J}_n(\mathbf{r})\big) = \lambda_n B\big(P(T)\mathbf{J}_n(\mathbf{r})\big). \tag{C.24}
$$

As explained in section 3.4.2, $P(T)\mathbf{J}_n$ is an eigenfunction belonging to the in general d-fold degenerate eigenvalue λ_n for any T of the symmetry group. It can thus be expressed as a linear combination of d eigenfunctions $\mathbf{J}_{n,1}, \mathbf{J}_{n,2}, \ldots, \mathbf{J}_{n,d}$ belonging to the same eigenvalue:

$$
P(T)\mathbf{J}_{n,\nu}(\mathbf{r}) = \sum_{\mu=1}^{d} \Gamma_{\mu\nu}(T)\mathbf{J}_{n,\mu}(\mathbf{r}), \qquad \nu = 1, 2, \ldots, d, \tag{C.25}
$$

i.e., the eigenfunctions transform under symmetry operations in the same way as basis functions of the irreducible representations according to (3.22). The weighting coefficients $\Gamma_{\mu\nu}$ can be collected into $d \times d$ representation matrices $\boldsymbol{\Gamma}(T)$ which must form a homomorphic mapping according to (3.18). In order to prove this, the action of two transformation operators in succession (3.15)

is examined [77]. On the one hand, this can be written as follows with (C.25) and using (3.15) and (3.14) [75, 77]:

$$
\begin{aligned}
P(T_1 T_2)\mathbf{J}_{n,\nu}(\mathbf{r}) &= P(T_1)\big(P(T_2)\mathbf{J}_{n,\nu}(\mathbf{r})\big) \\
&= P(T_1)\Big(\sum_{\mu=1}^{d} \Gamma_{\mu\nu}(T_2)\mathbf{J}_{n,\mu}(\mathbf{r})\Big) \\
&= \sum_{\mu=1}^{d} \Gamma_{\mu\nu}(T_2) P(T_1)\mathbf{J}_{n,\mu}(\mathbf{r}) \\
&= \sum_{\mu=1}^{d}\sum_{\kappa=1}^{d} \Gamma_{\mu\nu}(T_2)\Gamma_{\kappa\mu}(T_1)\mathbf{J}_{n,\kappa}(\mathbf{r}) \\
&= \sum_{\kappa=1}^{d} [\mathbf{\Gamma}(T_1)\mathbf{\Gamma}(T_2)]_{\kappa\nu}\,\mathbf{J}_{n,\kappa}(\mathbf{r}), \qquad (\text{C.26})
\end{aligned}
$$

where $[\cdot]_{\kappa\nu}$ denotes the element of the κ-th row and the ν-th column of the matrix product. On the other hand, this can also be written as [77]

$$
P(T_1 T_2)\mathbf{J}_{n,\nu}(\mathbf{r}) = \sum_{\kappa=1}^{d} \Gamma_{\kappa\nu}(T_1 T_2)\mathbf{J}_{n,\kappa}(\mathbf{r}). \qquad (\text{C.27})
$$

Comparing the weighting coefficients in both equations finally yields

$$
\mathbf{\Gamma}(T_1 T_2) = \mathbf{\Gamma}(T_1)\mathbf{\Gamma}(T_2), \qquad (\text{C.28})
$$

i.e., a homomorphic mapping, proving that (C.25) indeed describes the transformation of eigenfunctions according to a representation. The representation is irreducible since the dimension of the representation is dictated by the degeneracy of the respective eigenvalue and thus minimal.

The derivation conducted in section 3.4.2 in the context of characteristic modes is applicable to arbitrary eigenvalue problems. If the operators of the eigenvalue problem are invariant under symmetry operations, the eigenfunctions are basis functions of the irreducible representations of the symmetry group.

D Computation of Representation Matrices

In this appendix, the computation of representation matrices is carried out explicitly for the sake of illustration by means of two examples. For this purpose, the symmetry group D_3 (equilateral triangular plate) and the symmetry group D_4 (square plate) are chosen as they are most extensively discussed in this thesis.

D.1 Representation Matrices of Triangular Plate

The representation matrices of the two-dimensional third irreducible representation $\Gamma^{(3)}$ of the symmetry group D_3 presented in Table 4.5 are computed. The computation is based on the two scalar basis functions

$$\psi_1^{(3)}(x',y') = x', \qquad \psi_2^{(3)}(x',y') = y', \tag{D.1}$$

defined on an equilateral triangular domain with $y' \in \left[\frac{1}{\sqrt{3}}x' - \frac{a}{3}, -\frac{1}{\sqrt{3}}x' + \frac{a}{3} \right]$[114] and $x' \in \left[-R_i, R_u \right]$[115], as shown in Fig. 4.6.

First, it is checked that the two basis functions are indeed orthogonal:

$$\left\langle \psi_1^{(3)}(x',y'), \psi_2^{(3)}(x',y') \right\rangle = \int\limits_{-a/(2\sqrt{3})}^{a/\sqrt{3}} \int\limits_{x'/\sqrt{3}-a/3}^{-x'/\sqrt{3}+a/3} x'y' \mathrm{d}y' \mathrm{d}x' = 0. \tag{D.2}$$

Additionally, the basis functions need to be normalized:[116]

$$K = \left\langle \psi_1^{(3)}(x',y'), \psi_1^{(3)}(x',y') \right\rangle = \left\langle \psi_2^{(3)}(x',y'), \psi_2^{(3)}(x',y') \right\rangle$$

$$= \int\limits_{-a/(2\sqrt{3})}^{a/\sqrt{3}} \int\limits_{x'/\sqrt{3}-a/3}^{-x'/\sqrt{3}+a/3} x'^2 \mathrm{d}y' \mathrm{d}x' = \int\limits_{-a/(2\sqrt{3})}^{a/\sqrt{3}} \int\limits_{x'/\sqrt{3}-a/3}^{-x'/\sqrt{3}+a/3} y'^2 \mathrm{d}y' \mathrm{d}x' = \frac{a^4}{32\sqrt{3}}. \tag{D.3}$$

---

[114] $-\frac{1}{\sqrt{3}}x' + \frac{a}{3}$ and $\frac{1}{\sqrt{3}}x' - \frac{a}{3}$ describe the upper and the lower edge, respectively, of the equilateral triangular plate as linear functions of x', see Fig. 4.1(a).

[115] $R_i = \frac{a}{2\sqrt{3}}$, $R_u = \frac{a}{\sqrt{3}}$.

[116] In this case, both functions yield the same normalization constant.

T	$\mathbf{R}(T)$	$P(T)f(\mathbf{r}')$
E	$\begin{pmatrix} 1 & 0 & 0 \\ 0 & 1 & 0 \\ 0 & 0 & 1 \end{pmatrix}$	$f(x',y',z')$
C_{3z}	$\begin{pmatrix} -\frac{1}{2} & \frac{\sqrt{3}}{2} & 0 \\ -\frac{\sqrt{3}}{2} & -\frac{1}{2} & 0 \\ 0 & 0 & 1 \end{pmatrix}$	$f\left(-\frac{1}{2}x' - \frac{\sqrt{3}}{2}y', \frac{\sqrt{3}}{2}x' - \frac{1}{2}y', z'\right)$
C_{3z}^2	$\begin{pmatrix} -\frac{1}{2} & -\frac{\sqrt{3}}{2} & 0 \\ \frac{\sqrt{3}}{2} & -\frac{1}{2} & 0 \\ 0 & 0 & 1 \end{pmatrix}$	$f\left(-\frac{1}{2}x' + \frac{\sqrt{3}}{2}y', -\frac{\sqrt{3}}{2}x' - \frac{1}{2}y', z'\right)$
C_{2x}	$\begin{pmatrix} 1 & 0 & 0 \\ 0 & -1 & 0 \\ 0 & 0 & -1 \end{pmatrix}$	$f(x',-y',-z')$
C_{2A}	$\begin{pmatrix} -\frac{1}{2} & \frac{\sqrt{3}}{2} & 0 \\ \frac{\sqrt{3}}{2} & \frac{1}{2} & 0 \\ 0 & 0 & -1 \end{pmatrix}$	$f\left(-\frac{1}{2}x' + \frac{\sqrt{3}}{2}y', \frac{\sqrt{3}}{2}x' + \frac{1}{2}y', -z'\right)$
C_{2B}	$\begin{pmatrix} -\frac{1}{2} & -\frac{\sqrt{3}}{2} & 0 \\ -\frac{\sqrt{3}}{2} & \frac{1}{2} & 0 \\ 0 & 0 & -1 \end{pmatrix}$	$f\left(-\frac{1}{2}x' - \frac{\sqrt{3}}{2}y', -\frac{\sqrt{3}}{2}x' + \frac{1}{2}y', -z'\right)$

Table D.1   Rotation matrices and scalar transformation operators of symmetry group D_3.

The elements of the representation matrices are now computed systematically using (3.60). The required scalar transformation operators computed according to (3.12) are provided in Table D.1. In order to obtain unitary representation matrices, the results are divided by the normalization constant K:

$$\Gamma_{11}^{(3)}(E) = \frac{1}{K}\left\langle \psi_1^{(3)}(x',y'), P(E)\psi_1^{(3)}(x',y') \right\rangle$$

$$= \frac{1}{K} \int_{-a/(2\sqrt{3})}^{a/\sqrt{3}} \int_{x'/\sqrt{3}-a/3}^{-x'/\sqrt{3}+a/3} x'x'\,\mathrm{d}y'\,\mathrm{d}x' = 1, \qquad \text{(D.4a)}$$

$$\Gamma_{12}^{(3)}(E) = \frac{1}{K}\left\langle \psi_1^{(3)}(x',y'), P(E)\psi_2^{(3)}(x',y') \right\rangle$$

$$= \frac{1}{K} \int_{-a/(2\sqrt{3})}^{a/\sqrt{3}} \int_{x'/\sqrt{3}-a/3}^{-x'/\sqrt{3}+a/3} x'y'\,\mathrm{d}y'\,\mathrm{d}x' = 0, \qquad \text{(D.4b)}$$

$$\Gamma_{21}^{(3)}(E) = \frac{1}{K}\left\langle \psi_2^{(3)}(x',y'), P(E)\psi_1^{(3)}(x',y')\right\rangle$$

$$= \frac{1}{K}\int\limits_{-a/(2\sqrt{3})}^{a/\sqrt{3}}\int\limits_{x'/\sqrt{3}-a/3}^{-x'/\sqrt{3}+a/3} y'x'\mathrm{d}y'\mathrm{d}x' = 0, \qquad (D.4c)$$

$$\Gamma_{22}^{(3)}(E) = \frac{1}{K}\left\langle \psi_2^{(3)}(x',y'), P(E)\psi_2^{(3)}(x',y')\right\rangle$$

$$= \frac{1}{K}\int\limits_{-a/(2\sqrt{3})}^{a/\sqrt{3}}\int\limits_{x'/\sqrt{3}-a/3}^{-x'/\sqrt{3}+a/3} y'y'\mathrm{d}y'\mathrm{d}x' = 1. \qquad (D.4d)$$

$$\Gamma_{11}^{(3)}(C_{2x}) = \frac{1}{K}\left\langle \psi_1^{(3)}(x',y'), P(C_{2x})\psi_1^{(3)}(x',y')\right\rangle$$

$$= \frac{1}{K}\int\limits_{-a/(2\sqrt{3})}^{a/\sqrt{3}}\int\limits_{x'/\sqrt{3}-a/3}^{-x'/\sqrt{3}+a/3} x'x'\mathrm{d}y'\mathrm{d}x' = 1, \qquad (D.5a)$$

$$\Gamma_{12}^{(3)}(C_{2x}) = \frac{1}{K}\left\langle \psi_1^{(3)}(x',y'), P(C_{2x})\psi_2^{(3)}(x',y')\right\rangle$$

$$= \frac{1}{K}\int\limits_{-a/(2\sqrt{3})}^{a/\sqrt{3}}\int\limits_{x'/\sqrt{3}-a/3}^{-x'/\sqrt{3}+a/3} x'(-y')\mathrm{d}y'\mathrm{d}x' = 0, \qquad (D.5b)$$

$$\Gamma_{21}^{(3)}(C_{2x}) = \frac{1}{K}\left\langle \psi_2^{(3)}(x',y'), P(C_{2x})\psi_1^{(3)}(x',y')\right\rangle$$

$$= \frac{1}{K}\int\limits_{-a/(2\sqrt{3})}^{a/\sqrt{3}}\int\limits_{x'/\sqrt{3}-a/3}^{-x'/\sqrt{3}+a/3} y'x'\mathrm{d}y'\mathrm{d}x' = 0, \qquad (D.5c)$$

$$\Gamma_{22}^{(3)}(C_{2x}) = \frac{1}{K}\left\langle \psi_2^{(3)}(x',y'), P(C_{2x})\psi_2^{(3)}(x',y')\right\rangle$$

$$= \frac{1}{K}\int\limits_{-a/(2\sqrt{3})}^{a/\sqrt{3}}\int\limits_{x'/\sqrt{3}-a/3}^{-x'/\sqrt{3}+a/3} y'(-y')\mathrm{d}y'\mathrm{d}x' = -1. \qquad (D.5d)$$

$$\Gamma_{11}^{(3)}(C_{3z}) = \frac{1}{K}\left\langle \psi_1^{(3)}(x',y'), P(C_{3z})\psi_1^{(3)}(x',y')\right\rangle$$

$$= \frac{1}{K}\int\limits_{-a/(2\sqrt{3})}^{a/\sqrt{3}}\int\limits_{x'/\sqrt{3}-a/3}^{-x'/\sqrt{3}+a/3} x'\left(-\frac{1}{2}x' - \frac{\sqrt{3}}{2}y'\right)\mathrm{d}y'\mathrm{d}x' = -\frac{1}{2}, \quad \text{(D.6a)}$$

$$\Gamma_{12}^{(3)}(C_{3z}) = \frac{1}{K}\left\langle \psi_1^{(3)}(x',y'), P(C_{3z})\psi_2^{(3)}(x',y')\right\rangle$$

$$= \frac{1}{K}\int\limits_{-a/(2\sqrt{3})}^{a/\sqrt{3}}\int\limits_{x'/\sqrt{3}-a/3}^{-x'/\sqrt{3}+a/3} x'\left(\frac{\sqrt{3}}{2}x' - \frac{1}{2}y'\right)\mathrm{d}y'\mathrm{d}x' = \frac{\sqrt{3}}{2}, \quad \text{(D.6b)}$$

$$\Gamma_{21}^{(3)}(C_{3z}) = \frac{1}{K}\left\langle \psi_2^{(3)}(x',y'), P(C_{3z})\psi_1^{(3)}(x',y')\right\rangle$$

$$= \frac{1}{K}\int\limits_{-a/(2\sqrt{3})}^{a/\sqrt{3}}\int\limits_{x'/\sqrt{3}-a/3}^{-x'/\sqrt{3}+a/3} y'\left(-\frac{1}{2}x' - \frac{\sqrt{3}}{2}y'\right)\mathrm{d}y'\mathrm{d}x' = -\frac{\sqrt{3}}{2}, \quad \text{(D.6c)}$$

$$\Gamma_{22}^{(3)}(C_{3z}) = \frac{1}{K}\left\langle \psi_2^{(3)}(x',y'), P(C_{3z})\psi_2^{(3)}(x',y')\right\rangle$$

$$= \frac{1}{K}\int\limits_{-a/(2\sqrt{3})}^{a/\sqrt{3}}\int\limits_{x'/\sqrt{3}-a/3}^{-x'/\sqrt{3}+a/3} y'\left(\frac{\sqrt{3}}{2}x' - \frac{1}{2}y'\right)\mathrm{d}y'\mathrm{d}x' = -\frac{1}{2}. \quad \text{(D.6d)}$$

$$\Gamma_{11}^{(3)}(C_{3z}^2) = \frac{1}{K}\left\langle \psi_1^{(3)}(x',y'), P(C_{3z}^2)\psi_1^{(3)}(x',y')\right\rangle$$

$$= \frac{1}{K}\int\limits_{-a/(2\sqrt{3})}^{a/\sqrt{3}}\int\limits_{x'/\sqrt{3}-a/3}^{-x'/\sqrt{3}+a/3} x'\left(-\frac{1}{2}x' + \frac{\sqrt{3}}{2}y'\right)\mathrm{d}y'\mathrm{d}x' = -\frac{1}{2}, \quad \text{(D.7a)}$$

$$\Gamma_{12}^{(3)}(C_{3z}^2) = \frac{1}{K}\left\langle \psi_1^{(3)}(x',y'), P(C_{3z}^2)\psi_2^{(3)}(x',y')\right\rangle$$

$$= \frac{1}{K}\int\limits_{-a/(2\sqrt{3})}^{a/\sqrt{3}}\int\limits_{x'/\sqrt{3}-a/3}^{-x'/\sqrt{3}+a/3} x'\left(-\frac{\sqrt{3}}{2}x' - \frac{1}{2}y'\right)\mathrm{d}y'\mathrm{d}x' = -\frac{\sqrt{3}}{2}, \quad \text{(D.7b)}$$

$$\Gamma_{21}^{(3)}(C_{3z}^2) = \frac{1}{K}\left\langle \psi_2^{(3)}(x',y'), P(C_{3z}^2)\psi_1^{(3)}(x',y')\right\rangle$$

$$= \frac{1}{K}\int\limits_{-a/(2\sqrt{3})}^{a/\sqrt{3}}\int\limits_{x'/\sqrt{3}-a/3}^{-x'/\sqrt{3}+a/3} y'\left(-\frac{1}{2}x' + \frac{\sqrt{3}}{2}y'\right)dy'dx' = \frac{\sqrt{3}}{2}, \quad \text{(D.7c)}$$

$$\Gamma_{22}^{(3)}(C_{3z}^2) = \frac{1}{K}\left\langle \psi_2^{(3)}(x',y'), P(C_{3z}^2)\psi_2^{(3)}(x',y')\right\rangle$$

$$= \frac{1}{K}\int\limits_{-a/(2\sqrt{3})}^{a/\sqrt{3}}\int\limits_{x'/\sqrt{3}-a/3}^{-x'/\sqrt{3}+a/3} y'\left(-\frac{\sqrt{3}}{2}x' - \frac{1}{2}y'\right)dy'dx' = -\frac{1}{2}. \quad \text{(D.7d)}$$

$$\Gamma_{11}^{(3)}(C_{2A}) = \frac{1}{K}\left\langle \psi_1^{(3)}(x',y'), P(C_{2A})\psi_1^{(3)}(x',y')\right\rangle$$

$$= \frac{1}{K}\int\limits_{-a/(2\sqrt{3})}^{a/\sqrt{3}}\int\limits_{x'/\sqrt{3}-a/3}^{-x'/\sqrt{3}+a/3} x'\left(-\frac{1}{2}x' + \frac{\sqrt{3}}{2}y'\right)dy'dx' = -\frac{1}{2}, \quad \text{(D.8a)}$$

$$\Gamma_{12}^{(3)}(C_{2A}) = \frac{1}{K}\left\langle \psi_1^{(3)}(x',y'), P(C_{2A})\psi_2^{(3)}(x',y')\right\rangle$$

$$= \frac{1}{K}\int\limits_{-a/(2\sqrt{3})}^{a/\sqrt{3}}\int\limits_{x'/\sqrt{3}-a/3}^{-x'/\sqrt{3}+a/3} x'\left(\frac{\sqrt{3}}{2}x' + \frac{1}{2}y'\right)dy'dx' = \frac{\sqrt{3}}{2}, \quad \text{(D.8b)}$$

$$\Gamma_{21}^{(3)}(C_{2A}) = \frac{1}{K}\left\langle \psi_2^{(3)}(x',y'), P(C_{2A})\psi_1^{(3)}(x',y')\right\rangle$$

$$= \frac{1}{K}\int\limits_{-a/(2\sqrt{3})}^{a/\sqrt{3}}\int\limits_{x'/\sqrt{3}-a/3}^{-x'/\sqrt{3}+a/3} y'\left(-\frac{1}{2}x' + \frac{\sqrt{3}}{2}y'\right)dy'dx' = \frac{\sqrt{3}}{2}, \quad \text{(D.8c)}$$

$$\Gamma_{22}^{(3)}(C_{2A}) = \frac{1}{K}\left\langle \psi_2^{(3)}(x',y'), P(C_{2A})\psi_2^{(3)}(x',y')\right\rangle$$

$$= \frac{1}{K}\int\limits_{-a/(2\sqrt{3})}^{a/\sqrt{3}}\int\limits_{x'/\sqrt{3}-a/3}^{-x'/\sqrt{3}+a/3} y'\left(\frac{\sqrt{3}}{2}x' + \frac{1}{2}y'\right)dy'dx' = \frac{1}{2}. \quad \text{(D.8d)}$$

$$\Gamma_{11}^{(3)}(C_{2B}) = \frac{1}{K}\left\langle \psi_1^{(3)}(x',y'), P(C_{2B})\psi_1^{(3)}(x',y') \right\rangle$$

$$= \frac{1}{K} \int\limits_{-a/(2\sqrt{3})}^{a/\sqrt{3}} \int\limits_{x'/\sqrt{3}-a/3}^{-x'/\sqrt{3}+a/3} x'\left(-\frac{1}{2}x' - \frac{\sqrt{3}}{2}y'\right)\mathrm{d}y'\mathrm{d}x' = -\frac{1}{2}, \quad \text{(D.9a)}$$

$$\Gamma_{12}^{(3)}(C_{2B}) = \frac{1}{K}\left\langle \psi_1^{(3)}(x',y'), P(C_{2B})\psi_2^{(3)}(x',y') \right\rangle$$

$$= \frac{1}{K} \int\limits_{-a/(2\sqrt{3})}^{a/\sqrt{3}} \int\limits_{x'/\sqrt{3}-a/3}^{-x'/\sqrt{3}+a/3} x'\left(-\frac{\sqrt{3}}{2}x' + \frac{1}{2}y'\right)\mathrm{d}y'\mathrm{d}x' = -\frac{\sqrt{3}}{2}, \quad \text{(D.9b)}$$

$$\Gamma_{21}^{(3)}(C_{2B}) = \frac{1}{K}\left\langle \psi_2^{(3)}(x',y'), P(C_{2B})\psi_1^{(3)}(x',y') \right\rangle$$

$$= \frac{1}{K} \int\limits_{-a/(2\sqrt{3})}^{a/\sqrt{3}} \int\limits_{x'/\sqrt{3}-a/3}^{-x'/\sqrt{3}+a/3} y'\left(-\frac{1}{2}x' - \frac{\sqrt{3}}{2}y'\right)\mathrm{d}y'\mathrm{d}x' = -\frac{\sqrt{3}}{2}, \quad \text{(D.9c)}$$

$$\Gamma_{22}^{(3)}(C_{2B}) = \frac{1}{K}\left\langle \psi_2^{(3)}(x',y'), P(C_{2B})\psi_2^{(3)}(x',y') \right\rangle$$

$$= \frac{1}{K} \int\limits_{-a/(2\sqrt{3})}^{a/\sqrt{3}} \int\limits_{x'/\sqrt{3}-a/3}^{-x'/\sqrt{3}+a/3} y'\left(-\frac{\sqrt{3}}{2}x' + \frac{1}{2}y'\right)\mathrm{d}y'\mathrm{d}x' = \frac{1}{2}. \quad \text{(D.9d)}$$

D.2 Representation Matrices of Square Plate

The representation matrices of the two-dimensional fifth irreducible representation $\Gamma^{(5)}$ of the symmetry group D_4 presented in Table 3.15 are computed. The computation is based on the two vector-valued basis functions

$$\psi_1^{(5)}(x',y') = \begin{pmatrix} |x'| \\ |y'| \end{pmatrix}, \qquad \psi_2^{(5)}(x',y') = \begin{pmatrix} |x'| \\ -|y'| \end{pmatrix}, \qquad \text{(D.10)}$$

defined on a square domain with $x',y' \in \left[-\frac{a}{2}, \frac{a}{2}\right]$, as shown in Fig. 3.9.

First, it is checked that the two basis functions are indeed orthogonal:

$$\left\langle \psi_1^{(5)}(x',y'), \psi_2^{(5)}(x',y') \right\rangle = \int\limits_{-a/2}^{a/2} \int\limits_{-a/2}^{a/2} \begin{pmatrix} |x'| \\ |y'| \end{pmatrix} \cdot \begin{pmatrix} |x'| \\ -|y'| \end{pmatrix} dx'dy'$$

$$= \int\limits_{-a/2}^{a/2} \int\limits_{-a/2}^{a/2} (x'^2 - y'^2) dx'dy' = 0. \qquad \text{(D.11)}$$

Additionally, the basis functions need to be normalized:[117]

$$K = \left\langle \psi_1^{(5)}(x',y'), \psi_1^{(5)}(x',y') \right\rangle = \left\langle \psi_2^{(5)}(x',y'), \psi_2^{(5)}(x',y') \right\rangle$$

$$= \int\limits_{-a/2}^{a/2} \int\limits_{-a/2}^{a/2} \begin{pmatrix} |x'| \\ |y'| \end{pmatrix} \cdot \begin{pmatrix} |x'| \\ |y'| \end{pmatrix} dx'dy' = \int\limits_{-a/2}^{a/2} \int\limits_{-a/2}^{a/2} \begin{pmatrix} |x'| \\ -|y'| \end{pmatrix} \cdot \begin{pmatrix} |x'| \\ -|y'| \end{pmatrix} dx'dy'$$

$$= \int\limits_{-a/2}^{a/2} \int\limits_{-a/2}^{a/2} (x'^2 + y'^2) dx'dy' = \frac{a^4}{6}. \qquad \text{(D.12)}$$

The results below are divided by the normalization constant K in order to obtain unitary representation matrices.

The elements of the representation matrices are now computed systematically using (3.60) and the transformation operators in Table 3.7:

$$\Gamma_{11}^{(5)}(E) = \frac{1}{K} \left\langle \psi_1^{(5)}(x',y'), P(E)\psi_1^{(5)}(x',y') \right\rangle$$

$$= \frac{1}{K} \int\limits_{-a/2}^{a/2} \int\limits_{-a/2}^{a/2} \begin{pmatrix} |x'| \\ |y'| \end{pmatrix} \cdot \begin{pmatrix} |x'| \\ |y'| \end{pmatrix} dx'dy' = 1, \qquad \text{(D.13a)}$$

$$\Gamma_{12}^{(5)}(E) = \frac{1}{K} \left\langle \psi_1^{(5)}(x',y'), P(E)\psi_2^{(5)}(x',y') \right\rangle$$

$$= \frac{1}{K} \int\limits_{-a/2}^{a/2} \int\limits_{-a/2}^{a/2} \begin{pmatrix} |x'| \\ |y'| \end{pmatrix} \cdot \begin{pmatrix} |x'| \\ -|y'| \end{pmatrix} dx'dy' = 0, \qquad \text{(D.13b)}$$

---

[117]In this case, both functions yield the same normalization constant.

$$\Gamma_{21}^{(5)}(E) = \frac{1}{K}\left\langle \psi_2^{(5)}(x',y'), P(E)\psi_1^{(5)}(x',y')\right\rangle$$

$$= \frac{1}{K}\int\limits_{-a/2}^{a/2}\int\limits_{-a/2}^{a/2}\begin{pmatrix}|x'|\\-|y'|\end{pmatrix}\cdot\begin{pmatrix}|x'|\\|y'|\end{pmatrix}\mathrm{d}x'\mathrm{d}y' = 0, \qquad\text{(D.13c)}$$

$$\Gamma_{22}^{(5)}(E) = \frac{1}{K}\left\langle \psi_2^{(5)}(x',y'), P(E)\psi_2^{(5)}(x',y')\right\rangle$$

$$= \frac{1}{K}\int\limits_{-a/2}^{a/2}\int\limits_{-a/2}^{a/2}\begin{pmatrix}|x'|\\-|y'|\end{pmatrix}\cdot\begin{pmatrix}|x'|\\-|y'|\end{pmatrix}\mathrm{d}x'\mathrm{d}y' = 1. \qquad\text{(D.13d)}$$

$$\Gamma_{11}^{(5)}(C_{4z}) = \frac{1}{K}\left\langle \psi_1^{(5)}(x',y'), P(C_{4z})\psi_1^{(5)}(x',y')\right\rangle$$

$$= \frac{1}{K}\int\limits_{-a/2}^{a/2}\int\limits_{-a/2}^{a/2}\begin{pmatrix}|x'|\\|y'|\end{pmatrix}\cdot\begin{pmatrix}|x'|\\-|y'|\end{pmatrix}\mathrm{d}x'\mathrm{d}y' = 0, \qquad\text{(D.14a)}$$

$$\Gamma_{12}^{(5)}(C_{4z}) = \frac{1}{K}\left\langle \psi_1^{(5)}(x',y'), P(C_{4z})\psi_2^{(5)}(x',y')\right\rangle$$

$$= \frac{1}{K}\int\limits_{-a/2}^{a/2}\int\limits_{-a/2}^{a/2}\begin{pmatrix}|x'|\\|y'|\end{pmatrix}\cdot\begin{pmatrix}-|x'|\\-|y'|\end{pmatrix}\mathrm{d}x'\mathrm{d}y' = -1, \qquad\text{(D.14b)}$$

$$\Gamma_{21}^{(5)}(C_{4z}) = \frac{1}{K}\left\langle \psi_2^{(5)}(x',y'), P(C_{4z})\psi_1^{(5)}(x',y')\right\rangle$$

$$= \frac{1}{K}\int\limits_{-a/2}^{a/2}\int\limits_{-a/2}^{a/2}\begin{pmatrix}|x'|\\-|y'|\end{pmatrix}\cdot\begin{pmatrix}|x'|\\-|y'|\end{pmatrix}\mathrm{d}x'\mathrm{d}y' = 1, \qquad\text{(D.14c)}$$

$$\Gamma_{22}^{(5)}(C_{4z}) = \frac{1}{K}\left\langle \psi_2^{(5)}(x',y'), P(C_{4z})\psi_2^{(5)}(x',y')\right\rangle$$

$$= \frac{1}{K}\int\limits_{-a/2}^{a/2}\int\limits_{-a/2}^{a/2}\begin{pmatrix}|x'|\\-|y'|\end{pmatrix}\cdot\begin{pmatrix}-|x'|\\-|y'|\end{pmatrix}\mathrm{d}x'\mathrm{d}y' = 0. \qquad\text{(D.14d)}$$

$$\Gamma_{11}^{(5)}(C_{2z}) = \frac{1}{K}\left\langle \psi_1^{(5)}(x',y'), P(C_{2z})\psi_1^{(5)}(x',y')\right\rangle$$

$$= \frac{1}{K} \int\limits_{-a/2}^{a/2} \int\limits_{-a/2}^{a/2} \begin{pmatrix} |x'| \\ |y'| \end{pmatrix} \cdot \begin{pmatrix} -|x'| \\ -|y'| \end{pmatrix} \mathrm{d}x' \mathrm{d}y' = -1, \qquad \text{(D.15a)}$$

$$\Gamma_{12}^{(5)}(C_{2z}) = \frac{1}{K} \left\langle \psi_1^{(5)}(x',y'), P(C_{2z})\psi_2^{(5)}(x',y') \right\rangle$$

$$= \frac{1}{K} \int\limits_{-a/2}^{a/2} \int\limits_{-a/2}^{a/2} \begin{pmatrix} |x'| \\ |y'| \end{pmatrix} \cdot \begin{pmatrix} -|x'| \\ |y'| \end{pmatrix} \mathrm{d}x' \mathrm{d}y' = 0, \qquad \text{(D.15b)}$$

$$\Gamma_{21}^{(5)}(C_{2z}) = \frac{1}{K} \left\langle \psi_2^{(5)}(x',y'), P(C_{2z})\psi_1^{(5)}(x',y') \right\rangle$$

$$= \frac{1}{K} \int\limits_{-a/2}^{a/2} \int\limits_{-a/2}^{a/2} \begin{pmatrix} |x'| \\ -|y'| \end{pmatrix} \cdot \begin{pmatrix} -|x'| \\ -|y'| \end{pmatrix} \mathrm{d}x' \mathrm{d}y' = 0, \qquad \text{(D.15c)}$$

$$\Gamma_{22}^{(5)}(C_{2z}) = \frac{1}{K} \left\langle \psi_2^{(5)}(x',y'), P(C_{2z})\psi_2^{(5)}(x',y') \right\rangle$$

$$= \frac{1}{K} \int\limits_{-a/2}^{a/2} \int\limits_{-a/2}^{a/2} \begin{pmatrix} |x'| \\ -|y'| \end{pmatrix} \cdot \begin{pmatrix} -|x'| \\ |y'| \end{pmatrix} \mathrm{d}x' \mathrm{d}y' = -1. \qquad \text{(D.15d)}$$

$$\Gamma_{11}^{(5)}(C_{4z}^{-1}) = \frac{1}{K} \left\langle \psi_1^{(5)}(x',y'), P(C_{4z}^{-1})\psi_1^{(5)}(x',y') \right\rangle$$

$$= \frac{1}{K} \int\limits_{-a/2}^{a/2} \int\limits_{-a/2}^{a/2} \begin{pmatrix} |x'| \\ |y'| \end{pmatrix} \cdot \begin{pmatrix} -|x'| \\ |y'| \end{pmatrix} \mathrm{d}x' \mathrm{d}y' = 0, \qquad \text{(D.16a)}$$

$$\Gamma_{12}^{(5)}(C_{4z}^{-1}) = \frac{1}{K} \left\langle \psi_1^{(5)}(x',y'), P(C_{4z}^{-1})\psi_2^{(5)}(x',y') \right\rangle$$

$$= \frac{1}{K} \int\limits_{-a/2}^{a/2} \int\limits_{-a/2}^{a/2} \begin{pmatrix} |x'| \\ |y'| \end{pmatrix} \cdot \begin{pmatrix} |x'| \\ |y'| \end{pmatrix} \mathrm{d}x' \mathrm{d}y' = 1, \qquad \text{(D.16b)}$$

$$\Gamma_{21}^{(5)}(C_{4z}^{-1}) = \frac{1}{K} \left\langle \psi_2^{(5)}(x',y'), P(C_{4z}^{-1})\psi_1^{(5)}(x',y') \right\rangle$$

$$= \frac{1}{K} \int\limits_{-a/2}^{a/2} \int\limits_{-a/2}^{a/2} \begin{pmatrix} |x'| \\ -|y'| \end{pmatrix} \cdot \begin{pmatrix} -|x'| \\ |y'| \end{pmatrix} \mathrm{d}x' \mathrm{d}y' = -1, \qquad \text{(D.16c)}$$

$$\Gamma_{22}^{(5)}(C_{4z}^{-1}) = \frac{1}{K}\left\langle \psi_2^{(5)}(x',y'), P(C_{4z}^{-1})\psi_2^{(5)}(x',y') \right\rangle$$

$$= \frac{1}{K}\int\limits_{-a/2}^{a/2}\int\limits_{-a/2}^{a/2} \begin{pmatrix} |x'| \\ -|y'| \end{pmatrix}\cdot\begin{pmatrix} |x'| \\ |y'| \end{pmatrix}\mathrm{d}x'\mathrm{d}y' = 0. \tag{D.16d}$$

$$\Gamma_{11}^{(5)}(C_{2x}) = \frac{1}{K}\left\langle \psi_1^{(5)}(x',y'), P(C_{2x})\psi_1^{(5)}(x',y') \right\rangle$$

$$= \frac{1}{K}\int\limits_{-a/2}^{a/2}\int\limits_{-a/2}^{a/2} \begin{pmatrix} |x'| \\ |y'| \end{pmatrix}\cdot\begin{pmatrix} |x'| \\ -|y'| \end{pmatrix}\mathrm{d}x'\mathrm{d}y' = 0, \tag{D.17a}$$

$$\Gamma_{12}^{(5)}(C_{2x}) = \frac{1}{K}\left\langle \psi_1^{(5)}(x',y'), P(C_{2x})\psi_2^{(5)}(x',y') \right\rangle$$

$$= \frac{1}{K}\int\limits_{-a/2}^{a/2}\int\limits_{-a/2}^{a/2} \begin{pmatrix} |x'| \\ |y'| \end{pmatrix}\cdot\begin{pmatrix} |x'| \\ |y'| \end{pmatrix}\mathrm{d}x'\mathrm{d}y' = 1, \tag{D.17b}$$

$$\Gamma_{21}^{(5)}(C_{2x}) = \frac{1}{K}\left\langle \psi_2^{(5)}(x',y'), P(C_{2x})\psi_1^{(5)}(x',y') \right\rangle$$

$$= \frac{1}{K}\int\limits_{-a/2}^{a/2}\int\limits_{-a/2}^{a/2} \begin{pmatrix} |x'| \\ -|y'| \end{pmatrix}\cdot\begin{pmatrix} |x'| \\ -|y'| \end{pmatrix}\mathrm{d}x'\mathrm{d}y' = 1, \tag{D.17c}$$

$$\Gamma_{22}^{(5)}(C_{2x}) = \frac{1}{K}\left\langle \psi_2^{(5)}(x',y'), P(C_{2x})\psi_2^{(5)}(x',y') \right\rangle$$

$$= \frac{1}{K}\int\limits_{-a/2}^{a/2}\int\limits_{-a/2}^{a/2} \begin{pmatrix} |x'| \\ -|y'| \end{pmatrix}\cdot\begin{pmatrix} |x'| \\ |y'| \end{pmatrix}\mathrm{d}x'\mathrm{d}y' = 0. \tag{D.17d}$$

$$\Gamma_{11}^{(5)}(C_{2y}) = \frac{1}{K}\left\langle \psi_1^{(5)}(x',y'), P(C_{2y})\psi_1^{(5)}(x',y') \right\rangle$$

$$= \frac{1}{K}\int\limits_{-a/2}^{a/2}\int\limits_{-a/2}^{a/2} \begin{pmatrix} |x'| \\ |y'| \end{pmatrix}\cdot\begin{pmatrix} -|x'| \\ |y'| \end{pmatrix}\mathrm{d}x'\mathrm{d}y' = 0, \tag{D.18a}$$

$$\Gamma_{12}^{(5)}(C_{2y}) = \frac{1}{K}\left\langle \psi_1^{(5)}(x',y'), P(C_{2y})\psi_2^{(5)}(x',y') \right\rangle$$

$$= \frac{1}{K} \int\limits_{-a/2}^{a/2} \int\limits_{-a/2}^{a/2} \begin{pmatrix} |x'| \\ |y'| \end{pmatrix} \cdot \begin{pmatrix} -|x'| \\ -|y'| \end{pmatrix} \mathrm{d}x' \mathrm{d}y' = -1, \qquad \text{(D.18b)}$$

$$\Gamma_{21}^{(5)}(C_{2y}) = \frac{1}{K} \Big\langle \psi_2^{(5)}(x',y'), P(C_{2y})\psi_1^{(5)}(x',y') \Big\rangle$$

$$= \frac{1}{K} \int\limits_{-a/2}^{a/2} \int\limits_{-a/2}^{a/2} \begin{pmatrix} |x'| \\ -|y'| \end{pmatrix} \cdot \begin{pmatrix} -|x'| \\ |y'| \end{pmatrix} \mathrm{d}x' \mathrm{d}y' = -1, \qquad \text{(D.18c)}$$

$$\Gamma_{22}^{(5)}(C_{2y}) = \frac{1}{K} \Big\langle \psi_2^{(5)}(x',y'), P(C_{2y})\psi_2^{(5)}(x',y') \Big\rangle$$

$$= \frac{1}{K} \int\limits_{-a/2}^{a/2} \int\limits_{-a/2}^{a/2} \begin{pmatrix} |x'| \\ -|y'| \end{pmatrix} \cdot \begin{pmatrix} -|x'| \\ -|y'| \end{pmatrix} \mathrm{d}x' \mathrm{d}y' = 0. \qquad \text{(D.18d)}$$

$$\Gamma_{11}^{(5)}(C_{2A}) = \frac{1}{K} \Big\langle \psi_1^{(5)}(x',y'), P(C_{2A})\psi_1^{(5)}(x',y') \Big\rangle$$

$$= \frac{1}{K} \int\limits_{-a/2}^{a/2} \int\limits_{-a/2}^{a/2} \begin{pmatrix} |x'| \\ |y'| \end{pmatrix} \cdot \begin{pmatrix} |x'| \\ |y'| \end{pmatrix} \mathrm{d}x' \mathrm{d}y' = 1, \qquad \text{(D.19a)}$$

$$\Gamma_{12}^{(5)}(C_{2A}) = \frac{1}{K} \Big\langle \psi_1^{(5)}(x',y'), P(C_{2A})\psi_2^{(5)}(x',y') \Big\rangle$$

$$= \frac{1}{K} \int\limits_{-a/2}^{a/2} \int\limits_{-a/2}^{a/2} \begin{pmatrix} |x'| \\ |y'| \end{pmatrix} \cdot \begin{pmatrix} -|x'| \\ |y'| \end{pmatrix} \mathrm{d}x' \mathrm{d}y' = 0, \qquad \text{(D.19b)}$$

$$\Gamma_{21}^{(5)}(C_{2A}) = \frac{1}{K} \Big\langle \psi_2^{(5)}(x',y'), P(C_{2A})\psi_1^{(5)}(x',y') \Big\rangle$$

$$= \frac{1}{K} \int\limits_{-a/2}^{a/2} \int\limits_{-a/2}^{a/2} \begin{pmatrix} |x'| \\ -|y'| \end{pmatrix} \cdot \begin{pmatrix} |x'| \\ |y'| \end{pmatrix} \mathrm{d}x' \mathrm{d}y' = 0, \qquad \text{(D.19c)}$$

$$\Gamma_{22}^{(5)}(C_{2A}) = \frac{1}{K} \Big\langle \psi_2^{(5)}(x',y'), P(C_{2A})\psi_2^{(5)}(x',y') \Big\rangle$$

$$= \frac{1}{K} \int\limits_{-a/2}^{a/2} \int\limits_{-a/2}^{a/2} \begin{pmatrix} |x'| \\ -|y'| \end{pmatrix} \cdot \begin{pmatrix} -|x'| \\ |y'| \end{pmatrix} \mathrm{d}x' \mathrm{d}y' = -1. \qquad \text{(D.19d)}$$

$$\Gamma_{11}^{(5)}(C_{2B}) = \frac{1}{K}\left\langle \psi_1^{(5)}(x',y'), P(C_{2B})\psi_1^{(5)}(x',y') \right\rangle$$

$$= \frac{1}{K} \int\limits_{-a/2}^{a/2} \int\limits_{-a/2}^{a/2} \begin{pmatrix} |x'| \\ |y'| \end{pmatrix} \cdot \begin{pmatrix} -|x'| \\ -|y'| \end{pmatrix} dx'dy' = -1, \qquad \text{(D.20a)}$$

$$\Gamma_{12}^{(5)}(C_{2B}) = \frac{1}{K}\left\langle \psi_1^{(5)}(x',y'), P(C_{2B})\psi_2^{(5)}(x',y') \right\rangle$$

$$= \frac{1}{K} \int\limits_{-a/2}^{a/2} \int\limits_{-a/2}^{a/2} \begin{pmatrix} |x'| \\ |y'| \end{pmatrix} \cdot \begin{pmatrix} |x'| \\ -|y'| \end{pmatrix} dx'dy' = 0, \qquad \text{(D.20b)}$$

$$\Gamma_{21}^{(5)}(C_{2B}) = \frac{1}{K}\left\langle \psi_2^{(5)}(x',y'), P(C_{2B})\psi_1^{(5)}(x',y') \right\rangle$$

$$= \frac{1}{K} \int\limits_{-a/2}^{a/2} \int\limits_{-a/2}^{a/2} \begin{pmatrix} |x'| \\ -|y'| \end{pmatrix} \cdot \begin{pmatrix} -|x'| \\ -|y'| \end{pmatrix} dx'dy' = 0, \qquad \text{(D.20c)}$$

$$\Gamma_{22}^{(5)}(C_{2B}) = \frac{1}{K}\left\langle \psi_2^{(5)}(x',y'), P(C_{2B})\psi_2^{(5)}(x',y') \right\rangle$$

$$= \frac{1}{K} \int\limits_{-a/2}^{a/2} \int\limits_{-a/2}^{a/2} \begin{pmatrix} |x'| \\ -|y'| \end{pmatrix} \cdot \begin{pmatrix} |x'| \\ -|y'| \end{pmatrix} dx'dy' = 1. \qquad \text{(D.20d)}$$

Bibliography

[1] L. C. Godara, "Applications of antenna arrays to mobile communications. I. Performance improvement, feasibility, and system considerations," *Proceedings of the IEEE*, vol. 85, no. 7, pp. 1031–1060, 1997.

[2] A. J. Paulraj, D. A. Gore, R. U. Nabar, and H. Bolcskei, "An overview of MIMO communications – a key to gigabit wireless," *Proceedings of the IEEE*, vol. 92, no. 2, pp. 198–218, 2004.

[3] J. Mietzner, R. Schober, L. Lampe, W. H. Gerstacker, and P. A. Hoeher, "Multiple-antenna techniques for wireless communications – a comprehensive literature survey," *IEEE Communications Surveys Tutorials*, vol. 11, no. 2, pp. 87–105, 2009.

[4] C. A. Balanis and P. I. Ioannides, *Introduction to Smart Antennas*, ser. Synthesis Lectures on Antennas.   San Rafael, CA, USA: Morgan & Claypool, 2007.

[5] C. A. Balanis, *Antenna Theory: Analysis and Design*, 3rd ed.   Hoboken, NJ, USA: John Wiley & Sons, 2005.

[6] L. C. Godara, "Application of antenna arrays to mobile communications. II. Beam-forming and direction-of-arrival considerations," *Proceedings of the IEEE*, vol. 85, no. 8, pp. 1195–1245, 1997.

[7] J. H. Winters, J. Salz, and R. D. Gitlin, "The impact of antenna diversity on the capacity of wireless communication systems," *IEEE Transactions on Communications*, vol. 42, no. 234, pp. 1740–1751, 1994.

[8] S. N. Diggavi, N. Al-Dhahir, A. Stamoulis, and A. R. Calderbank, "Great expectations: the value of spatial diversity in wireless networks," *Proceedings of the IEEE*, vol. 92, no. 2, pp. 219–270, 2004.

[9] D. G. Brennan, "Linear diversity combining techniques," *Proceedings of the IEEE*, vol. 91, no. 2, pp. 331–356, 2003.

[10] S. M. Alamouti, "A simple transmit diversity technique for wireless communications," *IEEE Journal on Selected Areas in Communications*, vol. 16, no. 8, pp. 1451–1458, 1998.

[11] J. Winters, "On the capacity of radio communication systems with diversity in a Rayleigh fading environment," *IEEE Journal on Selected Areas in Communications*, vol. 5, no. 5, pp. 871–878, 1987.

[12] G. J. Foschini, "Layered space-time architecture for wireless communication in a fading environment when using multi-element antennas," *Bell Labs Technical Journal*, vol. 1, no. 2, pp. 41–59, 1996.

[13] R. G. Vaughan and J. B. Andersen, "Antenna diversity in mobile communications," *IEEE Transactions on Vehicular Technology*, vol. 36, no. 4, pp. 149–172, 1987.

[14] G. D. Durgin, *Space-Time Wireless Channels*, ser. Prentice Hall Communications Engineering and Emerging Technologies Series. Upper Saddle River, NJ, USA: Prentice Hall PTR, 2003.

[15] T. Brown, E. De Carvalho, and P. Kyritsi, *Practical Guide to the MIMO Radio Channel with MATLAB Examples*. Hoboken, NJ, USA: John Wiley & Sons, 2012.

[16] D. Manteuffel, "MIMO antenna design challenges," in *2009 Loughborough Antennas & Propagation Conference*, Nov 2009, pp. 50–56.

[17] C.-N. Chuah, D. N. C. Tse, J. M. Kahn, and R. A. Valenzuela, "Capacity scaling in MIMO wireless systems under correlated fading," *IEEE Transactions on Information Theory*, vol. 48, no. 3, pp. 637–650, 2002.

[18] C. Waldschmidt and W. Wiesbeck, "Compact wide-band multimode antennas for MIMO and diversity," *IEEE Transactions on Antennas and Propagation*, vol. 52, no. 8, pp. 1963–1969, 2004.

[19] B. Clerckx and C. Oestges, *MIMO Wireless Networks*, 2nd ed. Oxford, UK: Academic Press, 2013.

[20] T. Svantesson, "An antenna solution for MIMO channels: the multimode antenna," in *Conference Record of the Thirty-Fourth Asilomar Conference on Signals, Systems and Computers (Cat. No.00CH37154)*, vol. 2, 2000, pp. 1617–1621.

[21] R. G. Vaughan and J. B. Andersen, "A multiport patch antenna for mobile communications," in *1984 14th European Microwave Conference*, 1984, pp. 607–612.

[22] F. Demmerle and W. Wiesbeck, "A biconical multibeam antenna for space-division multiple access," *IEEE Transactions on Antennas and Propagation*, vol. 46, no. 6, pp. 782–787, 1998.

[23] R. Garbacz and R. Turpin, "A generalized expansion for radiated and scattered fields," *IEEE Transactions on Antennas and Propagation*, vol. 19, no. 3, pp. 348–358, May 1971.

[24] R. Harrington and J. Mautz, "Theory of characteristic modes for conducting bodies," *IEEE Transactions on Antennas and Propagation*, vol. 19, no. 5, pp. 622–628, Sep 1971.

[25] Y. Chen and C. Wang, *Characteristic Modes: Theory and Applications in Antenna Engineering*. Hoboken, NJ, USA: John Wiley & Sons, 2015. [Online]. Available: https://ieeexplore.ieee.org/servlet/opac?bknumber=8040064

[26] R. Harrington and J. Mautz, "Control of radar scattering by reactive loading," *IEEE Transactions on Antennas and Propagation*, vol. 20, no. 4, pp. 446–454, 1972.

[27] M. Cabedo-Fabres, E. Antonino-Daviu, A. Valero-Nogueira, and M. Bataller, "The theory of characteristic modes revisited: A contribution to the design of antennas for modern applications," *Antennas and Propagation Magazine, IEEE*, vol. 49, no. 5, pp. 52–68, Oct 2007.

[28] M. Cabedo Fabrés, "Systematic design of antennas using the theory of characteristic modes," Ph.D. dissertation, Universitat Politècnica de València, 2007. [Online]. Available: http://hdl.handle.net/10251/1883

[29] E. Antonino Daviu, "Analysis and design of antennas for wireless communications using modal methods," Ph.D. dissertation, Universitat Politècnica de València, 2008. [Online]. Available: http://hdl.handle.net/10251/2188

[30] M. Vogel, G. Gampala, D. Ludick, U. Jakobus, and C. J. Reddy, "Characteristic mode analysis: Putting physics back into simulation," *IEEE Antennas and Propagation Magazine*, vol. 57, no. 2, pp. 307–317, 2015.

[31] D. Manteuffel, "Characteristic mode based antenna design – a straight forward approach to small form factor antenna integration," in *2015 9th European Conference on Antennas and Propagation (EuCAP)*, 2015, pp. 1–5.

[32] J. J. Adams and J. T. Bernhard, "A modal approach to tuning and bandwidth enhancement of an electrically small antenna," *IEEE Transactions on Antennas and Propagation*, vol. 59, no. 4, pp. 1085–1092, 2011.

[33] Z. Miers, H. Li, and B. K. Lau, "Design of bandwidth-enhanced and multiband MIMO antennas using characteristic modes," *IEEE Antennas and Wireless Propagation Letters*, vol. 12, pp. 1696–1699, 2013.

[34] J. J. Adams and J. T. Bernhard, "Broadband equivalent circuit models for antenna impedances and fields using characteristic modes," *IEEE Transactions on Antennas and Propagation*, vol. 61, no. 8, pp. 3985–3994, 2013.

[35] J. L. T. Ethier and D. A. McNamara, "Antenna shape synthesis without prior specification of the feedpoint locations," *IEEE Transactions on Antennas and Propagation*, vol. 62, no. 10, pp. 4919–4934, 2014.

[36] B. Yang and J. J. Adams, "Systematic shape optimization of symmetric MIMO antennas using characteristic modes," *IEEE Transactions on Antennas and Propagation*, vol. 64, no. 7, pp. 2668–2678, 2016.

[37] E. Safin and D. Manteuffel, "Manipulation of characteristic wave modes by impedance loading," *IEEE Transactions on Antennas and Propagation*, vol. 63, no. 4, pp. 1756–1764, 2015.

[38] S. K. Chaudhury, W. L. Schroeder, and H. J. Chaloupka, "MIMO antenna system based on orthogonality of the characteristic modes of a mobile device," in *2007 2nd International ITG Conference on Antennas*, March 2007, pp. 58–62.

[39] E. Antonino-Daviu, M. Cabedo-Fabres, M. Gallo, M. Ferrando-Bataller, and M. Bozzetti, "Design of a multimode MIMO antenna using characteristic modes," in *2009 3rd European Conference on Antennas and Propagation*, 2009, pp. 1840–1844.

[40] S. K. Chaudhury, H. J. Chaloupka, and A. Ziroff, "Multiport antenna systems for MIMO and diversity," in *Proceedings of the Fourth European Conference on Antennas and Propagation*, April 2010, pp. 1–5.

[41] R. Martens, E. Safin, and D. Manteuffel, "Selective excitation of characteristic modes on small terminals," in *Proceedings of the 5th European Conference on Antennas and Propagation (EuCAP)*, April 2011, pp. 2492–2496.

[42] ——, "Inductive and capacitive excitation of the characteristic modes of small terminals," in *2011 Loughborough Antennas & Propagation Conference*, Nov 2011, pp. 1–4.

[43] R. Martens and D. Manteuffel, "Systematic design method of a mobile multiple antenna system using the theory of characteristic modes," *IET Microwaves, Antennas & Propagation*, vol. 8, no. 12, pp. 887–893, Sep. 2014.

[44] R. Martens, J. Holopainen, E. Safin, J. Ilvonen, and D. Manteuffel, "Optimal dual-antenna design in a small terminal multiantenna system," *IEEE Antennas and Wireless Propagation Letters*, vol. 12, pp. 1700–1703, 2013.

[45] H. Li, Z. T. Miers, and B. K. Lau, "Design of orthogonal MIMO handset antennas based on characteristic mode manipulation at frequency bands below 1 GHz," *IEEE Transactions on Antennas and Propagation*, vol. 62, no. 5, pp. 2756–2766, May 2014.

[46] D. Manteuffel and R. Martens, "Compact multimode multielement antenna for indoor UWB massive MIMO," *IEEE Transactions on Antennas and Propagation*, vol. 64, no. 7, pp. 2689–2697, 2016.

[47] M. Bouezzeddine and W. L. Schroeder, "Design of a wideband, tunable four-port MIMO antenna system with high isolation based on the theory of characteristic modes," *IEEE Transactions on Antennas and Propagation*, vol. 64, no. 7, pp. 2679–2688, July 2016.

[48] W. Su, Q. Zhang, S. Alkaraki, Y. Zhang, X. Zhang, and Y. Gao, "Radiation energy and mutual coupling evaluation for multimode MIMO antenna based on the theory of characteristic mode," *IEEE Transactions on Antennas and Propagation*, vol. 67, no. 1, pp. 74–84, 2019.

[49] D. W. Kim and S. Nam, "Systematic design of a multiport MIMO antenna with bilateral symmetry based on characteristic mode analysis," *IEEE Transactions on Antennas and Propagation*, vol. 66, no. 3, pp. 1076–1085, March 2018.

[50] N. L. Johannsen and P. A. Hoeher, "Single-element beamforming using multi-mode antenna patterns," *IEEE Wireless Communications Letters*, vol. 9, no. 7, pp. 1120–1123, 2020.

[51] R. Pöhlmann, S. A. Almasri, S. Zhang, T. Jost, A. Dammann, and P. A. Hoeher, "On the potential of multi-mode antennas for direction-of-arrival estimation," *IEEE Transactions on Antennas and Propagation*, vol. 67, no. 5, pp. 3374–3386, 2019.

[52] P. A. Hoeher, D. Manteuffel, N. Doose, and N. Peitzmeier, "Ultra-wideband massive MIMO communications using multi-mode antennas," *Frequenz*, vol. 71, no. 9-10, pp. 439–448, 2017. [Online]. Available: https://www.degruyter.com/view/journals/freq/71/9-10/article-p439.xml

[53] P. A. Hoeher and N. Doose, "A massive MIMO terminal concept based on small-size multi-mode antennas," *Transactions on Emerging Telecommunications Technologies*, vol. 28, no. 2, p. e2934, 2017. [Online]. Available: https://onlinelibrary.wiley.com/doi/abs/10.1002/ett.2934

[54] N. L. Johannsen, N. Peitzmeier, P. A. Hoeher, and D. Manteuffel, "M4 — Multi-Mode Massive MIMO," in *Wireless 100 Gbps And Beyond. Architectures, Approaches and Findings of German Research Foundation (DFG) Priority Programme SPP1655*, 1st ed., R. Kraemer and S. Scholz, Eds.   Frankfurt (Oder), Germany: IHP – Innovations for High Performance Microelectronics, 2020, ch. 6.

[55] ——, "On the feasibility of multi-mode antennas in UWB and IoT applications below 10 GHz," *IEEE Communications Magazine*, vol. 58, no. 3, pp. 69–75, 2020.

[56] N. Peitzmeier and D. Manteuffel, "Selective excitation of characteristic modes on an electrically large antenna for MIMO applications," in *12th European Conference on Antennas and Propagation (EuCAP 2018)*, April 2018, pp. 1–5.

[57] L. D. Landau and E. M. Lifshitz, *Quantum Mechanics: Non-Relativistic Theory*, 3rd ed., ser. Course of Theoretical Physics. Oxford, UK: Pergamon Press, 1977, ch. XII. The Theory of Symmetry.

[58] J. Knorr, "Consequences of symmetry in the computation of characteristic modes for conducting bodies," *IEEE Transactions on Antennas and Propagation*, vol. 21, no. 6, pp. 899–902, Nov 1973.

[59] R. Harrington and J. Mautz, "Computation of characteristic modes for conducting bodies," *IEEE Transactions on Antennas and Propagation*, vol. 19, no. 5, pp. 629–639, Sep 1971.

[60] K. R. Schab, J. M. Outwater, and J. T. Bernhard, "Classifying characteristic mode crossing avoidances with symmetry and energy coupling," in *2016 IEEE International Symposium on Antennas and Propagation (APSURSI)*, June 2016, pp. 13–14.

[61] K. R. Schab and J. T. Bernhard, "A group theory rule for predicting eigenvalue crossings in characteristic mode analyses," *IEEE Antennas and Wireless Propagation Letters*, vol. 16, pp. 944–947, 2017.

[62] E. Safin and D. Manteuffel, "Advanced eigenvalue tracking of characteristic modes," *IEEE Transactions on Antennas and Propagation*, vol. 64, no. 7, pp. 2628–2636, July 2016.

[63] M. Masek, M. Capek, L. Jelinek, and K. Schab, "Modal tracking based on group theory," *IEEE Transactions on Antennas and Propagation*, vol. 68, no. 2, pp. 927–937, Feb 2020.

[64] R. F. Harrington, *Time-Harmonic Electromagnetic Fields*, ser. IEEE Press Series on Electromagnetic Wave Theory. Piscataway, NJ, USA: Wiley-IEEE Press, 2001. [Online]. Available: https://ieeexplore.ieee.org/servlet/opac?bknumber=5264717

[65] J. A. Stratton, *Electromagnetic Theory*, ser. International Series in Pure and Applied Physics. New York, NY, USA: McGraw-Hill, 1941. [Online]. Available: https://ieeexplore.ieee.org/servlet/opac?bknumber=7362911

[66] F. W. Byron and R. W. Fuller, *Mathematics of Classical and Quantum Physics*, ser. Addison-Wesley Series in Advanced Physics. Reading, MA, USA: Addison-Wesley, 1970, vol. 2.

[67] E. Safin and D. Manteuffel, "Reconstruction of the characteristic modes on an antenna based on the radiated far field," *IEEE Transactions on Antennas and Propagation*, vol. 61, no. 6, pp. 2964–2971, June 2013.

[68] R. F. Harrington, *Field Computation by Moment Methods*, ser. IEEE Press Series on Electromagnetic Waves. Piscataway, NJ, USA: Wiley-IEEE Press, 1993. [Online]. Available: https://ieeexplore.ieee.org/servlet/opac?bknumber=5264934

[69] S. Rao, D. Wilton, and A. Glisson, "Electromagnetic scattering by surfaces of arbitrary shape," *IEEE Transactions on Antennas and Propagation*, vol. 30, no. 3, pp. 409–418, May 1982.

[70] S. N. Makarov, *Antenna and EM Modeling with MATLAB*. Hoboken, NJ, USA: John Wiley & Sons, 2002.

[71] *MATLAB version 9.8.0.1359463 (R2020a)*, The MathWorks, Inc., 1 Apple Hill Drive, Natick, MA 01760, USA, 2020.

[72] E. Safin, "Modal analysis methods for small antenna design," Ph.D. dissertation, Christian-Albrechts-Universität zu Kiel, 2017. [Online]. Available: https://macau.uni-kiel.de/receive/diss_mods_00020241

[73] R. Klein, *Algorithmische Geometrie: Grundlagen, Methoden, Anwendungen*, 2nd ed. Berlin, Germany: Springer, 2005. [Online]. Available: https://link.springer.com/book/10.1007%2F3-540-27619-X

[74] R. Martens and D. Manteuffel, "A feed network for the selective excitation of specific characteristic modes on small terminals," in *2012 6th European Conference on Antennas and Propagation (EuCAP)*, March 2012, pp. 1842–1846.

[75] J. F. Cornwell, *Group Theory in Physics: An Introduction*. San Diego, CA, USA: Academic Press, 1997.

[76] R. McWeeny, *Symmetry: An Introduction to Group Theory and its Applications*, ser. The International Encyclopedia of Physical Chemistry and Chemical Physics; Topic 1: Mathematical Techniques. Oxford, UK: Pergamon Press, 1963.

[77] M. Tinkham, *Group Theory and Quantum Mechanics*. New York, NY, USA: McGraw-Hill, 1964.

[78] G. F. Koster, *Properties of the Thirty-Two Point Groups*. Cambridge, MA, USA: M.I.T. Press, 1963.

[79] F. W. Byron and R. W. Fuller, *Mathematics of Classical and Quantum Physics*, ser. Addison-Wesley Series in Advanced Physics. Reading, MA, USA: Addison-Wesley, 1969, vol. 1.

[80] J. H. Wilkinson, *The Algebraic Eigenvalue Problem*, ser. Monographs on numerical analysis. Oxford, UK: Clarendon Press, 1988.

[81] L. M. Tel and E. Perez-Romero, "Density of elements in continuous point groups," *Journal of Chemical Education*, vol. 65, no. 7, p. 585, 1988. [Online]. Available: https://doi.org/10.1021/ed065p585

[82] A. Friedrich, L. Berkelmann, T. Martinelli, B. Geck, O. Klemp, and I. Kriebitzsch, "An active three-dimensional GPS patch antenna using MID-technology," in *2015 European Microwave Conference (EuMC)*, Sep. 2015, pp. 1395–1398.

[83] R. J. Garbacz, "A generalized expansion for radiated and scattered fields," Ph.D. dissertation, The Ohio State University, 1968.

[84] J. E. Hansen, *Spherical Near-Field Antenna Measurements*, ser. IET Electromagnetic Waves Series. London, UK: IET, 1988.

[85] M. Abramowitz and I. Stegun, *Handbook of Mathematical Functions with Formulas, Graphs, and Tables*, ser. National Bureau of Standards Applied Mathematics Series. Washington, DC, USA: U.S. Government Printing Office, 1964. [Online]. Available: https://dlmf.nist.gov/

[86] S. Zhang and J. Jin, *Computation of Special Functions*. New York, NY, USA: John Wiley & Sons, 1996.

[87] L.-W. Li, X.-K. Kang, and M.-S. Leong, *Spheroidal Wave Functions in Electromagnetic Theory*, ser. Wiley Series in Microwave and Optical Engineering. New York, NY, USA: John Wiley & Sons, 2002.

[88] M. Capek, V. Losenicky, L. Jelinek, and M. Gustafsson, "Validating the characteristic modes solvers," *IEEE Transactions on Antennas and Propagation*, vol. 65, no. 8, pp. 4134–4145, 2017.

[89] J. Meixner, "Strenge Theorie der Beugung elektromagnetischer Wellen an der vollkommen leitenden Kreisscheibe," *Zeitschrift für Naturforschung A*, vol. 3, no. 8-11, pp. 506–518, 1948. [Online]. Available: https://www.degruyter.com/view/journals/zna/3/8-11/article-p506.xml

[90] R. Valkonen, A. Lehtovuori, and D. Manteuffel, "Capacitive coupling elements – changing the way of designing antennas," in *The 8th European Conference on Antennas and Propagation (EuCAP 2014)*, 2014, pp. 229–233.

[91] R. Ledig, "Coupling element antennas for small terminals based on the characteristic modes," Ph.D. dissertation, Christian-Albrechts-Universität zu Kiel, 2015. [Online]. Available: https://macau.uni-kiel.de/receive/diss_mods_00018351

[92] D. M. Pozar, *Microwave Engineering*, 2nd ed. New York, NY, USA: John Wiley & Sons, 1998.

[93] C. Volmer, "Compact antenna arrays in mobile communications: A quantitative analysis of radiator coupling," Ph.D. dissertation, Technische Universität Ilmenau, Dec 2009. [Online]. Available: https://www.db-thueringen.de/receive/dbt_mods_00014752

[94] *Empire XPU 7.70*, IMST GmbH, Carl-Friedrich-Gauss-Str. 2–4, Kamp-Lintfort 47475, Germany, 2020.

[95] *RO4000 Series High Frequency Circuit Materials*, Rogers Corporation, 100 S. Roosevelt Avenue, Chandler, AZ 85226, USA, 2018, data sheet. [Online]. Available: https://www.rogerscorp.com/-/media/project/rogerscorp/documents/advanced-connectivity-solutions/english/data-sheets/ro4000-laminates-ro4003c-and-ro4350b---data-sheet.pdf

[96] *RO4000 Series Bondply*, Rogers Corporation, 100 S. Roosevelt Avenue, Chandler, AZ 85226, USA, 2019, data sheet. [Online]. Available: https://www.rogerscorp.com/-/media/project/rogerscorp/documents/advanced-connectivity-solutions/english/data-sheets/ro4400-series-bondply-data-sheet---ro4450f-ro4450t-and-ro4460g2-bondply.pdf

[97] *141 Semi-rigid Coax Cable with Tinned Aluminum Outer Conductor*, Pasternack Enterprises, Inc., P.O. Box 16759, Irvine, CA 92623, USA,

2020, data sheet. [Online]. Available: https://www.pasternack.com/ images/ProductPDF/PE-SR402AL-STRAIGHT.pdf

[98] N. Peitzmeier and D. Manteuffel, "Upper bounds and design guidelines for realizing uncorrelated ports on multimode antennas based on symmetry analysis of characteristic modes," *IEEE Transactions on Antennas and Propagation*, vol. 67, no. 6, pp. 3902–3914, 2019.

[99] *SMA Straight Jack PCB*, Rosenberger Hochfrequenztechnik GmbH & Co. KG, P.O. Box 1260, Tittmoning 84526, Germany, 2020, data sheet. [Online]. Available: https://products.rosenberger.com/_ocassets/ db/32K10A-40ML5.pdf

[100] J. Rahola, "Bandwidth potential and electromagnetic isolation: Tools for analysing the impedance behaviour of antenna systems," in *2009 3rd European Conference on Antennas and Propagation*, 2009, pp. 944–948.

[101] J. Villanen, J. Ollikainen, O. Kivekas, and P. Vainikainen, "Coupling element based mobile terminal antenna structures," *IEEE Transactions on Antennas and Propagation*, vol. 54, no. 7, pp. 2142–2153, 2006.

[102] M. Capek, P. Hazdra, M. Masek, and V. Losenicky, "Analytical representation of characteristic mode decomposition," *IEEE Transactions on Antennas and Propagation*, vol. 65, no. 2, pp. 713–720, Feb 2017.

Curriculum Vitae

Personal Details

Name	Nikolai Peitzmeier
Date of Birth	19 July 1988
Place of Birth	Luebbecke, Germany
Nationality	German

Academic Education

04/2015–07/2021	Leibniz University Hannover Ph.D. Electrical Engineering and Information Technology Thesis: "Systematic Analysis and Design of Multimode Antennas Based on Symmetry Properties of Characteristic Modes"
10/2012–12/2014	Leibniz University Hannover M.Sc. Electrical Engineering and Information Technology Field of Study: Communications Engineering Thesis: "Analysis and Design of RFID Transponders for MIMO Transmission via Backscatter Modulation Considering Antenna Mutual Coupling"
10/2009–01/2013	Leibniz University Hannover B.Sc. Electrical Engineering and Information Technology Field of Study: Communications Engineering Thesis: "Analysis of Selected Circular Antenna Structures for Use within Metal Objects"

Work Experience

01/2015–07/2021	Leibniz University Hannover Institute of Microwave and Wireless Systems Research Assistant

10/2013–03/2014	deister electronic, Barsinghausen Internship at UHF department
10/2011–09/2013	Leibniz University Hannover Institute of Microwave and Wireless Systems Student Assistant
11/2011–02/2012	Leibniz University Hannover Institute of Electronic Materials and Devices Teaching Assistant in Physics for Electrical Engineers
05/2009–07/2009	WAGO Kontakttechnik, Minden Internship at Test Laboratory

Publications

Book Chapter	N. L. Johannsen, N. Peitzmeier, P. A. Hoeher, and D. Manteuffel, "M4 — Multi-Mode Massive MIMO," in *Wireless 100 Gbps And Beyond. Architectures, Approaches and Findings of German Research Foundation (DFG) Priority Programme SPP1655*, 1st ed., R. Kraemer and S. Scholz, Eds. Frankfurt (Oder), Germany: IHP – Innovations for High Performance Microelectronics, 2020, ch. 6.
Journal Articles	N. Peitzmeier, T. Hahn, and D. Manteuffel, "Systematic Design of Multimode Antennas for MIMO Applications by Leveraging Symmetry," *IEEE Transactions on Antennas and Propagation*, in press, 2021.
	N. L. Johannsen, N. Peitzmeier, P. A. Hoeher, and D. Manteuffel, "On the feasibility of multi-mode antennas in UWB and IoT applications below 10 GHz," *IEEE Communications Magazine*, vol. 58, no. 3, pp. 69–75, 2020.
	N. Peitzmeier and D. Manteuffel, "Upper bounds and design guidelines for realizing uncorrelated ports on multimode antennas based on symmetry analysis of characteristic modes," *IEEE Transactions on Antennas and Propagation*, vol. 67, no. 6, pp. 3902–3914, 2019.
	E. Denicke, H. Hartmann, N. Peitzmeier, and B. Geck, "Backscatter beamforming: A transponder for novel MIMO

RFID transmission schemes," *IEEE Journal of Radio Frequency Identification*, vol. 2, no. 2, pp. 80–85, 2018.

P. A. Hoeher, D. Manteuffel, N. Doose, and N. Peitzmeier, "Ultra-wideband massive MIMO communications using multi-mode antennas," *Frequenz*, vol. 71, no. 9-10, pp. 439–448, 2017.

Conferences   L. Grundmann, N. Peitzmeier, and D. Manteuffel, "Investigation of Direction of Arrival Estimation Using Characteristic Modes," in *2021 15th European Conference on Antennas and Propagation (EuCAP)*, 2021, pp. 1–5.

N. Peitzmeier and D. Manteuffel, "Systematic design method for asymmetric multiport antennas based on characteristic modes," in *2020 14th European Conference on Antennas and Propagation (EuCAP)*, 2020, pp. 1–5.

N. Peitzmeier and D. Manteuffel, "Systematic design of an ultra-wideband six-port multi-mode antenna element using symmetry properties of characteristic modes," in *2019 International Conference on Electromagnetics in Advanced Applications (ICEAA)*, 2019, pp. 466–471.

N. Peitzmeier and D. Manteuffel, "Multi-mode antenna concept based on symmetry analysis of characteristic modes," in *2019 13th European Conference on Antennas and Propagation (EuCAP)*, 2019, pp. 1–5.

N. Peitzmeier and D. Manteuffel, "Beamforming concept for multi-beam antennas based on characteristic modes," in *2018 IEEE International Symposium on Antennas and Propagation & USNC/URSI National Radio Science Meeting*, 2018, pp. 1113–1114.

H. Hartmann, N. Peitzmeier, and D. Manteuffel, "Wideband equivalent circuit model for smartphone antennas based on characteristic modes," in *2018 IEEE International Symposium on Antennas and Propagation & USNC/URSI National Radio Science Meeting*, 2018, pp. 1787–1788.

N. Peitzmeier and D. Manteuffel, "Selective excitation of characteristic modes on an electrically large antenna for MIMO applications," in *2018 12th European Conference on Antennas and Propagation (EuCAP)*, 2018, pp. 1–5.

Y. Chen, K. Schab, M. Čapek, M. Mašek, B. K. Lau, H. Aliakbari, Y. Haykir, Q. Wu, W. J. Strydom, N. Peitzmeier, M. Jovicic, S. Genovesi, and F. A. Dicandia, "Benchmark problem definition and cross-validation for characteristic mode solvers," in *2018 12th European Conference on Antennas and Propagation (EuCAP)*, 2018, pp. 1–5.

Patent   D. Manteuffel and N. Peitzmeier, "Mobilfunk-Basisstation zur Ausbildung einer Mobilfunk-Zelle," German Patent DE 10 2018 114 879, July 11, 2019.